THESIS FOR THE DEGREE OF LICENTIATE OF ENGINEERING

Synchronous Machines with High-Frequency Brushless Excitation for Vehicle Applications

JUNFEI TANG

Division of Electric Power Engineering

Department of Electrical Engineering

CHALMERS UNIVERSITY OF TECHNOLOGY

Gothenburg, Sweden 2019

Synchronous Machines with High-Frequency Brushless Excitation for Vehicle Applications

JUNFEI TANG

Licentiate Thesis at Chalmers University of Technology

Technical Report No R010/2019

ISSN 1403-266X

Division of Electric Power Engineering

Department of Electrical Engineering

Chalmers University of Technology

SE-412 79 Gothenburg

Sweden

Telephone +46 (0)31-772 1000

Chalmers Library, Reproservice

Gothenburg, Sweden 2019

Synchronous Machines with High-Frequency Brushless Excitation for Vehicle Applications

Junfei Tang

Department of Electrical Engineering

Division of Electric Power Engineering

Abstract

Electrically excited synchronous machines (EESM) are becoming an alternative to permanent magnet synchronous machines (PMSM) in electric vehicle (EV) applications. This mainly attributes to the zero usage of rare-earth material as well as the capabilities of high starting torque and good field weakening provided by EESM. EESM also improves safety in case of converter failure at high speed. The prevalence of wireless power transfer (WPT) technologies enables the employment of high frequency brushless excitation in EESM. This reduces the friction loss and maintenance effort compared with traditional excitation through brushes and sliprings.

Hence this study aims at investigating the potential of EESM with high frequency brushless excitation in EV applications. Modeling, design and control are the main aspects of interest in this study. Due to the varieties of different vehicle applications, this study covers the developments of three EESM drive systems, one for mild hybrid vehicles, one for electric passenger cars and one for heavy duty vehicles.

To achieve a comprehensive understanding of the system, modeling is firstly studied. This includes the modeling of the machine as well as the modeling of the high frequency brushless excitation system. Nonlinear properties of magnetic material are taken into considerations. Based on the machine modeling, the vector loci of current, voltage, torque and power factor in dq-frame as well as the envelop in torque-speed map are derived analytically. One step further, algorithms to achieve unity power factor along with minimizations of copper loss or field current are studied. To achieve unity power factor at high speed, the field excitation needs to be stronger than the armature reaction.

The design of the system starts with profiling of the specifications for the three applications. The varieties in specifications lead to the differences in design strategies. This study adopts a general design procedure with interactions of FEM analysis and operation point iterations. Then the design strategies are established based on each set of design specifications to tune the parameters of the machine geometry accordingly. The design for mild hybrid vehicles emphasizes on widening the flux path. In terms of the design for electric passenger cars, a good balance is required between copper area and flux path. Comparisons between open-slot and closed-slot designs bring a trade-off of torque ripples and average torque. Adding ferrite to the top of rotor slots introduces a study of influence from the ferrite pieces to the

field excitation. This includes a possible ease of local saturation in rotor and a reduction of copper losses etc. As for the machine design for heavy-duty vehicles, investigations show that, the adjustable field in EESM brings a significant benefit in field weakening operation.

A 48 V EESM with high frequency brushless excitation for mild hybrid vehicles is prototyped. The experimental results of both machine and exciter are consistent with the FEM calculation results. This verifies the modeling and the methods that are applied in the design and analysis.

One challenge for the prevalence of EESM is the difficulty to access the field winding after assembly. As a solution, an algorithm is developed to estimate the field winding current and temperature. The dc-link current is utilized as a feedback in the algorithm to correct the estimations. The current and temperature variations are tracked quite well. As one step further, a closed-loop field current control is established. The ability to track field current reference is experimental verified as well. This closed-loop field current control enables a complete dynamic closed-loop control of the EESM.

Index Terms: Electrically excited synchronous machines, electric vehicles, brushless excitation, machine modeling, machine design, machine control.

Acknowledgement

I would like to take the opportunity here to thank all of those that have had positive impact of this work.

Firstly, I would like to express my gratitude to my main supervisor Yujing Liu for his continuous support during the work. His enthusiastic spirits have encouraged me to explore the areas that I enjoyed. His knowledge and experience as well as his innovative thinking have improved my understanding of engineering and research. Further, I would like to thank my co-supervisor Stefan Lundberg for his vital support in both theorical analysis and practical implementations. His conscientious attitude, meticulous thinking and extensive experience to tackle challenges are impressive. I would like to thank my examiner Ola Carlson, especially for his guidance in study planning and his feedbacks of this thesis work.

I am grateful for all the supports from the division. Special thanks go to Xiaoliang Huang for his help with drive systems, Jian Zhan for his guidance in machine design and help in machine assembly, Daniel Pehrman for his tutorials in all aspects of engineering, Georgios Mademlis for all the discussions we have and the enjoyment of sparks in the lab together, Chih-Han Kuo for his professional assistance in digital processor programing, Felix Mannerhagen for his advices and help in mechanical work, Robert Karlsson for his advices with circuit design and many other collogues in our electric power engineering division.

This project is financially supported by the Swedish Energy Agency. I appreciate the support of this study from the agency, the advices from the reference group and the discussions with the collogues from Lund in collaboration.

Finally, I would like to thank my family who give me essential support to pursue my doctoral study.

Junfei Tang

Gothenburg, Sweden

September 2019

List of Abbreviations

ADC	Analogue to Digital Converter
BEV	Battery Electric Vehicle
CNG	Compressed Natural Gas
DAC	Digital to Analogue Converter
DSP	Digital Signal Processor
EESM	Electrically Excited Synchronous Machine
EV	Electric Vehicle
FEM	Finite Element Method
GHG	Green-House Gas
PHEV	Plug-in Hybrid Electric Vehicle
PMSM	Permanent Magnet Synchronous Machine
PWM	Pulse Width Modulation
RMS	Root Mean Square
SynRM	Synchronous Reluctance Machine
SVPWM	Space Vector Pulse Width Modulation
WPT	Wireless Power Transfer

List of Symbols

A, a	Phase A
B, b	Phase B
C, c	Phase C; Capacitance
d	Direct-Axis
E, e	EMF
f	Field
h	Heat transfer coefficient
i	Current
J	Current density
L	Inductance; Length
M	Mutual inductance
m	Number of phases
N	Number of turns
P	Active power
p	Instantaneous active power; Number of pole pairs
Q	Reactive power; Total number of slots
q	Instantaneous reactive power; Number of slots per pole per phase; Quadrature-axis
S	Apparent power
t	Time
u	Voltage
x	Electrical quantity in general
ψ	Flux linkage
λ	Thermal conductivity

Contents

Chapter 1

Introduction

1.1 Background

Electric Vehicles (EVs) have become a fast-growing area in recent years due to an increase of environmental concerns from society. Lifecycle analysis of EVs has shown that even powered by the most carbon-intensive electricity, the greenhouse emission (GHG) from an EV is still lower than a conventional diesel vehicle [1]. And, as the grid starts to accept more renewable electricity, the climate impact caused by EVs will be even lower. Figure 1-1 shows the comparison of GHG emissions per km pursued in [2]. A reduction in GHG emissions is demonstrated with an increasing degree of electrification. Therefore, the electrification of vehicles has shown an undisputed approach to a sustainable society in the future. Consequently, from the data collected in [3], the global electric car sales surpassed 1 million vehicles in 2017, and was approaching to 2 million in 2018 as shown in Figure 1-2. And in order to keep consistent with the Paris Declaration, the stock of EVs need to achieve over 20 million by 2020, and over 110 million by 2030 [4].

1.1.1 Rare-Earth Electric Machines in EV Applications

Electric machines are one of the key components in EVs. To achieve a compact design, rare-earth materials are widely used nowadays. The application of rare-earth materials in electric vehicles start to prevail since Toyota Prius was launched in 1997 [5]. Rare-earth material, especially Neodymium Iron Boron (NdFeB), allows a strong magnetic field to be generated

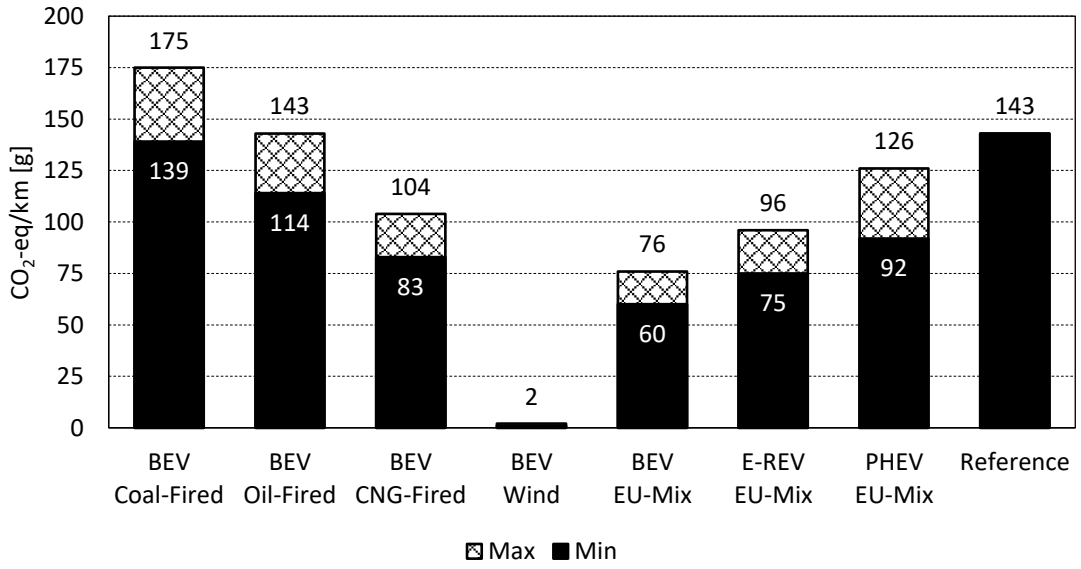

Figure 1-1 Comparison of GHG emissions per km. The data for the figure is from [2].

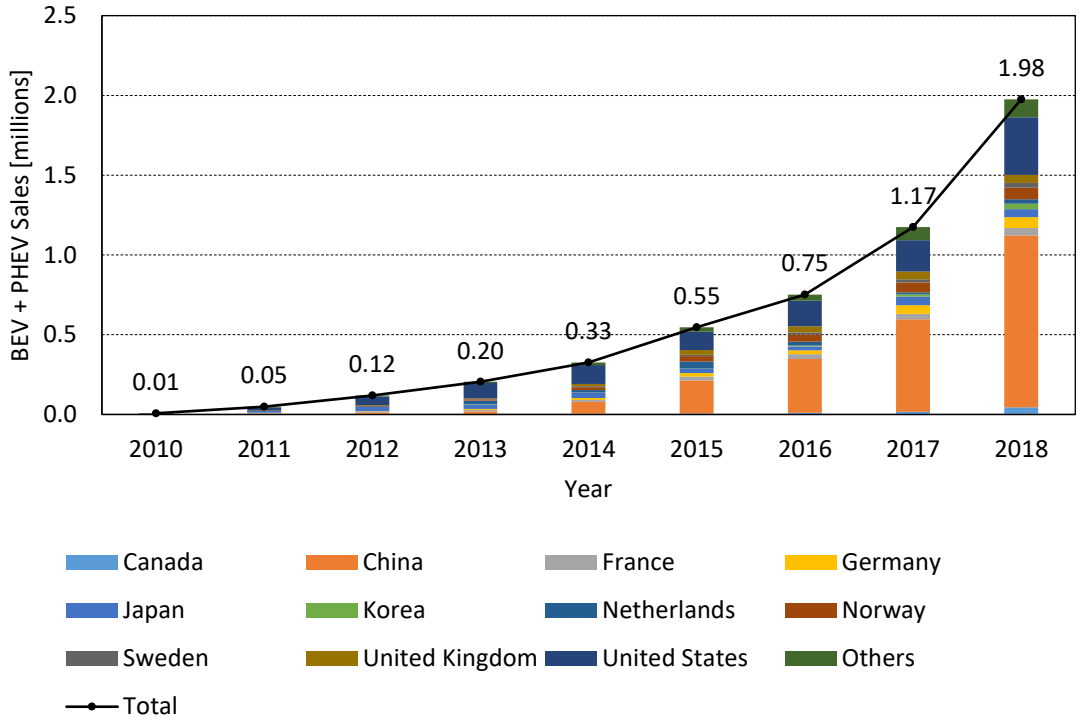

Figure 1-2 Fast growing of the global electric car sales, 2010-2018. The data for the figure is from [3].

from a small volume, and this has significantly increased torque and power densities of electric machines. A comparison between rare-earth-free material ferrite and rare-earth material NdFeB is made in Figure 1-3, with the data from [5] [6] [7]. As can be seen, the maximum energy product $(B \cdot H)_{\max}$ [8] [9] of NdFeB is generally seven times higher than that of ferrite, which means NdFeB shows a prominent advantage with respect to rare-earth-free magnet materials [5]. However, regarding the application of rare-earth material in electric vehicles, more concerns have been raised in various areas, from market imbalance, environmental and performance perspectives.

1.1.1.1 Imbalance between Demand and Supply

In general, the rare-earth material used in an electric machine is less than 5% by mass, but more than 70% by material cost and 25% of material related greenhouse gas emission [10] [5]. If the electrification of vehicles follows the same approach as before, a tremendous

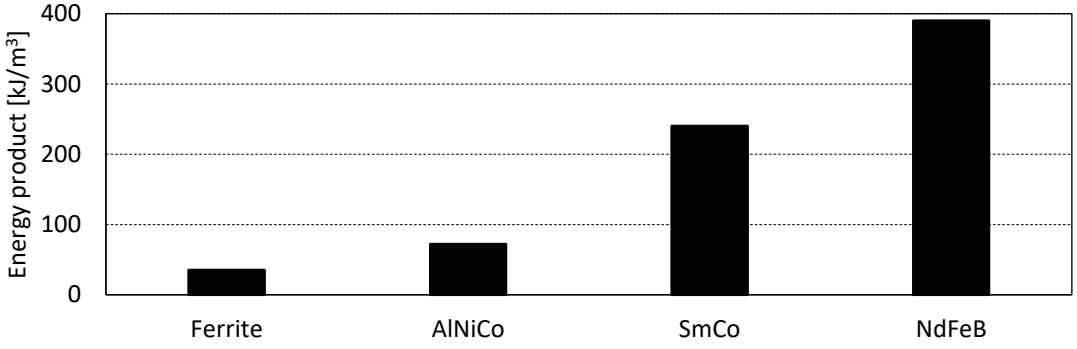

Figure 1-3 Comparison of typical maximum energy products between ferrite and rare-earth magnets. The data for the figure is from [6] [7].

amount of rare-earth material needs to be consumed. According to the estimation in [11], the demand of NdFeB magnet in EV will become 14 times higher in 2020 compared to that in 2015. However, the growth of NdFeB magnet production will be less than 100% during the same time interval [12]. Therefore, the production capacity seems not able to keep pace with the demand increment and there becomes a huge gap between the demand and supply.

1.1.1.2 Environmental Risk

It has been widely recognized that the extraction and refinement process of rare-earth oxides are the sources of serious pollution [10] [5]. The research from automotive industry agrees with this and suggests that NdFeB magnets may be, per unit mass, more damaging than other materials commonly used in electric machines. The production of NdFeB permanent magnets is a relatively complicated process, which mainly includes smelting, casting, milling, sintering, forming, electroplating, and magnetization. And among all the processes, smelting, casting, sintering and electroplating consume huge amount of electric energy, and generate a large amount of waste slag and waste gas at the same time, which cause great challenges to the environment. In addition, electroplating is a significant source of water pollution, which requires an extremely complicated wastewater treatment system. Furthermore, the recycling of NdFeB has been investigated but until now there are still concerns relating to the quality and repeatability of such recycled magnetic materials [13].

1.1.1.3 Performance and Safety Risk

As the temperature goes higher, rare-earth magnets risk demagnetization. And once the rare-earth magnets are demagnetized, the torque production capability will reduce dramatically. Furthermore, the magnetic flux cannot be shut down even in fault conditions. This can lead to high faulty current, and it is extremely dangerous when a fault happens at high speed operation since the strong magnetic flux will induce high voltages in the stator windings.

1.1.2 Development of EESM in EV Applications

Due to the reasons illustrated above, a tendency has appeared to develop rare-earth-free machines. Following this stream, induction machines (IM) and electrically excited synchronous machines (EESM) have become popular candidates. Figure 1-4 shows a comparison of the rotors of IM, PMSM and EESM. As shown in (a), aluminum or copper bars

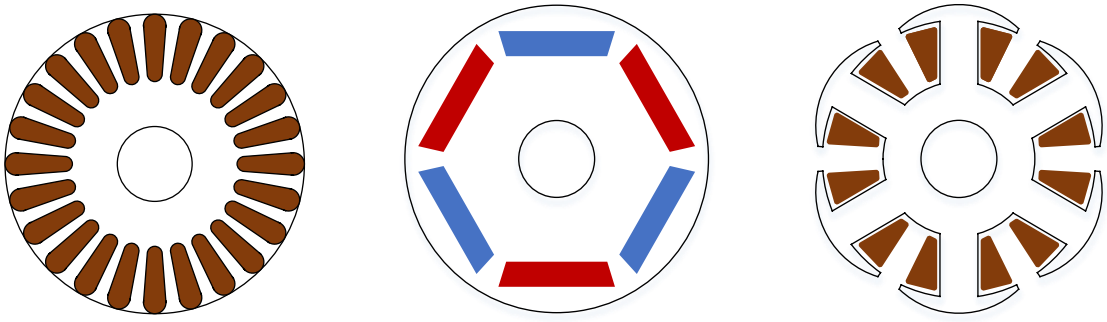

(a) IM (b) PMSM (c) EESM

Figure 1-4 Comparison of rotors of IM, PMSM and EESM.

are commonly applied in the rotor of IM, in which the field current is induced by the flux created by the stator winding. Then the field current from the rotor excites the machine. Since the field current originates from the stator side, power factor is usually low for IM. An interior PMSM rotor is shown in (b), where rare earth magnets are placed in the rotor. The magnets generate the magnetic flux in the machine without any electric current, which gives low losses in the rotor. An EESM rotor is shown in (c), which employs copper windings instead of rare-earth magnets to generate the magnetic flux, and it shows advantages in the following aspects:

- Firstly, EESM is free of rare earth material and therefore is more environmentally friendly with lower cost, easier to produce and easier to recycle.
- And as for the performance, EESM is able to deliver a higher torque in the low speed region by injecting both a high armature current in the stator winding and a high excitation current in the field winding.
- In addition, unlike the injection of negative d-axis current to decrease the flux level in PMSM field-weakening, EESM can achieve a wider speed range by reducing the excitation current to reduce the back-EMF.
- Furthermore, EESM offers one more freedom of field current adjustment, and this means a possibility to realize a thermal balance control between stator and rotor winding, e.g. when the rotor is experiencing a high temperature, the stator current can increase, and the rotor current can decrease while the torque can be maintained at the same level.
- Finally, the flexibility of flux also brings a new strategy of sensorless control, which is to inject high-frequency signal on the field current, and the rotor angle information can be extracted from the harmonics in the stator currents.

Although EESM gives promising performance without consumption of rare earth material, some areas need to be explored and challenges need to be dealt with before EESM becomes prevalent.

1.1.2.1 Machine Design

In traction applications, the specifications for the machine design is different from case to case. In terms of mild-hybrid cars, the electric machines are mainly used to assist the start-up the vehicle. And this requires a high peak torque in the low speed region. In contrast, as for heavy duty vehicles, the electric machines are mainly operating constantly at high speed region. And this requires a high efficiency at that specific constant operation point. Design and test of EESM drive systems have been performed in [14], [15], [16] and [17] for electric vehicle applications. Efforts are spent to design and optimize rotor shape so that efficiency and torque production capability are improved. However, a systematic design strategy to each specific application is not concluded.

1.1.2.2 Field Excitation

In terms of sending power to the field winding, high-frequency brushless excitation, which transfers power with no mechanical contact, becomes interesting [14] [15] [17] [18] [19] [20] [21] and [22]. The avoidance of brushes and slip rings reduces friction losses. And efforts to clear the dust, to replace the brushes as well as to maintain the sliprings are not needed any

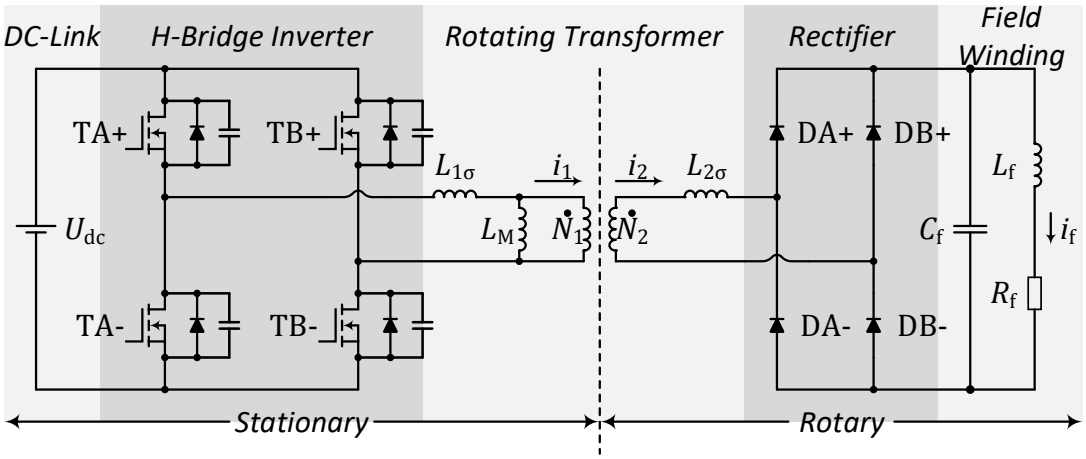

Figure 1-5 Schematic of wireless excitation system dynamic model.

more. A general schematic of the high-frequency brushless excitation system is shown in Figure 1-5. A rotating transformer is introduced between the power supply and the field winding. The primary side stands still and receives power from an H-bridge inverter under phase-shift control. Through an airgap the power is transferred to the secondary side. The secondary side rotates together with the rotor, and a diode rectifier converts the AC power to DC power again and the power flows to the field winding.

Some early studies have explored this area. In [14] [15], the design and control of the brushless excitation system have been described. PCB winding has been employed to withstand the centrifugal force, which end up with around 35% fill factor. In [23], a compact high-frequency brushless excitation system is designed and tested with a standalone EESM. The output capacitance of the switch and the leakage inductance of the transformer are used to achieve Zero-Voltage Switching (ZVS). The system efficiency reaches 97.6%. In [18], a geometry optimization has been performed to achieve the minimum volume of the transformer. It has been concluded that radial-flux excitation gives higher efficiency to the system compared with the axial-flux excitation. In [19], interleaved windings and resonant compensation have been introduced. The overall design parameters, including the rotating transformer geometries and the capacitance for compensation, are optimized. It is confirmed that significant improvement of power transfer capability has been achieved. In [20], the transformer is fit inside the space of the stator end turns, and SiC diodes are employed. The transformer core and the windings are constructed from high-temperature-rated material so that the components can survive in the high temperature environment. These studies have proved that a compact design of high-frequency brushless excitation system is applicable in EESM drive systems.

Apart from inductive power transfer, capacitive power transfer technology has been proposed in EESM field excitation as well [17]. However, the capacitive coupling requires a small airgap with a large area. In order to achieve this, five rotary plates are sandwiched between six stationary plates with 100 mm as the diameter and 115 μm as the airgap. Consequently, reliability issues due to mechanical vibrations become a concern. In addition, the frequency needed is at MHz range (500 kHz – 2.0 MHz in [17]) which brings EMI issues as well. Therefore, this is currently not the main stream of the study.

However, in practical implementations, since the field current is not physically accessible when the machine is operating, an estimation algorithm of field current needs investigation, so that a closed-loop field current control can be established. And to investigate this, a simple but effective modeling of the high-frequency brushless excitation system needs to be implemented as well.

1.1.2.3 Machine Control

One more dimension of control freedom is provided by the adjustable EESM field excitation. Different field current optimization strategies have been proposed by introducing a magnetic equivalent circuit model or a dynamic equivalent core losses resistance in order to improve the efficiency including both iron core losses and copper losses [24] [25]. Since the iron-core loss is negligible compared to the copper loss in most of the operation regions of an EESM in vehicle applications, the strategy to minimize the total copper loss including both the stator side and the rotor side has been analyzed for efficiency improvement [26]. Control of power factor is also under consideration when deciding the current references [27]. To sum up the previous studies, the focus is mainly to minimize the losses. However, due to complicated operation situations for traction motors, losses may not be the only quantity to minimize, and various strategies therefore need to be investigated.

Sensorless control of EESM is of great interest as well. In [28] and [29], sensorless control by high-frequency signal injection to the field winding of EESM through brush and slipring is implemented. This mechanism is of advantage since it is independent from saliency of the machine. Besides, an inverter-integrated rotor for sensorless control is studied in [30], whereas in [31], an excitation machine in mounted on the shaft of the EESM, which acts as a sensor for the rotor position detection of the EESM. Nevertheless, high-frequency signal injection with the high-frequency brushless exciter has never been claimed to be a huge challenge and has not been solved yet.

In terms of dynamic current control, state space feedback algorithm with direct design of discrete-time controller is proposed in the control of permanent magnet synchronous machines and synchronous reluctance machines [32]. The method is claimed to be easy to implement with improvement in the dynamic performance and robustness. However, in EESM, this is still a field to explore.

1.1.2.4 Thermal Modeling and Management

EESM employs a copper winding to generate the flux in the rotor and the copper winding itself needs to dissipate heat during operation. As for thermal modeling, convection heat transfer and flow calculations of electric machines are analyzed in [33], where the formulations are empirical and dimensionless. The thermal modeling of wound rotor induction machines is studied in [34] and [35]. However, specifically, thermal modeling of traction EESM still lacks attention. In addition, as there is a long distance for the heat to transfer from rotor copper to stator cooling jacket, the cooling condition for copper winding is not promising unless special thermal management is developed.

1.2 Aim and Scope of the Study

This study aims to investigate the potential of EESM with high-frequency brushless exciter in vehicle applications. The study is a concept development which is expected to be applied for mild-hybrid vehicles, electric passenger cars and heavy-duty vehicles. The study covers machine design, high-frequency brushless field excitation, control, prototyping and experimental verifications. Investigations to derive machine specifications are not within the scope. To achieve an optimal machine design is a complicated multi-target optimization problem, including electromagnetics, thermal, noise, vibration and the complexity of manufacturing, and therefore, it is not the focus of this conceptual study. Instead, to obtain a design that satisfies the specifications is enough in this study.

1.3 Contributions of the Study

1.3.1.1 Machine Design

The procedure of EESM design for vehicle applications has been studied. The design criterion to achieve unity power factor in the field-weakening envelop of EESM is concluded. Comparisons have been done between different EESM geometrical designs, e.g. open and closed-slot, with and without ferrite assistance. An experimental verification of a 20 kW EESM has been pursued [36]. A 60 kW EESM design is compared with a 60 kW PMSM design, with the same stator, by the use of FEM simulations. A pre-study of a 200 kW EESM for heavy-duty application has been pursued as well.

1.3.1.2 High-Frequency Brushless Excitation

A 2 kW high-frequency brushless excitation system is prototyped as a concept verification [36]. A simplified but effective dynamic model of high-frequency brushless excitation system has been developed [37]. Since the field winding is physically inaccessible, to achieve closed-loop control of field current, an algorithm to dynamically estimate the field current and field winding temperature is necessary. There is a lack of study in this area previously and an algorithm has been implemented in this research. The modeling and algorithm have been verified with the 2 kW high-frequency brushless excitation prototype.

1.3.1.3 Machine Control

Various solutions of d-, q- and field steady are available in state currents at each point inside the torque-speed operation envelop of an EESM, based on different optimization targets. Previous studies mainly focused on the minimization of overall losses. However, in EESM, the losses from field winding is more critical for the safe operation of the machine. Therefore, this study mainly focuses on the balance of the minimizations of copper loss of stator and field windings [38]. In case of dynamic current control, a closed-loop field current control is implemented, with the assistance of the estimation algorithm.

1.4 List of Publications

The contents of the following publications originate from this thesis work.

J. Tang, Y. Liu and N. Sharma, "Modeling and Experimental Verification of High-Frequency Inductive Brushless Exciter for Electrically Excited Synchronous Machines," in IEEE Transactions on Industry Applications, vol. 55, no. 5, pp. 4613-4623, Sept.-Oct. 2019.

J. Tang and Y. Liu, "Design and Experimental Verification of a 48 V 20 kW Electrically Excited Synchronous Machine for Mild Hybrid Vehicles," in 2018 XIII International Conference on Electrical Machines (ICEM), Alexandroupoli, Greece, 2018.

J. Tang and Y. Liu, "Study of Voltage Spikes and Temperature Rise in Power Module Based Integrated Converter for 48 V 20 kW Electrically Excited Synchronous Machines," in APEC 2018, San Antonio, Taxes, USA, 2018.

J. Tang and Y. Liu, "Comparison of Copper Loss Minimization and Field Current Minimization for Electrically Excited Synchronous Motor in Mild Hybrid Drives," in 19th European Conference on Power Electronics and Applications (EPE'17 ECCE Europe), Warsaw, Poland, 2017.

Y. Liu, D. Pehrman, O. Lykartsis, J. Tang and T. Liu, "High frequency exciter of electrically excited synchronous motors for vehicle applications," in 2016 XXII International Conference on Electrical Machines (ICEM), Lausanne, Switzerland, 2016.

Chapter 2

Modeling of Machine and Excitation System

In order to design and analyze the machine along with the excitation system, to establish a proper model is necessary. The modeling of the machine together with the high-frequency brushless excitation system is described in this chapter. The machine modeling includes electrical and thermal aspects, whereas the modeling of the high-frequency brushless excitation system includes the electrical part only.

2.1 Machine Electrical Modeling

The electrical modeling of the machine starts from the three-phase frame, i.e. the abc-frame. Thereafter, the abc-dq transformation is performed and the model in dq-frame is established.

2.1.1 Modeling in ABC-Frame

The stator voltages are composed by resistive voltage drops and electromotive forces (EMF) due to the derivative of magnetic flux linkages

$$\begin{bmatrix} u_\mathrm{a} \\ u_\mathrm{b} \\ u_\mathrm{c} \\ u_\mathrm{f} \end{bmatrix} = \begin{bmatrix} R_\mathrm{a} & 0 & 0 & 0 \\ 0 & R_\mathrm{b} & 0 & 0 \\ 0 & 0 & R_\mathrm{c} & 0 \\ 0 & 0 & 0 & R_\mathrm{f} \end{bmatrix} \begin{bmatrix} i_\mathrm{a} \\ i_\mathrm{b} \\ i_\mathrm{c} \\ i_\mathrm{f} \end{bmatrix} + \frac{\mathrm{d}}{\mathrm{d}t} \begin{bmatrix} \psi_\mathrm{a} \\ \psi_\mathrm{b} \\ \psi_\mathrm{c} \\ \psi_\mathrm{f} \end{bmatrix} \tag{2-1}$$

where u denotes voltages, R denotes resistances, i denotes currents, ψ denotes flux linkages, t denotes time and a, b, c and f denote Phases A, B, C and field respectively. If the machine is operating in the linear region of the BH curve, the flux linkages can be further expressed as [39]

$$\begin{bmatrix} \psi_\mathrm{a} \\ \psi_\mathrm{b} \\ \psi_\mathrm{c} \\ \psi_\mathrm{f} \end{bmatrix} = L_\mathrm{abcf} \begin{bmatrix} i_\mathrm{a} \\ i_\mathrm{b} \\ i_\mathrm{c} \\ i_\mathrm{f} \end{bmatrix} = \begin{bmatrix} L_\mathrm{a}(\theta_\mathrm{r}) & M_\mathrm{ab}(\theta_\mathrm{r}) & M_\mathrm{ac}(\theta_\mathrm{r}) & M_\mathrm{af}(\theta_\mathrm{r}) \\ M_\mathrm{ba}(\theta_\mathrm{r}) & L_\mathrm{b}(\theta_\mathrm{r}) & M_\mathrm{bc}(\theta_\mathrm{r}) & M_\mathrm{bf}(\theta_\mathrm{r}) \\ M_\mathrm{ca}(\theta_\mathrm{r}) & M_\mathrm{cb}(\theta_\mathrm{r}) & L_\mathrm{c}(\theta_\mathrm{r}) & M_\mathrm{cf}(\theta_\mathrm{r}) \\ M_\mathrm{fa}(\theta_\mathrm{r}) & M_\mathrm{fb}(\theta_\mathrm{r}) & M_\mathrm{fc}(\theta_\mathrm{r}) & L_\mathrm{f} \end{bmatrix} \begin{bmatrix} i_\mathrm{a} \\ i_\mathrm{b} \\ i_\mathrm{c} \\ i_\mathrm{f} \end{bmatrix} \tag{2-2}$$

where L denotes self-inductances, M denotes mutual-inductances, θ_r denotes rotor angle with respect to the axis of Phase A (a-axis). In the L_abcf matrix, L_f is the rotor self-inductance which is a constant, whereas other inductances are variables dependent on rotor position θ_r. With the help of Figure 2-1, the tendency of these rotor-position-dependent inductances can be figured out.

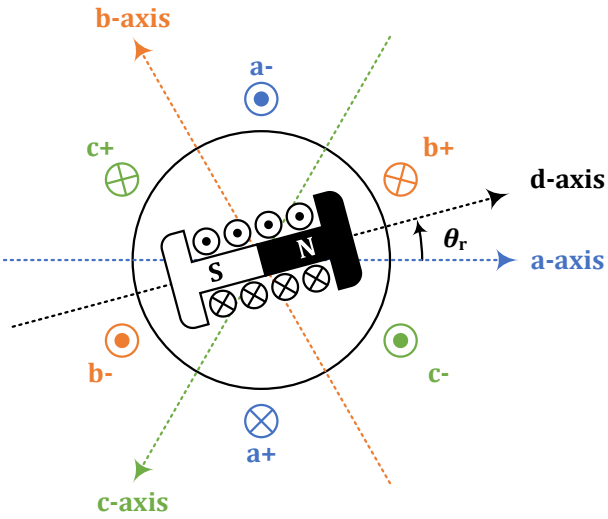

Figure 2-1 Schematic of EESM windings in space.

When $\theta_r = 0$, the rotor is aligned with the a-axis:

- The reluctance of Phase A reaches the minimum and therefore, the $L_a(\theta_r)$ achieves the maximum.
- The b- and c-axis share the magnetic path maximally, which means Phase B and C share the flux maximally and therefore, the mutual-inductances of Phase B and C, $M_{bc}(\theta_r)$ and $M_{cb}(\theta_r)$, achieve the maximum.
- The excitation flux generated by i_f enhances the a-axis flux maximally and therefore, the $M_{af}(\theta_r)$ and $M_{fa}(\theta_r)$ achieve the maximum.

When $\theta_r = \pi$, the rotor is anti-aligned with the a-axis:

- $L_a(\theta_r)$, $M_{bc}(\theta_r)$ and $M_{cb}(\theta_r)$ still achieve the maximum since they are independent from i_f.
- The excitation flux generated by i_f suppresses the a-axis flux maximally and therefore, the $M_{af}(\theta_r)$ and $M_{fa}(\theta_r)$ achieve the minimum.

The expressions of the inductances when the rotor is aligned with other axes can be addressed similarly. Assuming that the inductance dependent on the angle is sinusoidal, as shown in Figure 2-2, then the *wave model* can be established as [39]

$$\begin{aligned} L_a(\theta_r) &= L_{s\cdot avg} + L_{s\cdot delta} \cdot \cos(2\theta_r) \\ L_b(\theta_r) &= L_{s\cdot avg} + L_{s\cdot delta} \cdot \cos\left(2\theta_r + \frac{2\pi}{3}\right) \\ L_c(\theta_r) &= L_{s\cdot avg} + L_{s\cdot delta} \cdot \cos\left(2\theta_r - \frac{2\pi}{3}\right) \end{aligned} \tag{2-3}$$

$$\begin{aligned} M_{ab}(\theta_r) = M_{ba}(\theta_r) &= M_{s\cdot avg} + L_{s\cdot delta} \cdot \cos\left(2\theta_r - \frac{2\pi}{3}\right) \\ M_{bc}(\theta_r) = M_{cb}(\theta_r) &= M_{s\cdot avg} + L_{s\cdot delta} \cdot \cos(2\theta_r) \\ M_{ca}(\theta_r) = M_{ac}(\theta_r) &= M_{s\cdot avg} + L_{s\cdot delta} \cdot \cos\left(2\theta_r + \frac{2\pi}{3}\right) \end{aligned} \tag{2-4}$$

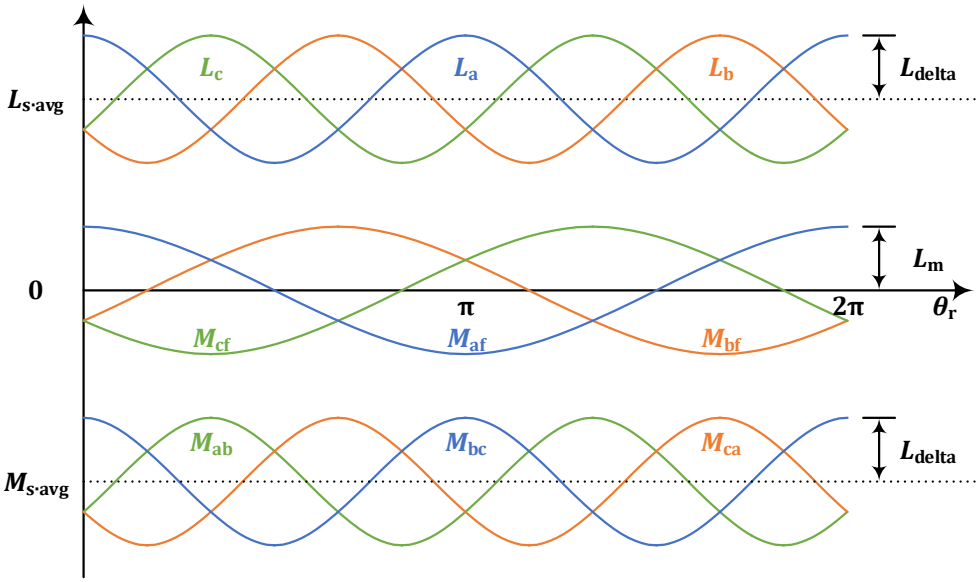

Figure 2-2 Inductance wave model of EESM.
The waveforms are an example for illustration and the amplitudes are not to scale.

$$\begin{aligned} M_{\mathrm{af}}(\theta_{\mathrm{r}}) &= M_{\mathrm{fa}}(\theta_{\mathrm{r}}) = L_{\mathrm{m}} \cdot \cos(\theta_{\mathrm{r}}) \\ M_{\mathrm{bf}}(\theta_{\mathrm{r}}) &= M_{\mathrm{fb}}(\theta_{\mathrm{r}}) = L_{\mathrm{m}} \cdot \cos\left(\theta_{\mathrm{r}} - \frac{2\pi}{3}\right) \\ M_{\mathrm{cf}}(\theta_{\mathrm{r}}) &= M_{\mathrm{fc}}(\theta_{\mathrm{r}}) = L_{\mathrm{m}} \cdot \cos\left(\theta_{\mathrm{r}} + \frac{2\pi}{3}\right) \end{aligned} \tag{2-5}$$

where $L_{\mathrm{s\cdot avg}}$ and $M_{\mathrm{s\cdot avg}}$ are the average of the stator self-inductance and the stator mutual-inductance over one electric period respectively, $L_{\mathrm{s\cdot delta}}$ is the peak-to-average inductance variation of the stator, L_{m} is the amplitude of the stator-rotor mutual-inductance variation. It should be pointed out that, $M_{\mathrm{s\cdot avg}}$ is negative, since the flux generated by the Phase A coil goes oppositely to the Phase B coil.

2.1.2 Coordinate Transformation

As can be noticed in (2-2), the modeling of the EESM in abc-frame is complicated since the inductance matrix L_{abcf} is dependent on the rotor position. In machine design, it is common to analyze the direct-axis (d-axis) and quadrature-axis (q-axis) flux paths separately. The d- and q-axis flux paths of the EESM are shown in Figure 2-3, where the d-axis is defined as the rotor main flux path and the q-axis is defined as 90°, electrical angle, leading the d-axis. The basic adjustment of rotor geometry is performed based on the flux distribution in dq-frame. Besides, in machine control, it is a mature technology to control DC quantities in dq-frame instead of AC quantities in abc-frame. These are the major reasons why $\mathrm{abc} \rightarrow \mathrm{dq}$ transformation is performed.

The $\mathrm{abc} \leftrightarrow \alpha\beta\gamma$ transformation was proposed in [40] while the $\alpha\beta\gamma \leftrightarrow \mathrm{dqo}$ transformation was proposed in [41]. With a combination of these two transformations, the three-phase electrical quantities, e.g. flux linkages, voltages and currents, can be presented in the dq-frame, and vise versa

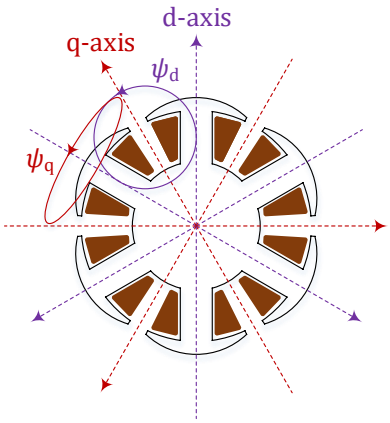

Figure 2-3 The d- and q-axis of EESM.

$$\begin{bmatrix} x_d \\ x_q \\ x_o \end{bmatrix} = T_{abc\to dqo} \begin{bmatrix} x_a \\ x_b \\ x_c \end{bmatrix} \qquad \begin{bmatrix} x_a \\ x_b \\ x_c \end{bmatrix} = T_{dqo\to abc} \begin{bmatrix} x_d \\ x_q \\ x_o \end{bmatrix} \tag{2-6}$$

where x denotes any electrical quantity, d denotes d-axis, q denotes q-axis, o denotes zero-sequence, $T_{abc\to dqo}$ denotes the abc → dqo transformation matrix and $T_{dqo\to abc}$ denotes the dqo → abc transformation matrix. The transformation matrices are

$$T_{abc\to dqo} = k_1 \begin{bmatrix} \cos(\phi_r) & \cos\left(\phi_r - \frac{2}{3}\pi\right) & \cos\left(\phi_r + \frac{2}{3}\pi\right) \\ -\sin(\phi_r) & -\sin\left(\phi_r - \frac{2}{3}\pi\right) & -\sin\left(\phi_r + \frac{2}{3}\pi\right) \\ k_0 & k_0 & k_0 \end{bmatrix} \tag{2-7}$$

$$T_{abc\to dqo} = \frac{2}{3k_1} \begin{bmatrix} \cos(\phi_r) & -\sin(\phi_r) & \frac{1}{2k_0} \\ \cos\left(\phi_r - \frac{2}{3}\pi\right) & -\sin\left(\phi_r - \frac{2}{3}\pi\right) & \frac{1}{2k_0} \\ \cos\left(\phi_r + \frac{2}{3}\pi\right) & -\sin\left(\phi_r + \frac{2}{3}\pi\right) & \frac{1}{2k_0} \end{bmatrix} \tag{2-8}$$

where ϕ_r is the angle of the rotor flux with respect to a-axis, and in synchronous machines, the rotor angle equals the rotor flux angle

$$\theta_r = \phi_r \tag{2-9}$$

The scaling factors k_1 and k_0 in (2-7) and (2-8) are added to the transformation in order to fit different preferences. The *amplitude-invariant transformation* and *power-invariant transformation* are the two popular ones.

2.1.2.1 Amplitude-Invariant Transformation

As the name indicates, the idea of *amplitude-invariant transformation* is to match the amplitude of the dqo quantities to the amplitude of the abc quantities

$$\sqrt{{x_\mathrm{d}}^2 + {x_\mathrm{q}}^2} = \left|\underline{x}_\mathrm{dq}\right| = \hat{x}_\mathrm{a} = \hat{x}_\mathrm{b} = \hat{x}_\mathrm{c} \tag{2-10}$$

where $\left|\underline{x}_\mathrm{dq}\right|$ means the amplitude of the vector in dq-frame, $\hat{x}_\mathrm{a}$, $\hat{x}_\mathrm{b}$ and $\hat{x}_\mathrm{c}$ are the amplitudes of the a, b and c quantities. To achieve this, the scaling factors are

$$k_1 = \frac{2}{3} \qquad k_0 = \frac{1}{2} \tag{2-11}$$

but other scaling factors must be applied in the instantaneous power calculation in dq-frame

$$u_\mathrm{a} \cdot i_\mathrm{a} + u_\mathrm{b} \cdot i_\mathrm{b} + u_\mathrm{c} \cdot i_\mathrm{c} = p = \frac{3}{2} \cdot u_\mathrm{d} \cdot i_\mathrm{d} + \frac{3}{2} \cdot u_\mathrm{q} \cdot i_\mathrm{q} + 3 \cdot u_\mathrm{o} \cdot i_\mathrm{o} \tag{2-12}$$

where p means instantaneous power. This is because $T_{\mathrm{abc}\to\mathrm{dqo}}$ is not unitary in *amplitude-invariant transformation*. Please note that the zero sequence is the same as in the symmetrical components transformation [42].

2.1.2.2 Power-Invariant Transformation

The idea of *power-invariant transformation* is to make sure that the instantaneous power calculated through inner-product of voltage and current vectors in the dqo-frame is consistent with that calculated in the abc-frame, i.e.

$$u_\mathrm{a} \cdot i_\mathrm{a} + u_\mathrm{b} \cdot i_\mathrm{b} + u_\mathrm{c} \cdot i_\mathrm{c} = p = u_\mathrm{d} \cdot i_\mathrm{d} + u_\mathrm{q} \cdot i_\mathrm{q} + u_\mathrm{o} \cdot i_\mathrm{o} \tag{2-13}$$

And in order to achieve this, $T_{\mathrm{abc}\to\mathrm{dqo}}$ and $T_{\mathrm{dqo}\to\mathrm{abc}}$ need to be unitary, which yields the scaling factors as

$$k_1 = \frac{\sqrt{2}}{\sqrt{3}} \qquad k_0 = \frac{\sqrt{2}}{2} \tag{2-14}$$

The unitarity of $T_{\mathrm{abc}\to\mathrm{dqo}}$ and $T_{\mathrm{dqo}\to\mathrm{abc}}$ in *power-invariant transformation* means that they are the transpose and inverse of each other.

2.1.2.3 Coordinate Transformation in EESM

Usually the mid-point of the motor is not grounded, and therefore, the zero-sequence component in the current cannot appear. Then the $\mathrm{abc} \to \mathrm{dq}$ and $\mathrm{dq} \to \mathrm{abc}$ transformations can be formulated as

$$T_{\mathrm{abc}\to\mathrm{dq}} = k_1 \begin{bmatrix} \cos(\theta_\mathrm{r}) & \cos\left(\theta_\mathrm{r} - \frac{2}{3}\pi\right) & \cos\left(\theta_\mathrm{r} + \frac{2}{3}\pi\right) \\ -\sin(\theta_\mathrm{r}) & -\sin\left(\theta_\mathrm{r} - \frac{2}{3}\pi\right) & -\sin\left(\theta_\mathrm{r} + \frac{2}{3}\pi\right) \end{bmatrix} \tag{2-15}$$

$$T_{\mathrm{dq}\to\mathrm{abc}} = \frac{2}{3k_1}\begin{bmatrix} \cos(\theta_\mathrm{r}) & -\sin(\theta_\mathrm{r}) \\ \cos\left(\theta_\mathrm{r} - \frac{2}{3}\pi\right) & -\sin\left(\theta_\mathrm{r} - \frac{2}{3}\pi\right) \\ \cos\left(\theta_\mathrm{r} + \frac{2}{3}\pi\right) & -\sin\left(\theta_\mathrm{r} + \frac{2}{3}\pi\right) \end{bmatrix} \tag{2-16}$$

where $T_{\mathrm{abc}\to\mathrm{dq}}$ is the $\mathrm{abc}\to\mathrm{dq}$ transformation matrix and $T_{\mathrm{dq}\to\mathrm{abc}}$ is the $\mathrm{dq}\to\mathrm{abc}$ transformation matrix. Taking the field winding into consideration, the complete transformation in EESM becomes

$$\begin{bmatrix} x_\mathrm{d} \\ x_\mathrm{q} \\ x_\mathrm{f} \end{bmatrix} = \begin{bmatrix} T_{\mathrm{abc}\to\mathrm{dq}} & 0 \\ 0 & 1 \end{bmatrix} \begin{bmatrix} x_\mathrm{a} \\ x_\mathrm{b} \\ x_\mathrm{c} \\ x_\mathrm{f} \end{bmatrix} \qquad \begin{bmatrix} x_\mathrm{a} \\ x_\mathrm{b} \\ x_\mathrm{c} \\ x_\mathrm{f} \end{bmatrix} = \begin{bmatrix} T_{\mathrm{dq}\to\mathrm{abc}} & 0 \\ 0 & 1 \end{bmatrix} \begin{bmatrix} x_\mathrm{d} \\ x_\mathrm{q} \\ x_\mathrm{f} \end{bmatrix} \tag{2-17}$$

2.1.3 Modeling in DQ-Frame

With the abc-dq transformation, the machine can be modeled in the dq-frame.

2.1.3.1 Flux Linkage Equations

The flux linkage equation in the dq-frame can be derived from the flux linkage equation (2-2) in the abc-frame

$$\begin{bmatrix} \psi_\mathrm{d} \\ \psi_\mathrm{q} \\ \psi_\mathrm{f} \end{bmatrix} = L_{\mathrm{dqf}} \begin{bmatrix} i_\mathrm{d} \\ i_\mathrm{q} \\ i_\mathrm{f} \end{bmatrix} = \begin{bmatrix} T_{\mathrm{abc}\to\mathrm{dq}} & 0 \\ 0 & 1 \end{bmatrix} L_{\mathrm{abcf}} \begin{bmatrix} T_{\mathrm{dq}\to\mathrm{abc}} & 0 \\ 0 & 1 \end{bmatrix} \begin{bmatrix} i_\mathrm{d} \\ i_\mathrm{q} \\ i_\mathrm{f} \end{bmatrix} \tag{2-18}$$

Then, the inductance matrix L_{dqf} can be derived from L_{abcf}, as indicated in (2-17)

$$L_{\mathrm{dqf}} = \begin{bmatrix} T_{\mathrm{abc}\to\mathrm{dq}} & 0 \\ 0 & 1 \end{bmatrix} L_{\mathrm{abc}} \begin{bmatrix} T_{\mathrm{dq}\to\mathrm{abc}} & 0 \\ 0 & 1 \end{bmatrix} = \begin{bmatrix} L_\mathrm{d} & 0 & \frac{3}{2}k_1 L_\mathrm{m} \\ 0 & L_\mathrm{q} & 0 \\ \frac{1}{k_1}L_\mathrm{m} & 0 & L_\mathrm{f} \end{bmatrix} \tag{2-19}$$

where L_d is the d-axis inductance and L_q is the q-axis inductance

$$\begin{aligned} L_\mathrm{d} &= L_{\mathrm{s\cdot avg}} - M_{\mathrm{s\cdot avg}} + \frac{3}{2}L_{\mathrm{s\cdot delta}} \\ L_\mathrm{q} &= L_{\mathrm{s\cdot avg}} - M_{\mathrm{s\cdot avg}} - \frac{3}{2}L_{\mathrm{s\cdot delta}} \end{aligned} \tag{2-20}$$

In case *power-invariant transformation* is applied, then

$$L_{\mathrm{dqf}} = \begin{bmatrix} L_{\mathrm{d}} & 0 & \frac{\sqrt{3}}{\sqrt{2}} L_{\mathrm{m}} \\ 0 & L_{\mathrm{q}} & 0 \\ \frac{\sqrt{3}}{\sqrt{2}} L_{\mathrm{m}} & 0 & L_{\mathrm{f}} \end{bmatrix} \tag{2-21}$$

which is symmetric. However, if *amplitude-invariant transformation* is applied, then

$$L_{\mathrm{dqf}} = \begin{bmatrix} L_{\mathrm{d}} & 0 & L_{\mathrm{m}} \\ 0 & L_{\mathrm{q}} & 0 \\ \frac{3}{2} L_{\mathrm{m}} & 0 & L_{\mathrm{f}} \end{bmatrix} \tag{2-22}$$

which is not symmetric, and to express the flux linkages separately in this case

$$\begin{aligned} \psi_{\mathrm{d}} &= L_{\mathrm{d}} \cdot i_{\mathrm{d}} + L_{\mathrm{m}} \cdot i_{\mathrm{f}} \\ \psi_{\mathrm{q}} &= L_{\mathrm{q}} \cdot i_{\mathrm{q}} \\ \psi_{\mathrm{f}} &= L_{\mathrm{f}} \cdot i_{\mathrm{f}} + \frac{3}{2} \cdot L_{\mathrm{m}} \cdot i_{\mathrm{d}} \end{aligned} \tag{2-23}$$

In this work, *amplitude-invariant transformation* ($k_1 = \frac{2}{3}$) is selected due to the simple expressions in flux linkage equations.

2.1.3.2 Voltage Equations

The dynamic stator voltage equation of the machine can be derived in vector form

$$\begin{aligned} & \underline{u}_{\mathrm{s}}^{\mathrm{s}} = R_{\mathrm{s}} \cdot \underline{i}_{\mathrm{s}}^{\mathrm{s}} + \frac{\mathrm{d}\underline{\psi}_{\mathrm{s}}^{\mathrm{s}}}{\mathrm{d}t} \\ \Rightarrow \quad & \underline{u}_{\mathrm{s}} = R_{\mathrm{s}} \cdot \underline{i}_{\mathrm{s}} + \frac{\mathrm{d}\underline{\psi}_{\mathrm{s}}}{\mathrm{d}t} + \mathrm{j}\omega_{\mathrm{r}} \cdot \underline{\psi}_{\mathrm{s}} \\ \Rightarrow \quad & u_{\mathrm{d}} + \mathrm{j}u_{\mathrm{q}} = R_{\mathrm{s}} \cdot \left(i_{\mathrm{d}} + \mathrm{j}i_{\mathrm{q}}\right) + \frac{\mathrm{d}\left(\psi_{\mathrm{d}} + \mathrm{j}\psi_{\mathrm{q}}\right)}{\mathrm{d}t} + \mathrm{j}\omega_{\mathrm{r}} \cdot \left(\psi_{\mathrm{d}} + \mathrm{j}\psi_{\mathrm{q}}\right) \end{aligned} \tag{2-24}$$

where $\underline{u}_{\mathrm{s}}^{\mathrm{s}}$, $\underline{i}_{\mathrm{s}}^{\mathrm{s}}$ and $\underline{\psi}_{\mathrm{s}}^{\mathrm{s}}$ mean the stator voltage, current and flux linkage in the αβ-frame; $\underline{u}_{\mathrm{s}}$, $\underline{i}_{\mathrm{s}}$ and $\underline{\psi}_{\mathrm{s}}$ mean the stator voltage, current and flux linkage in the dq-frame. Then, in matrix format, the stator along with the field equations can be summarized as

$$\begin{bmatrix} u_{\mathrm{d}} \\ u_{\mathrm{q}} \\ u_{\mathrm{f}} \end{bmatrix} = \begin{bmatrix} R_{\mathrm{s}} & 0 & 0 \\ 0 & R_{\mathrm{s}} & 0 \\ 0 & 0 & R_{\mathrm{f}} \end{bmatrix} \begin{bmatrix} i_{\mathrm{d}} \\ i_{\mathrm{q}} \\ i_{\mathrm{f}} \end{bmatrix} + \begin{bmatrix} 0 & -\omega_{\mathrm{r}} & 0 \\ \omega_{\mathrm{r}} & 0 & 0 \\ 0 & 0 & 0 \end{bmatrix} \begin{bmatrix} \psi_{\mathrm{d}} \\ \psi_{\mathrm{q}} \\ \psi_{\mathrm{f}} \end{bmatrix} + \frac{\mathrm{d}}{\mathrm{d}t} \begin{bmatrix} \psi_{\mathrm{d}} \\ \psi_{\mathrm{q}} \\ \psi_{\mathrm{f}} \end{bmatrix} \tag{2-25}$$

And assuming constant inductances, (2-25) becomes

$$\begin{bmatrix} u_\mathrm{d} \\ u_\mathrm{q} \\ u_\mathrm{f} \end{bmatrix} = \begin{bmatrix} R_\mathrm{s} & -\omega_\mathrm{r} L_\mathrm{q} & 0 \\ \omega_\mathrm{r} L_\mathrm{d} & R_\mathrm{s} & \omega_\mathrm{r} L_\mathrm{m} \\ 0 & 0 & R_\mathrm{f} \end{bmatrix} \begin{bmatrix} i_\mathrm{d} \\ i_\mathrm{q} \\ i_\mathrm{f} \end{bmatrix} + \begin{bmatrix} L_\mathrm{d} & 0 & L_\mathrm{m} \\ 0 & L_\mathrm{q} & 0 \\ \frac{3}{2} L_\mathrm{m} & 0 & L_\mathrm{f} \end{bmatrix} \begin{bmatrix} \frac{di_\mathrm{d}}{dt} \\ \frac{di_\mathrm{q}}{dt} \\ \frac{di_\mathrm{f}}{dt} \end{bmatrix} \tag{2-26}$$

Please notice that coupling terms $-\omega_\mathrm{r} L_\mathrm{q} i_\mathrm{q}$, $\omega_\mathrm{r} L_\mathrm{d} i_\mathrm{d}$ and $\omega_\mathrm{r} L_\mathrm{m} i_\mathrm{f}$ appear in the d- and q-axis equations. The term $\omega_\mathrm{r} L_\mathrm{m} i_\mathrm{f}$ is usually regarded as the back-EMF term

$$e_\mathrm{m} = \omega_\mathrm{r} \cdot L_\mathrm{m} \cdot i_\mathrm{f} \tag{2-27}$$

and the EMF along d- and q-axis can be defined as well

$$e_\mathrm{d} = -\omega_\mathrm{r} \cdot L_\mathrm{q} \cdot i_\mathrm{q} = -x_\mathrm{q} \cdot i_\mathrm{q} \tag{2-28}$$

$$e_\mathrm{q} = \omega_\mathrm{r} \cdot L_\mathrm{d} \cdot i_\mathrm{d} + \omega_\mathrm{r} \cdot L_\mathrm{m} \cdot i_\mathrm{f} = x_\mathrm{d} \cdot i_\mathrm{d} + e_\mathrm{m} \tag{2-29}$$

where x denotes reactances, e denotes EMF and m means mutual. In steady state, the current derivatives in dq-frame become zero, which means

$$\begin{bmatrix} U_\mathrm{d} \\ U_\mathrm{q} \\ U_\mathrm{f} \end{bmatrix} = \begin{bmatrix} R_\mathrm{s} & -\omega_\mathrm{r} L_\mathrm{q} & 0 \\ \omega_\mathrm{r} L_\mathrm{d} & R_\mathrm{s} & \omega_\mathrm{r} L_\mathrm{m} \\ 0 & 0 & R_\mathrm{f} \end{bmatrix} \begin{bmatrix} I_\mathrm{d} \\ I_\mathrm{q} \\ I_\mathrm{f} \end{bmatrix} \tag{2-30}$$

The ratio between d- and q-axis inductances is defined as saliency ratio [43]

$$k_\mathrm{dq} = \frac{L_\mathrm{d}}{L_\mathrm{q}} \tag{2-31}$$

In case $k_\mathrm{dq} = 1$, then the machine is defined as “non-salient”, whereas in case $k_\mathrm{dq} \neq 1$, then the machine is defined as “salient”. The difference between L_d and L_q is defined as L_Δ

$$L_\Delta = L_\mathrm{d} - L_\mathrm{q} = 3 \cdot L_{\mathrm{s \cdot delta}} \tag{2-32}$$

As will be shown in the following sections, L_Δ contributes to the reluctance torque production.

2.1.3.3 Electromagnetic Power

Based on the modeling in dq-frame, the *electromagnetic power* p_em can be calculated as

$$p_\mathrm{em} = \frac{3}{2} \cdot \mathrm{Re}\{\underline{e}_s \cdot \underline{i}_s^{\,*}\} = \frac{3}{2} \cdot \left(e_\mathrm{d} \cdot i_\mathrm{d} + e_\mathrm{q} \cdot i_\mathrm{q}\right) = \frac{3}{2} \cdot \left[e_\mathrm{m} + \left(x_\mathrm{d} - x_\mathrm{q}\right) \cdot i_\mathrm{d}\right] \cdot i_\mathrm{q} \tag{2-33}$$

where $\underline{e}_s^{\,*}$ mean the conjugate of stator EMF vector in dq-frame. If resistive voltage drop, $R_\mathrm{s} \cdot \underline{i}_\mathrm{s}$, and transients, $L_\mathrm{d} \cdot \frac{\mathrm{d}i_\mathrm{d}}{\mathrm{d}t}$ and $L_\mathrm{q} \cdot \frac{\mathrm{d}i_\mathrm{q}}{\mathrm{d}t}$, are neglected, then in steady state,

$$U_\mathrm{d} = -x_\mathrm{q} \cdot I_\mathrm{q} \quad \Rightarrow \quad I_\mathrm{q} = -\frac{U_\mathrm{d}}{x_\mathrm{q}} = \frac{U_\mathrm{s} \cdot \sin\delta}{x_\mathrm{q}}$$
$$U_\mathrm{q} = x_\mathrm{d} \cdot I_\mathrm{d} + E_\mathrm{m} \quad \Rightarrow \quad I_\mathrm{d} = \frac{U_\mathrm{q} - E_\mathrm{m}}{x_\mathrm{d}} = \frac{U_\mathrm{s} \cdot \cos\delta - E_\mathrm{m}}{x_\mathrm{d}} \tag{2-34}$$

The electromagnetic power in steady state P_em therefore becomes

$$P_\mathrm{em} = \frac{3}{2} \cdot \left[\frac{E_\mathrm{m} \cdot U_\mathrm{s}}{x_\mathrm{d}} \cdot \sin\delta + \frac{{U_\mathrm{s}}^2 \cdot \left(x_\mathrm{d} - x_\mathrm{q}\right)}{2 \cdot x_\mathrm{d} \cdot x_\mathrm{q}} \cdot \sin 2\delta \right] \tag{2-35}$$

And in case of a non-salient machine,

$$P_\mathrm{em} = \frac{3}{2} \cdot \frac{E \cdot U}{x_\mathrm{d}} \cdot \sin\delta \tag{2-36}$$

If power-invariant transformation is applied, then the factor $\frac{3}{2}$ in the equation disappears. From electromagnetic power, electromagnetic torque can be calculated, as well as the efficiency of the machine.

2.1.3.4 Electromagnetic Torque

The electromagnetic torque T_em can be calculated from electromagnetic power

$$T_\mathrm{em} = \frac{P_\mathrm{em}}{\Omega_\mathrm{r}} = \frac{3}{2} \cdot p \cdot \mathrm{Im}\left\{ \underline{\psi}_\mathrm{s}^{\,*} \cdot \underline{i}_s \right\} = \frac{3}{2} \cdot p \cdot \left(\psi_\mathrm{d} \cdot i_\mathrm{q} - \psi_\mathrm{q} \cdot i_\mathrm{d} \right) \tag{2-37}$$

where p denotes number of pole pairs and Ω_r denotes mechanical speed. In case of constant d- and q-axis inductances, then

$$T_\mathrm{em} = \frac{3}{2} \cdot p \cdot \left[L_\mathrm{m} \cdot i_\mathrm{f} + \left(L_\mathrm{d} - L_\mathrm{q} \right) \cdot i_\mathrm{d} \right] \cdot i_\mathrm{q} \tag{2-38}$$

As can be seen, T_em can be decomposed into two components, a synchronous torque component, which is due to the interaction between field excitation and q-axis current

$$T_\mathrm{syn} = \frac{3}{2} \cdot p \cdot L_\mathrm{m} \cdot i_\mathrm{f} \cdot i_\mathrm{q} \tag{2-39}$$

and a reluctance torque component, which is due to the difference between d- and q-axis inductances

$$T_\mathrm{rel} = \frac{3}{2} \cdot p \cdot \left(L_\mathrm{d} - L_\mathrm{q} \right) \cdot i_\mathrm{d} \cdot i_\mathrm{q} \tag{2-40}$$

For a non-salient EESM, the reluctance torque component disappears.

2.1.4 Loss Model

2.1.4.1 Copper Loss Model

The total copper loss P_{Cu} is composed of stator copper loss $P_{\mathrm{Cu.s}}$ and field copper loss $P_{\mathrm{Cu.f}}$

$$P_{\mathrm{Cu}} = P_{\mathrm{Cu.s}} + P_{\mathrm{Cu.f}} \tag{2-41}$$

The stator copper loss is

$$P_{\mathrm{Cu.s}} = \left({i_{\mathrm{a}}}^2 + {i_{\mathrm{b}}}^2 + {i_{\mathrm{c}}}^2\right) \cdot R_{\mathrm{s}} = \frac{3}{2} \cdot \left({i_{\mathrm{d}}}^2 + {i_{\mathrm{q}}}^2\right) \cdot R_{\mathrm{s}} = \frac{3}{2} \cdot {i_{\mathrm{s}}}^2 \cdot R_{\mathrm{s}} \tag{2-42}$$

where i_{s} is the amplitude of the stator phase current, while the field copper loss is

$$P_{\mathrm{Cu.f}} = {i_{\mathrm{f}}}^2 \cdot R_{\mathrm{f}} \tag{2-43}$$

With (2-41), (2-42) and (2-43), the distributions of i_{d}, i_{q} and i_{f} can be presented on the surface of an oblate spheroid, providing a constant P_{Cu}

$$\frac{{i_{\mathrm{d}}}^2}{a^2} + \frac{{i_{\mathrm{q}}}^2}{b^2} + \frac{{i_{\mathrm{f}}}^2}{c^2} = 1 \tag{2-44}$$

Since usually R_{f} is much larger than R_{s} in traction applications, the semi-axes follow

$$a = b = \sqrt{\frac{2}{3}\frac{P_{\mathrm{Cu}}}{R_{\mathrm{s}}}} \gg \sqrt{\frac{P_{\mathrm{Cu}}}{R_{\mathrm{f}}}} = c \tag{2-45}$$

This provides an intuitive view of copper loss in three-dimensional space.

2.1.4.2 Iron-Core Loss Model

The iron-core loss P_{Fe} of lamination steel is modeled as the sum of hysteresis loss $P_{\mathrm{Fe.h}}$, classical eddy current loss $P_{\mathrm{Fe.c}}$ and excess eddy current loss $P_{\mathrm{Fe.e}}$ [44]

$$P_{\mathrm{Fe}} = P_{\mathrm{Fe.h}} + P_{\mathrm{Fe.c}} + P_{\mathrm{Fe.e}} \tag{2-46}$$

Among them, the hysteresis loss is

$$P_{\mathrm{Fe.h}} = k_{\mathrm{h}} \cdot f \cdot {B_{\mathrm{m}}}^2 \cdot M \tag{2-47}$$

the classical eddy current loss is

$$P_{\mathrm{Fe.c}} = k_{\mathrm{c}} \cdot f^2 \cdot {B_{\mathrm{m}}}^2 \cdot M \tag{2-48}$$

and the excess eddy current loss is

$$P_{\mathrm{Fe.e}} = k_{\mathrm{e}} \cdot f^{1.5} \cdot {B_{\mathrm{m}}}^{1.5} \cdot M \tag{2-49}$$

where k_{h} is hysteresis loss coefficient, k_{c} is classical eddy current loss coefficient, k_{e} is excess eddy current loss coefficient, f is frequency, B_{m} is the maximum of flux density and M is the mass of the lamination steel. The values of k_{h} and k_{c} for commonly used lamination steels in automotive machines are available in Appendix A, whereas the values of k_{e} of these materials are negligible. Therefore, it is applicable to only consider $P_{\mathrm{Fe.h}}$ and $P_{\mathrm{Fe.c}}$, which means

$$P_{\mathrm{Fe}} \propto {B_{\mathrm{m}}}^2 \cdot M \tag{2-50}$$

This indicates that, the iron-core loss at a frequency f_2 can be scaled from the iron-core loss at another frequency f_1, i.e.

$$\frac{P_{\mathrm{Fe.2}}}{P_{\mathrm{Fe.1}}} = \frac{k_{\mathrm{h}} \cdot f_2 \cdot {B_{\mathrm{m}}}^2 \cdot M + k_{\mathrm{c}} \cdot {f_2}^2 \cdot {B_{\mathrm{m}}}^2 \cdot M}{k_{\mathrm{h}} \cdot f_1 \cdot {B_{\mathrm{m}}}^2 \cdot M + k_{\mathrm{c}} \cdot {f_1}^2 \cdot {B_{\mathrm{m}}}^2 \cdot M} = \frac{k_{\mathrm{h}} \cdot f_2 + k_{\mathrm{c}} \cdot {f_2}^2}{k_{\mathrm{h}} \cdot f_1 + k_{\mathrm{c}} \cdot {f_1}^2} \tag{2-51}$$

To model the iron-core loss more accurately, additional iron losses due to rotational fields and sheet cutting can be considered as well [45]. And the corrected iron-core loss $P_{\mathrm{Fe.cor}}$ becomes

$$P_{\mathrm{Fe.cor}} = P_{\mathrm{Fe}} \cdot k_{\mathrm{rot}} \cdot k_{\mathrm{cut}} \tag{2-52}$$

where k_{rot} is the rotation correction factor and k_{cut} is the sheet cutting correction factor. From the results in [45], the range of k_{rot} are 1.04 – 1.06 for machines in MW range whereas around 1.02 for machines in kW range. For a strip width thinner than 30 mm, k_{cut} is positive, whereas k_{cut} is negative for a strip width wider than 30 mm. For instance, k_{cut} is around 1.02 with a strip width of 10 mm.

2.1.4.3 Efficiency

The efficiency of EESM can be formulated as

$$\eta = \frac{P_{\mathrm{out}}}{P_{\mathrm{in}}} \times 100\% = \frac{P_{\mathrm{em}} - P_{\mathrm{mech}} - P_{\mathrm{stray}}}{P_{\mathrm{em}} + P_{\mathrm{Cu}} + P_{\mathrm{Fe}}} \times 100\% \tag{2-53}$$

where P_{mech} and P_{stray} in steady state operation can usually be estimated as [38]

$$P_{\mathrm{mech \cdot loss}} \approx P_{\mathrm{nom}} \cdot \left(\frac{f}{f_{\mathrm{nom}}}\right)^2 \cdot 0.5\% \tag{2-54}$$

$$P_{\mathrm{stray \cdot loss}} \approx P_{\mathrm{nom}} \cdot \left(\frac{I_{\mathrm{s}}}{I_{\mathrm{s \cdot nom}}}\right)^2 \cdot \left(\frac{f}{f_{\mathrm{nom}}}\right) \cdot 0.5\% \tag{2-55}$$

2.1.5 Dynamic Model with Non-linear Electromagnetic Properties

2.1.5.1 Electrical Dynamics

Figure 2-4 shows the dynamic model of the machine with non-linear electromagnetic properties, where the d- and q-axis inductances are not guaranteed to be constant any longer. In this case, the flux linkage maps of ψ_d and ψ_q as functions of i_d, i_q and i_f need to be obtained from electromagnetic Finite Element Method (FEM) calculations. The incremental inductances can be calculated from flux linkages

$$L_\mathrm{d}(i_\mathrm{d}, i_\mathrm{q}, i_\mathrm{f}) = \frac{\psi_\mathrm{d}(i_\mathrm{d} + \Delta i_\mathrm{d}, i_\mathrm{q}, i_\mathrm{f}) - \psi_\mathrm{d}(i_\mathrm{d} - \Delta i_\mathrm{d}, i_\mathrm{q}, i_\mathrm{f})}{2 \cdot \Delta i_\mathrm{d}} \tag{2-56}$$

$$L_\mathrm{q}(i_\mathrm{d}, i_\mathrm{q}, i_\mathrm{f}) = \frac{\psi_\mathrm{q}(i_\mathrm{d}, i_\mathrm{q} + \Delta i_\mathrm{q}, i_\mathrm{f}) - \psi_\mathrm{q}(i_\mathrm{d}, i_\mathrm{q} - \Delta i_\mathrm{q}, i_\mathrm{f})}{2 \cdot \Delta i_\mathrm{q}} \tag{2-57}$$

In the dynamic model, based on the flux linkages ψ_d and ψ_q as well as the resistive voltage drops $R_\mathrm{s} i_\mathrm{d}$ and $R_\mathrm{s} i_\mathrm{q}$, and according to (2-22), it is possible to calculate the flux linkage derivatives

$$\frac{\mathrm{d}\psi_\mathrm{d}}{\mathrm{d}t} = u_\mathrm{d} - R_\mathrm{s} i_\mathrm{d} + \omega_\mathrm{r} \psi_\mathrm{q} \tag{2-58}$$

$$\frac{\mathrm{d}\psi_\mathrm{q}}{\mathrm{d}t} = u_\mathrm{q} - R_\mathrm{s} i_\mathrm{q} - \omega_\mathrm{r} \psi_\mathrm{d} \tag{2-59}$$

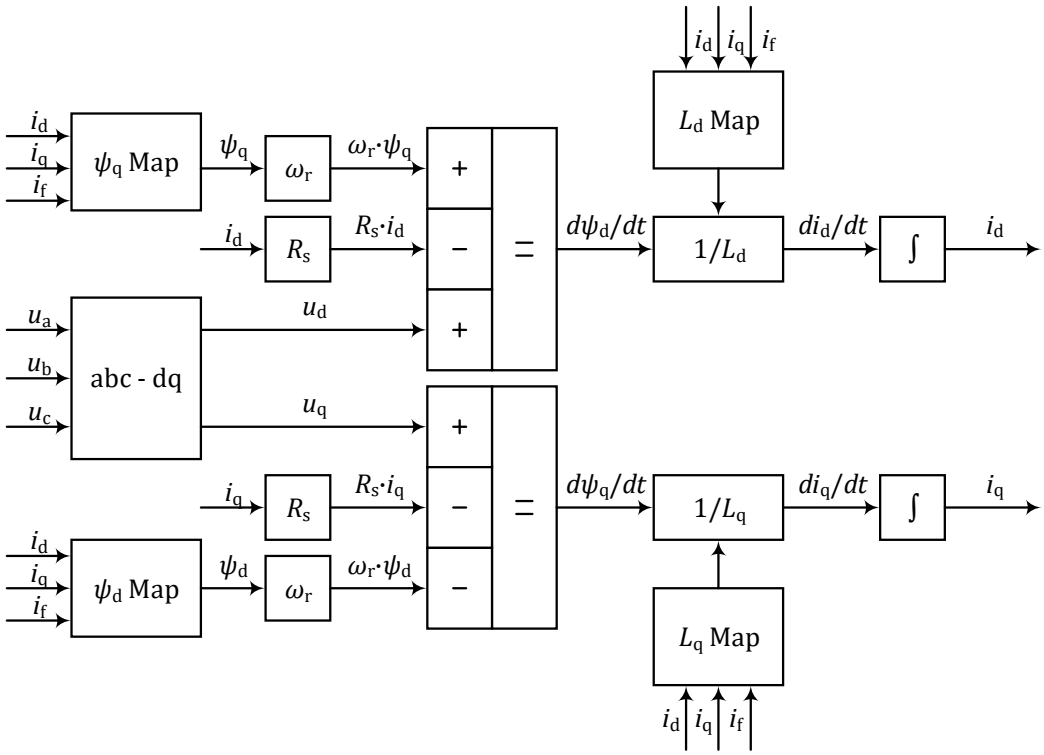

Figure 2-4 Dynamic non-linear model of EESM electrical part.

Then with the incremental inductances L_d and L_q, $\frac{\mathrm{d}i_\mathrm{d}}{\mathrm{d}t}$ and $\frac{\mathrm{d}i_\mathrm{q}}{\mathrm{d}t}$ can be calculated

$$\frac{\mathrm{d}i_\mathrm{d}}{\mathrm{d}t} = \frac{1}{L_\mathrm{d}} \frac{\mathrm{d}\psi_\mathrm{d}}{\mathrm{d}t} \tag{2-60}$$

$$\frac{\mathrm{d}i_\mathrm{q}}{\mathrm{d}t} = \frac{1}{L_\mathrm{q}} \frac{\mathrm{d}\psi_\mathrm{q}}{\mathrm{d}t} \tag{2-61}$$

It should be pointed out that the inductances here are incremental inductances instead of the apparent ones [28]. Thereafter, by taking integrations of the currents, i_d and i_q can be obtained, which are used to simulate the $\frac{\mathrm{d}i_\mathrm{d}}{\mathrm{d}t}$ and $\frac{\mathrm{d}i_\mathrm{q}}{\mathrm{d}t}$ in the next step.

2.1.5.2 Copper and Iron-Core Losses

The dynamic models of copper and iron-core losses of EESM are presented in Figure 2-5 and Figure 2-6. The expression of copper loss is the same as in (2-41), (2-42) and (2-43). As for the iron-core loss modeling, an iron-core loss map p_Fe as the function of i_d, i_q and i_f can be calculated in FEM at a base speed, and then scaling is applied based on (2-51) to find the instantaneous iron-core loss

$$p_\mathrm{Fe}\left(i_\mathrm{d}, i_\mathrm{q}, i_\mathrm{f}, f\right) = \frac{k_\mathrm{h} \cdot f + k_\mathrm{c} \cdot f^2}{k_\mathrm{h} \cdot f_\mathrm{base} + k_\mathrm{c} \cdot f_\mathrm{base}{}^2} \cdot p_\mathrm{Fe.base}\left(i_\mathrm{d}, i_\mathrm{q}, i_\mathrm{f}\right) \tag{2-62}$$

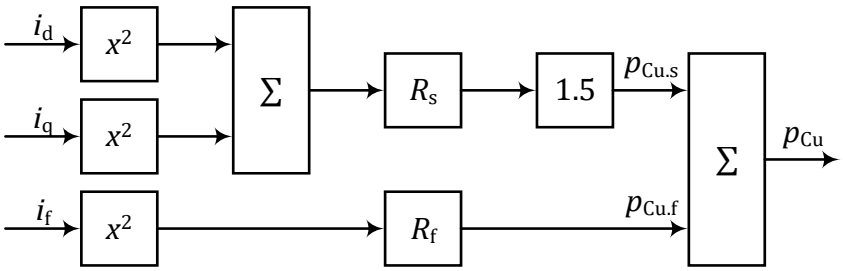

Figure 2-5 Dynamic copper loss model of EESM.

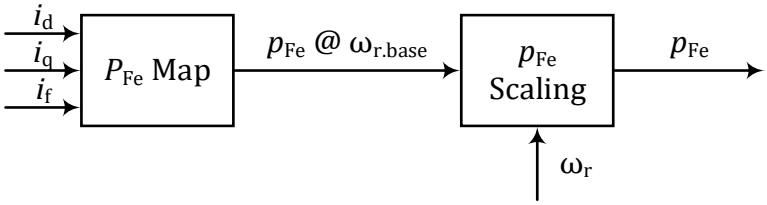

Figure 2-6 Dynamic iron-core loss model of EESM.

2.1.5.3 Efficiency and Power Factor

Neglecting the stray loss and mechanical loss, the instantaneous efficiency of EESM can be formulated as

$$\eta = \frac{p_{\text{out}}}{p_{\text{in}}} \times 100\% = \frac{p_{\text{em}}}{p_{\text{em}} + p_{\text{Cu}} + p_{\text{Fe}}} \times 100\% \tag{2-63}$$

In instantaneous power theory, the instantaneous power factor PF can be calculated as [46]

$$PF = \frac{p_{\text{s}}}{s_{\text{s}}} = \frac{p_{\text{s}}}{\sqrt{{p_{\text{s}}}^2 + {q_{\text{s}}}^2}} \tag{2-64}$$

where the active power p_{s} and the reactive power q_{s} are

$$p_{\text{s}} = u_{\text{a}} \cdot i_{\text{a}} + u_{\text{b}} \cdot i_{\text{b}} + u_{\text{c}} \cdot i_{\text{c}} = \frac{3}{2} \cdot \text{Re}\{\underline{u}_{\text{s}} \cdot \underline{i}_{\text{s}}^{*}\} = \frac{3}{2} \cdot (u_{\text{d}} \cdot i_{\text{d}} + u_{\text{q}} \cdot i_{\text{q}}) \tag{2-65}$$

$$q_{\text{s}} = \frac{u_{\text{ab}} \cdot i_{\text{c}} + u_{\text{bc}} \cdot i_{\text{a}} + u_{\text{ca}} \cdot i_{\text{b}}}{\sqrt{3}} = \frac{3}{2} \cdot \text{Im}\{\underline{u}_{\text{s}} \cdot \underline{i}_{\text{s}}^{*}\} = \frac{3}{2} \cdot (u_{\text{q}} \cdot i_{\text{d}} - u_{\text{d}} \cdot i_{\text{q}}) \tag{2-66}$$

Another approach to calculate the instantaneous power factor PF is to use the voltage vector angle and current vector angle

$$PF = \cos \varphi_{\text{PF}} = \cos(\theta_u - \theta_i) \tag{2-67}$$

where θ_u is the voltage vector angle, θ_u is the current vector angle and φ_{PF} is the power factor angle.

2.2 Machine Thermal Modeling

To assist the design and analysis of the machine, a thermal model is needed to estimate the thermal condition of the machine at different operation points. The schematics of the machine radial cross-section in terms of thermal modeling are shown in Figure 2-7. The stator structure is shown in (a). The copper winding in stator slot is simplied as an area of copper in

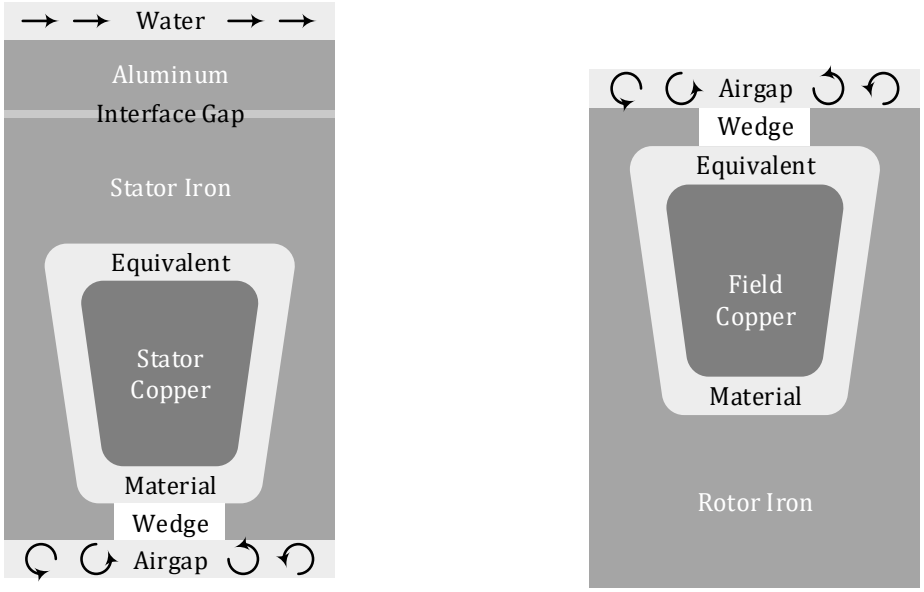

(a) Stator (b) Rotor

Figure 2-7 Schematics of machine structure in terms of thermal modeling.

the center, surrounded by an equivalent material with equivalent thermal conductivity [34] [35]. The winding together with the equivalent material is further enclosed by the stator iron. The stator iron is attached to an aluminum cooling jacket with an interface gap in the between. Inside the aluminum cooling jacket, there is a coolent channel, through which water flows to take the heat away. The stator iron has an interface with airgap as well in which convection occurs. The rotor structure is simplier, as shown in (b). The winding-slot structure is the same as the stator side and the rotor iron has an interface with airgap. Wedge in both cases are considered not as thermal conductive material.

With this simplified structure, a lumped parameter model is built. Material properties are illustrated in Appendix A. Heat transfer mechanisms are firstly presented, based on which the lumped parameter model is built. The consideration of adiabatic process to characterize peak operation of the machine is presented as well.

2.2.1 Conductive Heat Transfer

Conduction is the heat transfer through homogeneous and opaque solid and it originates from the difference in temperature between the warm and the cold part of the solid [47]. The conductive heat transfer P can be calculated by

$$P = \frac{T_1 - T_2}{R_{\text{th.cond}}} \tag{2-68}$$

where T_1 is the temperature at Point 1, T_2 is the temperature at Point 2 and $R_{\text{th.cond}}$ is the conductive thermal resistance. $R_{\text{th.cond}}$ can be calculated as

$$R_{\text{th.cond}} = \int_0^L \frac{1}{\lambda \cdot A(l)} \cdot dl \tag{2-69}$$

where λ is the thermal conductivity of the solid in W/(m·K) and A is the cross-section as a function of distance l.

In EESM, thermal conduction happens between different parts of the iron-core, from copper winding to the iron-core, and from the stator iron to the aluminum cooling jacket. The first is simple since the geometry is known and lamination iron is the only material. The later two are complicated and are explained as follows.

2.2.1.1 Conduction between Copper Winding and Iron Core

The slot-winding structure involves several different materials. In terms of the winding insulations, there are mainly three: the surface varnish of the strands, the impregnated vanish and the slot insulation [48]. For low-voltage AC machines (rated voltage lower than 1 kV), a thickness of 0.2-0.3 mm is usually reserved for slot insulation. In order to simplify the calculation, an equivalent slot thermal conductivity λ_{eq} is proposed in [49] [50] [34] [35]

$$\lambda_{\text{eq}} = 0.2425 \cdot [(1 - k_{\text{fill}}) \cdot A_{\text{slot}} \cdot L_{\text{core}}]^{-0.427} \tag{2-70}$$

where k_{fill} is the fill factor, i.e. the copper area divided by the slot cross-section area, A_{slot} is the slot cross-section area, L_{core} is the length of the iron-core. Figure 2-8 shows the curve of the equivalent slot thermal conductivity with respect to $(1-k_{\mathrm{fill}})\cdot A_{\mathrm{slot}}\cdot L_{\mathrm{core}}$.

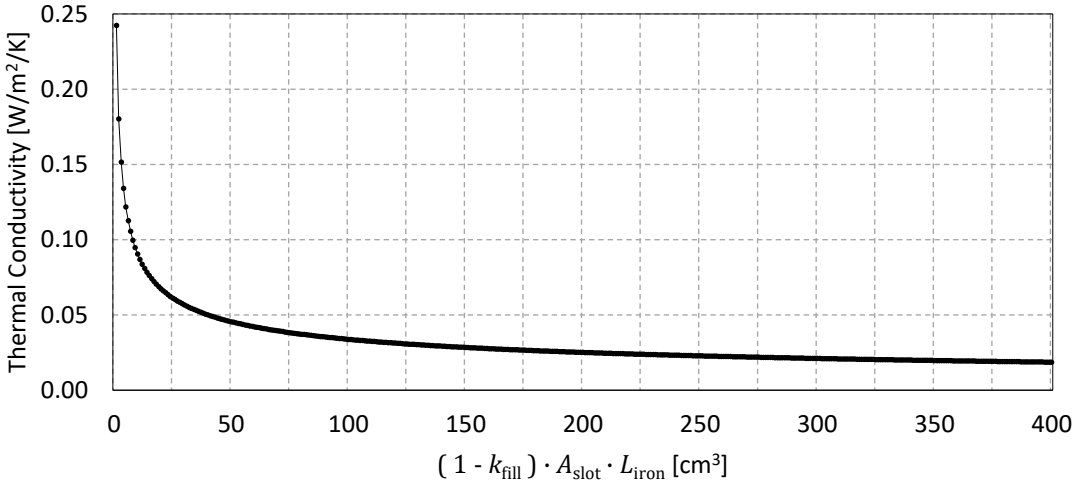

Figure 2-8 Equivalent slot thermal conductivity.

2.2.1.2 Conduction between Stator Iron Core and Aluminum Cooling Jacket

From the study in [49] [50], the interface gap between the stator iron core and aluminum cooling jacket is related to the imperfections along the touching surfaces. The imperfection is a complex function of material hardness, interface pressure, surface smoothness, and so forth. From an engineering perspective, one simple way to model the thermal contact is to utilize an average interference airgap. From the data presented in [50], the average interference airgap varies from 0.01 mm to 0.08 mm. And it is concluded that the thickness of average interference airgap is strongly influenced by the assembly process. Therefore, in this study, 0.05 mm is taken as the initial value to do the modeling.

2.2.2 Convective Heat Transfer

Convection is the type of heat transfer that occurs between different parts of fluid with temperature differences, or between the fluid and the wall licked by the fluid itself [51]. Several dimensionless numbers are for frequent use in convective heat transfer analysis, and they are summarized in Table 2-1.

Table 2-1. Dimensionless numbers of frequent use.

Name	Symbol	Meaning	Expression
Reynolds Number	Re	The ratio of inertial forces to viscous forces within a fluid	$\frac{\rho\cdot v\cdot l}{\mu}$
Nusselt Number	Nu	The ratio of convective to conductive heat transfer at a boundary in a fluid	$\frac{h\cdot d}{\lambda}$
Prandtl Number	Pr	The ratio of momentum diffusivity to thermal diffusivity	$\frac{c_{\mathrm{p}}\cdot\mu}{\lambda}$

The flow of a fluid can be classified as laminal flow, i.e. smooth flow, and turbulent flow, i.e. distorted flow. The schematics of laminal flow and turbulent flow are shown in Figure 2-9. In order to determine whether a flow is laminal or turbulent, the *Reynolds number*, which is the ratio between inertia force and viscous force, needs to be calculated

$$Re = \frac{\rho \cdot v \cdot l}{\mu} \tag{2-71}$$

where the density of the fluid ρ is in kg/m^3, the velocity of the fluid v is in m/s, the characteristic length l, i.e. the hydraulic diameter, is in m, the dynamic viscosity of the fluid μ is in kg/m·s and the kinematic viscosity of the fluid ν is in m^2/s. In terms of the flow in airgap, the hydraulic diameter is twice of the annular airgap thickness [52]. For a Re below 2000, the viscous force is dominated and the flow is certainly laminar, whereas for a Re above 3000, the inertia force is dominated and the flow is certainly turbulent [51].

(a) Laminar flow (b) Turbulent flow

Figure 2-9 Schematics of laminar flow and turbulent flow.

The convective heat transfer can be calculated by temperature difference and thermal resistance as well

$$P = \frac{T_1 - T_2}{R_{\text{th·conv}}} \tag{2-72}$$

and the convective thermal resistance $R_{\text{th·conv}}$ can be calculated as

$$R_{\text{th·conv}} = \frac{1}{h \cdot A} \tag{2-73}$$

where the heat transfer coefficient h is in W/(m^2·K). Further, h can be calculated as

$$h = \frac{\lambda \cdot Nu}{l} \tag{2-74}$$

where the thermal conductivity of the fluid λ is in W/(m·K), and the characteristic surface length l, i.e. the hydraulic diameter, is in m. Nu is the *Nusselt number*, which represents the ratio of convective to conductive heat transfer at a boundary in the fluid

$$Nu = \frac{h \cdot L}{\lambda} \tag{2-75}$$

And in order to determine Nu, the *Prandtl Number*, Pr, is sometimes necessary, which is defined as the ratio of momentum diffusivity to thermal diffusivity

$$Pr = \frac{c_{\mathrm{p}} \cdot \mu}{\lambda} \tag{2-76}$$

A low value of Pr , $Pr \ll 1$, means a domination of thermal diffusivity, whereas in case of a large Pr, $Pr \gg 1$, means a domination of momentum diffusivity.

2.2.2.1 Convection Thermal Resistance Between Coolant and Cooling Channels

In order to calculate h to characterize the convection between coolant and cooling channels, one approach is provided by [53], where the *Nusselt Number* can be calculated as

$$Nu = \frac{f}{8} \cdot \frac{(Re - 1000) \cdot Pr}{1 + 12.7 \cdot \left(\frac{f}{8}\right)^{\frac{1}{2}} \cdot \left(Pr^{\frac{2}{3}} - 1\right)} \tag{2-77}$$

where f is the friction factor and if the wall is smooth, then it can be approximated as

$$f = \frac{1}{(0.79 \cdot \ln Re - 1.64)^2} \tag{2-78}$$

and then, the heat transfer factor is calculated as in (2-74) where the characteristic surface length is the channel diameter.

2.2.2.2 Convection Thermal Resistance Between Iron-Core and Airgap

To calculate the heat transfer coefficient at the airgap, the type of airflow in the airgap has to be determined [52]. The Taylor number indicates the relative effects of inertial forces and viscosity for an annulus with rotation of one or more of the cylindrical surfaces. The Taylor number based on mean annulus radius $r_m = \frac{r_a + r_b}{2}$ is defined as

$$Ta_m = \frac{\Omega_a \cdot {r_m}^{0.5} \cdot (r_b - r_a)^{1.5}}{\nu} \tag{2-79}$$

where r_a and r_b are the inner and outer annulus radius respectively. Please be aware that ν is the Greek letter “nu” instead of the English letter “v”, and it is the kinematic viscosity of the fluid in m^2/s. The critical speed based on Taylor’s solution can be determined as

$$\Omega_{\mathrm{cr}} = \pi^2 \cdot \nu \cdot \sqrt{\frac{r_a + r_b}{2 \cdot S \cdot (r_b - r_a)^3 \cdot {r_a}^2 \cdot \left(1 - \frac{\Omega_{\mathrm{b}}}{\Omega_{\mathrm{a}}} \cdot \frac{{r_b}^2}{{r_a}^2}\right) \cdot \left(1 - \frac{\Omega_{\mathrm{b}}}{\Omega_{\mathrm{a}}}\right)}} \tag{2-80}$$

where Ω_{a} is the speed of the inner cylindrical surface, Ω_{b} is the speed of the outer cylindrical surface, and

$$S = 0.0571\left[\frac{1+\frac{\Omega_{\mathrm{b}}}{\Omega_{\mathrm{a}}}}{1-\frac{\Omega_{\mathrm{b}}}{\Omega_{\mathrm{a}}}} + 0.652\left(1-\frac{r_b}{r_a}\right)\right] + 0.00056\left[\frac{1+\frac{\Omega_{\mathrm{b}}}{\Omega_{\mathrm{a}}}}{1-\frac{\Omega_{\mathrm{b}}}{\Omega_{\mathrm{a}}}} + 0.652\left(1-\frac{r_b}{r_a}\right)\right]^{-1} \quad (2\text{-}81)$$

In case of outer stator, i.e. $\Omega_{\mathrm{b}} = 0$, and a narrow gap, i.e. $r_a \approx r_b$, then (2-80) becomes

$$\Omega_{\mathrm{cr}} = \pi^2 \cdot \nu \cdot \sqrt{\frac{1}{S \cdot (r_b - r_a)^3 \cdot r_m}} \quad (2\text{-}82)$$

Hence (2-81) becomes

$$S = 0.0571 + 0.00056 = 0.05766 \quad (2\text{-}83)$$

together with the assumption of a stationary outer cylinder, the critical speed gives a corresponding critical Taylor number $Ta_{m.cr}$ as

$$Ta_{m.cr} = \frac{\pi^2}{\sqrt{S}} = \sqrt{1697} = 41.19 \quad (2\text{-}84)$$

In case of a Taylor number smaller than $Ta_{m.cr}$, the air flow in the airgap remains a Couette flow, whereas in case of a Taylor number greater than $Ta_{m.cr}$, Taylor vortices can form. The critical speed in (2-82) in this case becomes

$$\Omega_{\mathrm{cr}} = \frac{41.19 \cdot \nu}{\sqrt{(r_b - r_a)^3 \cdot r_m}} \quad (2\text{-}85)$$

For a larger airgap size, i.e. when $r_a \approx r_b$ is not valid, the value of $Ta_{m.cr}$ needs to be corrected accordingly. However, for the sack of convenience, in order to use the same pricewise function to determine Nu for all geometries, a geometric factor can be defined to correct Ta_m instead of $Ta_{m.cr}$

$$F_g = \frac{\pi^2}{41.19 \cdot \sqrt{S}} \cdot \left(\frac{r_b + r_a}{2 \cdot r_a}\right) \quad (2\text{-}86)$$

In case $r_a \approx r_b$ is valid, $F_g = 1$. Then according to [54] [55] [56] [52], the *Nusselt Number* can be determined by the same pricewise function

$$Nu = \begin{cases} 2 \cdot \dfrac{\frac{r_b}{r_a} - 1}{\ln\left(\frac{r_b}{r_a}\right)} & \left(\dfrac{Ta_m}{F_g}\right)^2 < 1.7 \times 10^3 \\ 0.128 \cdot \left(\dfrac{Ta_m}{F_g}\right)^{0.734} & 1.7 \times 10^3 < \left(\dfrac{Ta_m}{F_g}\right)^2 < 10^4 \\ 0.409 \cdot \left(\dfrac{Ta_m}{F_g}\right)^{0.482} & 10^4 < \left(\dfrac{Ta_m}{F_g}\right)^2 < 10^7 \end{cases} \quad (2\text{-}87)$$

Then based on the definition of Nu, the heat transfer coefficient can be calculated as

$$h = \frac{\lambda \cdot Nu}{L} = \frac{\lambda \cdot Nu}{r_b - r_a} \quad (2\text{-}88)$$

2.2.3 Radiative Heat Transfer

Energy is emitted by a warm body through radiation in all directions. When the radiated energy hits another body, part of the energy is reflected, whereas the remaining part is absorbed by the body and transformed into heat. The heat transfer according to radiation can be calculated as [57]

$$P = \frac{{T_1}^4 - {T_2}^4}{R_{\text{th}}} \quad (2\text{-}89)$$

where T_1 is the temperature of the radiating surface while T_2 is that of the radiated one. Radiation only becomes significant at high temperatures and therefore it is neglected in this study.

2.2.4 Thermal Capacitance

In case thermal dynamics is of interest, thermal capacitance needs to be introduced. The thermal capacitance of each structure can be expressed as the multiplication of heat specific of the material and the mass, and the mass is the production of mass density and the volume

$$C_{\text{th}} = c \cdot m = c \cdot \rho_{\text{m}} \cdot Volumn = c \cdot \rho_{\text{m}} \cdot Area \cdot length \quad (2\text{-}90)$$

where ρ_{m} is the mass density and c is the specific heat of the material.

2.2.5 Lumped Parameter Model

Based on the schematics of structure shown in Figure 2-7, and the theories introduced in previous sections, a simplified lumped parameter thermal model can be formulated as shown in Figure 2-10. The stator windings and the field winding are the sources of heat, and they are denoted as Node 1 and 2 in the figure. The heat then flows to the iron core through the material with equivalent thermal conductivity as introduced in (2-70) in Section 2.2.1.1. The heat from the rotor is dissipated to the airgap and further to the stator iron core with the convection mechanism introduced in Section 2.2.2.2. The heat in stator then goes to the

aluminum jacket though the average interface gap of 0.05 mm as introduced in Section 2.2.1.2. Finally, the heat is taken away by the coolant in the form of convection as introduced in Section 2.2.2.1.

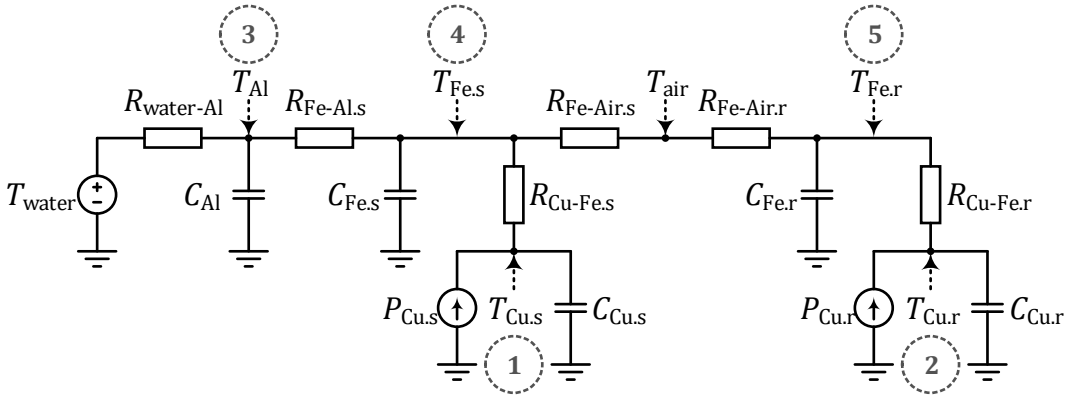

Figure 2-10 Schematic of a simplified lumped parameter thermal model for EESM.

2.2.6 Adiabatic Process

Adiabatic process is to study the temperature rise before any cooling mechanism takes effect. This study is performed to verify the peak operation of traction electric motors for 30 s [58]. The copper loss can be expressed as

$$P_{\text{Cu}} = I^2 \cdot R = I^2 \cdot \rho_{\text{r}} \cdot \frac{l}{A} = I \cdot J \cdot \rho_{\text{r}} \cdot l \tag{2-91}$$

in J/s. With (2-90), the copper thermal capacitance is expressed as

$$C_{\text{th}} = c \cdot \rho_{\text{m}} \cdot A_{\text{Cu}} \cdot l_{\text{Cu}} \tag{2-92}$$

where A_{Cu} is the cross section area of copper wire and l_{Cu} is the length of copper wire. Based on these, it becomes possible to calculate the temperature derivative when copper heats up itself

$$\frac{dT}{dt} = \frac{P_{\text{Cu}}}{C_{\text{th.Cu}}} = \frac{I \cdot J \cdot \rho_{\text{r}} \cdot l_{\text{Cu}}}{c_{\text{Cu}} \cdot \rho_{\text{m}} \cdot l_{\text{Cu}} \cdot A_{\text{Cu}}} = J^2 \cdot \frac{\rho_{\text{r}}}{c_{\text{Cu}} \cdot \rho_{\text{m}}} \tag{2-93}$$

With the parameters of copper, $\rho_{\text{r}} = 1.72 \times 10^{-8}$, $c_{\text{Cu}} = 3.9 \times 10^2$ and $\rho_{\text{m}} = 8.96 \times 10^3$ into the formula, then

$$\frac{dT}{dt} = 4.92 \times 10^{-3} \cdot J^2 \tag{2-94}$$

in A/mm^2. It should be pointed out that, in case of AC current, the current density here should be the root mean square (RMS) value. The temperature rise derivative of adiabatic process of copper in K/s is shown in Figure 2-11.

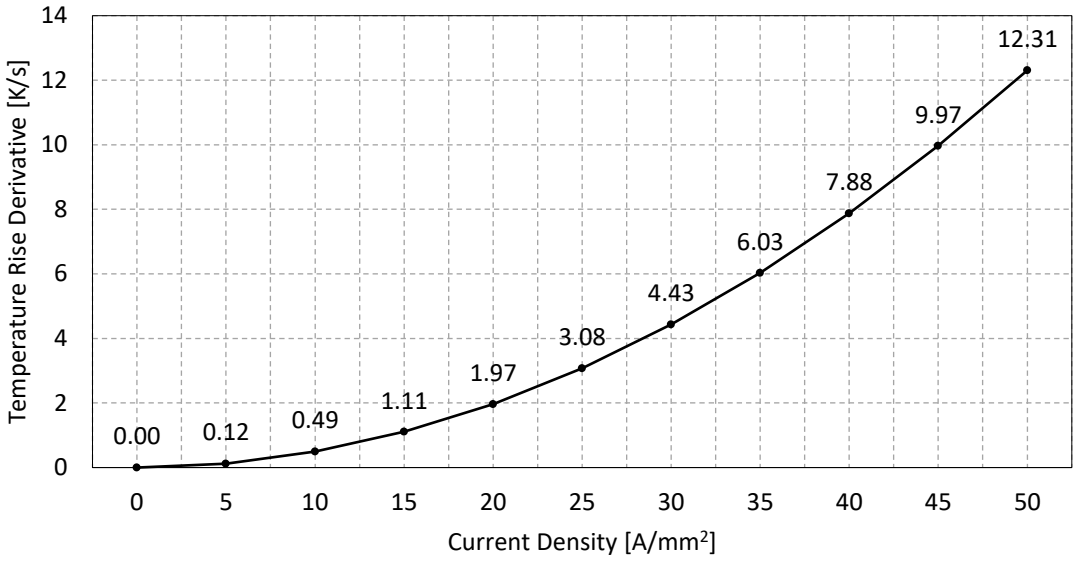

Figure 2-11 Temperature rise derivative during adiabatic process.

2.3 High-Frequency Brushless Excitation Modeling

The modeling of high-frequency brushless excitation system is established in this section. The electrical quantities of the system are described in Figure 2-12. The reason to have a capacitor across the field winding is to avoid high-frequency oscillations between the transformer leakage inductance and the diode stray capacitance [59].

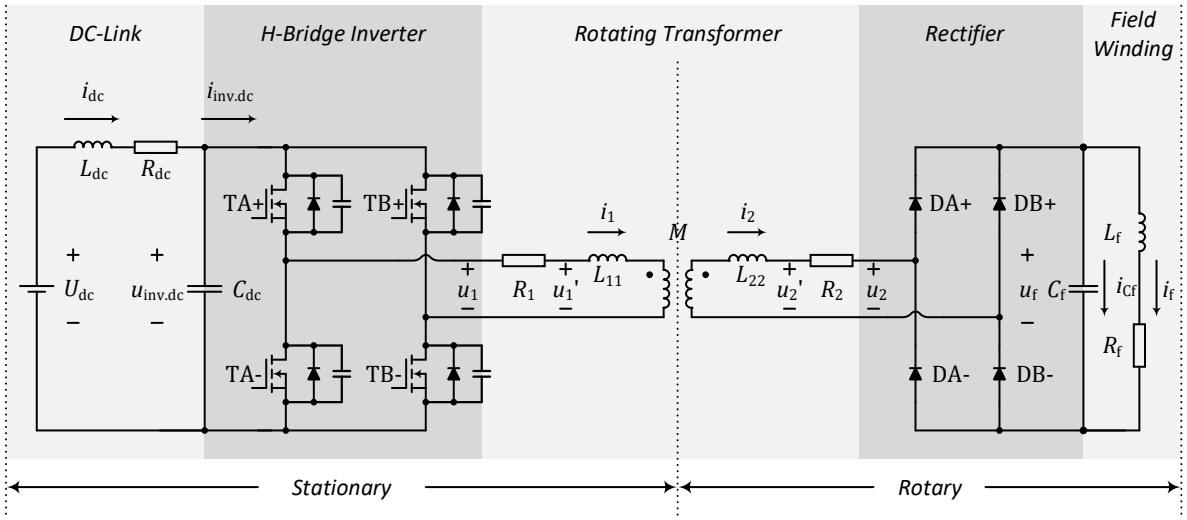

Figure 2-12 Schematic of wireless excitation system dynamic model.

2.3.1 Steady State Modeling

The steady state modeling characterizes the relationship between the input and output of the excitation system in steady state. In steady state, the output power equals the input power times the efficiency

$$U_{\mathrm{dc}} \cdot I_{\mathrm{dc}} \cdot \eta_{\mathrm{tot}} = P_{\mathrm{dc}} \cdot \eta_{\mathrm{tot}} = P_{\mathrm{f}} = {I_{\mathrm{f}}}^2 \cdot R_{\mathrm{f}} \tag{2-95}$$

where U_{dc} is the dc-link voltage, I_{dc} is the dc-link current, η_{tot} is the total efficiency, P_{dc} is the dc-link input power and P_{f} is the field winding output power. Therefore, the dc-link current is proportional to the square of the field current, by assuming an almost constant efficiency

$$I_{\mathrm{dc}} = \frac{R_{\mathrm{f}}}{U_{\mathrm{dc}} \cdot \eta_{\mathrm{tot}}} \cdot {I_{\mathrm{f}}}^2 \tag{2-96}$$

Due to the limitation of space and the centrifugal force during the rotation, it is not possible to place a C_{f} high enough to keep the field voltage as a pure DC quantity. Hence the field winding is neither in a voltage-stiff case nor in a current-still case, but somewhere in the between. It is therefore not straight forward to derive the waveforms analytically. However, an analytical solution roughly showing the relationship between the duty cycle and the field current can still be derived by considering the fundamental component [60]. The amplitude of the fundamental component of the inverter output voltage is

$$U_{1\cdot\mathrm{amp}} = \frac{4}{\pi} \cdot U_{\mathrm{dc}} \cdot \sin\left(\frac{\pi}{2} d\right) \tag{2-97}$$

where d is the duty cycle of the H-bridge inverter. Assuming lossless, and considering only the fundamental component, the mean absolute value of the fundamental component on the secondary side of the transformer becomes the field voltage and the field current can therefore be calculated as

$$I_{\mathrm{f}} = \frac{U_{\mathrm{f}}}{R_{\mathrm{f}}} = \frac{2}{\pi} \cdot \frac{N_2}{N_1} \cdot \frac{U_{1\cdot\mathrm{amp}}}{R_{\mathrm{f}}} = \frac{8}{\pi^2} \cdot \frac{N_2}{N_1} \cdot \frac{U_{\mathrm{dc}}}{R_{\mathrm{f}}} \cdot \sin\left(\frac{\pi}{2} d\right) \tag{2-98}$$

where N_1 is the number of turns of the primary winding and N_2 is the number of turns of the secondary winding. This expression means the I_{f} curve is in the shape of $\sin\left(\frac{\pi}{2} d\right)$. And the dc-link current can therefore be calculated by substituting (2-98)(2-110) into (2-96)

$$I_{\mathrm{dc}} = \frac{32}{\pi^4} \cdot \frac{{N_2}^2}{{N_1}^2} \cdot \frac{U_{\mathrm{dc}}}{R_{\mathrm{f}}} \cdot \frac{1 - \cos(\pi d)}{\eta_{\mathrm{tot}}} \tag{2-99}$$

which means the I_{dc} curve is in the shape of $[1 - \cos(\pi d)]$. Define a characteristic current

$$I_{\mathrm{char}} = \frac{{N_2}^2}{{N_1}^2} \cdot \frac{U_{\mathrm{dc}}}{R_{\mathrm{f}}} \tag{2-100}$$

then the ratio of $\frac{I_{\mathrm{dc}}}{I_{\mathrm{char}}}$ and $\frac{I_{\mathrm{f}}}{I_{\mathrm{char}}}$ are plotted in Figure 2-13, assuming $N_1 = N_2$ and $\eta_{\mathrm{tot}} = 100\%$. The experimental results showing the curve of I_{f} versus d, as well as the curve of I_{dc} versus d are available in Chapter 6.

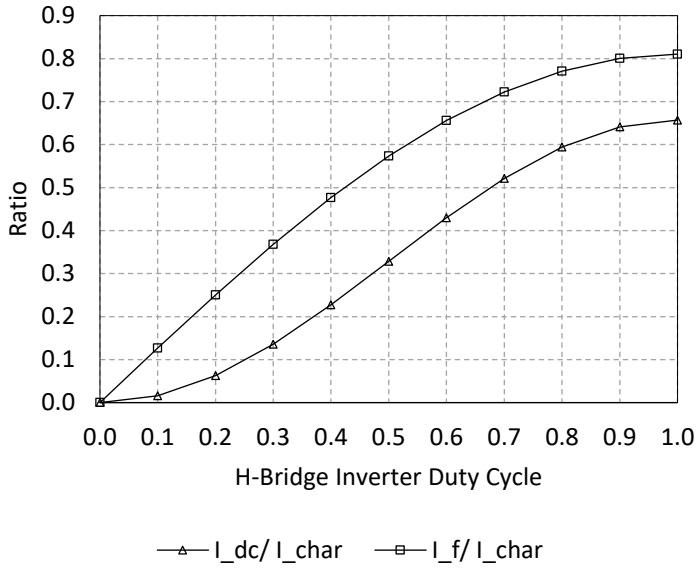

Figure 2-13 Current ratio.

2.3.2 Dynamic Modeling

To develop a reliable and modular dynamic model of the excitation system, the system is decomposed into several modules, dc-link, H-bridge inverter, transformer, rectifier and field winding, as shown in Figure 2-12. Each part can be described by a few differential equations or arithmetic equations. Necessary simplifications are introduced without sacrificing the accuracy too much, e.g. the diodes are described by a threshold voltage and an equivalent resistance. In some parts of the system, the circuit is nonlinear, and a few criteria are needed to judge the operation modes of the circuit. The judgement of the circuit modes is developed based on the physical understanding of the circuit, similar as in [61]. This simplifies calculation and reduces computation time.

In Figure 2-12, U_{dc} and i_{dc} are the voltage and current of the dc power source; R_{dc}, L_{dc} and C_{dc} are the dc-link resistance, inductance and capacitance respectively; $u_{\mathrm{inv.dc}}$ is the dc-link capacitor bank voltage, $i_{\mathrm{inv.dc}}$ is the dc-link current going to the switches; u_1 and u_2 are the transformer primary and secondary side terminal voltages, i_1 and i_2 are the transformer primary and secondary side currents, u_1' and u_2' are the transformer primary and secondary side voltages without resistive voltage drop; R_1 and R_2 are primary and secondary side resistances, L_{11} and L_{22} are primary and secondary side self-inductance, M is the mutual-inductance; R_{f}, L_{f} and C_{f} are the field winding resistance, inductance and capacitance respectively.

2.3.2.1 DC-Link

The dc-link inductance L_{dc} together with the dc-link capacitance C_{dc} are energy storage components and therefore the dc-link current, i_{dc} together with voltage across the capacitor, $u_{\mathrm{inv.dc}}$, are counted as states. The states can be described as

$$\begin{cases} \dfrac{di_{\mathrm{dc}}}{dt} = \dfrac{U_{\mathrm{dc}} - u_{\mathrm{inv.dc}} - R_{\mathrm{dc}} \cdot i_{\mathrm{dc}}}{L_{\mathrm{dc}}} \\ \dfrac{du_{\mathrm{inv.dc}}}{dt} = \dfrac{i_{\mathrm{dc}} - i_{\mathrm{inv.dc}}}{C_{\mathrm{dc}}} \end{cases} \tag{2-101}$$

Hence the current going into the inverter is considered as input to the model and is described as

$$i_{\mathrm{inv.dc}} = i_1 \cdot (s_{\mathrm{TA+}} - s_{\mathrm{TB+}}) \tag{2-102}$$

where i_1 denotes the output current of the inverter, s denotes the switching signal of the MOSFETs: $s = 0$ means off and $s = 1$ means on. When the upper switch is on, then the bottom is off simultaneously and vice versa. Apart from that, blanking time is also implemented, when the two switches are off simultaneously for a short while to prevent any shoot-circuit of dc-link.

2.3.2.2 H-Bridge Inverter

The dc-link capacitor voltage and transformer current are the inputs, whereas the transformer input voltage is the output of this module. The inverter is composed by two phases, A and B, and the voltage of each leg $u_{\mathrm{inv.A}}$ and $u_{\mathrm{inv.B}}$ can be described as

$$u_{\mathrm{inv.A}} = \begin{cases} \dfrac{u_{\mathrm{inv.dc}}}{2} - R_{\mathrm{ds}} \cdot i_1 & s_{\mathrm{TA+}} = 1 \quad s_{\mathrm{TA-}} = 0 \\ R_{\mathrm{ds}} \cdot i_1 - \dfrac{u_{\mathrm{inv.dc}}}{2} & s_{\mathrm{TA+}} = 0 \quad s_{\mathrm{TA-}} = 1 \end{cases} \tag{2-103}$$

$$u_{\mathrm{inv.B}} = \begin{cases} \dfrac{u_{\mathrm{inv.dc}}}{2} - R_{\mathrm{ds}} \cdot i_1 & s_{\mathrm{TB+}} = 1 \quad s_{\mathrm{TB-}} = 0 \\ R_{\mathrm{ds}} \cdot i_1 - \dfrac{u_{\mathrm{inv.dc}}}{2} & s_{\mathrm{TB+}} = 0 \quad s_{\mathrm{TB-}} = 1 \end{cases} \tag{2-104}$$

where R_{ds} is the drain-source resistance of the MOSFET. Then, the inverter output voltage u_1 is the difference between the outputs of Phase A and B

$$u_1 = u_{\mathrm{inv.A}} - u_{\mathrm{inv.B}} \tag{2-105}$$

During blanking time, the drain-source capacitance of each MOSFET, C_{ds}, charges and discharges, as illustrated in Figure 2-14. Before the blanking interval starts, as shown in (a), the upper leg conducts, and the lower leg capacitance is charged to U_{dc}. When the blanking interval starts, as shown in (b), both upper and lower switch are off, but the current needs to continue flowing due to the inductance of the transformer. The lower leg diode cannot conduct immediately since the voltage across it is at U_{dc}. Therefore, a discharging process of the lower leg capacitance voltage commences. The sum of the upper and lower leg capacitance voltage should be at U_{dc}, so the discharging of the lower leg capacitance happens together with the charging of the upper leg capacitance. This continues until the charging and discharging completes as shown in (c). Thereafter, the lower leg diode takes all the current. The charging and discharging process can be described as

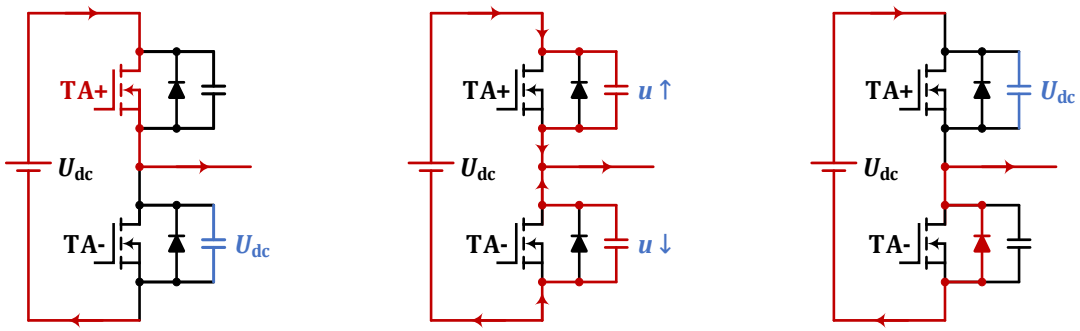

(a) Before charging (b) During charging (c) After charging

Figure 2-14 Charging and discharging of drain-source capacitances during blanking time.

$$\begin{aligned} C_{\mathrm{ds}}\frac{du_{\mathrm{A+}}}{dt} &= i_{\mathrm{A+}} \qquad C_{\mathrm{ds}}\frac{du_{\mathrm{B+}}}{dt} = i_{\mathrm{B+}} \\ C_{\mathrm{ds}}\frac{du_{\mathrm{A-}}}{dt} &= i_{\mathrm{A-}} \qquad C_{\mathrm{ds}}\frac{du_{\mathrm{B-}}}{dt} = i_{\mathrm{B-}} \end{aligned} \tag{2-106}$$

where C_{ds} is the drain-source capacitance of each MOSFET, $u_{\mathrm{A+}}$, $u_{\mathrm{A-}}$, $u_{\mathrm{B+}}$ and $u_{\mathrm{B-}}$ are the voltages across the upper leg of Phase A, lower leg of Phase A, upper leg of Phase B, lower leg of Phase B respectively, and $i_{\mathrm{A+}}$, $i_{\mathrm{A-}}$, $i_{\mathrm{B+}}$ and $i_{\mathrm{B-}}$ are the currents through the upper leg of Phase A, lower leg of Phase A, upper leg of Phase B, lower leg of Phase B respectively. The constraints during the charging and discharging process can be described as

$$u_{\mathrm{A+}} + u_{\mathrm{A-}} = u_{\mathrm{inv.dc}} = u_{\mathrm{B+}} + u_{\mathrm{B-}} \tag{2-107}$$

Therefore, from (2-106) and (2-107),

$$i_{\mathrm{A+}} + i_{\mathrm{A-}} = C_{\mathrm{ds}}\frac{du_{\mathrm{A+}}}{dt} + C_{\mathrm{ds}}\frac{du_{\mathrm{A-}}}{dt} = C_{\mathrm{ds}}\frac{d(u_{\mathrm{A+}} + u_{\mathrm{A-}})}{dt} = C_{\mathrm{ds}}\frac{du_{\mathrm{inv.dc}}}{dt} \tag{2-108}$$

$$i_{\mathrm{B+}} + i_{\mathrm{B-}} = C_{\mathrm{ds}}\frac{du_{\mathrm{B+}}}{dt} + C_{\mathrm{ds}}\frac{du_{\mathrm{B-}}}{dt} = C_{\mathrm{ds}}\frac{d(u_{\mathrm{B+}} + u_{\mathrm{B-}})}{dt} = C_{\mathrm{ds}}\frac{du_{\mathrm{inv.dc}}}{dt} \tag{2-109}$$

Since,

$$i_{\mathrm{A+}} - i_{\mathrm{A-}} = i_1 = i_{\mathrm{B-}} - i_{\mathrm{B+}} \tag{2-110}$$

from (2-108), (2-109) and (2-110), it can be concluded that

$$i_{\mathrm{A+}} = i_{\mathrm{B-}} = \frac{C_{\mathrm{ds}}\frac{du_{\mathrm{inv.dc}}}{dt} + i_1}{2} \tag{2-111}$$

$$i_{\mathrm{B+}} = i_{\mathrm{A-}} = \frac{C_{\mathrm{ds}}\frac{du_{\mathrm{inv.dc}}}{dt} - i_1}{2} \tag{2-112}$$

The voltage derivatives can therefore be solved as

$$\frac{du_{\text{inv.A}}}{dt} = \frac{du_{\text{A}-}}{dt} = \frac{i_{\text{A}-}}{C_{\text{ds}}} = \frac{\frac{du_{\text{inv.dc}}}{dt} - \frac{i_1}{C_{\text{ds}}}}{2} \approx -\frac{1}{2}\frac{i_1}{C_{\text{ds}}} \tag{2-113}$$

$$\frac{du_{\text{inv.B}}}{dt} = \frac{du_{\text{B}-}}{dt} = \frac{i_{\text{B}-}}{C_{\text{ds}}} = \frac{\frac{du_{\text{inv.dc}}}{dt} + \frac{i_1}{C_{\text{ds}}}}{2} \approx \frac{1}{2}\frac{i_1}{C_{\text{ds}}} \tag{2-114}$$

The approximation "≈" is valid when the dc-link capacitance is big enough so that $u_{\text{inv.dc}}$ is with almost no fluctuation. With (2-113) and (2-114), $u_{\text{inv.A}}$ and $u_{\text{inv.B}}$ can be obtained by take integrations of $-\frac{1}{2}\frac{i_1}{C_{\text{ds}}}$ and $\frac{1}{2}\frac{i_1}{C_{\text{ds}}}$ respectively. And this charging or discharging process continues until the anti-parallel diodes of the MOSFETs are forward-biased. Thereafter,

$$u_{\text{inv.A}} = \begin{cases} -\frac{u_{\text{inv.dc}}}{2} - V_{\text{F.inv}} & i_1 > 0 \\ \frac{u_{\text{inv.dc}}}{2} + V_{\text{F.inv}} & i_1 < 0 \end{cases} \tag{2-115}$$

$$u_{\text{inv.B}} = \begin{cases} \frac{u_{\text{inv.dc}}}{2} + V_{\text{F.inv}} & i_1 > 0 \\ -\frac{u_{\text{inv.dc}}}{2} - V_{\text{F.inv}} & i_1 < 0 \end{cases} \tag{2-116}$$

2.3.2.3 Rotating Transformer

The transformer terminal voltages are considered as the input whereas the transformer currents are considered as the outputs. The transformer can be described as

$$u_1' = L_{11} \cdot \frac{di_1}{dt} - M \cdot \frac{di_2}{dt} \tag{2-117}$$

$$u_2' = M \cdot \frac{di_1}{dt} - L_{22} \cdot \frac{di_2}{dt} \tag{2-118}$$

where u_1' and u_2' are the voltage drops across the transformer inductances only, i.e. they are equal to the terminal voltage u_1 and u_2 compensated by the voltage drops across the resistances $R_1 \cdot i_1$ and $R_2 \cdot i_2$

$$u_1' = (u_1 - R_1 \cdot i_1) \tag{2-119}$$

$$u_2' = (u_2 + R_2 \cdot i_2) \tag{2-120}$$

The current derivatives can therefore be described as

$$\frac{di_1}{dt} = -\frac{L_{22}}{M^2 - L_{11}L_{22}}u_1' + \frac{M}{M^2 - L_{11}L_{22}}u_2' \tag{2-121}$$

$$\frac{di_2}{dt} = -\frac{M}{M^2 - L_{22}L_{11}}u_1' + \frac{L_{11}}{M^2 - L_{22}L_{11}}u_2' \tag{2-122}$$

2.3.2.4 Rectifier

In this module, the transformer secondary current, field voltage and current are the inputs whereas rectifier capacitor current and transformer secondary voltage are the outputs. The rectifier has two operation modes, the power transferring mode when two diodes in diagonal positions conduct, as shown in Figure 2-15 (a) and (b), and the commutation mode when all the four diodes conduct, as shown in Figure 2-15 (c). The method to judge these two modes are introduced in the end of this section.

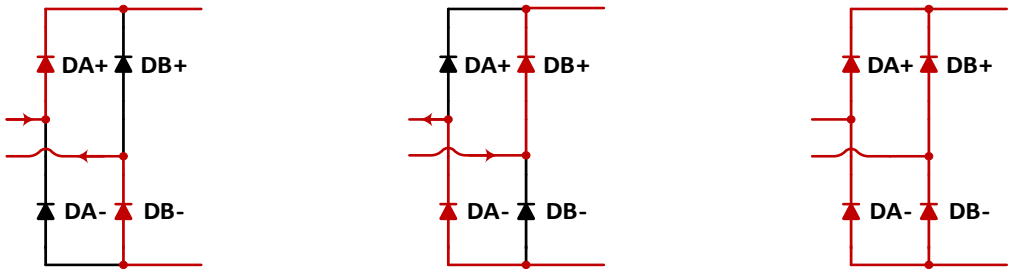

(a) Power transferring mode ($i_2 > 0$)(b) Power transferring mode ($i_2 < 0$) (c) Commutation mode

Figure 2-15 Power transferring mode and commutation mode.

During power transferring mode, there are two cases depending on the direction of the transformer current. In case $i_2 > 0$, as shown in subplot (a), i_2 is divided into the rectifier output capacitor current and the field current

$$i_{C_\mathrm{f}} + i_\mathrm{f} - i_2 = 0 \tag{2-123}$$

whereas in case $i_2 < 0$, as shown in subplot (b), the transformer current i_2, the rectifier output capacitor and the field current add up to be zero

$$i_{C_\mathrm{f}} + i_\mathrm{f} + i_2 = 0 \tag{2-124}$$

To sum up, (2-123) and (2-124) can be expressed as

$$i_{C_\mathrm{f}} = |i_2| - i_\mathrm{f} \tag{2-125}$$

In addition, the transformer secondary voltage u_2 is decided by the field voltage and the diode forward voltage drop

$$u_2 = \mathrm{sign}(i_2) \cdot (u_\mathrm{f} + 2 \cdot u_\mathrm{D}) = \mathrm{sign}(i_2) \cdot [u_\mathrm{f} + 2 \cdot (V_{\mathrm{F0}} + R_\mathrm{d} \cdot |i_2|)] \tag{2-126}$$

where

$$u_\mathrm{D} = V_{\mathrm{F0}} + R_\mathrm{d} \cdot |i_2| \tag{2-127}$$

And, in case the capacitance is quite small, the field voltage will drop to a value that all the four diodes are forward-biased. Then it comes to the commutation mode, as shown in subplot (c), during which, the current through Leg A can be described as

$$i_{\mathrm{DA+}} - i_{\mathrm{DA-}} = i_2 \tag{2-128}$$

And the voltage can be described as

$$0 = u_{\mathrm{f}} + u_{\mathrm{DA+}} + u_{\mathrm{DA-}} \tag{2-129}$$

where $u_{\mathrm{DA+}}$ and $u_{\mathrm{DA-}}$ can be described by the approximated model of diodes

$$u_{\mathrm{DA+}} = V_{\mathrm{F0}} + R_{\mathrm{s}} \cdot i_{\mathrm{DA+}} \tag{2-130}$$

$$u_{\mathrm{DA-}} = V_{\mathrm{F0}} + R_{\mathrm{s}} \cdot i_{\mathrm{DA-}} \tag{2-131}$$

Then from (2-129), (2-130) and (2-131), it yields

$$i_{\mathrm{DA+}} + i_{\mathrm{DA-}} = -\frac{u_{\mathrm{f}} + 2 \cdot V_{\mathrm{F0}}}{R_{\mathrm{s}}} \tag{2-132}$$

Thereafter, from (2-128) and (2-132), $i_{\mathrm{DA+}}$ and $i_{\mathrm{DA-}}$ can be solved

$$i_{\mathrm{DA+}} = \frac{-\frac{u_{\mathrm{f}} + 2 \cdot V_{\mathrm{F0}}}{R_{\mathrm{d}}} + i_2}{2} \tag{2-133}$$

$$i_{\mathrm{DA-}} = \frac{-\frac{u_{\mathrm{f}} + 2 \cdot V_{\mathrm{F0}}}{R_{\mathrm{d}}} - i_2}{2} \tag{2-134}$$

The voltage drop across each diode can therefore be decided by the diode current

$$u_{\mathrm{DA+}} = V_{\mathrm{F0}} + R_{\mathrm{d}} \cdot i_{\mathrm{DA+}} \tag{2-135}$$

$$u_{\mathrm{DA-}} = V_{\mathrm{F0}} + R_{\mathrm{d}} \cdot i_{\mathrm{DA-}} \tag{2-136}$$

Similarly, $i_{\mathrm{DB+}}$, $i_{\mathrm{DB-}}$, $u_{\mathrm{DB+}}$ and $u_{\mathrm{DB-}}$ can be solved

$$i_{\mathrm{DB+}} = \frac{-\frac{u_{\mathrm{f}} + 2 \cdot V_{\mathrm{F0}}}{R_{\mathrm{d}}} - i_2}{2} = i_{\mathrm{DA-}} \tag{2-137}$$

$$i_{\mathrm{DB-}} = \frac{-\frac{u_{\mathrm{f}} + 2 \cdot V_{\mathrm{F0}}}{R_{\mathrm{d}}} + i_2}{2} = i_{\mathrm{DA+}} \tag{2-138}$$

$$u_{\mathrm{DB+}} = V_{\mathrm{F0}} + R_{\mathrm{d}} \cdot i_{\mathrm{DB+}} = u_{\mathrm{DA-}} \tag{2-139}$$

$$u_{\mathrm{DB-}} = V_{\mathrm{F0}} + R_{\mathrm{d}} \cdot i_{\mathrm{DB-}} = u_{\mathrm{DA+}} \tag{2-140}$$

In the end, the transformer secondary voltage and the capacitor current can be decided

$$u_2 = u_{\mathrm{DA-}} - u_{\mathrm{DB-}} = u_{\mathrm{DA-}} - u_{\mathrm{DA+}} \tag{2-141}$$

$$i_{C_{\mathrm{f}}} = i_{\mathrm{DA+}} + i_{\mathrm{DB+}} - i_{\mathrm{f}} = i_{\mathrm{DA+}} + i_{\mathrm{DA-}} - i_{\mathrm{f}} \tag{2-142}$$

As for the boundary condition between the two modes, it can be firstly assumed that the circuit is in commutation mode, based on which, $i_{\mathrm{DA+}}$ and $i_{\mathrm{DA-}}$ can be calculated by following (2-133) and (2-134). In case both $i_{\mathrm{DA+}}$ and $i_{\mathrm{DA-}}$ are positive, then the circuit is really in commutation mode. Otherwise, the circuit is in the power transferring mode.

2.3.2.5 Field Winding

The field winding is modeled by field winding resistance R_{f}, inductance L_{f}, as well as filter output capacitance C_{f}. The input is the capacitor current $i_{C_{\mathrm{f}}}$ and the outputs are the field voltage u_{f} and current $i_{L_{\mathrm{f}}}$

$$\frac{du_{\mathrm{f}}}{dt} = \frac{i_{C_{\mathrm{f}}}}{C_{\mathrm{f}}} \tag{2-143}$$

$$\frac{di_{L_{\mathrm{f}}}}{dt} = \frac{u_{\mathrm{f}} - R_{\mathrm{f.T}} \cdot i_{L_{\mathrm{f}}}}{L_{\mathrm{f}}} \tag{2-144}$$

where $R_{\mathrm{f.T}}$ is the temperature corrected field resistance. The field resistance at temperature T is scaled from the resistance at temperature 20°C

$$R_{\mathrm{f.T}} = R_{\mathrm{f.20°C}} \cdot [1 + \alpha_{\mathrm{Cu}} \cdot (T - 20)] \tag{2-145}$$

where α_{Cu} is the temperature coefficient of resistivity of copper.

Chapter 3

Steady-State Operation

In this chapter, the steady-state operation of EESM is discussed, including the characteristics in dq-frame, operation envelop, optimization of steady state operation with constant inductances and magnetic saturation.

3.1 EESM Characteristics in DQ-Frame

The vectors in dq-frame of EESM operation are presented in Figure 3-1, where θ_i is the *current vector angle*, θ_u is the *voltage vector angle*, φ_PF is the *power factor angle* and δ is the *load angle* (*power angle*). The current and voltage vector angles are defined with respect to the d-axis. The power factor angle is defined as the difference between the current and voltage angles

$$\varphi_\mathrm{PF} = \theta_\mathrm{u} - \theta_\mathrm{i} \tag{3-1}$$

The load angle (power angle) is defined as the difference between the voltage angle and the back-EMF. Since the back-EMF is always along q-axis, then

$$\delta = \theta_\mathrm{u} - \frac{\pi}{2} \tag{3-2}$$

These angles follow

$$\theta_\mathrm{i} + \varphi_\mathrm{PF} = \theta_\mathrm{u} = \delta + \frac{\pi}{2} \tag{3-3}$$

The d- and q-axis current components can be expressed in polar form as

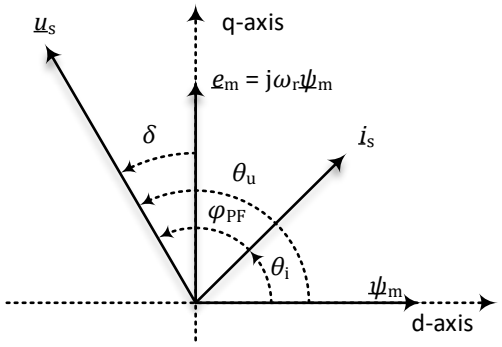

Figure 3-1 Angles in EESM dq-frame.

$$I_{\mathrm{d}} = I_{\mathrm{s}} \cdot \cos\theta_{\mathrm{i}} \tag{3-4}$$

$$I_{\mathrm{q}} = I_{\mathrm{s}} \cdot \sin\theta_{\mathrm{i}} \tag{3-5}$$

And so as for the d- and q-axis voltage components

$$U_{\mathrm{d}} = U_{\mathrm{s}} \cdot \cos\theta_{\mathrm{u}} \tag{3-6}$$

$$U_{\mathrm{q}} = U_{\mathrm{s}} \cdot \sin\theta_{\mathrm{u}} \tag{3-7}$$

Here the lower-case letters u and i mean instantaneous quantities, whereas if upper-case letters U and I are used, then they mean steady state quantities.

3.1.1 Current Limit Circle and Voltage Limit Ellipse

3.1.1.1 Current Limit Circle

The stator current is limited by the current output capability of the power electronic converter and the cross-section of the copper wires of the machine winding. These two aspects decide a maximum current amplitude $I_{\mathrm{s.max}}$ for the operation of the machine

$$I_{\mathrm{d}}{}^2 + I_{\mathrm{q}}{}^2 = I_{\mathrm{s}}{}^2 \leq I_{\mathrm{s.max}}{}^2 \tag{3-8}$$

The current limit can therefore be plotted as a circle with a radius of $I_{\mathrm{s.max}}$ are illustrated in Figure 3-2.

3.1.1.2 Voltage Limit Ellipse

Similarly, the stator voltage is limited by the voltage output capability of the power electronic converter and the insulation level of the machine winding. These two aspects decide a maximum voltage amplitude $U_{\mathrm{s.max}}$ for the operation of the machine

$$U_{\mathrm{d}}{}^2 + U_{\mathrm{q}}{}^2 = U_{\mathrm{s}}{}^2 \leq U_{\mathrm{s.max}}{}^2 \tag{3-9}$$

With third harmonic injection or with space vector pulse width modulation (SVPWM),

$$U_{\mathrm{s.max}} = \frac{U_{\mathrm{dc}}}{\sqrt{3}} \tag{3-10}$$

Assuming the resistive voltage drops are neglected, then the voltage limit criterion (3-9) can be described as

$$\psi_{\mathrm{d}}{}^2 + \psi_{\mathrm{q}}{}^2 = \left(\frac{U_{\mathrm{s}}}{\omega_{\mathrm{r}}}\right)^2 \leq \left(\frac{U_{\mathrm{s.max}}}{\omega_{\mathrm{r}}}\right)^2 \tag{3-11}$$

And in case of constant inductances, (3-11) becomes

$$(L_\mathrm{d}\cdot I_\mathrm{d}+L_\mathrm{m}\cdot I_\mathrm{f})^2+\left(L_\mathrm{q}\cdot I_\mathrm{q}\right)^2=\left(\frac{U_\mathrm{s}}{\omega_\mathrm{r}}\right)^2\le\left(\frac{U_\mathrm{s.max}}{\omega_\mathrm{r}}\right)^2 \tag{3-12}$$

which can be further formulated as an ellipse

$$\frac{(I_\mathrm{d}+I_\mathrm{d.0})^2}{a^2}+\frac{{I_\mathrm{q}}^2}{b^2}\le 1 \tag{3-13}$$

with

$$a^2=\left(\frac{U_\mathrm{s.max}}{\omega_\mathrm{r}L_\mathrm{d}}\right)^2 \qquad b^2=\left(\frac{U_\mathrm{s.max}}{\omega_\mathrm{r}L_\mathrm{q}}\right)^2 \qquad I_\mathrm{d.0}=\frac{L_\mathrm{m}}{L_\mathrm{d}}I_\mathrm{f} \tag{3-14}$$

where a is the major semi-axis, b is the minor semi-axis and $(-I_\mathrm{d.0},0)$ is the center of the ellipse. The eccentricity of the ellipse is decided by the saliency ratio of the machine

$$e=\sqrt{1-\frac{b^2}{a^2}}=\sqrt{1-\frac{L_\mathrm{d}}{L_\mathrm{q}}}=\sqrt{1-k_\mathrm{dq}} \tag{3-15}$$

In PMSM studies a *characteristic current* is usually defined as $\frac{\psi_\mathrm{m}}{L_\mathrm{d}}$ [62] [63], and similarly here for EESM studies a *characteristic current* can be defined as $I_\mathrm{d.0}=\frac{L_\mathrm{m}}{L_\mathrm{d}}I_\mathrm{f}$, which decides the center of the voltage limit ellipse. The center of the ellipse $(-I_\mathrm{d.0},0)$ shifts as the field current changes as illustrated in Figure 3-2 (a). And, as the speed ω_r increases, a and b decrease which means a collapse of the ellipse to its center as illustrated in Figure 3-2 (b).

At low speed, the current limit circle is inside the voltage limit ellipse. As the speed goes higher, the voltage limit ellipse starts to cut the current limit circle. And in case of $I_\mathrm{d.0}>I_\mathrm{s}$, the voltage limit ellipse will detach the current limit circle at high speed, whereas in case of $I_\mathrm{d.0}<I_\mathrm{s}$, the voltage limit ellipse will become totally inside the current limit circle. However, no matter how the ellipse collapses or shifts, the eccentricity remains the same.

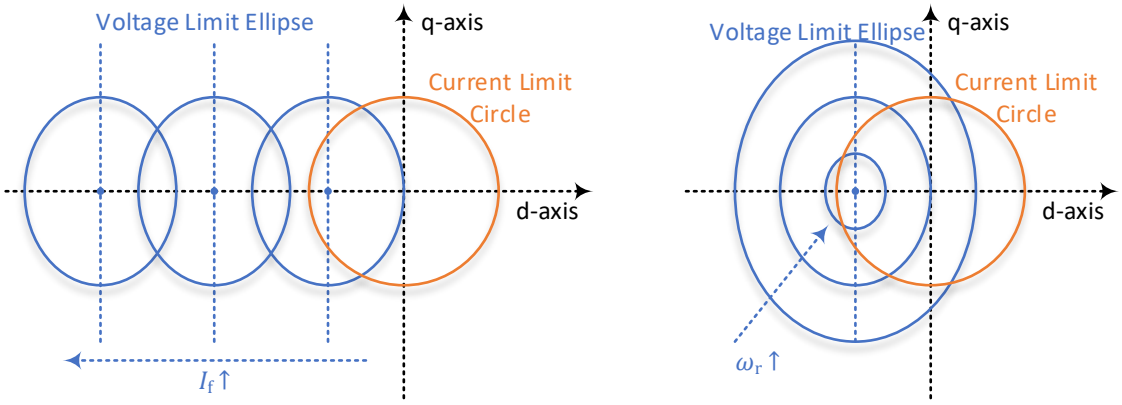

(a) Increase of field current (b) Increase of speed

Figure 3-2 Current limit circle and voltage limit ellipse of EESM in dq-frame.

3.1.1.3 Intersection

It is the common area of the current limit circle and the voltage limit ellipse that defines the possible operation area in the dq-frame. Therefore it becomes interesting to find the intersection of the two. The derived results will be used in the envelop study later in this chapter.

When the current and voltage limit ellipses intersect, the speed ω_r can be solved from (3-12) and it can be expressed by d- and q-axis current components in polar form

$$\begin{aligned}\omega_\mathrm{r} &= \frac{U_\mathrm{s.max}}{\sqrt{(L_\mathrm{d}\cdot I_\mathrm{d}+L_\mathrm{m}\cdot I_\mathrm{f})^2+\left(L_\mathrm{q}\cdot I_\mathrm{q}\right)^2}} \\ &= \frac{U_\mathrm{s.max}}{\sqrt{(L_\mathrm{d}\cdot I_\mathrm{s.max}\cdot\cos\theta_\mathrm{I}+L_\mathrm{m}\cdot I_\mathrm{f})^2+\left(L_\mathrm{q}\cdot I_\mathrm{s.max}\cdot\sin\theta_\mathrm{I}\right)^2}}\end{aligned} \tag{3-16}$$

The speeds when tangential intersection occurs can be found out by

$$\frac{\mathrm{d}\omega_\mathrm{r}}{\mathrm{d}\theta_\mathrm{I}}=0 \quad\Rightarrow\quad L_\mathrm{m}\cdot I_\mathrm{f}\cdot L_\mathrm{d}\cdot I_\mathrm{s.max}\cdot\sin\theta_\mathrm{I}+\frac{{L_\mathrm{d}}^2-{L_\mathrm{q}}^2}{2}\cdot{I_\mathrm{s.max}}^2\cdot\sin 2\theta_\mathrm{I}=0 \tag{3-17}$$

The solutions at $\theta_\mathrm{I}=0°$ and $180°$ are always available

$$\begin{aligned}\omega_\mathrm{r}(\theta_\mathrm{I}=0°) &= \frac{U_\mathrm{s}}{L_\mathrm{m}\cdot I_\mathrm{f}+L_\mathrm{d}\cdot I_\mathrm{s}} \\ \omega_\mathrm{r}(\theta_\mathrm{I}=180°) &= \frac{U_\mathrm{s}}{|L_\mathrm{m}\cdot I_\mathrm{f}-L_\mathrm{d}\cdot I_\mathrm{s}|}\end{aligned} \tag{3-18}$$

And $\omega_\mathrm{r}(\theta_\mathrm{I}=180°)$ is the maximum speed, which depends on the field current

$$\omega_\mathrm{r.max}=\omega_\mathrm{r}(\theta_\mathrm{I}=180°)=\begin{cases}\dfrac{U_\mathrm{s}}{L_\mathrm{m}\cdot I_\mathrm{f}-L_\mathrm{d}\cdot I_\mathrm{s}} & \text{if} \quad I_\mathrm{f}>\dfrac{L_\mathrm{d}}{L_\mathrm{m}}I_\mathrm{s} \\ \infty & \text{if} \quad I_\mathrm{f}=\dfrac{L_\mathrm{d}}{L_\mathrm{m}}I_\mathrm{s} \\ \dfrac{U_\mathrm{s}}{L_\mathrm{d}\cdot I_\mathrm{s}-L_\mathrm{m}\cdot I_\mathrm{f}} & \text{if} \quad I_\mathrm{f}<\dfrac{L_\mathrm{d}}{L_\mathrm{m}}I_\mathrm{s}\end{cases} \tag{3-19}$$

3.1.2 Electromagnetic Torque

The electromagnetic torque curves in dq-frame can be derived, and together with the voltage limit ellipse as well as the current limit circle, it becomes intuitive to know how much torque is reachable within the voltage and current limit. In case of constant inductances, from the torque formula (2-38), the q-axis current can be solved as

$$I_{\mathrm{q}} = \frac{2}{3 \cdot p} \cdot \frac{T_{\mathrm{em}}}{\psi_{\mathrm{m}} + \left(L_{\mathrm{d}} - L_{\mathrm{q}}\right) \cdot I_{\mathrm{d}}} \tag{3-20}$$

which means the I_{q} along the equal-torque curve can be expressed as a hyperbola

$$I_{\mathrm{q}} = \frac{2}{3 \cdot p} \cdot \frac{1}{L_{\mathrm{d}} - L_{\mathrm{q}}} \cdot \frac{T_{\mathrm{em}}}{\frac{L_{\mathrm{m}}}{L_{\mathrm{d}} - L_{\mathrm{q}}} \cdot I_{\mathrm{f}} + I_{\mathrm{d}}} = \frac{k_1}{I_{\mathrm{d}} + k_2} \tag{3-21}$$

where

$$k_1 = \frac{2}{3 \cdot p} \cdot \frac{T_{\mathrm{em}}}{L_{\mathrm{d}} - L_{\mathrm{q}}} \qquad k_2 = \frac{L_{\mathrm{m}}}{L_{\mathrm{d}} - L_{\mathrm{q}}} \cdot I_{\mathrm{f}} \tag{3-22}$$

And this indicates that, for a non-salient EESM, the current locus will be horizontal, whereas for a salient EESM, if $L_{\mathrm{d}} > L_{\mathrm{q}}$, the asymptotic lines will be horizontally shifted to the negative region and vice versa. Figure 3-3 illustrates the curves in case of $L_{\mathrm{d}} > L_{\mathrm{q}}$, $L_{\mathrm{d}} = L_{\mathrm{q}}$ and $L_{\mathrm{d}} < L_{\mathrm{q}}$ respectively. In plot (a), as L_{Δ} decreases, the asymptotic line of the hyperbola moves towards positive infinity, and if L_{Δ} decreases to zero, plot (a) becomes plot (b). Similar tendency applies for plot (c).

3.1.3 Unity Power Factor Ellipse

One advantage of EESM is that it can adjust the field current to improve power factor. Then it becomes interesting to know how unity power operation points are located in the dq-frame. The condition of unity power factor can be derived by setting (2-66) to zero. Neglecting the resistive voltage drops, it yields

$$Q_{\mathrm{s}} = \frac{3}{2} \cdot \left(U_{\mathrm{q}} \cdot I_{\mathrm{d}} - U_{\mathrm{d}} \cdot I_{\mathrm{q}}\right) = 0 \quad \Rightarrow \quad \psi_{\mathrm{d}} \cdot I_{\mathrm{d}} + \psi_{\mathrm{q}} \cdot I_{\mathrm{q}} = 0 \tag{3-23}$$

In case of constant inductances, the equation becomes

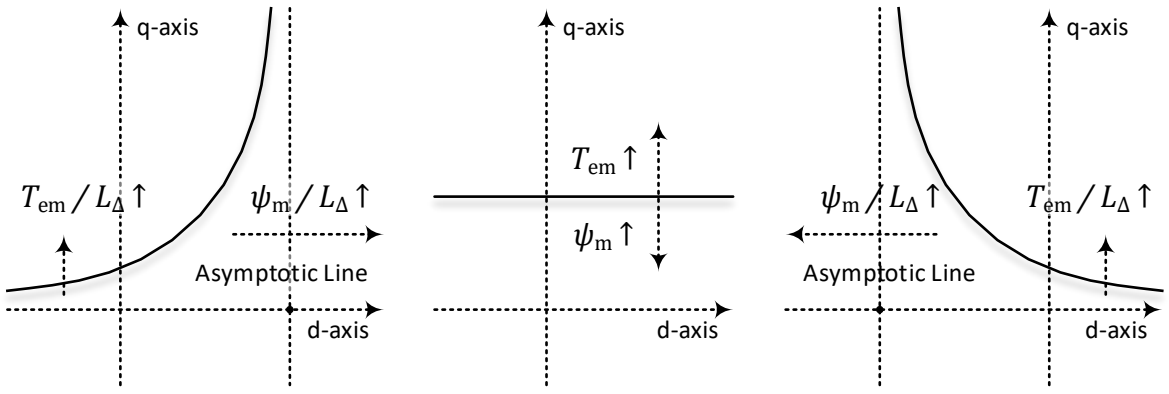

(a) $L_{\mathrm{d}} < L_{\mathrm{q}}$ (b) $L_{\mathrm{d}} = L_{\mathrm{q}}$ (c) $L_{\mathrm{d}} > L_{\mathrm{q}}$

Figure 3-3 Equal torque hyperbola of EESM in dq-frame.

$$L_{\mathrm{d}} \cdot {I_{\mathrm{d}}}^2 + L_{\mathrm{q}} \cdot {I_{\mathrm{q}}}^2 + L_{\mathrm{m}} \cdot I_{\mathrm{f}} \cdot I_{\mathrm{d}} = 0 \tag{3-24}$$

Obviously, since I_{f} is non-negative, to provide unity power factor, I_{d} must be negative. And, with a fixed I_{f}, (3-24) can be further reformulated as an equation of ellipse

$$\frac{(I_{\mathrm{d}} + a)^2}{a^2} + \frac{{I_{\mathrm{q}}}^2}{b^2} = 1 \tag{3-25}$$

with

$$a^2 = \frac{1}{4} \cdot \frac{{L_{\mathrm{m}}}^2}{{L_{\mathrm{d}}}^2} \cdot {I_{\mathrm{f}}}^2 \qquad b^2 = \frac{1}{4} \cdot \frac{{L_{\mathrm{m}}}^2}{L_{\mathrm{d}} \cdot L_{\mathrm{q}}} \cdot {I_{\mathrm{f}}}^2 \tag{3-26}$$

where a is the major semi-axis, b is the minor semi-axis and $(-a, 0)$ is the center of the ellipse. As shown in Figure 3-4 (a), the unity power factor ellipse expends and shrinks as the field current increases and decreases. The eccentricity of the ellipse is decided by saliency ratio of the machine as well

$$e = \sqrt{1 - \frac{b^2}{a^2}} = \sqrt{1 - \frac{L_{\mathrm{d}}}{L_{\mathrm{q}}}} = \sqrt{1 - k_{\mathrm{dq}}} \tag{3-27}$$

The current vector locates at the unity power factor ellipse makes the EESM operate at unit power factor. As can be noticed by comparing (3-14) and (3-26),

- The center of the voltage limit ellipse is twice farther of the center of the unit power factor ellipse.
- In case of $I_{\mathrm{d.0}} > I_{\mathrm{s}}$, the unity power factor ellipse will definitely intersect the current limit circle.

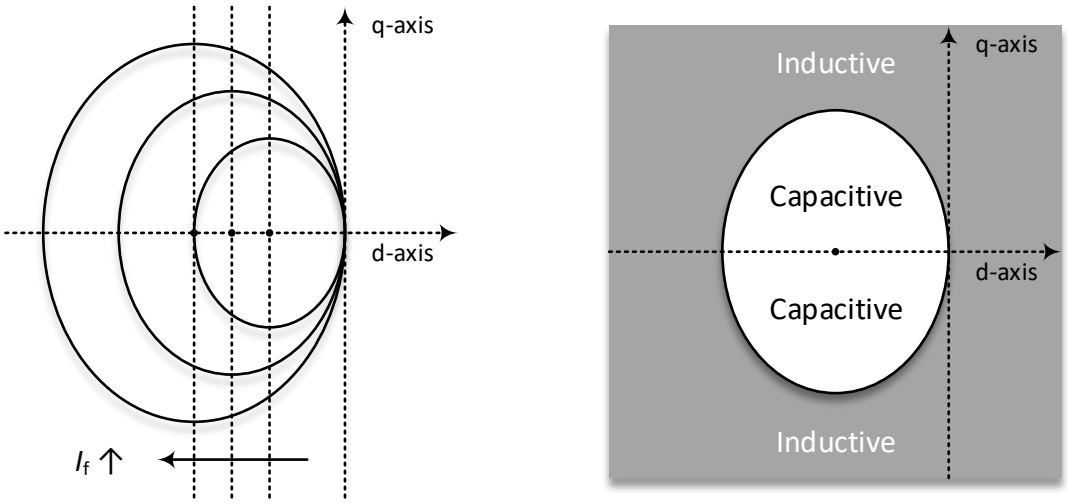

(a) Increase of field current (b) Capacitive and inductive area

Figure 3-4 Unity power factor ellipse of EESM in dq-frame ($L_{\mathrm{d}} > L_{\mathrm{q}}$).

- Inside the ellipse, the operation is capacitive, whereas outside is inductive, as shown in Figure 3-4 (b).

3.1.4 Equal Power Factor Curve

Neglecting resistive voltage drop, and according to (2-64), (2-65) and (2-66)

$$\tan\varphi_{\mathrm{PF}} = \frac{Q_{\mathrm{s}}}{P_{\mathrm{s}}} = \frac{L_{\mathrm{d}} \cdot {I_{\mathrm{d}}}^2 + L_{\mathrm{q}} \cdot {I_{\mathrm{q}}}^2 + L_{\mathrm{m}} \cdot I_{\mathrm{f}} \cdot I_{\mathrm{d}}}{\left(L_{\mathrm{d}} - L_{\mathrm{q}}\right) \cdot I_{\mathrm{d}} \cdot I_{\mathrm{q}} + L_{\mathrm{m}} \cdot I_{\mathrm{f}} \cdot I_{\mathrm{q}}} \tag{3-28}$$

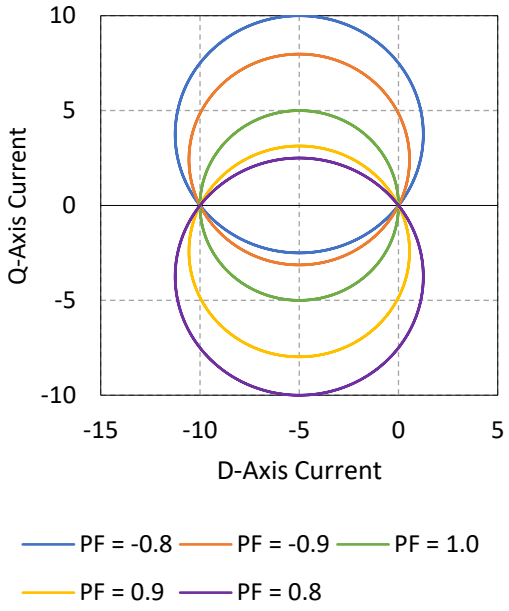

(a) $L_{\mathrm{m}}I_{\mathrm{f}} = 0.1\ [\mathrm{Wb}]$, $L_{\mathrm{d}} = 10\ [\mathrm{mH}]$, $L_{\mathrm{q}} = 10\ [\mathrm{mH}]$

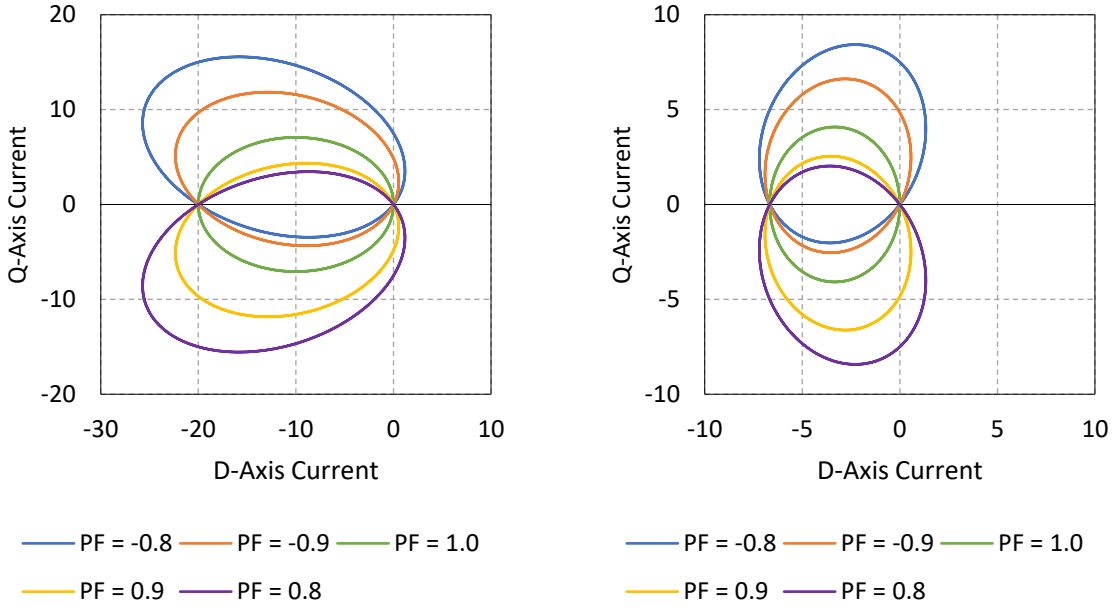

(b) $L_{\mathrm{m}}I_{\mathrm{f}} = 0.1\ [\mathrm{Wb}]$, $L_{\mathrm{d}} = 5\ [\mathrm{mH}]$, $L_{\mathrm{q}} = 10\ [\mathrm{mH}]$ (c) $L_{\mathrm{m}}I_{\mathrm{f}} = 0.1\ [\mathrm{Wb}]$, $L_{\mathrm{d}} = 15\ [\mathrm{mH}]$, $L_{\mathrm{q}} = 10\ [\mathrm{mH}]$

Figure 3-5 Equal power factor ellipse (negative power factor means inductive operation).

In polar form, (3-28) becomes,

$$I_s = \frac{L_m \cdot I_f \cdot (\cos\theta_I - \sin\theta_I \cdot \tan\varphi)}{\frac{L_d - L_q}{2} \cdot \sin 2\theta_I \cdot \tan\varphi_{PF} - L_d \cdot \cos^2\theta_I - L_q \cdot \sin^2\theta_I} \tag{3-29}$$

Figure 3-5 shows the power factor ellipse with PF = 0.8, 0.9 and 1.0 for both inductive and capacitive cases, and in cases of $L_d > L_q$, $L_d = L_q$ and $L_d < L_q$. For unity power factor, $\tan\varphi_{PF} = 0$, and then (3-29) becomes (3-24). It should be pointed out that at $\theta_I = 0$, (3-29) becomes

$$I_s = -\frac{L_m \cdot I_f}{L_d} \tag{3-30}$$

and this means all the equal power factor ellipse comes across the center of the voltage ellipse.

3.2 Operation Envelop in Torque-Speed Map

The discussion of operation area in torque-speed map assumes the motor to be lossless and in steady-state. Then the operation area of the EESM is limited by the stator voltage, stator current and field current

$$U_s = \sqrt{{U_d}^2 + {U_q}^2} \le U_{s\cdot max} \tag{3-31}$$

$$I_s = \sqrt{{I_d}^2 + {I_q}^2} \le I_{s\cdot max} \tag{3-32}$$

$$I_f \le I_{f\cdot max} \tag{3-33}$$

The torque-speed envelop is composed by the operation points with the highest torque at each speed. The torque-speed envelop can be divided into three sections as shown by the schematic in Figure 3-6, and the corresponding power-speed is presented in Figure 3-7.

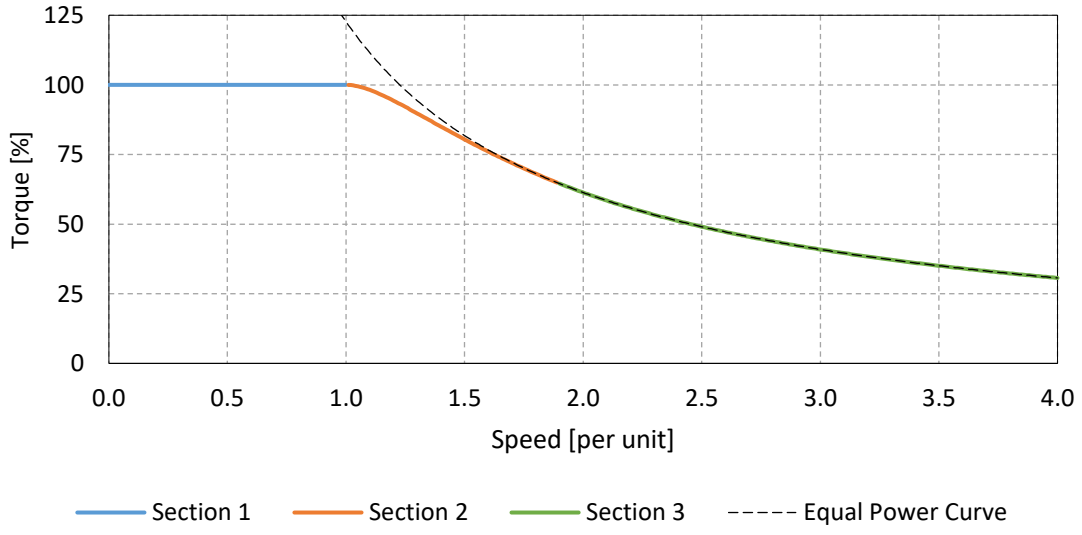

Figure 3-6 Schematic of torque-speed curve.

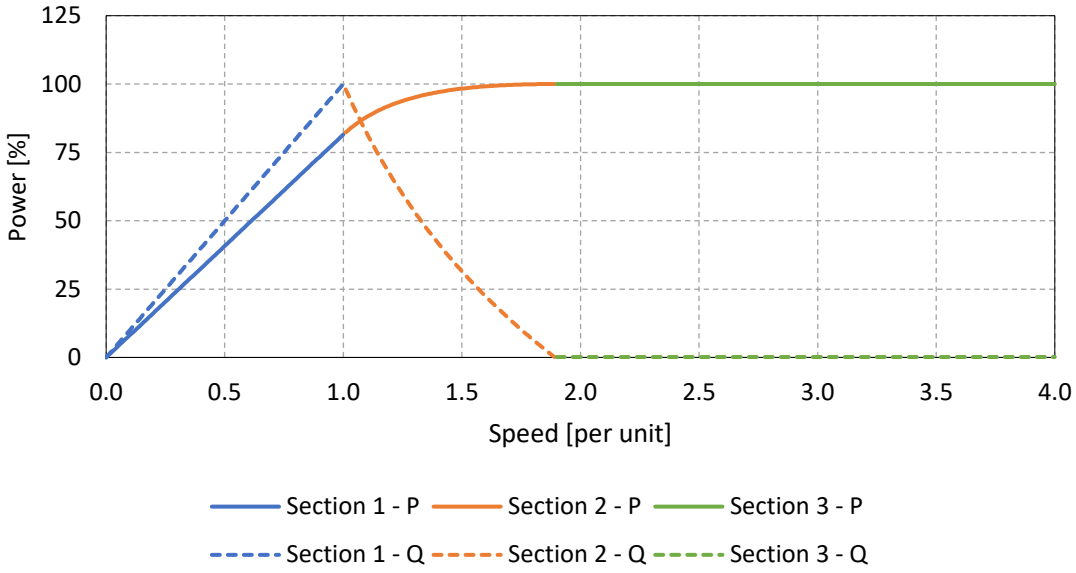

Figure 3-7 Schematic of power-speed curve.

3.2.1 Section 1: Low Speed Region (MTPA)

At low speed, the back-EMF is quite low and the constraint is the stator and field current limits

$$I_{\mathrm{s}} = I_{\mathrm{s\cdot max}} \qquad I_{\mathrm{f}} = I_{\mathrm{f\cdot max}} \tag{3-34}$$

The flux linkage created by the maximum field current is denoted as $\psi_{\mathrm{m\cdot max}}$, i.e.

$$\psi_{\mathrm{m\cdot max}} = L_{\mathrm{m}} \cdot I_{\mathrm{f\cdot max}} \tag{3-35}$$

In order to get the maximum torque out of a given current amplitude, a proper current angle needs to be found. The torque can therefore be expressed by $I_{\mathrm{s.max}}$ and θ_{I} in polar form as

$$T_{\mathrm{em}} = \frac{3p}{2} \cdot \left(\psi_{\mathrm{m\cdot max}} \cdot I_{\mathrm{s.max}} \cdot \sin\theta_{\mathrm{I}} + \frac{L_{\mathrm{d}} - L_{\mathrm{q}}}{2} \cdot {I_{\mathrm{s.max}}}^2 \cdot \sin 2\theta_{\mathrm{I}} \right) \tag{3-36}$$

And by setting

$$\frac{\mathrm{d}T_{\mathrm{em}}}{\mathrm{d}\theta_{\mathrm{I}}} = 0 \tag{3-37}$$

the solution can be obtained

$$\cos\theta_{\mathrm{I.MTPA}} = \frac{-\psi_{\mathrm{m\cdot max}} + \sqrt{{\psi_{\mathrm{m\cdot max}}}^2 + 8 \cdot \left(L_{\mathrm{d}} - L_{\mathrm{q}}\right)^2 \cdot {I_{\mathrm{s.max}}}^2}}{4 \cdot \left(L_{\mathrm{d}} - L_{\mathrm{q}}\right) \cdot I_{\mathrm{s.max}}} \tag{3-38}$$

This is the maximum torque that the EESM can achieve with a given $I_{\mathrm{f\cdot max}}$ and a given $I_{\mathrm{s\cdot max}}$. This solution is called the *Maximum Torque per Ampere* (MTPA) solution at maximum stator and field current. As speed increases, the stator voltage increases and the operation in Section

1 can be maintained until the stator voltage reaches the stator voltage limit. Hence the operation in Section 1 must satisfy

$$U_{\mathrm{s}} = \omega_{\mathrm{r}} \cdot \sqrt{(L_{\mathrm{d}} \cdot I_{\mathrm{d}} + \psi_{\mathrm{m\cdot max}})^2 + \left(L_{\mathrm{q}} \cdot I_{\mathrm{q}}\right)^2} \leq U_{\mathrm{s\cdot max}} \tag{3-39}$$

which gives the speed criterion

$$\omega_{\mathrm{r}} \leq \frac{U_{\mathrm{s\cdot max}}}{\sqrt{(L_{\mathrm{d}} \cdot I_{\mathrm{d}} + \psi_{\mathrm{m\cdot max}})^2 + \left(L_{\mathrm{q}} \cdot I_{\mathrm{q}}\right)^2}} = \omega_{\mathrm{r\cdot MTPA}} \tag{3-40}$$

In the d- and q-axis stator current plane, $\omega_{\mathrm{r\cdot MTPA}}$ is the speed when the stator voltage limit ellipse cuts the stator current limit circle at the MTPA operation point.

3.2.2 Section 2: Medium Speed Region

After ω_{r} reaches $\omega_{\mathrm{r\cdot MTPA}}$, the EESM cannot operate at MTPA any longer. The operation point has to move along the stator current limit circle in the anti-clockwise direction. In this case, (3-34) and (3-39) are still valid, and the operation point is located at the intersect of the current limit circle and the voltage limit ellipse. The intersection point can be solved as

$$\cos\theta_{\mathrm{I}} = \frac{-L_{\mathrm{d}}\psi_{\mathrm{m.max}} + \sqrt{(L_{\mathrm{d}}\psi_{\mathrm{m.max}})^2 - \left({L_{\mathrm{d}}}^2 - {L_{\mathrm{q}}}^2\right)\left[{\psi_{\mathrm{m.max}}}^2 + \left(L_{\mathrm{q}}I_{\mathrm{s}}\right)^2 - \left(\frac{U_{\mathrm{s.max}}}{\omega_{\mathrm{r}}}\right)^2\right]}}{\left({L_{\mathrm{d}}}^2 - {L_{\mathrm{q}}}^2\right)I_{\mathrm{s}}} \tag{3-41}$$

In case unity power factor ellipse intersects the current limit ellipse, Section 2 is valid until the operation point moves to the unity power factor (UPF) point which gives the current angle as

$$\cos\theta_{\mathrm{UPF}} = \frac{-\psi_{\mathrm{m\cdot max}} + \sqrt{{\psi_{\mathrm{m\cdot max}}}^2 - 4 \cdot \left(L_{\mathrm{d}} - L_{\mathrm{q}}\right) \cdot L_{\mathrm{q}} \cdot {I_{\mathrm{s\cdot max}}}^2}}{2 \cdot \left(L_{\mathrm{d}} - L_{\mathrm{q}}\right) \cdot I_{\mathrm{s\cdot max}}} \tag{3-42}$$

And this further gives the speed corresponding to the UPF point

$$\omega_{\mathrm{r\cdot UPF}} = \frac{U_{\mathrm{s\cdot max}}}{\sqrt{(L_{\mathrm{d}} \cdot I_{\mathrm{s\cdot max}} \cdot \cos\theta_{\mathrm{UPF}} + \psi_{\mathrm{m\cdot max}})^2 + \left(L_{\mathrm{q}} \cdot I_{\mathrm{s\cdot max}} \cdot \cos\theta_{\mathrm{UPF}}\right)^2}} \tag{3-43}$$

3.2.3 Section 3: High Speed Region (UPF)

In case the characteristic current is outside of the current limit circle, after the UPF is reached, in order to maintain the maximum torque, power factor should be kept as high as possible. This is done by shrinking the field current so that the current limit circle, the voltage limit ellipse and the unity power factor ellipse intersect at the same point. In other words, the excitation is decreased to avoid capacitive operation (over excitation). This means that

$$Q = L_{\mathrm{d}} \cdot {I_{\mathrm{d}}}^2 + L_{\mathrm{q}} \cdot {I_{\mathrm{q}}}^2 + L_{\mathrm{m}} \cdot I_{\mathrm{f}} \cdot I_{\mathrm{d}} = 0 \tag{3-44}$$

and

$$(L_{\mathrm{d}} \cdot I_{\mathrm{d}} + L_{\mathrm{m}} \cdot I_{\mathrm{f}})^2 + \left(L_{\mathrm{q}} \cdot I_{\mathrm{q}}\right)^2 = \left(\frac{U_{\mathrm{s}}}{\omega_{\mathrm{r}}}\right)^2 \tag{3-45}$$

hold at the same time. And this yields

$$\begin{aligned} & \left(L_{\mathrm{d}} \cdot I_{\mathrm{d}} - \frac{L_{\mathrm{d}} \cdot {I_{\mathrm{d}}}^2 + L_{\mathrm{q}} \cdot {I_{\mathrm{q}}}^2}{I_{\mathrm{d}}}\right)^2 + \left(L_{\mathrm{q}} \cdot I_{\mathrm{q}}\right)^2 = \left(\frac{U_{\mathrm{s}}}{\omega_{\mathrm{r}}}\right)^2 \\ \Rightarrow \quad & \left(\frac{I_{\mathrm{q}}}{I_{\mathrm{d}}}\right)^2 = \left(\frac{U_{\mathrm{s}}}{\omega_{\mathrm{r}} \cdot L_{\mathrm{q}} \cdot I_{\mathrm{s.max}}}\right)^2 \\ \Rightarrow \quad & \tan\theta_{\mathrm{I}} = \frac{I_{\mathrm{q}}}{I_{\mathrm{d}}} = -\frac{U_{\mathrm{s}}}{\omega_{\mathrm{r}} \cdot L_{\mathrm{q}} \cdot I_{\mathrm{s.max}}} \end{aligned} \tag{3-46}$$

The field current can be solved as

$$I_{\mathrm{f}} = -\frac{L_{\mathrm{d}} \cdot {I_{\mathrm{d}}}^2 + L_{\mathrm{q}} \cdot {I_{\mathrm{q}}}^2}{L_{\mathrm{m}} \cdot I_{\mathrm{d}}} \tag{3-47}$$

And gradually, the characteristic current is shifted towards the current limit circle to keep UPF. This means that the operation points along Section 3 are all at peak power, since current, voltage and power factor are all at maximum.

As a summary, Figure 3-8 shows the field current and dq-frame currents along the envelop corresponding to Figure 3-6. The field current decreases in Section 3 whereas the stator

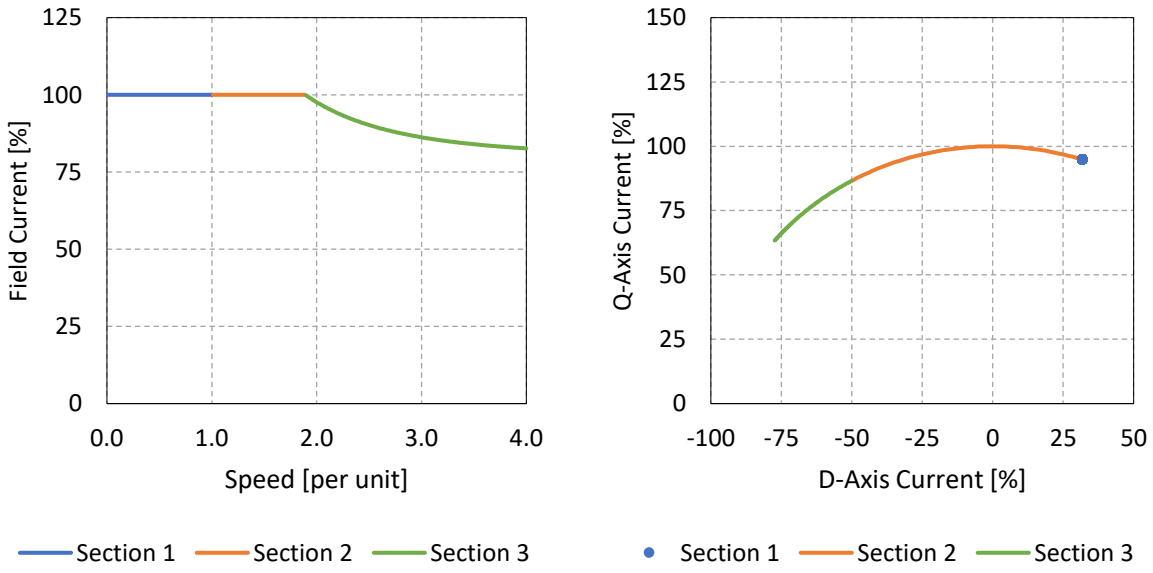

(a) Field current (b) D- and q-axis currents

Figure 3-8 D- and q-axis currents and field current.

current amplitude keeps the same in all three sections. The current vector stays at the MTPA point in Section 1, but moves anti-clockwise in Sections 2 and 3. It should be point out that, due to the voltage and current constraints, the combinations of d- and q-axis current components and the field current are unique along the envelop. However, inside the envelop, there are multiple solutions which lead to optimization study as will be discussed in the following sessions.

3.3 Optimization of Steady-State Operation

The steady-state optimization is to assign an optimized set of I_{d}, I_{q} and I_{f}, so that a preferred cost function is minimized within the constraints of stator current, field current, stator voltage and torque production. The constraints can be illustrated in Figure 3-9 and are listed as below

- Constraint 1: stator current

$$I_{\mathrm{d}}{}^2 + I_{\mathrm{q}}{}^2 = I_{\mathrm{s}}{}^2 \le I_{\mathrm{s.max}}{}^2 \tag{3-48}$$

- Constraint 2: field current

$$I_{\mathrm{f}} \le I_{\mathrm{f.max}} \tag{3-49}$$

- Constraint 3: stator voltage

$$\psi_{\mathrm{d}}{}^2 + \psi_{\mathrm{q}}{}^2 = \left(\frac{U_{\mathrm{s}}}{\omega_{\mathrm{r}}}\right)^2 \le \left(\frac{U_{\mathrm{s.max}}}{\omega_{\mathrm{r}}}\right)^2 \tag{3-50}$$

and with constant inductances

$$(L_{\mathrm{d}} \cdot I_{\mathrm{d}} + L_{\mathrm{m}} \cdot I_{\mathrm{f}})^2 + \left(L_{\mathrm{q}} \cdot I_{\mathrm{q}}\right)^2 = \left(\frac{U_{\mathrm{s}}}{\omega_{\mathrm{r}}}\right)^2 \le \left(\frac{U_{\mathrm{s.max}}}{\omega_{\mathrm{r}}}\right)^2 \tag{3-51}$$

- Constraint 4: electromagnetic torque

$$\psi_{\mathrm{d}} \cdot i_{\mathrm{q}} - \psi_{\mathrm{q}} \cdot i_{\mathrm{d}} = \frac{2}{3p} \cdot T_{\mathrm{em}} = \frac{2}{3p} \cdot T_{\mathrm{em.ref}} \tag{3-52}$$

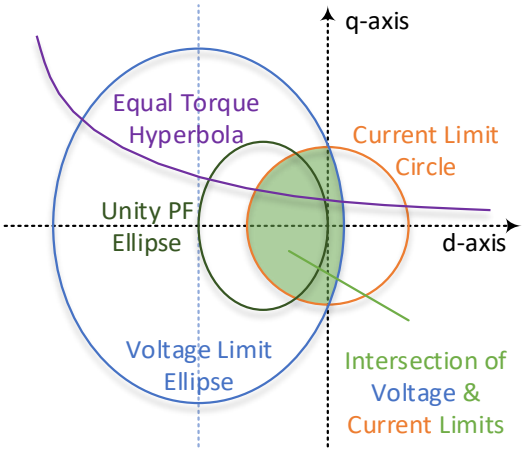

Figure 3-9 Optimization constraints.

and with constant inductances

$$\left[L_{\mathrm{m}} \cdot I_{\mathrm{f}} + \left(L_{\mathrm{d}} - L_{\mathrm{q}}\right) \cdot I_{\mathrm{d}}\right] \cdot I_{\mathrm{q}} = \frac{2}{3p} \cdot T_{\mathrm{em}} = \frac{2}{3p} \cdot T_{\mathrm{em.ref}} \tag{3-53}$$

Different optimization strategies are based on the definition of different cost functions. The optimized strategy can be verified by driving cycles. One of the widely applied driving cycles is the world-wide harmonized light duty test cycle (WLTC) as shown in Figure 3-10.

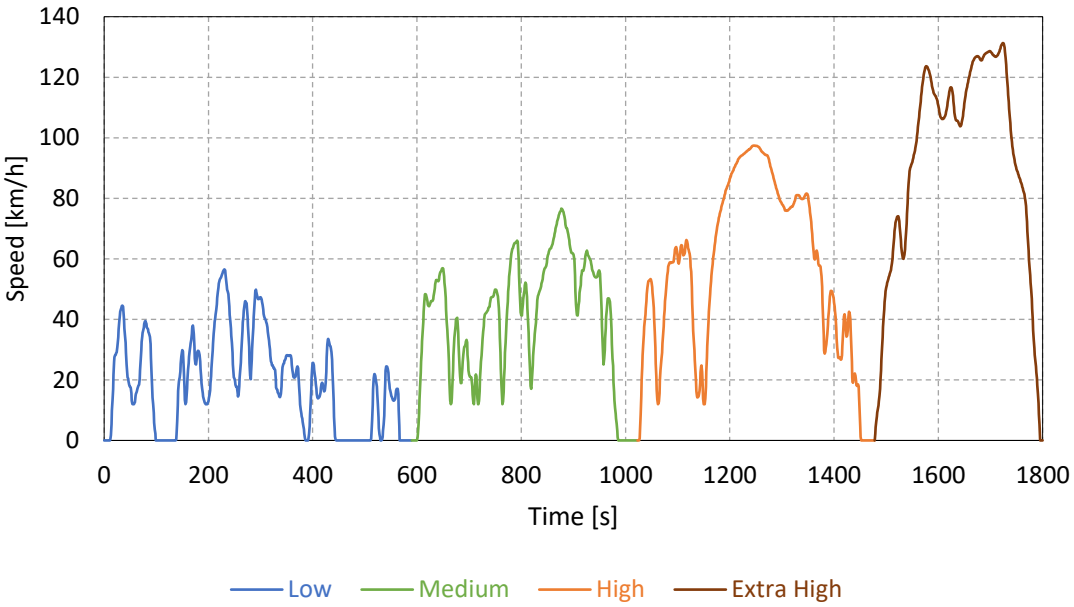

Figure 3-10 WLTC driving cycles.

3.3.1 Unity Power Factor (UPF) Algorithm

The *unity power factor* control is applied for the sake of fully utilizing the power capability of the inverter to deliver enough power to the EESM

$$\vec{S} = P + \mathrm{j}Q \quad \Rightarrow \quad S = \sqrt{P^2 + Q^2} \quad \xrightarrow{Q=0} \quad S = P \tag{3-54}$$

The application of the UPF control requires the EESM to self-compensate the reactive power consumed by the stator reactance. A negative d-axis current is injected in order to put the stator reactive power to zero viewing from outside the EESM

$$Q = \frac{3}{2} \cdot \left(U_{\mathrm{q}} \cdot I_{\mathrm{d}} - U_{\mathrm{d}} \cdot I_{\mathrm{q}}\right) = 0 \quad \Rightarrow \quad \frac{U_{\mathrm{q}}}{U_{\mathrm{d}}} = \frac{I_{\mathrm{q}}}{I_{\mathrm{d}}} = \tan\theta_{\mathrm{I}} \tag{3-55}$$

In EESM, the active power is

$$P = \frac{3}{2} \cdot \left(U_{\mathrm{d}} \cdot I_{\mathrm{d}} + U_{\mathrm{q}} \cdot I_{\mathrm{q}}\right) = \frac{3}{2} \cdot U_{\mathrm{d}} \cdot I_{\mathrm{d}} \cdot \left(1 + \tan^2\theta_{\mathrm{I}}\right) \tag{3-56}$$

In order to increase the power delivery P by a factor of k at a certain θ_{I}, then U_{d} and I_{d} shall increase by a factor of $\sqrt{k}$. In other words, under UPF control, the vector diagrams before and after a power increase form homothetic triangles as shown in Figure 3-11.

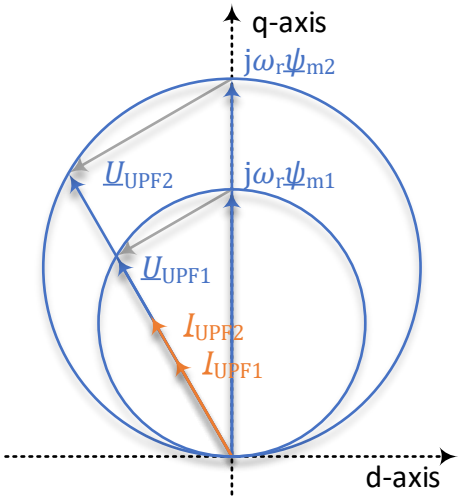

Figure 3-11 Vector diagram of active power increase in unity power factor control.

To obtain the solutions in unity power factor control, the operation point must fulfill three criterial: torque, voltage and zero reactive power. Figure 3-12 shows the vector diagram in unity power factor control. By setting reactive power to zero, the field current can be calculated, the same as (3-47), which yields

$$\tan\theta_{\mathrm{I}} = \frac{I_{\mathrm{q}}}{I_{\mathrm{d}}} = -\frac{U_{\mathrm{s}}}{\omega_{\mathrm{r}} \cdot L_{\mathrm{q}} \cdot I_{\mathrm{s}}} \tag{3-57}$$

The difference between (3-57) and (3-46) is that I_{s} is not necessarily at maximum here. It should be noticed that since the machine is analyzed in motor mode here, I_{d} is negative

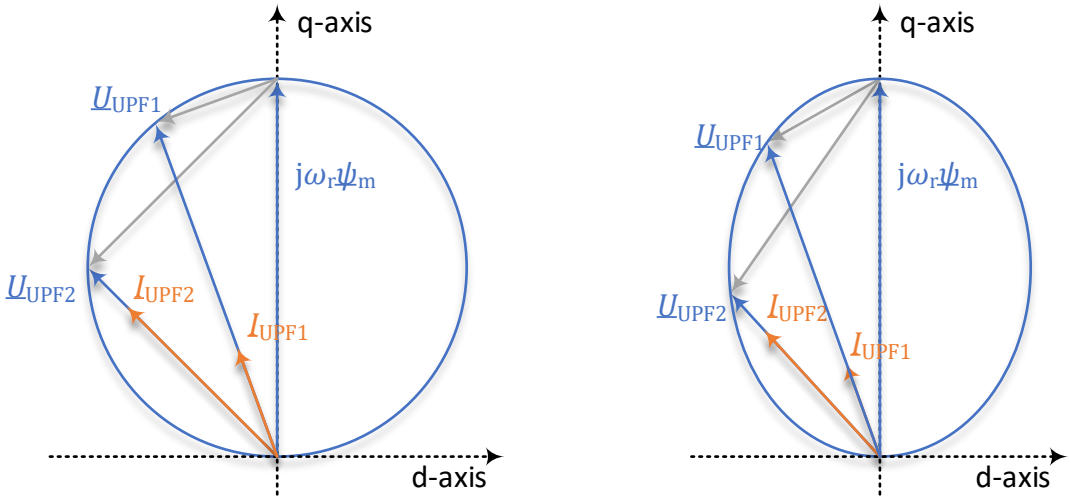

(a) $L_{\mathrm{d}} = L_{\mathrm{q}}$ $L_{\mathrm{d}} > L_{\mathrm{q}}$

Figure 3-12 Vector diagram in unity power factor control.

whereas I_q is positive, and therefore, only the negative $\tan\theta_\mathrm{I}$ solution is selected here. If the machine operates in generator mode, then the positive $\tan\theta_\mathrm{I}$ solution should be selected.

Now that the calculation of the current angle needs the current amplitude which can be obtained from the power balance, neglecting the stator copper losses,

$$T_\mathrm{em}\cdot\frac{\omega_\mathrm{r}}{p}=P=\frac{3}{2}\cdot U_\mathrm{s}\cdot I_\mathrm{s}\quad\Rightarrow\quad I_\mathrm{s}=\frac{2}{3}\cdot\frac{\omega_\mathrm{r}}{p}\cdot\frac{T_\mathrm{em}}{U_\mathrm{s}} \tag{3-58}$$

Thus $\tan\theta_\mathrm{I}$ can be solved by substituting (3-58) into (3-57)

$$\tan\theta_\mathrm{I}=-\frac{3}{2\cdot p}\cdot\frac{{U_\mathrm{s}}^2}{L_\mathrm{q}\cdot T_\mathrm{em}} \tag{3-59}$$

If the machine operates in generator mode, then either the T_em in (3-59) should be substituted as a negative value, or the negative sign in (3-59) should be discarded. Thereafter, I_d, I_q and I_f can be solved as

$$I_\mathrm{d}=I_\mathrm{s}\cdot\cos\theta_\mathrm{I} \tag{3-60}$$

$$I_\mathrm{d}=I_\mathrm{s}\cdot\sin\theta_\mathrm{I} \tag{3-61}$$

$$I_\mathrm{f}=-\frac{L_\mathrm{d}\cdot{I_\mathrm{d}}^2+L_\mathrm{q}\cdot{I_\mathrm{q}}^2}{L_\mathrm{m}\cdot I_\mathrm{d}} \tag{3-62}$$

Further, the relation between active power, stator voltage and EMF under UPF control can be analyzed as well. This discussion takes non-salient case only and the case of salient EESM should be similar. With a given U_s and E_m, the active power can be described as

$$P=\frac{U_\mathrm{s}\cdot E_\mathrm{m}}{X}\cdot\sin\delta \tag{3-63}$$

whereas along the Unity Power Factor Circle,

$$U_\mathrm{s}=E_\mathrm{m}\cdot\cos\delta \tag{3-64}$$

satisfies, and the active power at Unity Power Factor control can be derived as

$$P=\frac{{E_\mathrm{m}}^2}{X}\cdot\sin\delta\cdot\cos\delta=\frac{{E_\mathrm{m}}^2}{2\cdot X}\cdot\sin 2\delta \tag{3-65}$$

In conclusion, E_m decides the Unity Power Factor curve whereas U_s decides the general power curve. The intersection of the two curves is the possible operation point to achieve Unity Power Factor control as shown in Figure 3-13 (a). With a given U_s but an increasing E_m, the load angle δ increases as shown in Figure 3-13 (b) and vice versa in Figure 3-13 (c). The maximum active power under UPF control can be achieved with

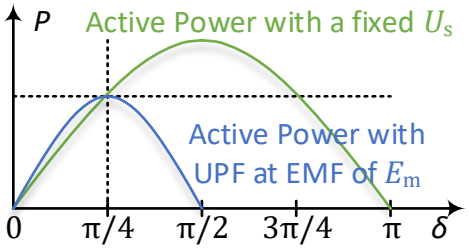

(a) Active power with U_s and unity power factor at E_m.

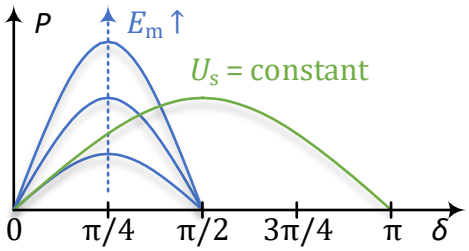

(b) Variations of field current.

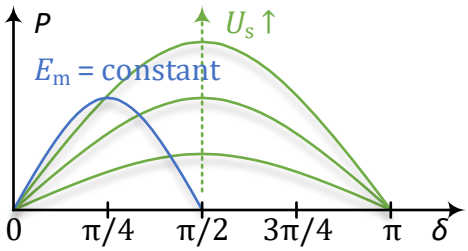

(c) Variations of stator voltage.

Figure 3-13 Active power output with unity power factor control.

$$\delta = 45° \tag{3-66}$$

And to achieve this, the applied stator voltage should follow

$$U_s = \frac{E_m}{\sqrt{2}} \tag{3-67}$$

3.3.2 Copper Loss Minimization Algorithm

3.3.2.1 Stator Copper Loss Minimization

The minimization of stator copper loss is actually the maximization of torque per ampere, known as *maximum torque per ampere (MTPA)* control in PMSM. According to (2-37), it is obvious that the maximum torque under a certain level of stator current can always be achieved by a maximum excitation current. Therefore, in the low speed region,

$$I_{f.MTPA} = I_{f.max} \tag{3-68}$$

The solution is almost the same as (3-38) except that the $I_{s.max}$ in (3-38) is I_s here since it is the I_s that needs to be minimized in this algorithm.

3.3.2.2 Rotor Copper Loss Minimization (Field Current Minimization)

A certain level of electromagnetic torque T_{em} can be achieved with a minimum rotor excitation I_f. The derivation is published in [38]. From the torque equation (2-38), the mutual flux linkage can be solved as

$$\psi_{\mathrm{m}} = \frac{2}{3p} \cdot \frac{T_{\mathrm{em}}}{I_{\mathrm{s}} \sin\theta_{\mathrm{I}}} + \left(L_{\mathrm{q}} - L_{\mathrm{d}}\right) \cdot I_{\mathrm{s}} \cdot \cos\theta_{\mathrm{I}} \tag{3-69}$$

When the torque T_{em} is decided, the flux linkage ψ_{m} is depended on the current amplitude I_{s} and the current angle θ_{I}. To find the minimum ψ_{m} under the same I_{s}, let

$$\frac{\partial \psi_{\mathrm{m}}}{\partial \theta_{\mathrm{I}}} = -\frac{2}{3p} \cdot \frac{T_{\mathrm{em}}}{I_{\mathrm{s}}} \frac{\cos\theta_{\mathrm{I}}}{\sin^2\theta_{\mathrm{I}}} + \left(L_{\mathrm{d}} - L_{\mathrm{q}}\right) \cdot I_{\mathrm{s}} \cdot \sin\theta_{\mathrm{I}} = 0 \tag{3-70}$$

which yields

$$\cos\theta_{\mathrm{I}} = \frac{3}{2} \cdot \frac{p}{T_{\mathrm{em}}} \cdot \left(L_{\mathrm{d}} - L_{\mathrm{q}}\right) \cdot {I_{\mathrm{s}}}^2 \cdot \sin^3\theta_{\mathrm{I}} \tag{3-71}$$

And this finally leads to

$$\cos\theta_{\mathrm{I}} = \sqrt{1 - \frac{1}{k^2}\left(\frac{1}{3}\right)^{\frac{1}{3}} c + \left(\frac{1}{9}\right)^{\frac{1}{3}} \frac{1}{c}} \tag{3-72}$$

where

$$k = \frac{3}{2} \cdot \frac{p}{T_{\mathrm{em}}} \cdot \left(L_{\mathrm{d}} - L_{\mathrm{q}}\right) \cdot {I_{\mathrm{s}}}^2 \tag{3-73}$$

$$c = \left(\frac{2}{-9k + \sqrt{3} \cdot \sqrt{4 + 27k^2}}\right)^{\frac{1}{3}} \tag{3-74}$$

3.3.2.3 Total Copper Loss Minimization

The derivation of total copper loss minimization is available in [26] and [38]

$$P_{\mathrm{Cu}} = P_{\mathrm{Cu \cdot s}} + P_{\mathrm{Cu \cdot r}} = \frac{3}{2} \cdot \left({I_{\mathrm{d}}}^2 + {I_{\mathrm{q}}}^2\right) \cdot R_{\mathrm{s}} + {I_{\mathrm{f}}}^2 \cdot R_{\mathrm{f}} \tag{3-75}$$

Apply Lagrange multiplier

$$\begin{aligned} \Lambda &= P_{\mathrm{Cu}} + \lambda(T_{\mathrm{em}} - T_{\mathrm{em.ref}}) \\ &= \frac{3}{2} \cdot \left({I_{\mathrm{d}}}^2 + {I_{\mathrm{q}}}^2\right) \cdot R_{\mathrm{s}} + {I_{\mathrm{f}}}^2 \cdot R_{\mathrm{f}} \\ &+ \lambda \cdot \left\{\frac{3p}{2} \cdot \left[L_{\mathrm{m}} \cdot I_{\mathrm{f}} + \left(L_{\mathrm{d}} - L_{\mathrm{q}}\right) \cdot I_{\mathrm{d}}\right] \cdot I_{\mathrm{q}} - T_{\mathrm{em.ref}}\right\} \end{aligned} \tag{3-76}$$

which gives

$$\frac{\partial \Lambda}{\partial I_{\mathrm{d}}} = 3 \cdot I_{\mathrm{d}} \cdot R_{\mathrm{s}} + \lambda \cdot \frac{3p}{2} \cdot \left(L_{\mathrm{d}} - L_{\mathrm{q}}\right) \cdot I_{\mathrm{q}} \tag{3-77}$$

$$\frac{\partial \Lambda}{\partial I_{\mathrm{q}}} = 3 \cdot I_{\mathrm{q}} \cdot R_{\mathrm{s}} + \lambda \cdot \frac{3p}{2} \cdot \left[L_{\mathrm{m}} \cdot I_{\mathrm{f}} + \left(L_{\mathrm{d}} - L_{\mathrm{q}} \right) \cdot I_{\mathrm{d}} \right] \tag{3-78}$$

$$\frac{\partial \Lambda}{\partial I_{\mathrm{f}}} = 2 \cdot I_{\mathrm{f}} \cdot R_{\mathrm{f}} + \lambda \cdot \frac{3p}{2} \cdot L_{\mathrm{m}} \cdot I_{\mathrm{q}} \tag{3-79}$$

To get the solutions, set

$$\frac{\partial \Lambda}{\partial I_{\mathrm{d}}} = \frac{\partial \Lambda}{\partial I_{\mathrm{q}}} = \frac{\partial \Lambda}{\partial I_{\mathrm{f}}} = 0 \tag{3-80}$$

then

$$\lambda = -\frac{3 I_{\mathrm{d}} R_{\mathrm{s}}}{\frac{3p}{2} \left(L_{\mathrm{d}} - L_{\mathrm{q}} \right) I_{\mathrm{q}}} = -\frac{3 I_{\mathrm{q}} R_{\mathrm{s}}}{\frac{3p}{2} \left[L_{\mathrm{m}} I_{\mathrm{f}} + \left(L_{\mathrm{d}} - L_{\mathrm{q}} \right) I_{\mathrm{d}} \right]} = -\frac{2 I_{\mathrm{f}} R_{\mathrm{f}}}{\frac{3p}{2} L_{\mathrm{m}} I_{\mathrm{q}}} \tag{3-81}$$

And this gives the solution as

$$I_{\mathrm{d.opt}} = c_{\mathrm{d}} \cdot I_{\mathrm{f.opt}} \tag{3-82}$$

$$I_{\mathrm{q.opt}} = c_{\mathrm{q}} \cdot I_{\mathrm{f.opt}} \tag{3-83}$$

$$I_{\mathrm{f.opt}} = \frac{I_{\mathrm{s}}}{\sqrt{{c_{\mathrm{d}}}^2 + {c_{\mathrm{q}}}^2}} \tag{3-84}$$

where c_{d} and c_{q} are the two coefficients assisting the calculation

$$c_{\mathrm{d}} = \frac{2}{3} \cdot \frac{R_{\mathrm{f}}}{R_{\mathrm{s}}} \cdot \frac{L_{\mathrm{d}} - L_{\mathrm{q}}}{L_{\mathrm{m}}} \tag{3-85}$$

$$c_{\mathrm{q}} = \sqrt{{c_{\mathrm{d}}}^2 + \frac{2}{3} \cdot \frac{R_{\mathrm{f}}}{R_{\mathrm{s}}}} \tag{3-86}$$

As can be noticed, under copper loss minimization, $I_{\mathrm{f.opt}}$, $I_{\mathrm{d.opt}}$ and $I_{\mathrm{q.opt}}$ are decided by $T_{\mathrm{em.ref}}$ along with the EESM parameters

$$I_{\mathrm{d.opt}} \propto I_{\mathrm{q.opt}} \propto I_{\mathrm{f.opt}} \propto \sqrt{T_{\mathrm{em.ref}}} \tag{3-87}$$

while the current angle in this case is

$$\theta_{\mathrm{I}} = \cos^{-1} \frac{-L_{\mathrm{m}} \cdot I_{\mathrm{f.opt}} + \sqrt{\left(L_{\mathrm{m}} \cdot I_{\mathrm{f.opt}} \right)^2 + 8 \cdot \left(L_{\mathrm{d}} - L_{\mathrm{q}} \right)^2 \cdot {I_{\mathrm{s.opt}}}^2}}{4 \cdot \left(L_{\mathrm{d}} - L_{\mathrm{q}} \right) \cdot I_{\mathrm{s.opt}}} = constant \tag{3-88}$$

And this indicates that copper losses are proportional to the torque

$$P_{\mathrm{Cu}} \propto P_{\mathrm{Cu\cdot s}} \propto P_{\mathrm{Cu\cdot r}} \propto T_{\mathrm{em.ref}} \tag{3-89}$$

Since the currents are proportional to each other, the voltages are proportional to each other as well

$$U_{\mathrm{d.opt}} \propto U_{\mathrm{q.opt}} \propto U_{\mathrm{f.opt}} \propto I_{\mathrm{d.opt}} \propto I_{\mathrm{q.opt}} \propto I_{\mathrm{f.opt}} \tag{3-90}$$

Therefore, under *copper loss minimization* control, the power factor becomes a constant

$$\begin{aligned} \cos\varphi &= \frac{P}{S} = \frac{P}{\sqrt{P^2+Q^2}} = \frac{1}{\sqrt{1+\left(\frac{Q}{P}\right)^2}} \\ &= \frac{1}{\sqrt{1+\left(\frac{U_{\mathrm{q.opt}}\cdot I_{\mathrm{d.opt}} - U_{\mathrm{d.opt}}\cdot I_{\mathrm{q.opt}}}{U_{\mathrm{d.opt}}\cdot I_{\mathrm{d.opt}} + U_{\mathrm{q.opt}}\cdot I_{\mathrm{q.opt}}}\right)^2}} = constant \end{aligned} \tag{3-91}$$

The comparison between MTPA and total copper loss minimization is done in Figure 3-14. It should be noticed that the MTPA algorithm, where only the stator copper loss is taken into consideration, is a special case of the total copper loss minimization algorithm. The set of I_{f}, I_{d} and I_{q} obtained from total copper loss minimization all at once, is the same as, to obtain I_{f} from total copper loss minimization and then to obtain I_{d} and I_{q} from MTPA with such I_{f}. In the 3D dqf-frame, the MTPA algorithm forms a surface whereas the total copper loss minimization forms a line.

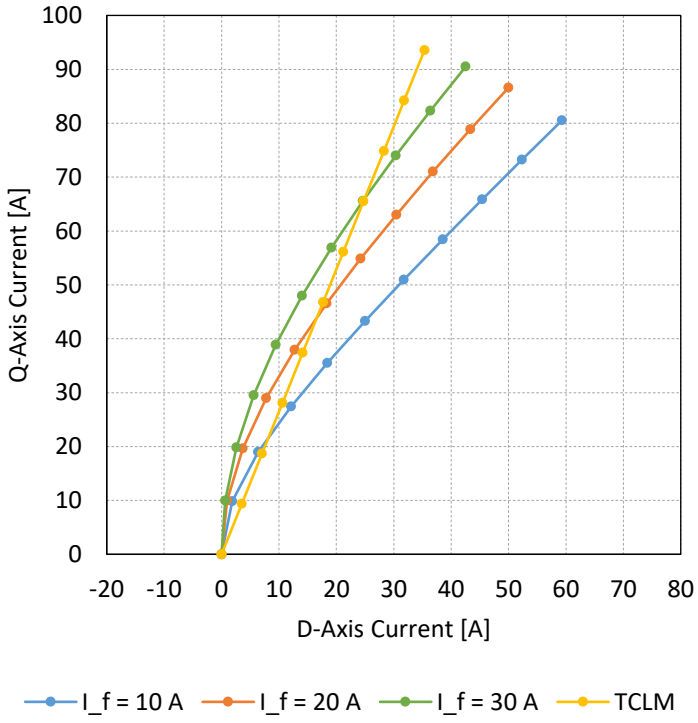

Figure 3-14 Copper loss minimization in dqf-frame ($L_{\mathrm{m}} = 10\ [\mathrm{mH}]$, $L_{\mathrm{d}} = 15\ [\mathrm{mH}]$, $L_{\mathrm{q}} = 10\ [\mathrm{mH}]$).

3.3.3 Optimization with Saturation

The analytical derivations presented previously are based on the assumption of constant inductances. However, practically at higher currents a real machine can saturate. This means that the inductance value decreases with an increase of current. In this case, a numerical method needs to be established so that the effects of saturations are taken into consideration in the optimization process.

Figure 3-15 shows the iteration algorithm for copper loss minimization with the flux linkage maps from the FEM analysis. The algorithm starts with a set of initial values, and then a parameter sweep is applied to I_s, θ_I and I_f around the initial values so that a 3D matrix of I_s, θ_I and I_f is generated. The sweep is performed with a range of k. As an example, k can be from 50% to 150%. Thereafter, the d- and q-axis flux linkages corresponding to each combination of I_s, θ_I and I_f are interpolated by looking up the flux linkage maps obtained from FEM. After that, the corresponding torques and voltages are calculated, and the 3D matrix is filtered so that the remaining combinations of I_s, θ_I and I_f fulfill all the criteria of current, voltage and torque limits. In the end, a cost function is applied. The cost function in the figure is the copper loss as an example, but it can also be the total loss or the field current,

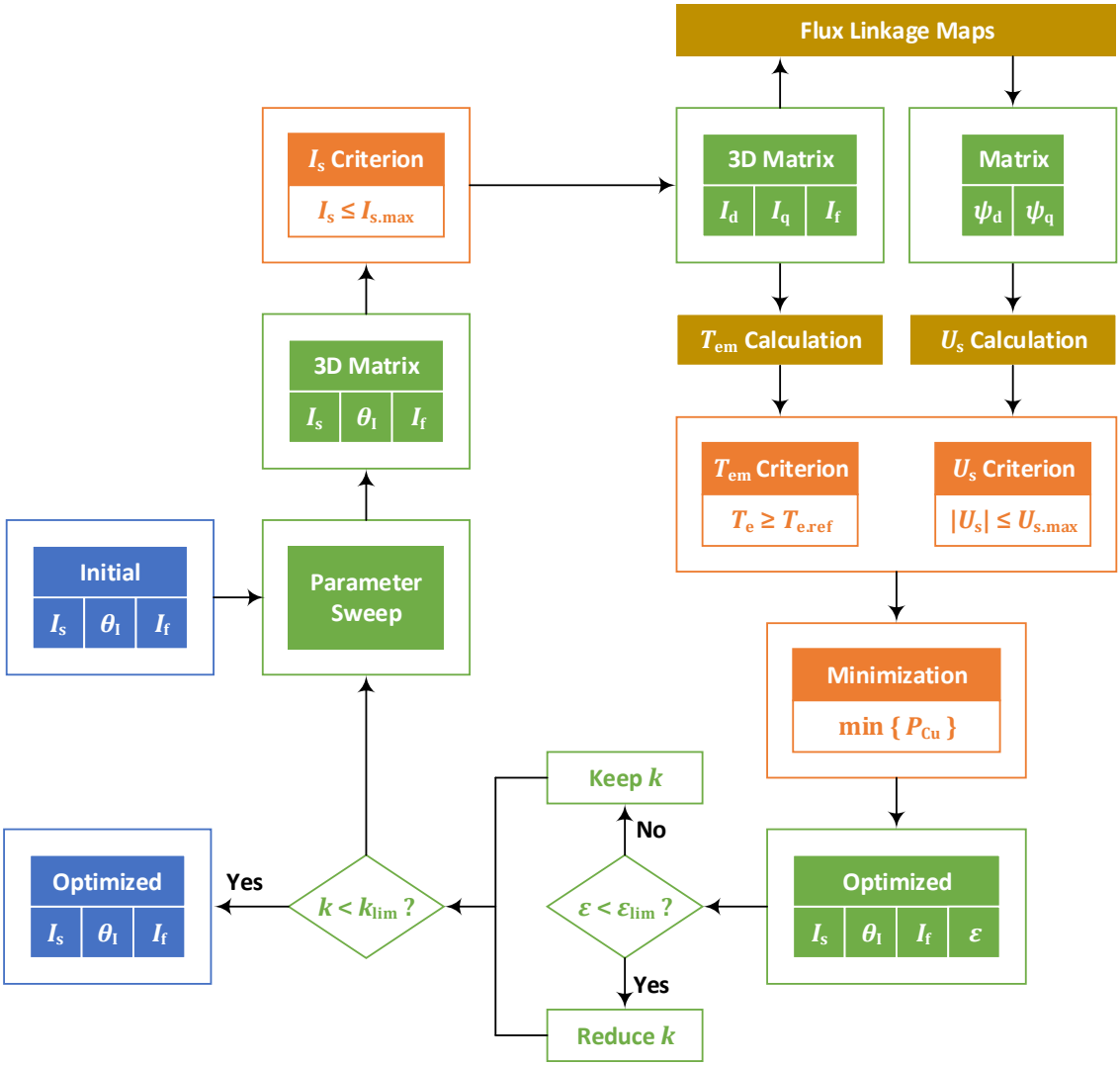

Figure 3-15 Iteration algorithm.

and so forth. Then the combination of I_{s}, θ_{I} and I_{f} with a minimum cost is the solution obtained in this iteration. At the same time, an error ε is calculated by comparing the I_{s}, θ_{I} and I_{f} obtained from this iteration and the ones from the previous iteration. In case ε is small enough, then the parameter sweep in the next iteration will be carried out in a smaller range so that the resolution can be improved. Then a new iteration starts with the I_{s}, θ_{I} and I_{f} obtained in the previous iteration. The iteration loop will continue until the searching range k becomes small enough, i.e. when the improvement of resolution by starting a new iteration is negligible. At this point, the results from the last iteration is considered as the optimal solution.

Chapter 4

Design of Machine and Excitation System

The specifications for electric machines vary from type to type. Firstly, the specifications in each application are introduced individually. Then a general procedure to do the design is introduced, followed by the parameter tuning strategy for each application accordingly.

4.1 Design Specifications

4.1.1 Specifications for Mild Hybrid Vehicles

In mild hybrid vehicles, the machine is mainly used for start-up and energy recovery. The focus therefore is the torque production capability at low speed. A set of specifications of a mild-hybrid vehicle is shown in Table 4-1 and the torque speed curves are shown in Figure 4-1 [36] [59] [37] [38]. A dc-link voltage of 48 V is the common voltage level in mild hybrid vehicles. A peak torque of 40 N·m for starting up the vehicle is required for 1 s. A power of 10 kW is needed for 30 s to accelerate the car at high speed and to recovery energy during braking. A power of 5 kW is the continuous level, and it is needed for moving the car at low speed, e.g. parking.

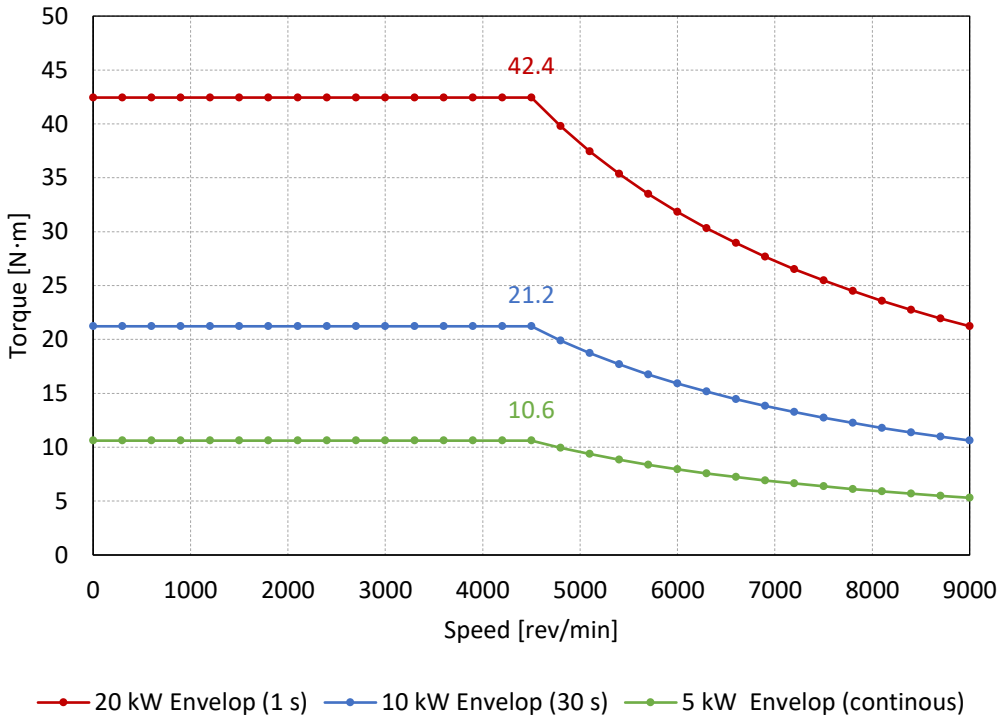

Figure 4-1 Torque-Speed curve of 48 V 10 kW (30 s power) EESM design specifications.

Table 4-1. Design specifications in a mild-hybrid vehicle application.

Parameter	Symbol	Value	Unit
DC-Link Voltage	U_{dc}	48	V
30 s Peak Power	P_{peak}	10	kW
Continuous Power	P_{cont}	5	kW
Maximum Speed	$n_{\mathrm{r.max}}$	9000	rev/min
Base Speed	$n_{\mathrm{r.base}}$	4500	rev/min
Maximum Torque (for 1 s)	T_{peak}	40	N·m
Maximum Phase Current Amplitude	I_{max}	707	A

4.1.2 Specifications for Electric Passenger Cars

In electric passenger cars, the motor is used more frequently. The set of specifications considered in this study is shown in Table 4-2 while the torque speed curves are shown in Figure 4-2. The operation for 30 s is around 70 kW while 35 kW is needed continuously. The specifications considered in this study are similar to the summaries from [64], e.g. Volkswagen e-up! (60 kW peak power, 210 N·m peak torque), supermini electric car Renault Zoe (65 kW peak power, 220 N·m peak torque), a medium sedan Renault Fluence (70 kW peak power, 226 N·m peak torque) and so forth. The dc-link voltage level is higher in this case, usually between 300 V and 400 V [64]. In this study, 360 V is considered as the nominal.

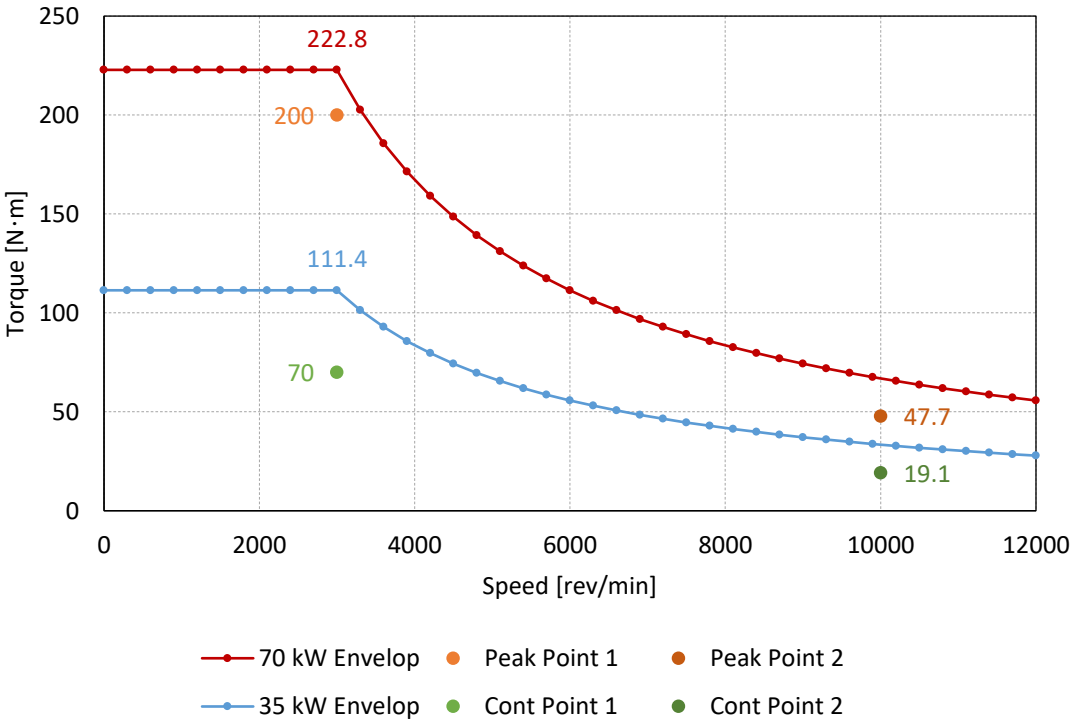

Figure 4-2 Torque-Speed curve of 360 V 70 kW EESM design specifications.

Hairpin windings are becoming a trend of traction motors, e.g. Prius 2017, Chevrolet Volt (Gen 2) [65]. In this study, a 70 kW EESM is developed by replacing the rotor of a 60 kW hairpin PMSM. The hairpin PMSM is developed for electric passenger cars with the outer diameter of

Table 4-2. Design specifications of EESM in electric passenger cars.

Parameter	Symbol	Value	Unit
DC-Link Voltage	U_{dc}	360	V
Peak Power	P_{peak}	70	kW
Continuous Power	P_{cont}	35	kW
Maximum Speed	$n_{\mathrm{r.max}}$	12000	rev/min
Base Speed	$n_{\mathrm{r.base}}$	3000	rev/min
Maximum Phase Current Amplitude	I_{max}	350	A

235 mm including cooling jacket and the length of 240 mm including front and rear end cap. The power density is 6 kW / L and torque density is 20 N·m / L. In Figure 4-2, the peak points and continuous points at low and high speed are marked for comparison with a hairpin PMSM.

4.1.3 Specifications for Heavy-Duty Vehicles

The application of traction motors in heavy-duty vehicles is quite special. The truck does not need to accelerate and deaccelerate frequently as the cars. Instead, it needs to run continuously at some specific operation points. The weight of the truck considered in this study is around 44 tons and the totally power needed is around 400 kW. In this case, usually two motors are needed to drive the truck, which means each motor needs to deliver 200 kW. The specifications used in this study are based on the references from Volvo FE Electric (185 kW peak power, 850 N·m peak torque), Volvo FL Electric (185 kW peak power, 425 N·m peak torque) [66] and Mercedes eActros (126 kW peak power, 485 N·m peak torque) [67].

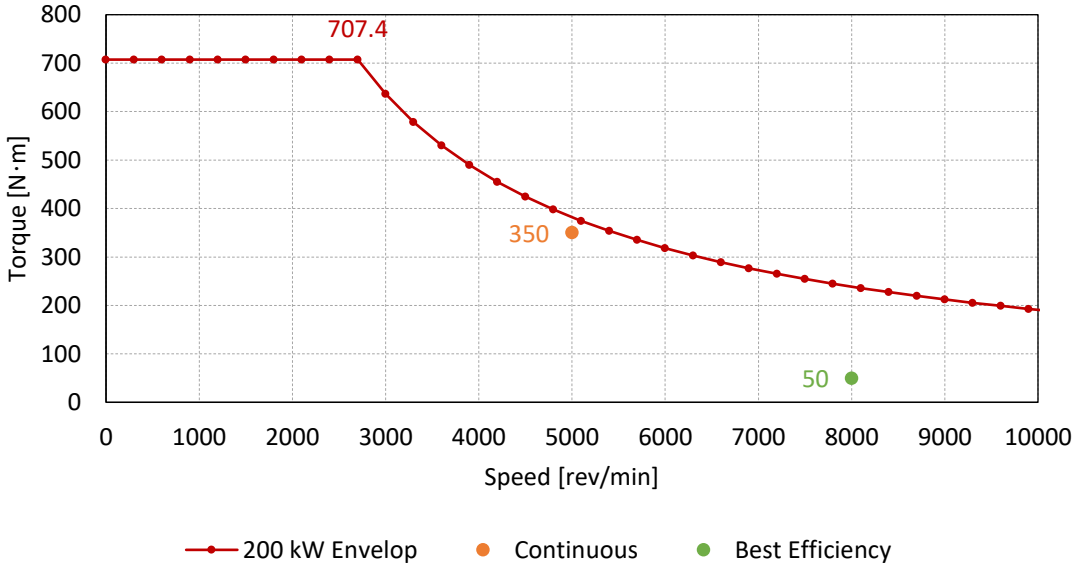

Figure 4-3 Torque-Speed curve of 1200 V 200 kW EESM design specifications.

A set of typical specifications in this case is shown in Table 4-3 and the correspondingly torque-speed curve is shown in Figure 4-3. The dc-link voltage is assumed to be 1200 V, and the number of turns can be adjusted with a different dc-link voltage. The most challenging case to start up the truck is on a slope of 12%, where 700 N·m is required from each motor.

Table 4-3. Design specifications of EESM in heavy-duty applications.

Parameter		Symbol	Value	Unit
DC-Link Voltage		U_{dc}	1200	V
Peak Power		P_{peak}	200	kW
Maximum Speed		n_{max}	10000	rev/min
Start-Up Operation	Torque	T_{peak}	700	N·m
Continuous Operation	Speed	n_{cont}	5000	rev/min
	Torque	T_{cont}	350	N·m
Best Efficiency Operation	Speed	$n_{\mathrm{best.eff}}$	8000	rev/min
	Torque	$T_{\mathrm{best.eff}}$	50	N·m
Maximum Phase Current Amplitude		I_{max}	215	A

The truck should also be able to rise a slope with 6% continuously at 50 km/h, and this is defined as continuous operation point. As for the operation that counts for most of time, the truck needs to run at 80 km/h on flat road. This is defined as the best efficiency point.

4.2 Machine Design

4.2.1 General Steps

Figure 4-4 shows the flow chart of the machine design. Firstly, the no-load operation at base speed is calculated. In this case, the stator current is set to zero, but the field current varies from zero to maximum. The maximum field current is decided by the maximum current density allowed in peak operation as discussed in Figure 2-11. The peak current density in field winding is selected around 10 A/mm^2 in [16]. However, the current density can be higher when the peak torque duration is defined shorter. The flux density distribution along the flux path is checked. Fast Fourier Transformations (FFT) are applied to back-EMF waveforms to obtain the fundamental component as well as the 6n±1 components of the line EMF waveforms. Number of turns are adjusted to meet the maximum voltage output capability of the inverter. Technics to reduce the harmonics can be applied so that torque ripple can be reduced. The explanations for how the torque ripple attributes to harmonics in voltage and current are concluded in Appendix D.

Secondly, the MTPA point at the base speed is calculated by fixing the stator and field currents at the maximum and sweeping the stator current angle. The maximum of stator current amplitude is decided by the inverter current capability. The temperature of the stator winding is checked in thermal simulations of the machine with the thermal models described in Section 2.2. The maximum torque achieved is then the peak torque of the machine. The terminal voltage is also checked in this case by (2-30) to guarantee that it is within the voltage output capability of the inverter. In case the specifications of the base point are not satisfied, then a tuning process can be performed which is described in Section 4.2.2.

Then the operation maps are of interest. In order to obtain the maps, the flux linkage maps are needed as the input of iteration algorithms. Hence in Step 3, a sweep of i_{d}, i_{q} and i_{f} is

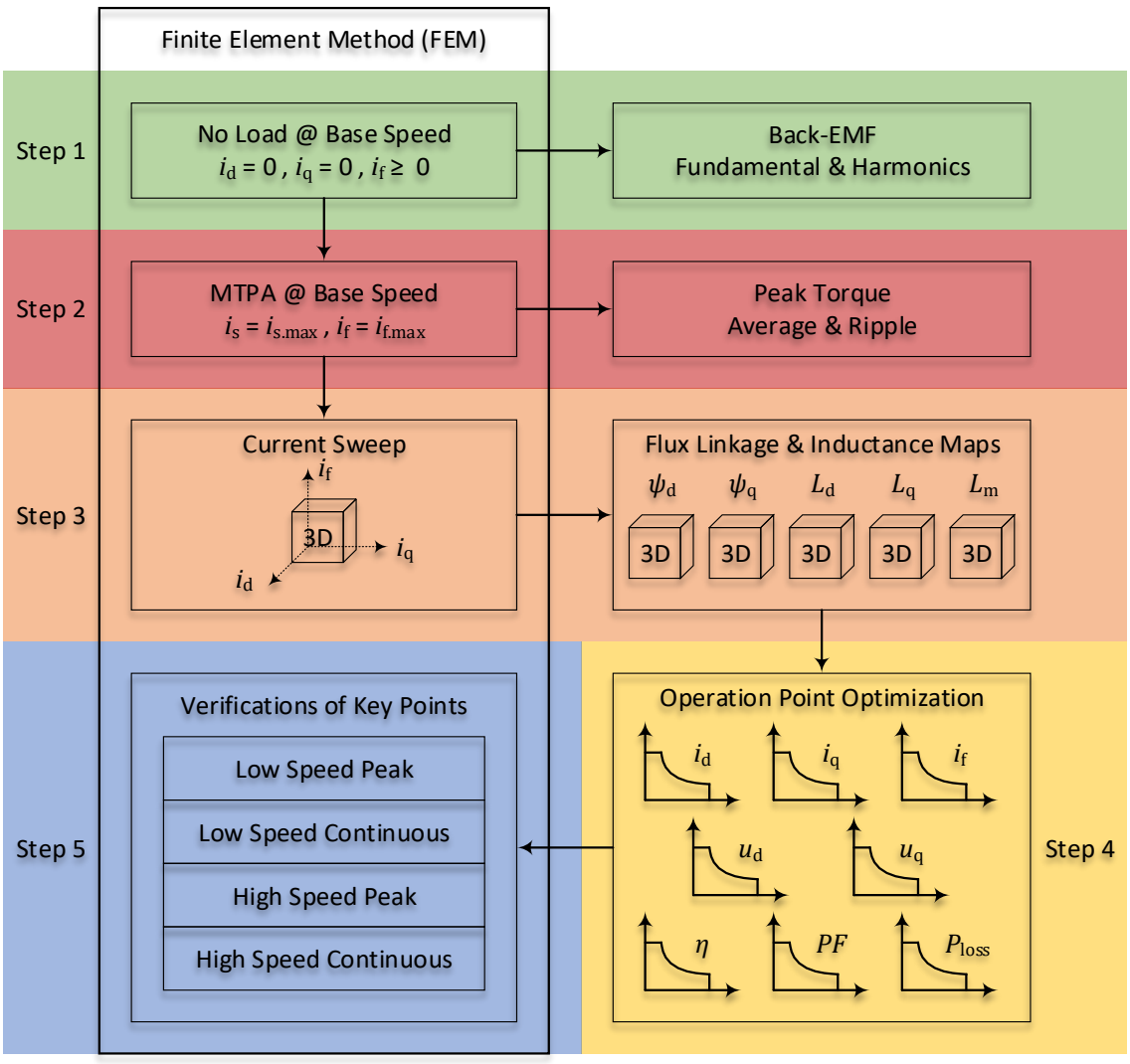

Figure 4-4 Flow chart of machine design steps.

applied, and the flux linkages in three-phase are recorded. Thereafter, abc-dq transformation is applied and the 3D flux linkage maps with respect i_d, i_q and i_f are obtained. Furthermore, the inductance maps can be obtained by (2-56) and (2-57).

Step 4 conducts the optimization mentioned in Figure 3-15 where the combination of d-axis, q-axis and field currents at each point of the torque-speed frame is obtained. And based on the combination of i_d, i_q and i_f, u_d, u_q and u_f as well as other properties, e.g. losses, efficiency and power factor, can be calculated.

The last step is to verify the key points defined by the design specifications. The verification needs to be done in both current source simulations and voltage source simulations. In each current source simulation, the i_d, i_q and i_f from iterations are the inputs of the FEM simulation and the u_d, u_q, T_{em} and P_{Fe} are the outputs to be compared with the iteration results. The current source simulation is to directly verify Step 3 and 4. In case a large error occurs in the between, then most probably, either the current sweep is to coarse or the iteration algorithm is configured improperly. Then, the voltage source simulation is to verify whether the methodology of using flux linkage maps to do iterations is suitable in this case or

not. Voltage source simulations take more time to get into steady state, but they are closer to the reality than current source simulations. Here, the key points are calculated in FEM directly. If the results at the key points between iterations and FEM simulations are similar, then the operation maps can be regarded convincing.

4.2.2 Tuning Strategies

The general tuning strategies in this study are concluded in Figure 4-5. Firstly an initial trial is made and then the back-EMF, flux distribution at no-load as well as the torque at the base point are checked. Adjustments are firstly made to change the geometry of the stator teeth, stator yoke, rotor pole and rotor shoe. The check and adjustments form an inner loop of tuning. In case the stator is generally more saturated than the rotor, then the slit ratio, which is the ratio between the rotor diameter and the stator diameter, needs to be tuned down and vise versa. This forms the outer loop of tuning.

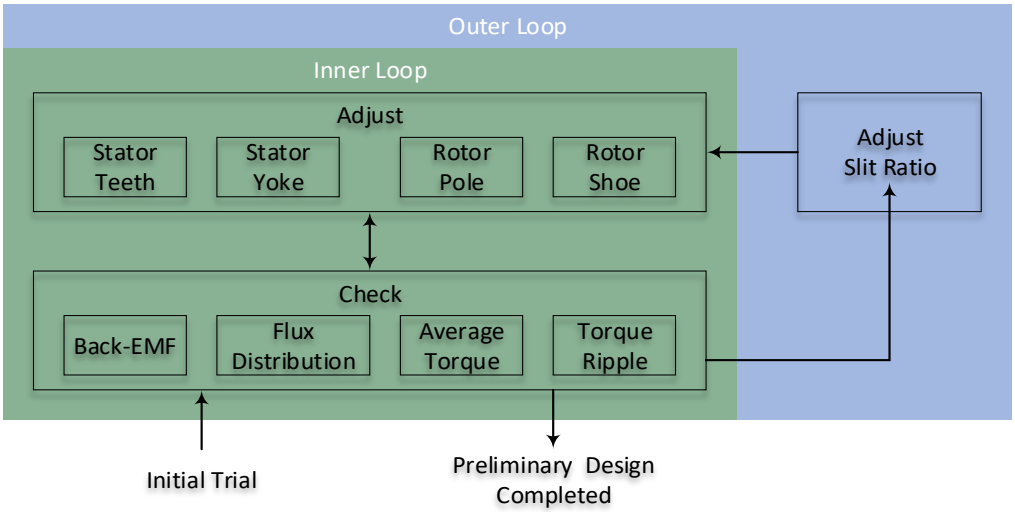

Figure 4-5 Flow chart of tuning strategies.

Specifically for different applications, in mild hybrid vehicles, since the peak torque is only needed for a very short time, a higher current density is allowed at peak torque than in other applications, e.g. 25 - 30 A/mm^2. Therefore, the main limitation is the saturation of the iron core. Hence the strategy is to apply a wide flux path, in both rotor pole and stator yoke and teeth, so that the iron core is not saturated at maximum current.

In electric passenger cars, a balanced design of electric machine needs to be achieved, and this requires a good balance between the cross-section of the copper area and the cross-section of the flux path in the iron core. Since the stator has been fixed, the remaining task is to tune the rotor geometry. A round shape design of the slot is selected in this case, which eases mechanical stresses and mechanical deformation. In addition, closed-slot and open-slot designs are compared and assistance of ferrite magnets is studied, to see if any benefit can be gained.

In heavy duty applications, the strategy is to guarantee the peak power operation point and to make the efficiency at the best-efficiency point as high as possible. In order to guarantee enough torque at the peak power operation point, unity power factor is supposed to be

satisfied so that all the stator current can be used to generate torque instead of helping excitation. This requires an sufficient amount of field current and thus an adequate amount of copper area in field winding. Apart from that, in order to guarantee a good efficiency at the best-efficiency point, total copper loss has to be minimized. This requires a minimization of the sum of stator and rotor copper losses.

4.2.3 Stator Winding

The stator winding arrangement includes the number of phases m, number of pole pairs p, number of slots per pole per phase q. The total number of slots Q therefore becomes

$$Q = 2 \cdot m \cdot p \cdot q \tag{4-1}$$

Following the tradition, the number of phases is set to be 3

$$m = 3 \tag{4-2}$$

As for the selection of p, a higher value will shorten the length of end-winding which can reduce copper losses. However, since the electrical speed ω_r is p times of the mechanical speed Ω_r

$$\omega_\mathrm{r} = p \cdot \Omega_\mathrm{r} = p \cdot \frac{\pi}{30} \cdot n_\mathrm{r} \tag{4-3}$$

where n_r is the speed in revolution per minute, a higher p requires a higher electrical speed ω_r, and consequently

- A higher iron-core loss, due to the fact that the eddy current iron-core loss is proportional to the square of ω_r and the hysteresis iron-core loss is proportional to ω_r.
- A higher fundamental frequency f_1 from the inverter

$$f_1 = \frac{\omega_\mathrm{r}}{2 \cdot \pi} = \frac{p \cdot n_\mathrm{r}}{60} \tag{4-4}$$

And frequency modulation index m_f becomes lower at high speed of the machine

$$m_\mathrm{f} = \frac{f_\mathrm{sw}}{f_1} \tag{4-5}$$

According to [68], m_f can minimally be 21 in case of asynchronous modulation. Then it becomes possible to calculate the maximum number of pole pairs allowed in consideration of switching

$$p_\mathrm{max} = \frac{2 \cdot \pi \cdot f_\mathrm{sw}}{m_\mathrm{f.min} \cdot \Omega_\mathrm{r.max}} = \frac{60 \cdot f_\mathrm{sw}}{m_\mathrm{f.min} \cdot n_\mathrm{r.max}} \tag{4-6}$$

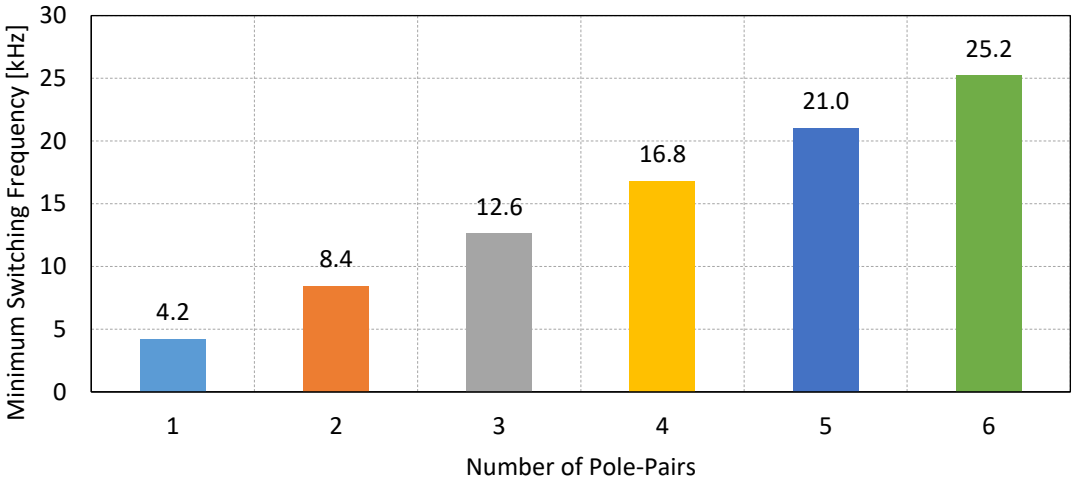

Figure 4-6 Minimum switching frequency with respect to number of pole-pairs @ 12000 rpm according to [68].

A comparison can be illustrated in Figure 4-6. In addition, the cutting-edge of the laminations affects the magnetic conductivity and increase the iron-core losses [45]. And an increase of p will increase Q, which makes this effect more significant.

To sum up, a higher number of pole pairs gives shorter end-winding which means lower copper loss, but it increases the fundamental frequency which increases the iron-core loss and the switching frequency for the power electronic converter. In traction motor applications, the p is usually selected as 4 or 5.

As for distributed windings, 8-Pole 48-Slot (8P48S) and 10-Pole 45-Slot (10P45S) are commonly used, especially the 8-Pole 48-Slot arrangement, e.g. Toyota Prius 2004 and 2010, Camry 2007, Honda Accord 2014, Lexus LS 600h 2008, as well as the BEV Nissan Leaf 2011 [64]. The 8-Pole 48-Slot (8P48S) is with

$$q = \frac{Q}{2mp} = \frac{48}{2 \times 3 \times 4} = 2 \tag{4-7}$$

and usually a shot pitch of one slot. The winding arrangement is illustrated in Figure 4-7 (a). The 10-Pole 45-Slot (10P45S) is with

$$q = \frac{Q}{2mp} = \frac{45}{2 \times 3 \times 5} = 1.5 \tag{4-8}$$

and winding arrangement is illustrated in Figure 4-7 (b). The winding factors at each harmonic order are be calculated and shown in Figure 4-7 (c). The formulas are described in Appendix C. As can be noticed, in both cases, the 5th and 7th harmonic components are damped. As for higher harmonic order, 8-Pole 48-Slot damps the 17th and 19th while 10-Pole 45-Slot damps the 11th and 13th.

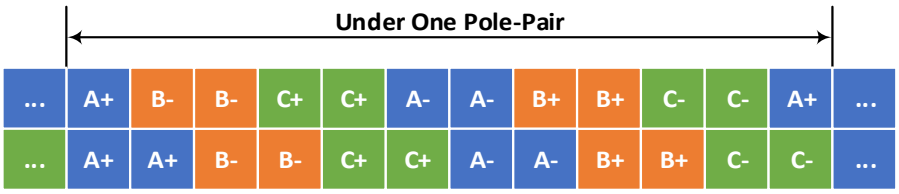

(a) Winding arrangement of 8-Pole 48-Slot in one electrical cycle

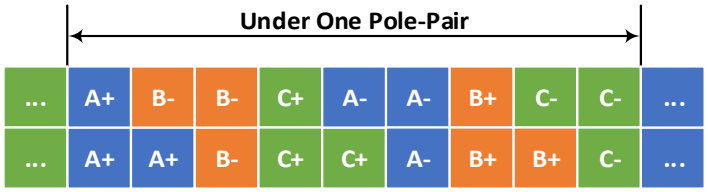

(b) Winding arrangement of 10-Pole 45 Slot in one electrical cycle

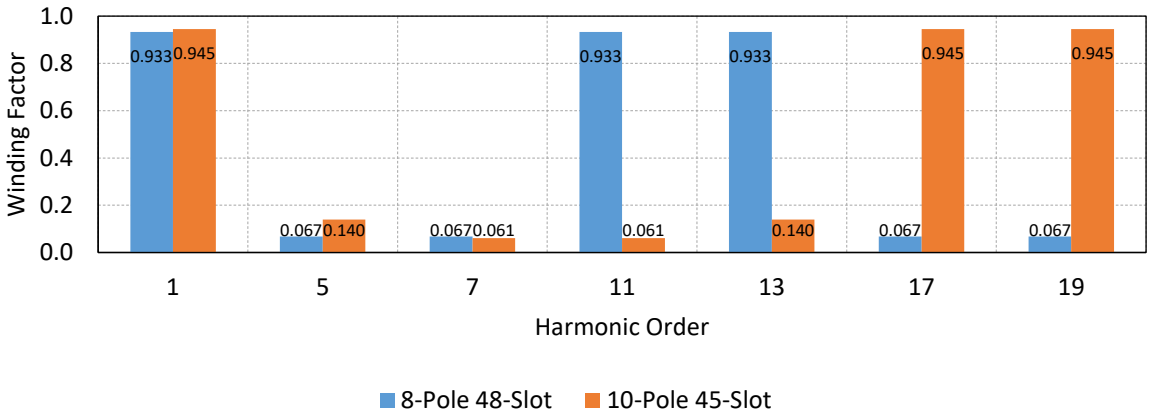

(c) Winding factor comparison

Figure 4-7 Winding arrangements of 8-Pole 48-Slot and 10-Pole 45 Slot.

4.2.4 Criterion for Unity Power Factor

In case unity power factor is necessary along the envelop at high speed, then the center of the voltage limit ellipse needs to be outside of the current limit circle, i.e. the characteristic current must be higher than or at least equal to the stator current amplitude

$$\frac{L_{\mathrm{m}}}{L_{\mathrm{d}}} \cdot I_{\mathrm{f.max}} = \frac{\psi_{\mathrm{m.max}}}{L_{\mathrm{d}}} = I_{\mathrm{d.0}} \geq I_{\mathrm{s.max}} \tag{4-9}$$

This means that the field excitation must be strong enough to dominate the flux distribution

$$\psi_{\mathrm{m.max}} \geq L_{\mathrm{d}} \cdot I_{\mathrm{s.max}} \tag{4-10}$$

Consequently, a sufficient amount of copper area in field winding as well as a low enough reluctance in the main flux path need to be satisfied to meet this criterion if unity power factor is necessary.

4.3 High-Frequency Brushless Exciter Design

4.3.1 H-Bridge Converter

4.3.1.1 Phase Shift Control

In phase-shift control, each phase is 50% pull-up and 50% pull-down. And it is the phase-shift between the two phases that decides the output voltage. In case of an inductive load, the current waveform becomes trapezoid. The waveforms are illustrated in Figure 4-8. u_{A} and u_{B} are the output voltage from Leg A and B respectively, u_{AB} is the voltage difference in the between, i is the output current and U_{dc} is the dc-link voltage. As can be noticed, by changing the phase-shift between u_{A} and u_{B}, the output voltage can be adjusted as well as the output current.

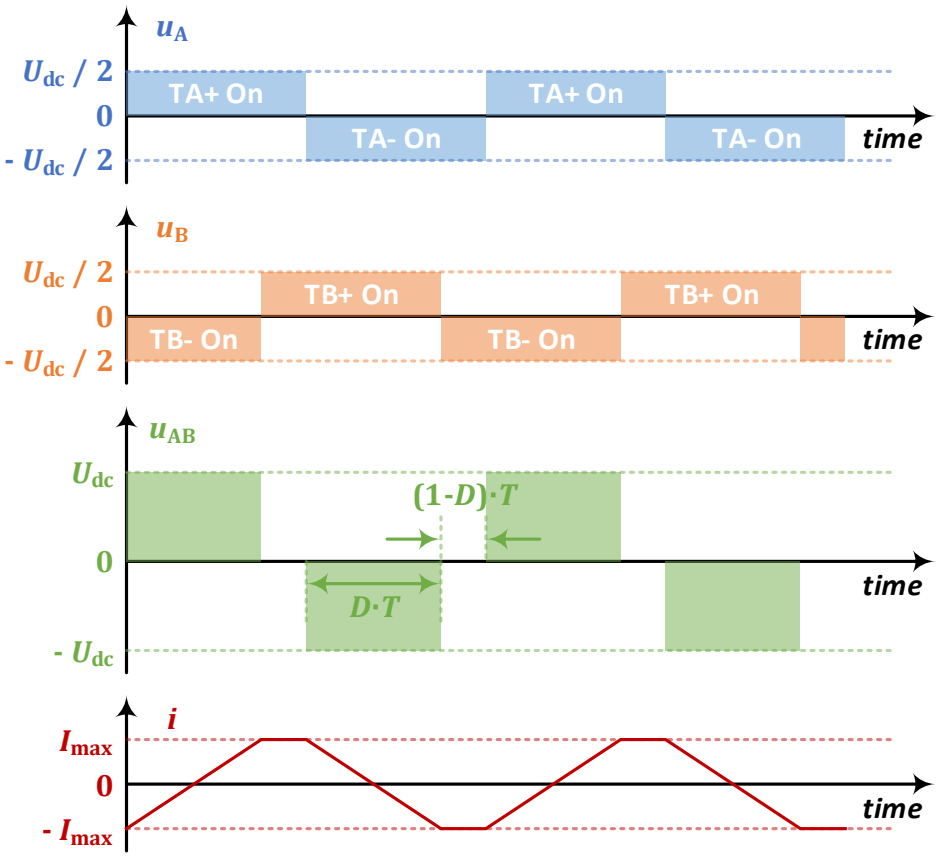

Figure 4-8 Phase-Shift control of H-bridge inverter.

The harmonics of the voltage waveform u_{AB} can be calculated by Fourier transform, from which

$$\frac{U_{h\cdot\mathrm{amp}}}{U_{\mathrm{dc}}} = \frac{4}{\pi \cdot h} \cdot \sin\left(h \cdot \frac{D \cdot \pi}{2}\right) \tag{4-11}$$

where h means the harmonic order and D means the duty cycle. The total rms of all harmonic contents can be formulated as

$$V_{\mathrm{tot\cdot rms}} = \sqrt{\frac{2}{T} \cdot {V_{\mathrm{d}}}^2 \cdot D\frac{T}{2}} = \sqrt{D}V_{\mathrm{d}} \tag{4-12}$$

The total THD can be formulated as

$$THD_{\mathrm{v}} = \frac{\sqrt{{V_{\mathrm{rms}}}^2 - {V_{1\cdot\mathrm{rms}}}^2}}{V_{1\cdot\mathrm{rms}}} \tag{4-13}$$

And this gives the lowest voltage THD of 0.290 at the duty cycle of 0.742. This can be noticed in Figure 4-9 where the harmonic distribution, the sum of all the harmonics as well as the voltage THD with respect to duty cycle are shown.

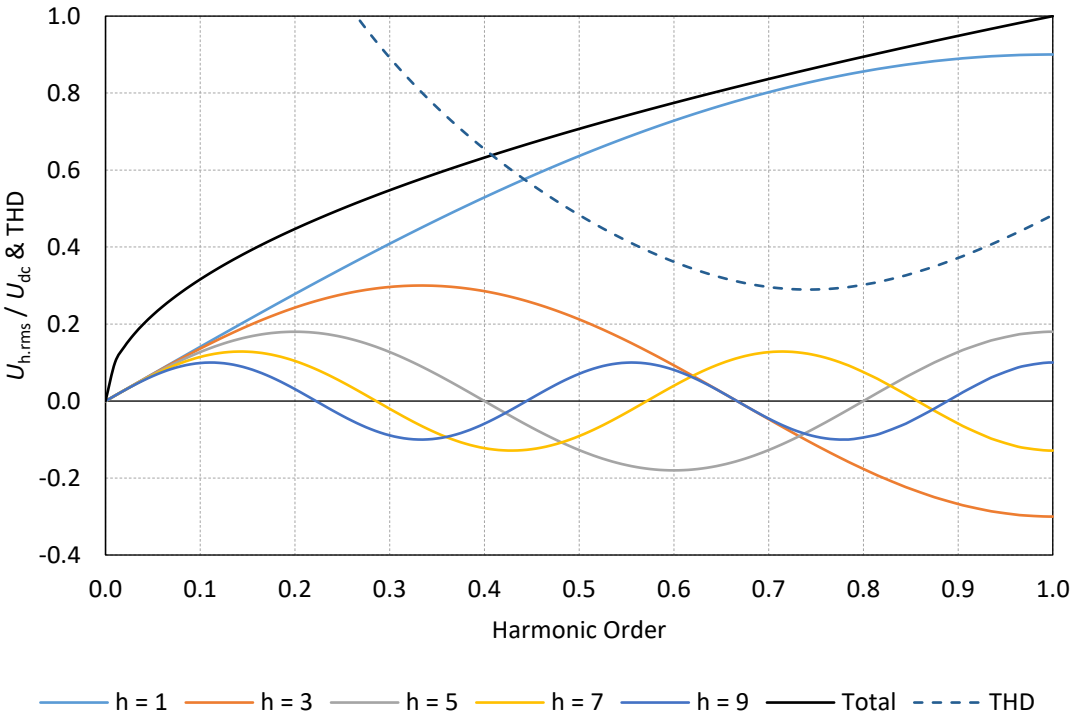

Figure 4-9 Harmonic distribution.

For the trapezoid current waveform, the rms value can be calculated by combining the triangular part and the flat part:

$$I_{\mathrm{rms}} = \sqrt{\frac{1}{T} \cdot \int_0^T i(t)^2 \mathrm{d}t} = \sqrt{\frac{2}{T} \cdot \int_0^{\frac{T}{2}} i(t)^2 \mathrm{d}t} = I_{\mathrm{max}}\sqrt{1 - \frac{2D}{3}} \tag{4-14}$$

And at $D = 0.742$

$$I_{\mathrm{rms}} = 0.711 \cdot I_{\mathrm{max}} \tag{4-15}$$

4.3.1.2 *Zero Voltage Switching*

The phase-shift modulation technique is applied to generate the switching signals to achieve zero voltage switching (ZVS). The schematic to illustrate the idea of ZVS is shown in Figure 4-10. In plot (a), TA+ and TB- are on, and the output voltage from the inverter is U_{dc}. After a time interval of DT, the inverter is going to turn off TB- and turn on TB+ as shown in Figure

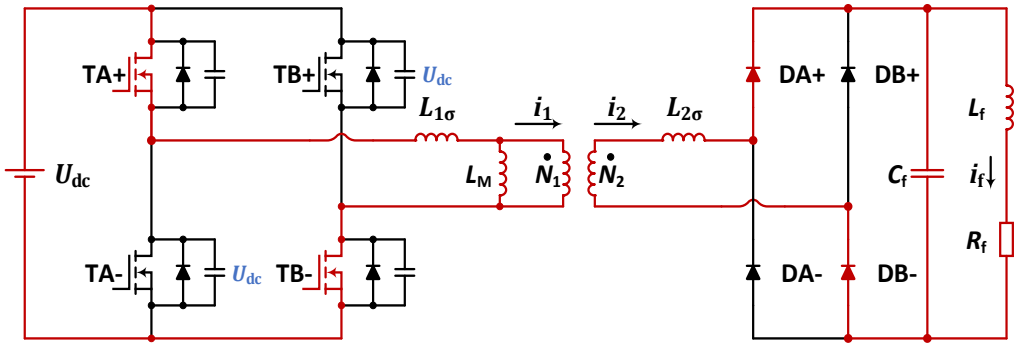

(a)

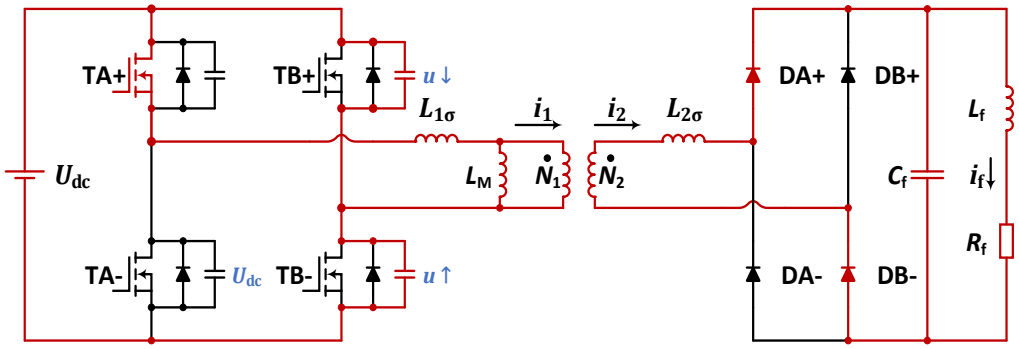

(b)

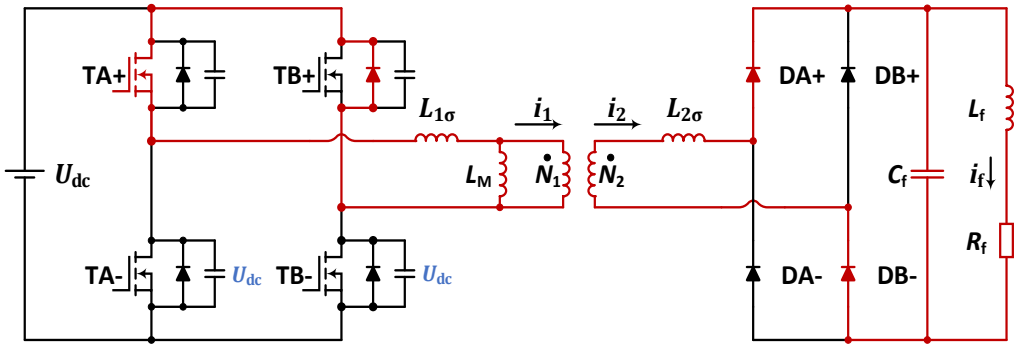

(c)

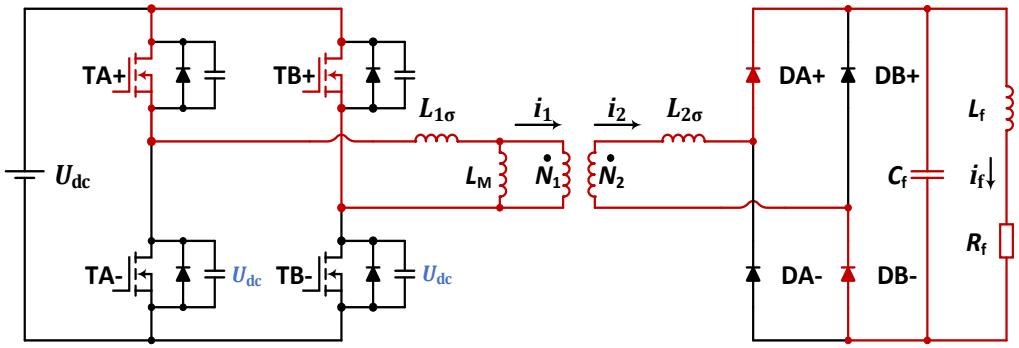

(d)

Figure 4-10 ZVS schematic.

4-8. In plot (b), it shows the blanking time when TB- is turned off but TB+ is not turned on yet. During this time, the transformer inductance tries to keep current flowing. This current charges the drain-source capacitance of TB- and discharges the drain-source capacitance of TB+. After the charging and discharging complete, the drain-source voltage of TB+ goes to zero and the diode of TB+ conducts, as shown in plot (c). In the end, the TB+ is turned on as shown in (d), and during the turn-on process, the drain-source voltage is always zero and this gives no switching loss.

Based on the mechanism of ZVS described above, two criteria can be concluded to determine ZVS. Firstly, the inductive energy storage in the transformer is larger than the capacitive energy storage in the parasitic capacitance of the switches, i.e.

$$\frac{1}{2} \cdot L_\sigma \cdot I^2 > \frac{1}{2} \cdot C_{\mathrm{ds.eq}} \cdot {U_{\mathrm{dc}}}^2 \tag{4-16}$$

where $C_{\mathrm{ds.eq}}$ is the equivalent drain-source capacitance, formulated as

$$C_{\mathrm{ds.eq}} = 2 \cdot \frac{4}{3} \cdot C_{\mathrm{oss}} = \frac{8}{3} \cdot C_{\mathrm{oss}} \tag{4-17}$$

The parameter C_{oss} can be found in the datasheet of the semiconductor switch. Since there are two drain-source capacitance in the loop, there comes the factor of 2, and $\frac{4}{3}$ is to estimate the C_{oss} at higher voltage than the condition mentioned in the datasheet [69].

The second criterion is that the blanking time is long enough for the energy to transfer from the inductance to the capacitance. The capacitance $C_{\mathrm{ds.eq}}$ and the inductance L_σ forms an LC circuit which gives a resonance frequency as

$$\omega_{\mathrm{ZVS}} = \frac{1}{\sqrt{L_\sigma \cdot C_{\mathrm{ds.eq}}}} \tag{4-18}$$

And in order to guarantee the discharging of TB+ is complete, the blanking time should be at least 1/4 of the resonance period, i.e.

$$T_{\mathrm{blank}} \geq \frac{T_{\mathrm{ZVS}}}{4} = \frac{\pi}{2} \frac{1}{\omega_{\mathrm{ZVS}}} = \frac{\pi}{2} \cdot \sqrt{L_\sigma \cdot C_{\mathrm{ds.eq}}} \tag{4-19}$$

4.3.1.3 Duty Cycle Loss

Duty cycle loss can be observed in H-bridge converter, where the duty cycle at the input of the rectifier is lower than the duty cycle at the output of the inverter. The explanation is given as illustrated in Figure 4-11. After TA+ and TB+ have been conducting as shown in Figure 4-10, TA+ turns off and TA- turns on. As a negative voltage is applied across the transformer, the current going through the transformer decreases. However, since the field current is kept constant by the field inductance, when the transformer current becomes lower than the field current, i.e. $|i_2| < i_{\mathrm{f}}$, the output capacitor C_{f} discharges to feed current into the field winding. In case C_{f} discharges completely, the sum of $i_{\mathrm{DA+}}$ and $i_{\mathrm{DB+}}$ must be equal to the field current

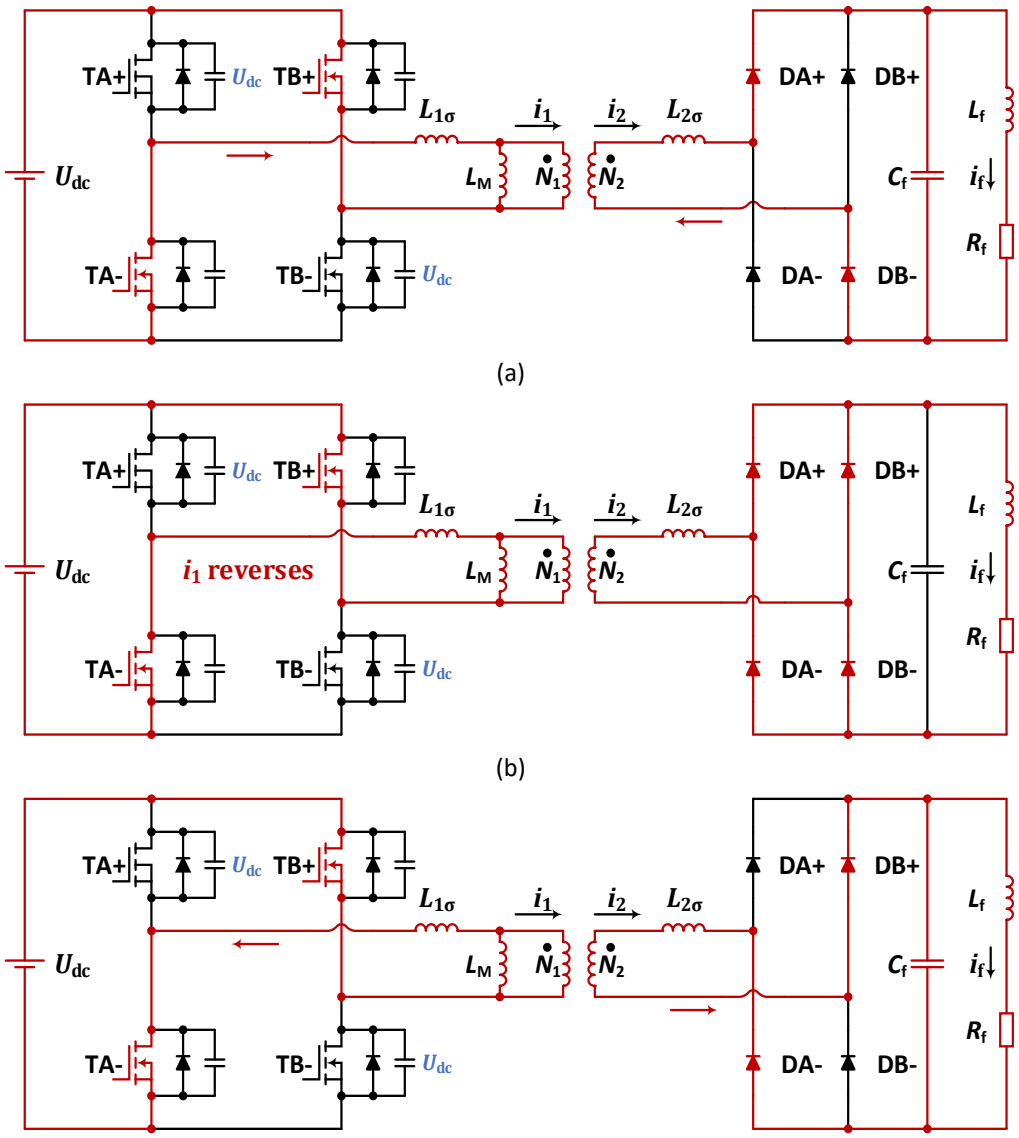

Figure 4-11 Duty cycle loss.

$$i_{\mathrm{DA+}} + i_{\mathrm{DB+}} = i_{\mathrm{f}} \tag{4-20}$$

Then the decrease of the transformer current to lower than i_{f}, i.e. $i_{\mathrm{DA+}} < i_{\mathrm{f}}$, must be compensated by introducing $i_{\mathrm{DB+}}$, which means that both DA+ and DB+ must conduct current at the same time as shown in (b). This further indicates that a short circuit of the secondary side of the transformer is introduced. Therefore, the output voltage of the transformer is clamped to zero by the short-circuit of the rectifier. The short-circuit remains until the transformer current reverses and reaches the field current level in (c). After that, the DB+ and DA- path can feed enough current to the field winding and that is when DA+ and DB- shut down and the short circuit disappears.

The duty cycle loss reduces the power transfer from the primary side to the secondary side and is therefore definitely not preferable. The duration of the duty cycle loss depends on how fast the transformer current can be reversed. And during short circuit of the rectifier in (b),

$$\frac{di_1}{dt} = \frac{u_{\mathrm{dc}}}{L_{1\sigma} + L_{\mathrm{M}} // \left(\frac{{N_1}^2}{{N_2}^2} L_{2\sigma}\right)} \tag{4-21}$$

Hence a higher dc-link voltage and a lower leakage-inductance can give a quicker current reverse and therefore a shorter loss of duty cycle. However, a lower leakage-inductance means a lower energy storage in the inductance and due to the criteria of ZVS, a lower leakage-inductance will reduce the range of ZVS, i.e ZVS cannot be achieved at a higher current level than in a higher self-inductance case. Hence one important issue to consider is the trade-off between the loss of duty cycle on the secondary side and the ZVS range [59].

4.3.2 Rotating Transformer

4.3.2.1 Geometry Type

There are mainly two geometry types of rotating transformer design as shown in Figure 4-12. The axial excitation design shown in (a) provides identical pot cores on both primary and secondary sides. This is a benefit in case of replacement and mass production. However, due to the limitation of axial tolerance, the airgap after assembly may differ from the design. The radial excitation design shown in (b) provides the opposite characteristics. Radial tolerance is easier to guarantee whereas the primary and secondary sides have different shapes.

(a) Axial excitation. (b) Radial excitation.

Figure 4-12 Axial and radial excitation.

4.3.2.2 Electromagnetic Design

Neglecting leakage flux, the optimal solution is to avoid bottle-neck in the flux path, in other words, to have equal cross-section along the flux path. And as a simplification of the geometry, the cross-section at three points are designed to be equal, one mid-point at each tooth and the mid-point at the yoke. The selections of points are as shown in Figure 4-13, taking axial excitation design as an example. Illustrated in parameters, it becomes

$$\begin{aligned} & \pi \cdot ({r_2}^2 - {r_1}^2) = 2\pi \cdot \frac{(r_2 + r_3) \cdot (w_2 - w_1)}{2} = \pi \cdot ({r_4}^2 - {r_3}^2) \\ \Rightarrow \quad & {r_2}^2 - {r_1}^2 = (r_2 + r_3) \cdot (w_2 - w_1) = {r_4}^2 - {r_3}^2 \end{aligned} \tag{4-22}$$

With the assistance of FEA, the flux density at the three points are to be checked as verification.

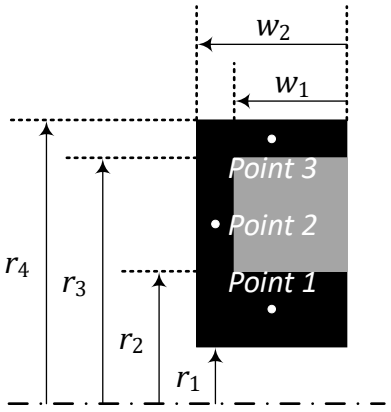

Figure 4-13 Parameters of axial excitation design.

4.3.2.3 Number of Turns

As for the selection of number of turns, firstly, the turns ratio needs to be decided. Neglecting leakage inductance, the field voltage should be equal to the dc-link voltage in case 1.0 duty cycle is applied. And in order to guarantee the maximum field current under minimum dc-link voltage at the highest temperature

$$\frac{N_2}{N_1} \approx \frac{U_{\mathrm{f.max}}}{U_{\mathrm{dc.min}}} = \frac{I_{\mathrm{f.max}} \cdot R_{\mathrm{f.max}}}{U_{\mathrm{dc.min}}} \tag{4-23}$$

Secondly, a higher number of turns reduces the flux density but increases the current density providing a fixed geometry. Following this relationship, the number of turns is adjusted simultaneously on both sides of the winding, to achieve a balance of the flux density and the current density.

Chapter 5

Dynamic Control

The dynamic control of EESM consists of both the three-phase currents on the stator side and the field current on the rotor side. In this chapter, firstly, a field current estimation algorithm is developed. Then a closed-loop field current control is illustrated. The stator current control is similar to the classical field-oriented control of PMSM and is briefly introduced in the end.

5.1 Estimation of Current and Temperature of Field Winding

Introducing a rotating transformer reduces the friction losses and efforts of maintenance, but also brings challenges to the prevalence of EESM. The field winding is physically inaccessible after assembly. This makes field current not possible to be measured directly. Nevertheless, to implement a closed-loop field current control, a feedback of instantaneous field current is needed. In addition, the heat generated by the field winding copper loss is a well-known challenge. Hence, estimating field winding temperature to protect the winding from over temperature becomes necessary. The aim of the study in this section is therefore to develop an online algorithm to estimate the current and temperature of the field winding, so that a closed-loop field current control and an over-temperature protection of field winding can be possibly implemented.

5.1.1 Schematic and Principle of the Algorithm

The schematic of the estimation algorithm is shown in Figure 5-1. The inputs to the algorithm are the duty cycle decided by the current controller, which adjusts the excitation level of the machine, as well as the dc-link input current of the H-Bridge inverter, which is the feedback of the algorithm and corrects the estimation. The outputs of the algorithm are the estimations of field current and field winding temperature.

The algorithm contains two datasets, one for field current and one for dc-link current, with the duty cycle and temperature as the inputs. The datasets in this algorithm can be either look-up tables or formulas. And the formulas can be derived analytically or developed by applying curve-fitting to the simulated or experimental data.

As the start, the algorithm firstly assumes a winding temperature, and the current controller gives a duty cycle. The duty cycle and the assumed winding temperature are fed into the datasets. Then the estimated steady-state field current and dc-link current are generated. Through dynamic response shaping processes, the steady-state estimations are shaped into instantaneous values. The estimated field current is fed into the current controller for field current control while the estimated dc-link current is compared with the measured dc-link current. The error in the between is then used to correct the temperature estimation. Thereafter, with the updated temperature estimation, the field current and dc-link current

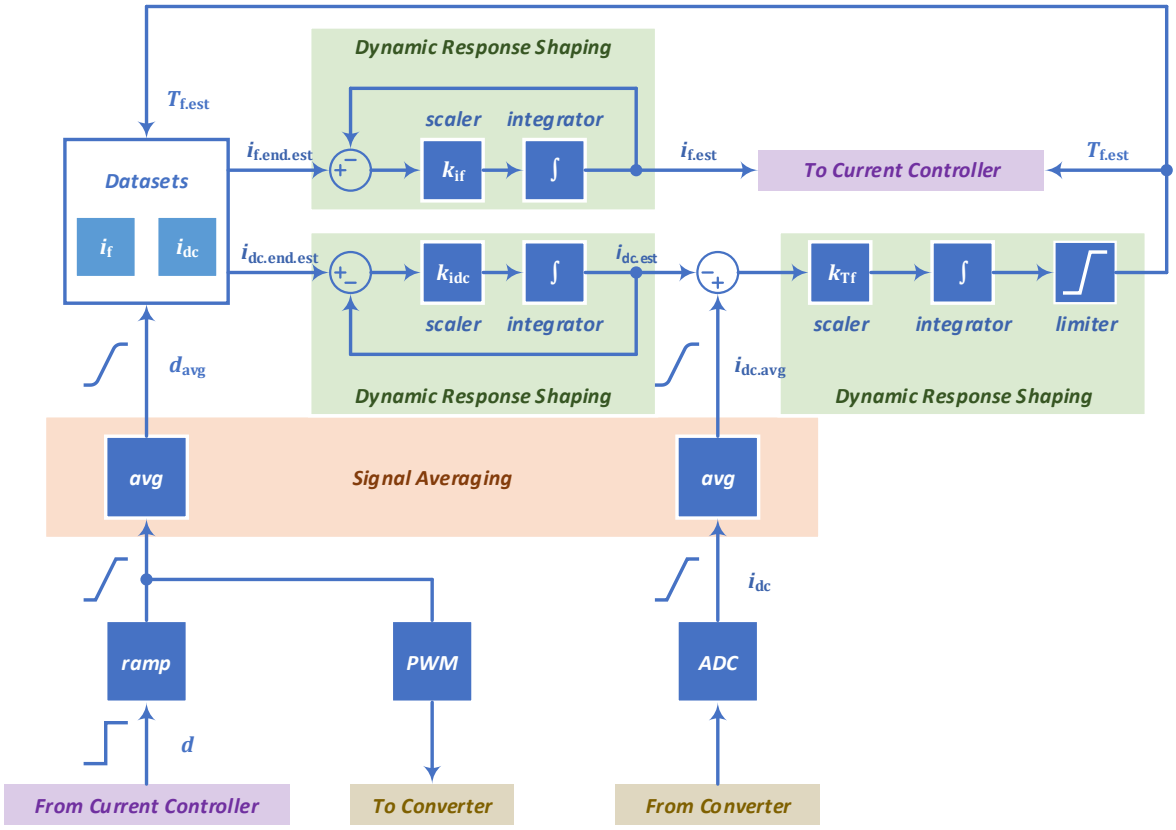

Figure 5-1 Schematic of the estimation algorithm.

estimations are updated as well. Hence the datasets together with the dc-link current and field winding temperature dynamic response shaping processes forms the temperature correction loop. The updates will continue until the error between the estimation and measurement of the dc-link current goes to zero.

5.1.2 Signal Filtering and Ramping

The algorithm requires a stable measurement of dc-link current. To achieve this, a moving average of the dc-link current measurement is implemented so that high frequency noise can be filtered out. In this study, an average of 100 samples is applied. However, this filtering will introduce a time delay. And since the measured dc-link current is compared with the estimated dc-link current which is calculated from the duty cycle, the duty cycle needs to be delayed by the same time duration so that the two signals in comparison can be synchronized. To realize this, the same moving average filter is added in the path through which the duty cycle signal is fed into the algorithm. In addition, the duty cycle is ramped in the machine control in practical situation, so that the back-EMF increases gradually, and the stator current controller has enough time to react.

5.1.3 Datasets

Datasets can be described by look-up tables, analytical or formulas generated by curve fitting of experimental data. Analytical solution can be derived if the rectifier output capacitance is high enough to keep the field voltage constant [60]. The results have been presented in (2-97)

and (2-98). If the criterion does not fit, then curve fitting of the experimental data can be applied.

5.1.4 Dynamic Response Shaping

The datasets give steady state estimations of the dc-link current and the field current. In order to shape a transient curve of current rising, an integrator is utilized to gradually eliminate the error between the instantaneous value and the steady state value of the estimation

$$i_{\mathrm{dc.est}} = k_{i_{\mathrm{dc}}} \cdot \int (i_{\mathrm{dc.end.est}} - i_{\mathrm{dc.est}}) \cdot dt \tag{5-1}$$

$$i_{\mathrm{f.est}} = k_{i_{\mathrm{f}}} \cdot \int (i_{\mathrm{f.end.est}} - i_{\mathrm{f.est}}) \cdot dt \tag{5-2}$$

where $i_{\mathrm{dc.est}}$ is the instantaneous dc-link current estimation, $i_{\mathrm{dc.end.est}}$ is the steady state dc-link current estimation, $k_{i_{\mathrm{dc}}}$ is the gain of the dc-link current shaping integration, $i_{\mathrm{f.est}}$ is the instantaneous field current estimation, $i_{\mathrm{f.end.est}}$ is the steady state field current estimation, $k_{i_{\mathrm{f}}}$ is the gain of the field current shaping integration. Then, the field winding temperature can be estimated

$$T_{\mathrm{f.est}} = k_{T_{\mathrm{f}}} \cdot \int \left(i_{\mathrm{dc.avg}} - i_{\mathrm{dc.est}}\right) \cdot dt \tag{5-3}$$

where $k_{T_{\mathrm{f}}}$ is the gain of the field winding shaping integration. The gains in (5-1), (5-2) and (5-3) are initially calculated from the time constant and the thermal capacity of the field winding, and then tuned in experiments. In order to avoid possible error, $T_{\mathrm{f.est}}$ is clamped within 0 and 200℃.

5.2 Field Current Control

With the estimated field current, it becomes possible to apply closed-loop control to field current. The schematic of the algorithm is shown in Figure 5-2. Firstly, the field current error $i_{\mathrm{f.err}}$ is calculated by comparing the reference value $i_{\mathrm{f.ref}}$ and the estimated value $i_{\mathrm{f.est}}$

$$i_{\mathrm{f.err}} = i_{\mathrm{f.ref}} - i_{\mathrm{f.est}} \tag{5-4}$$

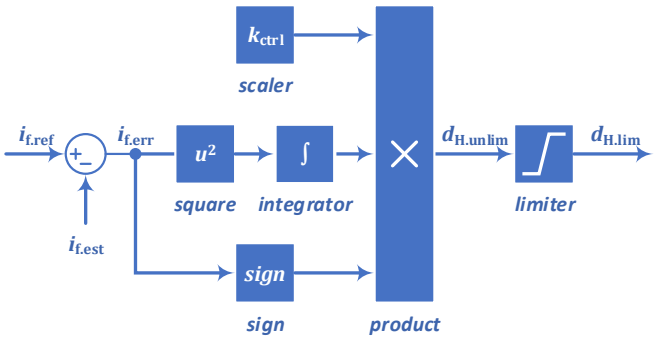

Figure 5-2 Closed-loop field current control.

Then, the error is squared and amplified by a scaler k_{ctrl}

$$d_{\mathrm{H.unlim}} = k_{\mathrm{ctrl}} \cdot \mathrm{sign}(i_{\mathrm{f.err}}) \cdot \int {i_{\mathrm{f.err}}}^2 \cdot dt \tag{5-5}$$

where $d_{\mathrm{H.unlim}}$ is the unlimited duty cycle and it is then clamped between 0 and 1 to be $d_{\mathrm{H.lim}}$. The reason to take the square is that, it is preferred to adjust the duty cycle in a big step when the error is large, whereas when the error becomes smaller, the duty cycle needs to be fine-tuned to avoid overshoot.

5.3 Stator Current Control

The controller to regulate d- and q-axis currents are presented in Figure 5-3. From (2-26), the current derivatives can be described as

$$\frac{\mathrm{d}i_{\mathrm{d}}}{\mathrm{d}t} = \frac{u_{\mathrm{d}} - R_{\mathrm{s}} i_{\mathrm{d}} + \omega_{\mathrm{r}} \psi_{\mathrm{q}} - L_{\mathrm{m}} \frac{\mathrm{d}i_{\mathrm{f}}}{\mathrm{d}t}}{L_{\mathrm{d}}} \tag{5-6}$$

$$\frac{\mathrm{d}i_{\mathrm{q}}}{\mathrm{d}t} = \frac{u_{\mathrm{q}} - R_{\mathrm{s}} i_{\mathrm{q}} - \omega_{\mathrm{r}} \psi_{\mathrm{d}}}{L_{\mathrm{q}}} \tag{5-7}$$

In Laplace domain, they become

$$I_{\mathrm{d}}(s) = \frac{U_{\mathrm{d}}(s) + \omega_{\mathrm{r}} \psi_{\mathrm{q}} + sL_{\mathrm{m}} I_{\mathrm{f}}(s)}{sL_{\mathrm{d}} + R_{\mathrm{s}}} \tag{5-8}$$

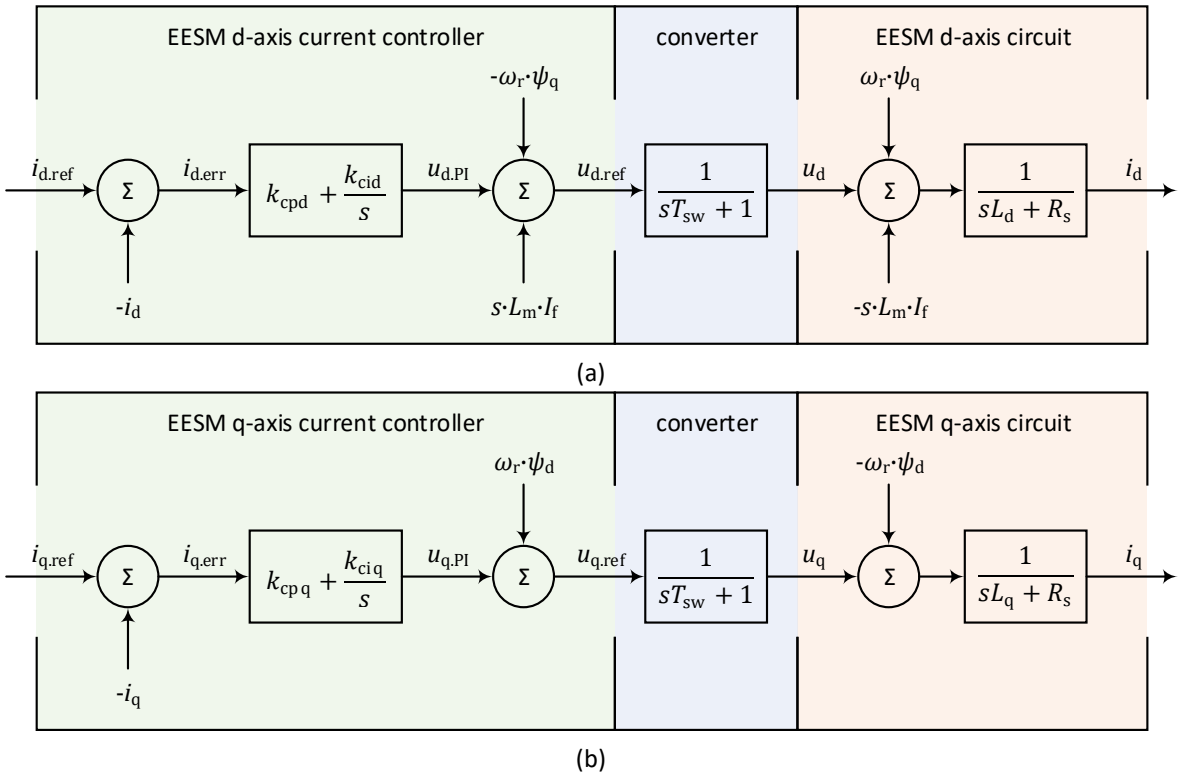

Figure 5-3 Closed-loop d- and q-axis currents control.

$$I_{\mathrm{q}}(s) = \frac{U_{\mathrm{q}}(s) - \omega_{\mathrm{r}}\psi_{\mathrm{d}}}{sL_{\mathrm{q}} + R_{\mathrm{s}}} \tag{5-9}$$

These are the classical field-oriented current controller as introduced in [70]. The three-phase currents are sampled and transformed into dq-frame. In the q-axis current control, the EMF term $\omega_{\mathrm{r}}\psi_{\mathrm{d}}$ is compensated by a feedforward term. The remaining part is an RL load $\frac{1}{sL_{\mathrm{q}}+R_{\mathrm{s}}}$ which is taken care of by a PI regulator. Since the converter process has a much higher bandwidth, $\frac{1}{sT_{\mathrm{sw}}+1}$, it can be assumed to be 1 for the controller design. To get a closed-loop transfer function as [70]

$$G_{\mathrm{cl}} = \frac{\alpha_{\mathrm{c}}}{s + \alpha_{\mathrm{c}}} \tag{5-10}$$

where α_{c} is the bandwidth of the first-order system, k_{pcq} and k_{icq} can be solved as

$$k_{\mathrm{pcq}} = \alpha_{\mathrm{c}} \cdot L_{\mathrm{q}} \tag{5-11}$$

$$k_{\mathrm{icq}} = \alpha_{\mathrm{c}} \cdot R_s \tag{5-12}$$

The d-axis current controller is designed similarly, with feedforward terms as $\omega_{\mathrm{r}}\psi_{\mathrm{q}}$ and $sL_{\mathrm{m}}I_{\mathrm{f}}$ the PI parameters can be solved as

$$k_{\mathrm{pcd}} = \alpha_{\mathrm{c}} \cdot L_{\mathrm{d}} \tag{5-13}$$

$$k_{\mathrm{icd}} = \alpha_{\mathrm{c}} \cdot R_s \tag{5-14}$$

The feedforward term $sL_{\mathrm{m}}I_{\mathrm{f}}$ in some cases can be neglected. Considering the prototype with 48 V dc-link voltage in this study, i_{f} goes from 0 to 20 A within 50 ms, and consider an L_{m} of 1 mH, then $sL_{\mathrm{m}}I_{\mathrm{f}}$ is 0.4 V, which is quite negligible.

In a first-order system, the rise time t_{rise} and the bandwidth α_{c} follow

$$t_{\mathrm{rise}} = \frac{\ln 9}{\alpha_{\mathrm{c}}} \tag{5-15}$$

This is how the design of the controller can be verified in simulations and experiments. The step response is first checked so it has an exponential shape and then the rise time is measured, if it is matching (5-15) the closed loop system has the right bandwidth. This conclusion is explained as follows.

The rise time is defined as the response rising from 10% to 90% of the reference, and as for a step input

$$u(t) = \varepsilon(t) \tag{5-16}$$

the response of a first-order system $y(t)$ can be described as

$$y(t) = (1 - e^{-\alpha_c t})\varepsilon(t) \tag{5-17}$$

The time intervals for the response to reach 10% and 90% of the steady state value are

$$y(t_1) = (1 - e^{-\alpha t_1})\varepsilon(t) = 0.1 \quad \Rightarrow \quad t_1 = -\frac{\ln 0.9}{\alpha} \tag{5-18}$$

$$y(t_2) = (1 - e^{-\alpha t_2})\varepsilon(t) = 0.9 \quad \Rightarrow \quad t_2 = -\frac{\ln 0.1}{\alpha} \tag{5-19}$$

respectively. And therefore, the rise time is

$$t_{\text{rise}} = t_2 - t_1 = -\frac{\ln 0.1}{\alpha} + \frac{\ln 0.9}{\alpha} = \frac{\ln 9}{\alpha} \tag{5-20}$$

Chapter 6

Results

6.1 EESM Development for Mild Hybrid Vehicle

6.1.1 Machine Design

Following the strategies described in the design chapter, a 4-polepair 24-slot EESM for mild hybrid vehicle has been deigned. The parameters of the deign are shown in Table 6-1. The outer dimensions of the machine are given from an existing car. The flux distribution of no-load operation and peak torque operation are calculated in FEM and presented in Figure 6-1.

Table 6-1 Parameters of a 4-polepair 24-slot EESM for mild hybrid vehicle.

Parameter	Symbol	Value	Unit
Active Length		80	mm
Stator Outer Diameter	$ODstator$	120	mm
Stator Inner Diameter	$IDstator$	90	mm
Air Gap	g	1	mm
Stator Slot Width	$Bs1$	5.56	mm
Stator Slot Depth	$Hs2$	4.5	mm
Rotor Pole Body Width		16.5	mm
Rotor Pole Body Height		14.5	mm
Number of Turns in Stator per Repeatable Group		6	
Number of Turns in Rotor per Pole Pair		150	
Steel Material		SURA M250-35A	

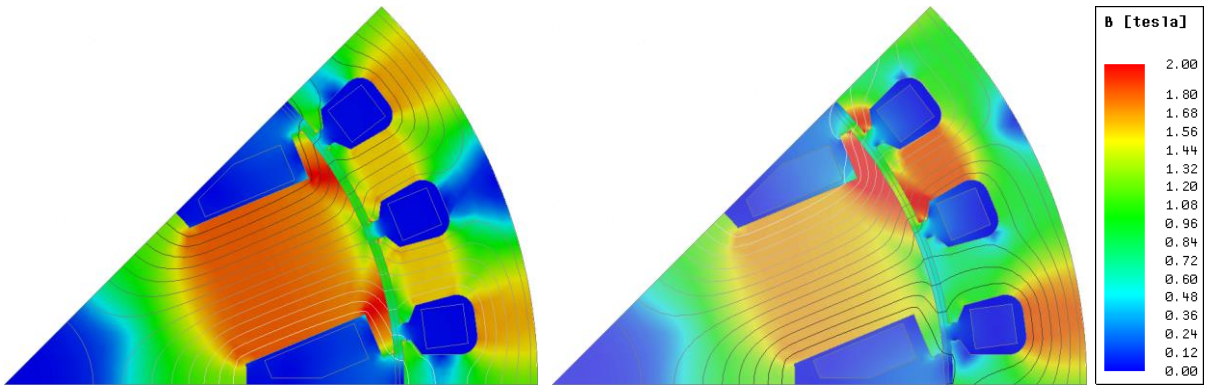

(a) No-load operation (b) Peak torque operation

Figure 6-1 Flux distribution in FEM.

In order to push as much torque as possible out of the motor, the flux path needs to be made as wide as possible to avoid magnetic saturation. To achieve this, an initial stator inner diameter is assumed and with the stator slot area as well as the rotor current density fixed, the slot width, slot depth, pole with and pole height are adjusted to maximize the flux going through the flux path. Thereafter, the stator inner diameter is adjusted as well and the same iteration is run again to search for the inner stator diameter that maximizes the flux. In the end, the optimum sizes of stator slot and rotor pole along with the optimum stator inner diameter are determined. As has been explained, the teeth and yoke of the stator and the pole body of the rotor are designed as wide as possible in order to avoid magnetic saturation. As can be noticed from the flux distributions, the flux density of the stator teeth, yoke and rotor pole body are around 1.6 T, which is slightly below the limit of saturation around 1.8 T.

In peak torque operation, the flux distribution is asymmetric. Local saturation can be found on one tip of the pole shoe whereas the saturation on the other tip is eased. This is due to cross-saturation. The d- and q-axis flux are in the same direction on one tip whereas on the other tip, the flux flow in the opposite direction and therefore cancelled [16].

In this application torque ripple is not considered as an important issue since the transmission and the wheels provide a high inertia which attenuates the ripple. The neglect of torque ripple indicates that the technique of distributed winding with short-pitch to cancel EMF harmonics is not necessary. Therefore, single layer with concentrated winding, i.e. one slot per pole per phase ($q = 1$), is applied. The single layer arrangement can guarantee as much copper area as possible. This means a maximum amount of current can be conducted. The concentrated winding arrangement maximizes the winding factor at fundamental frequency. However, it does not cancel the 5th and 7th EMF harmonics as can be seen in Figure 6-2. This figure shows the time domain and frequency domain of the no-load back-EMF of the designed motor at 4500 rev/min. Figure 6-3 shows the torque production where the 6th harmonic is visible, and the 6th harmonic in torque is due to the 5th and 7th harmonics in EMF.

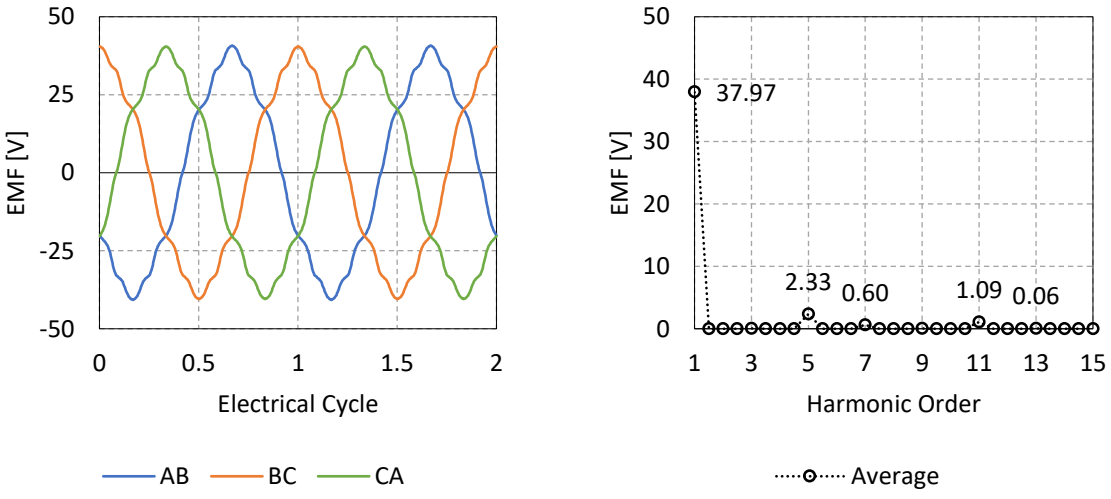

(a) Time domain (b) Frequency domain

Figure 6-2 No-load line back-EMF waveform in FEM.

The d- and q-axis flux linkage maps of the mild hybrid EESM at different levels of field current are shown in Figure 6-4. 20 A is the maximum field current level. The circle shows the current

limit of 500 A as the RMS value, i.e. 707 A as the amplitude. Following the tendency of the field current increase, the ψ_{d} and ψ_{q} contours on the dq-plane moves towards left with respect to the q-axis whereas the shapes of the contours remain the same. It is therefore possible to calculate ψ_{d} and ψ_{q} once at zero field current level and then shift the origin of the plane to the right when a field current is introduced. In other words, the d-axis current and the field current can be transformed from each other if ψ_{d} and ψ_{q} are the only concern. As can be noticed, the d-axis current influences ψ_{q} and the q-axis current influences ψ_{d}. In addition, the field current gives an impact on ψ_{q} as well. These indicate that a more accurate

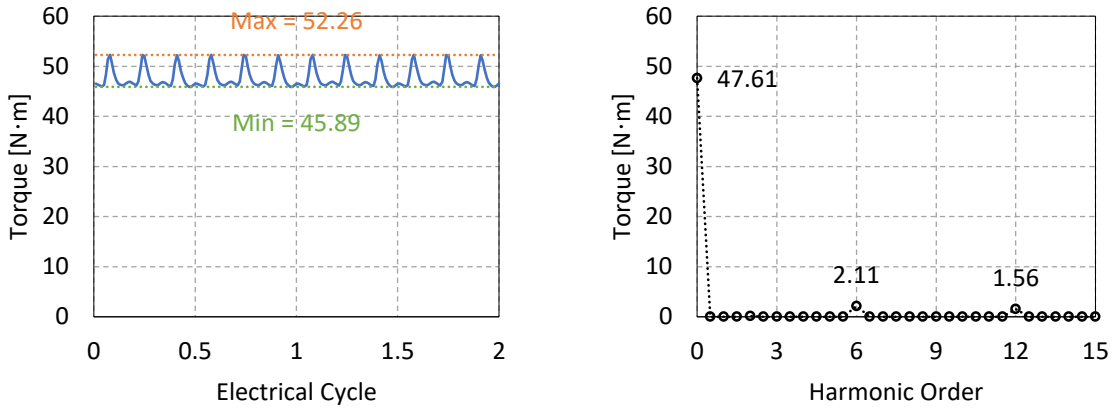

(a) Time domain (b) Frequency domain

Figure 6-3 Peak torque in FEM.

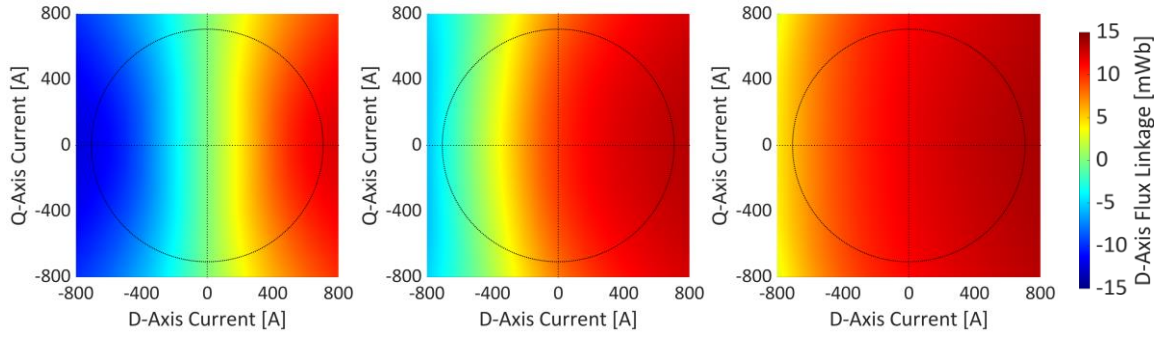

(a) ψ_{d} @ $I_{\mathrm{f}} = 0$ A (b) ψ_{d} @ $I_{\mathrm{f}} = 10$ A (c) ψ_{d} @ $I_{\mathrm{f}} = 20$ A

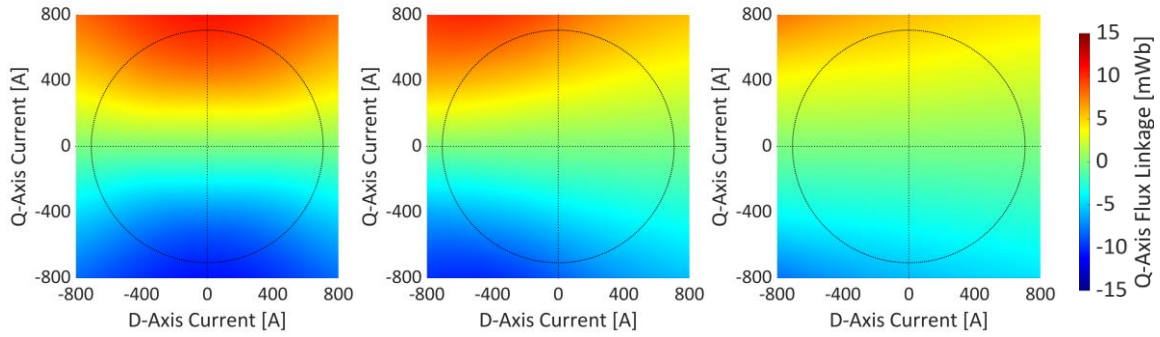

(d) ψ_{q} @ $I_{\mathrm{f}} = 0$ A (e) ψ_{q} @ $I_{\mathrm{f}} = 10$ A (f) ψ_{q} @ $I_{\mathrm{f}} = 20$ A

Figure 6-4 The d- and q-axis flux linkage maps of the mild hybrid EESM at three difference field currents.

model can be developed to include the mutual inductance between d- and q-axis windings as well as between the field winding and the q-axis winding.

Based on the flux linkages, the electromagnetic torque can be calculated with (2-40) and is shown in Figure 6-5. The MTPA curves in the torque maps are perpendicular to the torque contours shown as the black dots. It is interesting to notice that the MTPA curve firstly turn to the first quadrant at low field current level and then to the second quadrant as field current goes higher. This can be explained by the inductances along d- and q-axis.

Figure 6-6 shows the d- and q-axis inductance maps of the mild hybrid EESM. As the field current increases, the inductances decrease. And the d-axis inductance decreases more than the q-axis inductance since the d-axis flux path is saturated by the field current whereas the

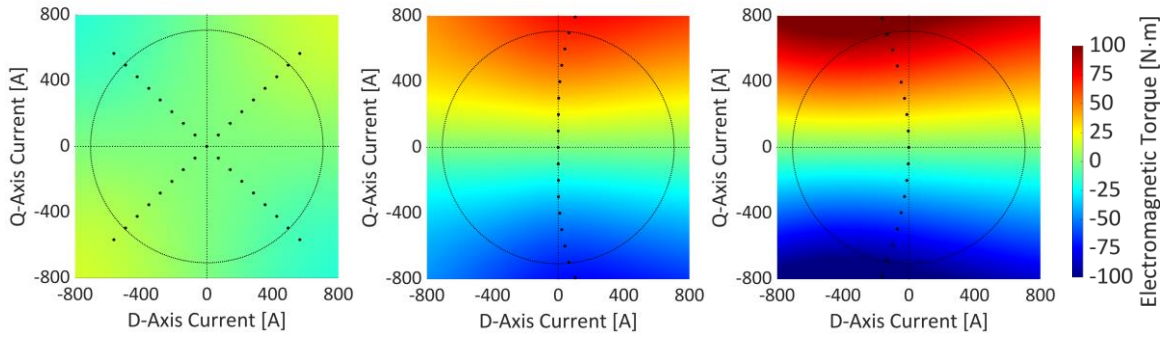

(a) T_{em} @ $I_{\mathrm{f}} = 0$ A (b) T_{em} @ $I_{\mathrm{f}} = 10$ A (c) T_{em} @ $I_{\mathrm{f}} = 20$ A

Figure 6-5 The torque maps of the mild hybrid EESM at three difference field currents. The dotted lines are the MTPA points.

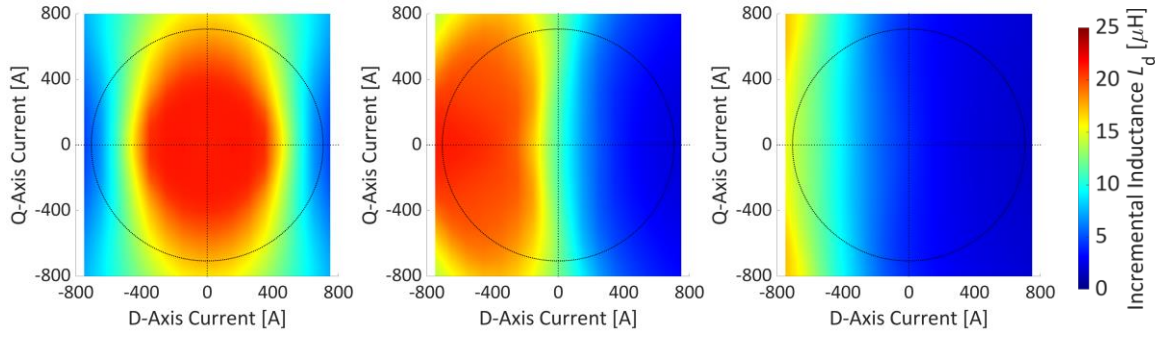

(a) L_{d} @ $I_{\mathrm{f}} = 0$ A (c) L_{d} @ $I_{\mathrm{f}} = 10$ A (e) L_{d} @ $I_{\mathrm{f}} = 20$ A

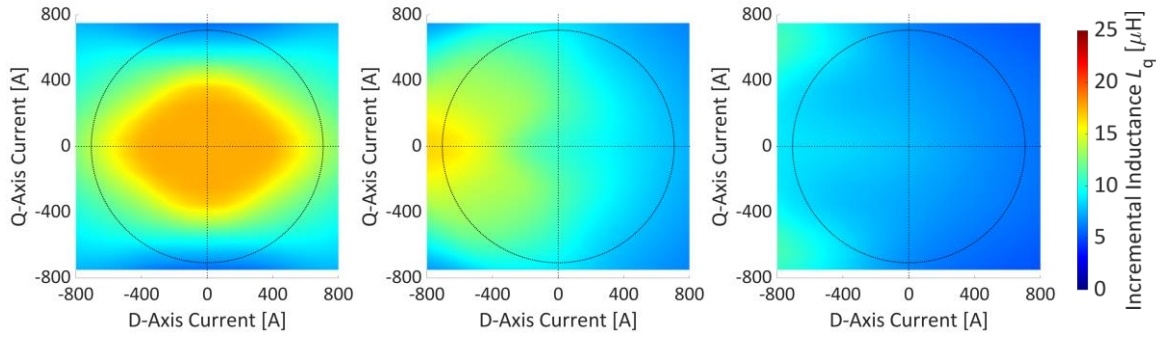

(b) L_{q} @ $I_{\mathrm{f}} = 0$ A (d) L_{q} @ $I_{\mathrm{f}} = 10$ A (f) L_{q} @ $I_{\mathrm{f}} = 20$ A

Figure 6-6 The d- and q-axis inductance maps of the mild hybrid EESM at three difference field currents.

q-axis flux path is only partly affected by field current due to cross-saturation, e.g. in the rotor pole shoe and the stator yoke. As a result, $L_{\mathrm{d}} > L_{\mathrm{q}}$ at lower field current whereas $L_{\mathrm{d}} < L_{\mathrm{q}}$at high field current. According to the electromagnetic torque curves introduced in Section 3.1.2, in case of $L_{\mathrm{d}} > L_{\mathrm{q}}$ the asymptotic lines of electromagnetic torque is located in the negative region. The MTPA curve in this case therefore goes to the positive region since the MTPA curve is the gradient of the torque contours. This is the case in Figure 6-5 (b), while as field current goes higher, then $L_{\mathrm{d}} < L_{\mathrm{q}}$, and the MTPA curve goes to the negative region as shown in Figure 6-5 (c).

Table 6-2 concludes the machine parameters identified in the design process. The resistances are calculated analytically. The inductances are calculated in FEM. These parameters are used in the control study and compared with the test data of the prototype.

Table 6-2. EESM parameters identified in design process.

Parameter	Symbol	Value	Unit
Stator Winding Resistance	R_{s}	3	mΩ
Field Winding Resistance	R_{f}	4.65	Ω
Stator D-Axis Inductance (unsaturated)	L_{d}	21.20	μH
Stator Q-Axis Inductance (unsaturated)	L_{q}	17.58	μH
Field Winding Inductance (unsaturated)	L_{f}	143	mH
Mutual Inductance (unsaturated)	L_{m}	1.176	mH

Figure 6-7 shows the iron core loss of the EESM at 4500 rpm. The iron core loss contours shift to the left gradually as the field current goes higher. This is due to the fact that, the iron-core loss is related to the flux density in the iron core and the point with zero-flux in dq-frame is shifted to the left gradually. Specifically, with zero field current, the point with zero d- and q-axis currents gives zero flux which is the origin of the dq-frame. When a field current is introduced, to achieve zero flux, a negative d-axis current has to be injected to cancel the main flux generated by field current. Therefore, the zero-flux point is shifted to the left of the origin.

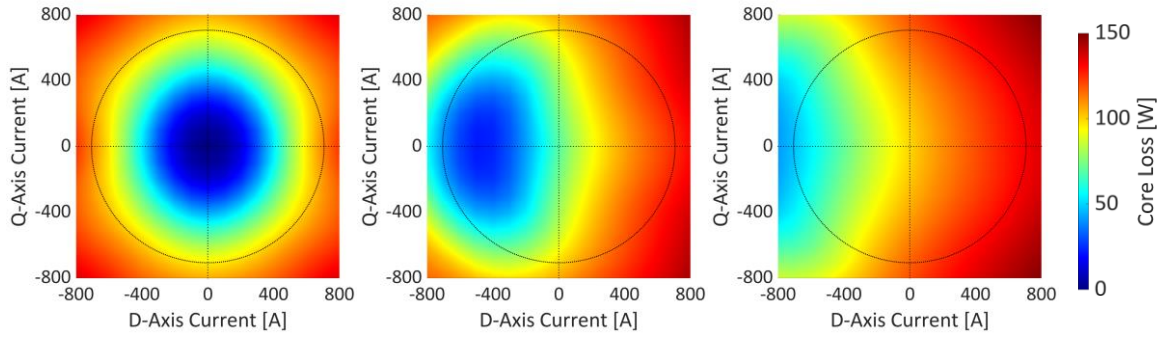

(b) L_{q} @ $I_{\mathrm{f}} = 0$ A (d) L_{q} @ $I_{\mathrm{f}} = 10$ A (f) L_{q} @ $I_{\mathrm{f}} = 20$ A

Figure 6-7 The core loss maps of the mild hybrid EESM.

Furthermore, in contrast to the flux linkage maps on dq-plane, the shapes of the contours on the iron core loss map are more and more distorted after a higher and higher field current is

introduced. Hence to get the iron core loss maps at different excitation levels, FEM simulations at each level are needed.

6.1.2 Field Excitation Design

The brushless excitation system is designed by following the considerations introduced in Section 4.3. The ferrite material used in the pot core is PC40 from TDK with a saturation flux density of 400 mT and a suitable frequency range between 100 and 400 kHz. The axial excitation design is selected with identical pot cores on both primary and secondary sides. As has been mentioned in Section 4.3.2, this gives benefits in case of replacement and mass production. The design considers the electromagnetic performance as well as mechanical strength. In terms of electromagnetics, the flux density along the flux path iron core is tuned to be as uniform as possible, whereas considering mechanical strength and manufacturing, the minimum thickness is set to 2 mm.

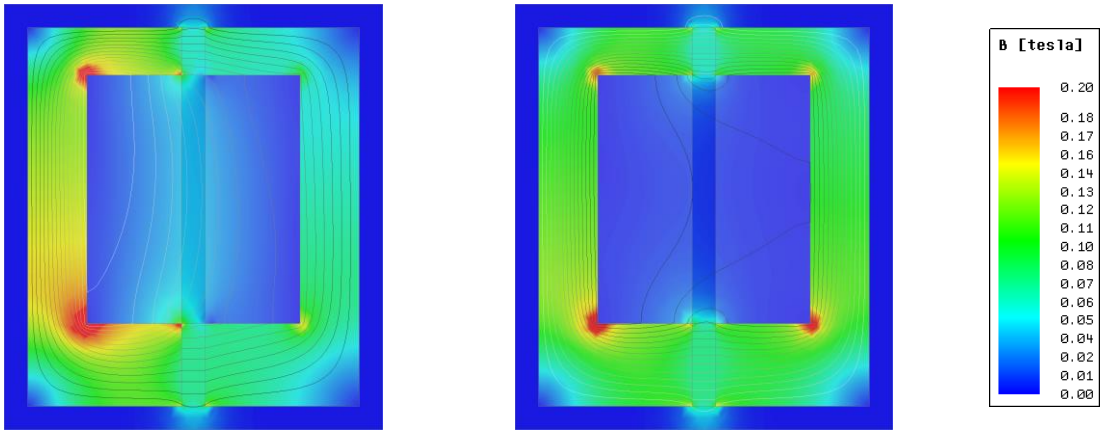

(a) Maximum flux density on primary side (b) Maximum flux density on secondary side

Figure 6-8 Flux distribution in the ferrite pot core.

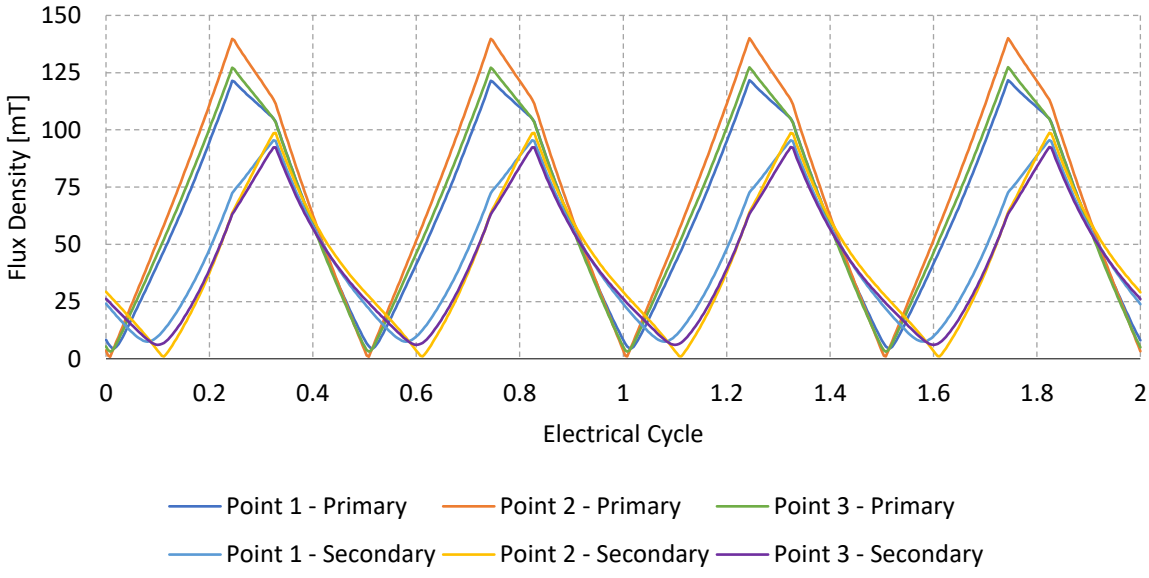

Figure 6-9 Flux density variations in FEM.

The flux distributions are shown in Figure 6-8. The Points 1, 2 and 3 are defined on both primary (stationary) side and secondary (rotary) side according to Figure 4-13. The flux densities of these points are illustrated in Figure 6-9. As can be noticed, the flux densities are far below 400 mT. The pot cores are over dimensioned to guarantee mechanical strength. In addition, the flux densities among all the three points on the same side are similar. This verifies the design strategy introduced in Section 4.3.2.2. Furthermore, the peak flux density of the primary side is higher than the peak of the secondary side. This is due to the flux leakage on the primary side, i.e. some flux lines only link with the primary side. This is unavoidable if identical pot cores are used on both sides of the transformer. Otherwise, the size of the secondary side pot core can be reduced.

Due to the low flux density compared with the saturation level, the frequency for power transfer is selected as 100 kHz, i.e. the lowest value within the frequency range. This frequency selection minimizes iron-core loss as well as switching losses of the H-Bridge inverter. The parameters of the brushless excitation system are shown in Table 6-3.

Table 6-3 Parameters of brushless excitation system of the mild hybrid EESM.

Parameter	Value	Unit
DC-link voltage	36 - 60	V
Inverter MOSFET maximum voltage	100	V
Inverter MOSFET maximum current @ 25℃	300	A
Transformer primary turns	3	
Transformer secondary turns	9	
Transformer primary side resistance	27	mΩ
Transformer secondary side resistance	9.5	mΩ
Rectifier diode threshold voltage	557	mV
Rectifier diode conduction resistance	4.0	mΩ
Switching frequency	100	kHz

6.1.3 Optimization of Steady State Operation

6.1.3.1 Copper Losses

The stator copper loss and field copper loss maps under copper loss minimization and field current minimization are compared in Figure 6-10 and Figure 6-11. The losses compared here only include the copper losses in the windings of the machine, excluding the copper loss of the rotating transformer in the brushless excitation system. As can be clearly seen, compared with copper loss minimization, field current minimization maximizes the usage of stator current which introduce a stator copper loss of over 2 kW in most of the operation area. As a result, the area of a field copper loss higher than 500 W is shrunk, e.g. in copper loss minimization, with a field copper loss of 500 W the machine delivers 25 N·m whereas in field current minimization, with the same field copper loss the machine delivers 35 N·m. It can be

concluded that the field current minimization algorithm reduces rotor copper loss effectively but with a significant sacrifice of stator copper losses.

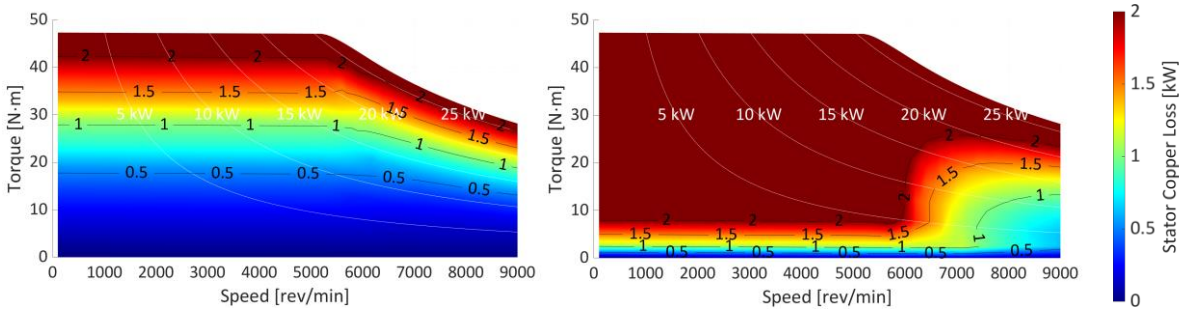

(a) Copper loss minimization (b) Field current minimization

Figure 6-10 Comparison of stator copper loss.

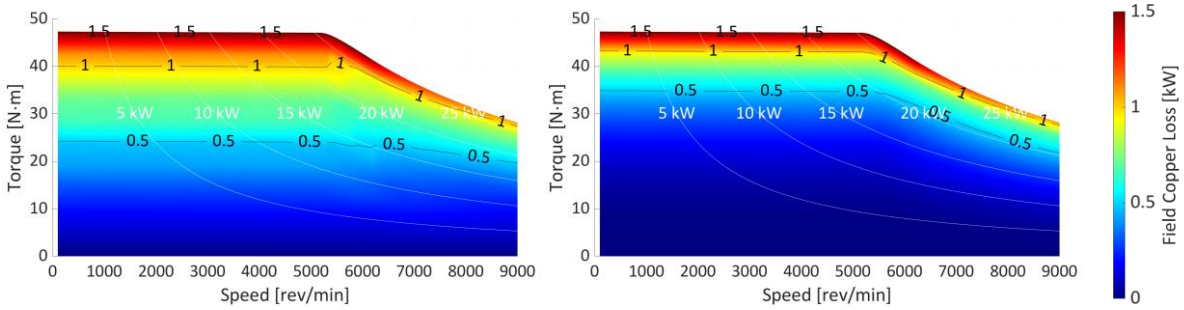

(a) Copper loss minimization (b) Field current minimization

Figure 6-11 Comparison of field copper loss.

6.1.3.2 Efficiency

The efficiency under copper loss minimization and field current minimization are calculated and presented in Figure 6-12 (a) and (b) respectively. As can be seen from the figures, the highest efficiency of the EESM occurs in the high-speed region but with medium torque level. The efficiency of the copper loss minimization strategy is significantly higher than the field current minimization strategy in most operation area of the map. This indicates that if energy-saving is of most concern, and if the EESM operates continuously, then the copper loss minimization is absolutely the first choice. However, if energy-saving is not of interest, e.g. the EESM operates in a generation mode to charge the battery and the battery is nearly fully charged, then the field current minimization strategy can be applied to reduce the amount of heat generated on the rotor side.

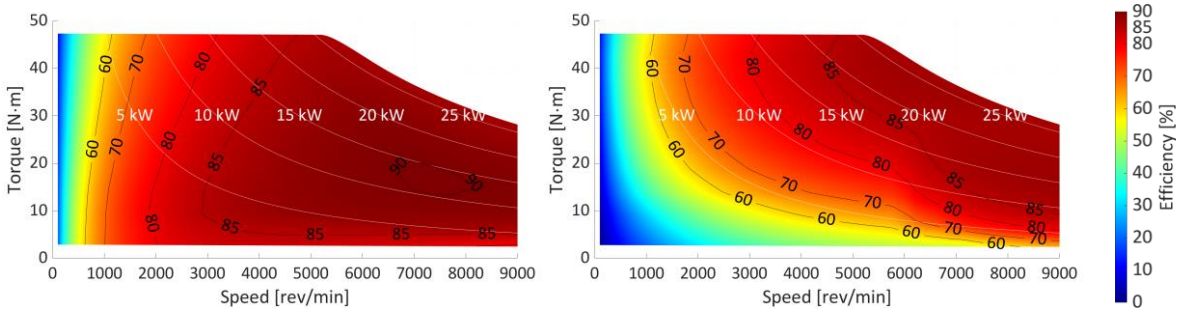

(a) Copper loss minimization (b) Field current minimization

Figure 6-12 Comparison of efficiency.

Iron core-losses are taken into account when calculating the efficiency, but are not taken into the minimization function due to two reasons. Firstly, the iron core-losses are quite minor compared with copper losses in most of the operation area. Secondarily, the copper losses are a more sever challenge compared with iron-core losses, since most copper losses are dissipated through iron-core and then to the cooling jacket.

6.1.3.3 Power Factor

The power factor maps under copper loss minimization and field current minimization are presented in Figure 6-13 (a) and (b) respectively. As can be noticed, the power factor in the copper loss minimization case is also significantly higher than the one in the field current minimization case over most of the operation area. Copper loss minimization can guarantee a power factor higher than 0.8 at any point of the operation map. Field current minimization only gives a high power factor in the high torque region which is due to the fact that the solution of the current vector is unique at any operation point along the boundary. The equal-power-factor lines of field current minimization are approximately parallel to each other. A comparison between Figure 6-13 (a) and (b) also shows that both of the highest power factor operation areas appear at high speed region and unity power factor appear at the high torque high speed region.

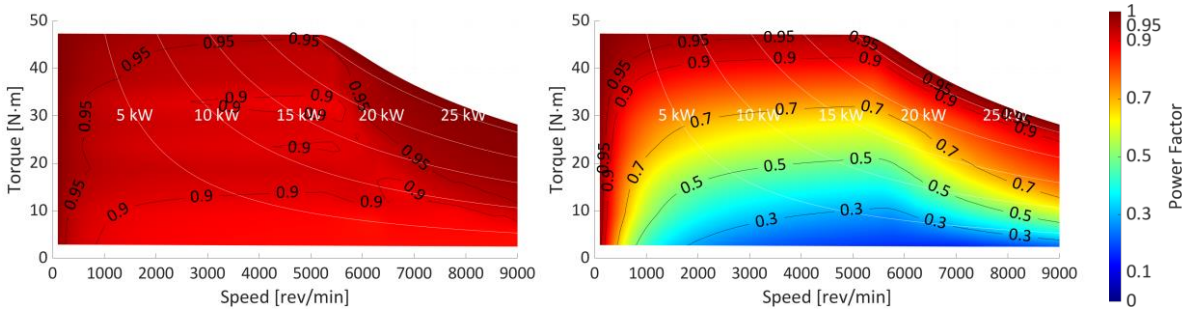

(a) Copper loss minimization (b) Field current minimization

Figure 6-13 Comparison of power factor.

6.1.3.4 Analysis with Driving Cycle

The performance of two control strategies, copper loss minimization and field current minimization, are compared in the WLTC driving cycles introduced in Figure 3-10. Figure 6-14 shows a dataset of torque and speed requested for electrical machines in mild hybrid vehicle under WLTC. The recording process of the dataset is not part of this study. A study to obtain records of electric machine utilization in mild hybrid vehicles can be found in [71].

An electrical machine in mild hybrid application is used mainly for accelerating and deaccelerating the vehicle instead of continuous running. This can be noticed by comparing Figure 6-14 (a) and (b). When the vehicle is running at almost constant speed, the torque output is zero, whereas the machine outputs torque when the vehicle is accelerating or deaccelerating. The comparison of stator copper loss and field copper loss are done in Figure 6-15 and Figure 6-16. As can be noticed, the stator copper loss is sacrificed to get a low field copper loss in field current minimization algorithm. In copper loss minimization, the shape of

the stator copper loss curve is similar to the rotor copper loss, which is due to the proportional relationship between the stator currents and field current introduced in Section 3.3.2.3. This

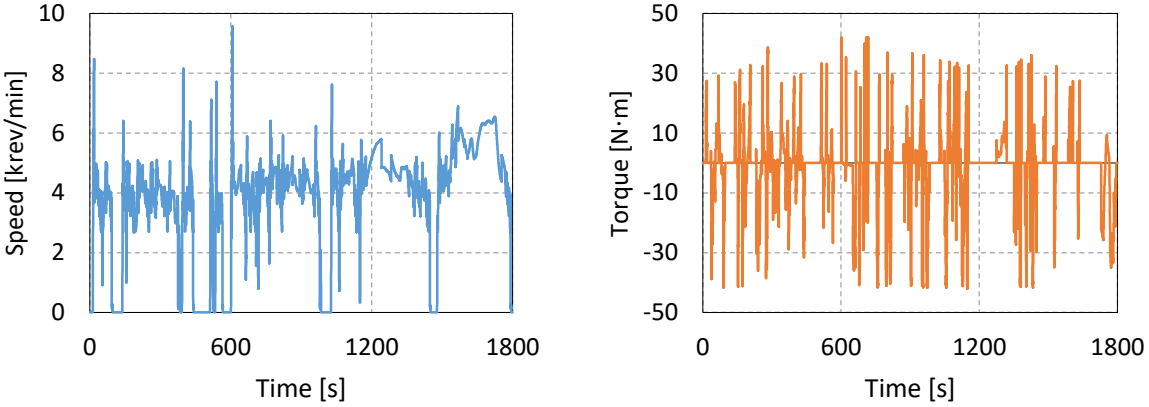

(a) Speed (b) Torque

Figure 6-14 Torque and speed requested for the EESM in mild hybrid vehicle.

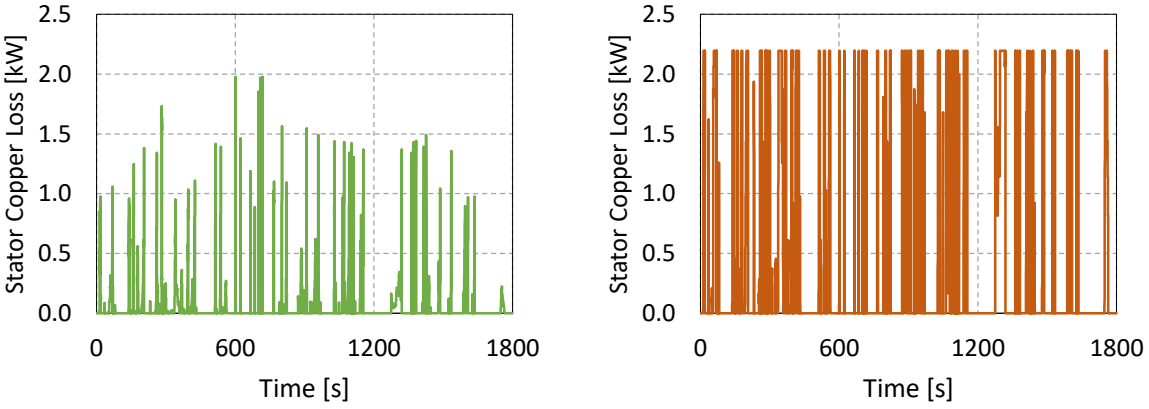

(a) Copper loss minimization (a) Field current minimization

Figure 6-15 Stator copper loss.

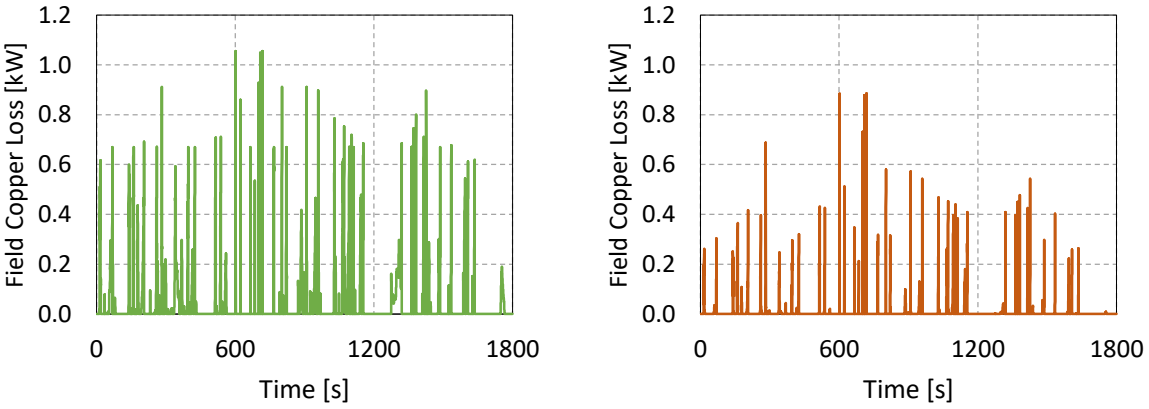

(a) Copper loss minimization (a) Field current minimization

Figure 6-16 Field copper loss.

relationship is not valid in field current minimization and therefore the shapes of the curves are quite different when comparing the (b) plots of Figure 6-15 and Figure 6-16.

With a constant sampling frequency, the average stator and field copper loss can be calculated, following

$$P = \frac{1}{N} \cdot \sum_{i=1}^{N} p_i \tag{6-1}$$

where N is the total number of samples, p is the instantaneous power at each sampling instant and i is the index of samples. The results are concluded in Table 6-4. As can be noticed, compared with copper loss minimization, the field current minimization gives over 6 times of the stator copper loss, but reduces the field copper loss by 80%. The total copper loss is approximately 4 times compared with copper loss minimization.

Table 6-4 Comparison of copper losses of copper loss minimization and field current minimization.

	Copper Loss Minimization	**Field Current Minimization**	**Ratio**
	CLM	**FCM**	**FCM / CLM**
Stator Copper Loss	56.44 W	370.38 W	6.56
Field Copper Loss	42.75 W	9.02 W	0.21
Total Copper Loss	99.19 W	379.41 W	3.83

As a conclusion, the field current minimization algorithm reduces field copper loss effectively but with a huge cost of stator copper loss. The total copper loss therefore becomes much higher as well, and the field winding temperature can be reduced with the cost of a higher temperature of stator winding. In practical implementations, it is suggested use a slider between copper loss minimization and field current minimization, to achieve a balance between temperatures of stator and field windings.

6.1.4 Dynamic Control

6.1.4.1 Field Current Estimation

An H-bridge inverter is used in the excitation system as shown in Figure 1-5. Figure 6-17 shows the sequence of the duty cycle applied to the inverter, which is to test the field current estimation algorithm developed in Section 5.1. The duty cycle ramps from 0 up to 1.0 at 0.5 s and ramps down to 0.5 s at 2.5 s. At 4.5 s, it ramps to 1.0 and at 6.5 s ramps down to 0.5 again.

A simplified thermal model according to Section 2.2.4 is implemented to describe the temperature rise of the field winding as shown in Figure 6-18. The copper loss of the field winding can be calculated as

$$p_{\mathrm{f}} = {i_{\mathrm{f}}}^2 \cdot R_{\mathrm{f}} \tag{6-2}$$

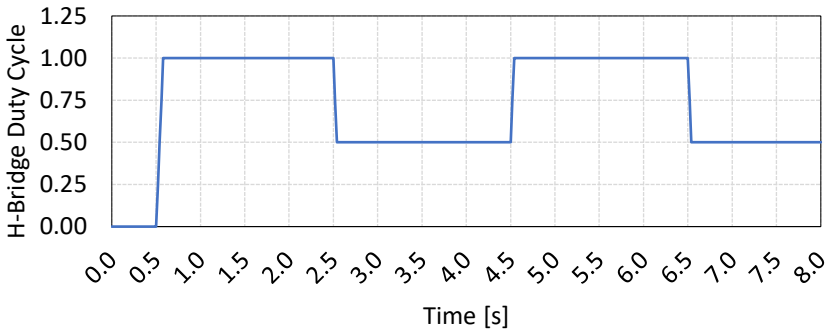

Figure 6-17 Sequence test of duty cycle.

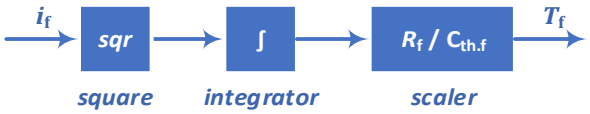

Figure 6-18 Thermal model of the field winding.

where p_f is the instantaneous field copper loss and i_f is the instantaneous field current. With a thermal capacitance $C_{th.f}$ of 360 J/K, the field winding temperature can be calculated by integration of the copper loss

$$T_f = \int \frac{p_f}{C_{th.f}} \cdot dt = \frac{R_f}{C_{th.f}} \cdot \int {i_f}^2 \cdot dt \tag{6-3}$$

where T_f is the field winding temperature. This is not a delicate thermal modeling of the machine winding. Instead, it is to introduce temperature variations and to evaluate the tracking performance of the estimation algorithm with such temperature variations.

To verify the dynamic tracking capability of the estimation algorithm, cases with different starting temperatures are simulated and the case with temperature starting at 30°C is shown in Figure 6-19. The initial value of the temperature estimation is 40°C and after the algorithm is activated at 0.5 s, the algorithm starts to eliminate the temperature estimation error. As can be noticed in (c), the dc-link current estimation, as the feedback of the algorithm, follows the real dc-link current well. This verifies the functionality of the integrator in the dynamic response shaping process.

The temperature estimation in (b) shows that the tendency of the estimated temperature follows the real temperature quite well. Error exists due to the accuracy of linear interpolation (look-up table, denoted TAB) and curve fitting (denoted CF). The tracking by using curve fitting gives slightly larger error than linear interpolation since curve fitting is an approximation of the curve. Spikes can be seen when the duty cycle steps, this is due to the error between the estimated and the real dc-link currents during the transients. And the dynamic response shaping process helps to reduce the spikes. Due to the successful estimations of the dc-link current and field winding temperature, the field current estimation follows the real value consequently as shown in (a).

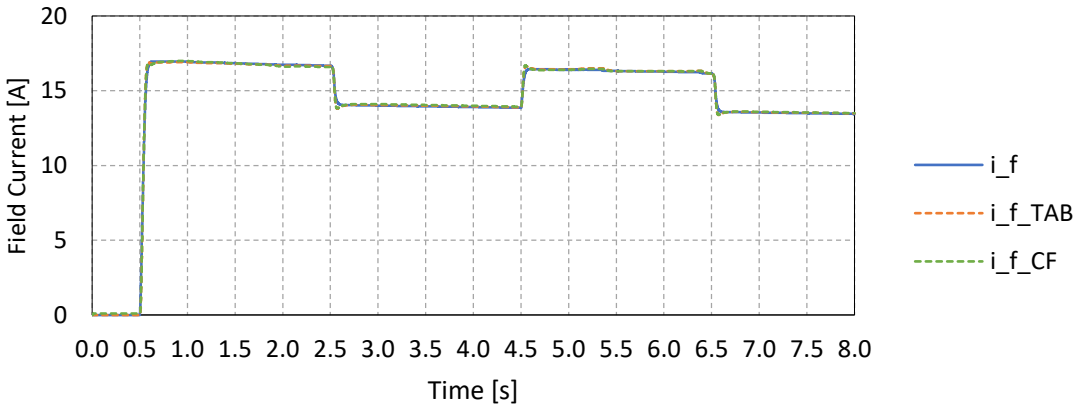

(a) Field current from 0 to 8 s

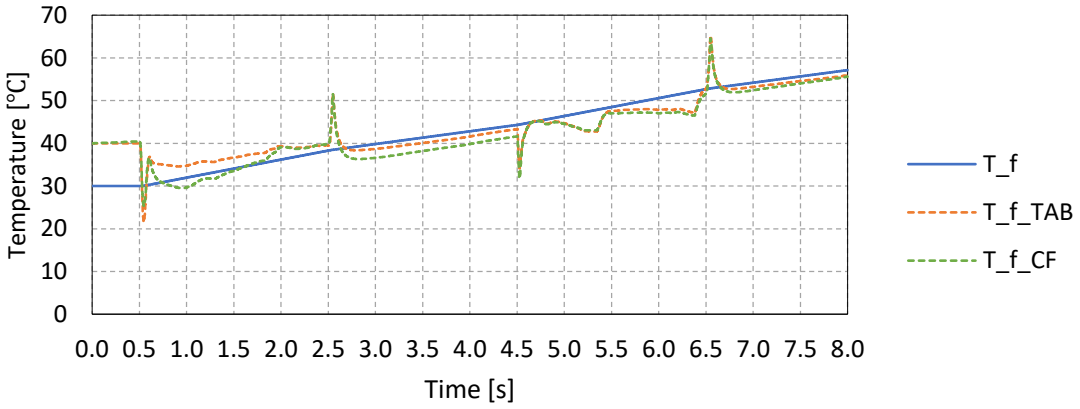

(b) Field winding temperature from 0 to 8 s

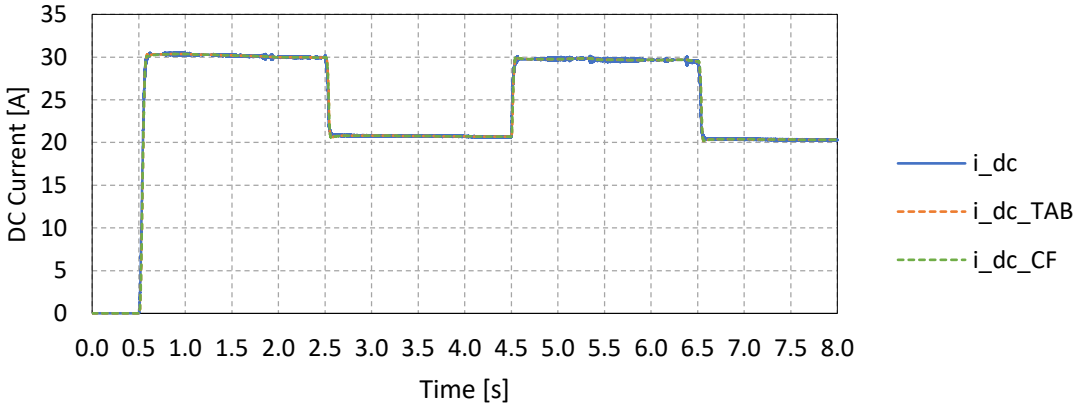

(c) DC-link current from 0 to 8 s

Figure 6-19 Duty cycle sequence simulation at 30°C. TAB means look-up table and CF means curve fitting.

The zoomed-in details of the field current estimation during the step are shown in Figure 6-20. Generally, the differences between the estimated and the real curves are quite minor during both the rising and falling of the field current.

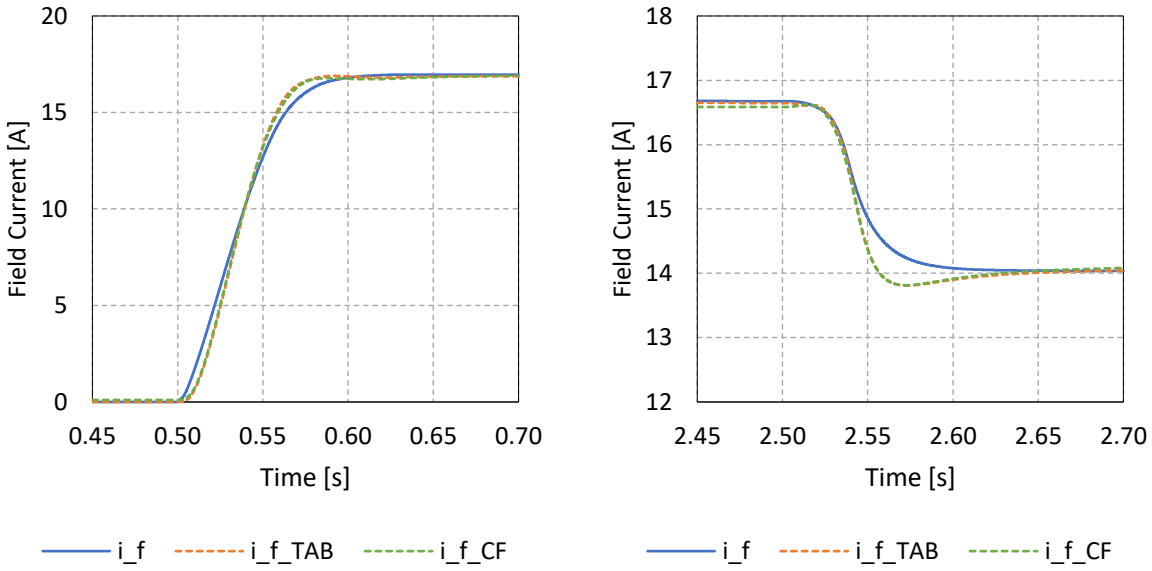

(a) Field current from 0.45 to 0.70 s

(b) Field current from 2.45 to 2.70 s

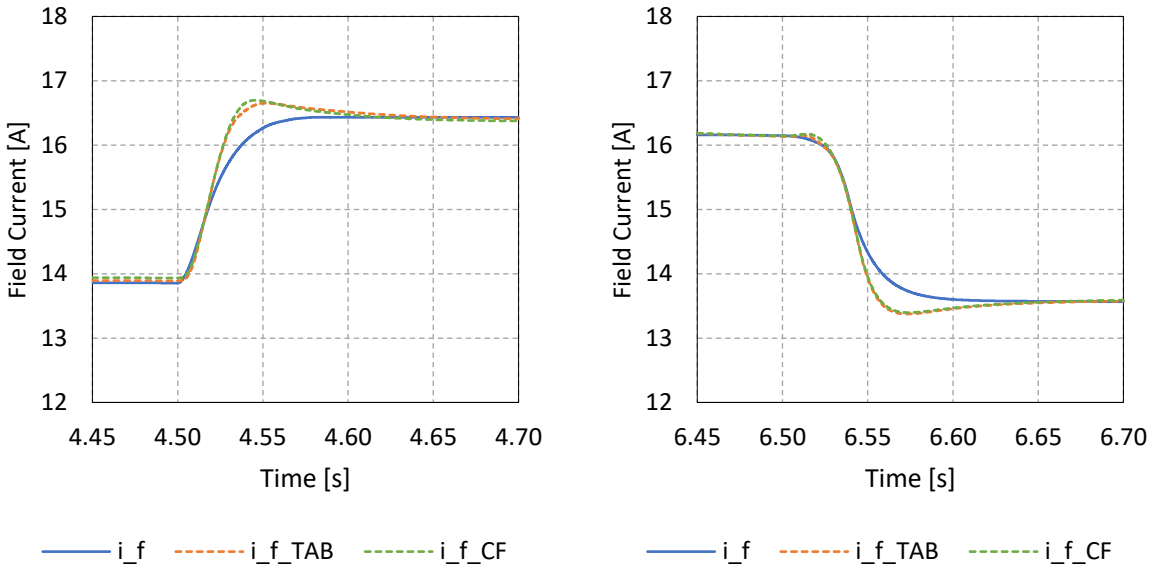

(c) Field current from 4.45 to 4.70 s

(d) Field current from 6.45 to 6.70 s

Figure 6-20 Duty cycle sequence simulation at 30℃. TAB means look-up table and CF means curve fitting.

6.1.4.2 Field Current Control

A sequence of field current reference is applied as shown in Figure 6-21. The field current reference ramps from 0 up to 18 A at 0.5 s and ramps down to 12 A at 2.5 s. At 4.5 A, it ramps to 18 A and at 6.5 s it ramps down to 12 A again. The overall performance is illustrated in (a). As can be seen, the reference exceeds the maximum current output capability with reference of 18 A. The gap between the reference and the real current enlarges as time passes due to the increase of temperature. In comparison, the current follows the reference of 12 A quite well.

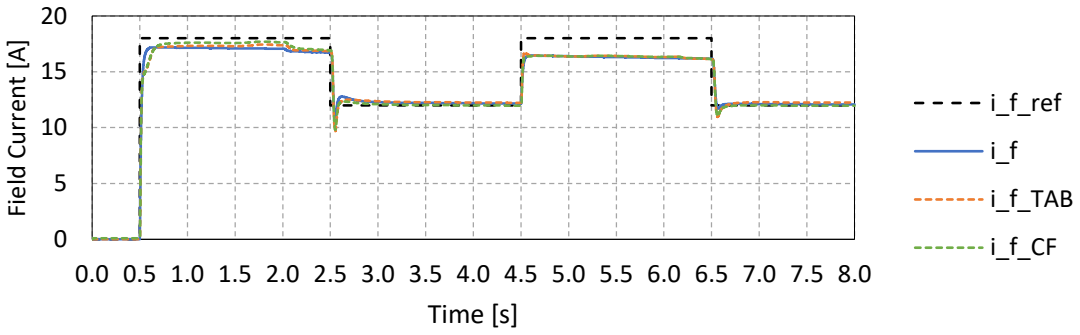

(a) Field current from 0 to 8 s

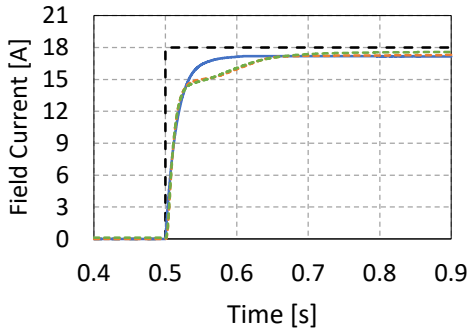

(b) Field current from 0.4 to 0.9 s

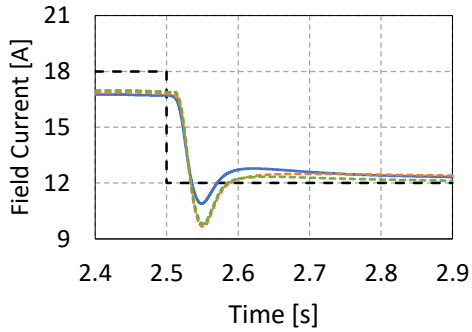

(c) Field current from 2.4 to 2.9 s

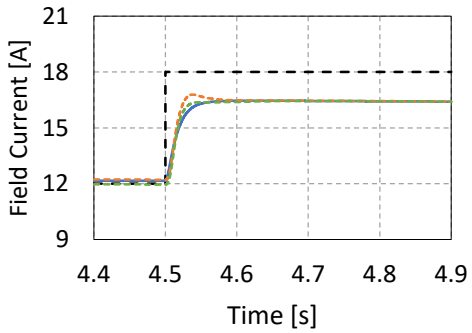

(d) Field current from 4.4 to 4.9 s

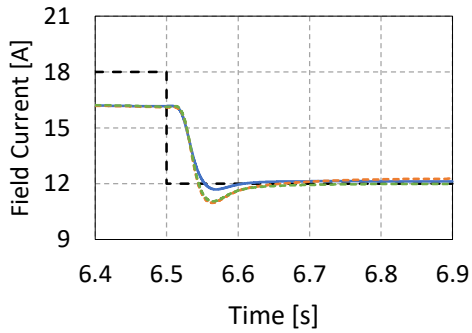

(e) Field current from 6.4 to 6.9 s

Figure 6-21 Closed-loop field current control at 30℃. TAB means look-up table and CF means curve fitting.

6.1.4.3 Stator Current Control

A non-linear dynamic model of the machine is built according to Section 2.1.5. The non-linearity of the machine model is described by utilizing the flux linkage maps and inductance maps from Section 6.1.1. Then field-oriented controller with PI regulator is established. The bandwidth of the PI controller is set at 1 kHz, one twentieth of the switching frequency. The proportional gain and integral gain are calculated either by assuming a constant unsaturated inductance value, i.e. linear controller, or taking interpolation of the data in the map dynamically, i.e. non-linear controller.

To study the performance of the controller, step responses are analyzed. The speed is set as constant at 750 rev/min. Steps of 100 A and 500 A q-axis current are compared in Figure 6-22. The vertical axis is normalized into percentage for the convenience of comparison. In the 100 A cases, the nonlinear and non-linear controller give no significant difference. The rise time is measured as 0.34 ms, and with (5-15), this rise time corresponds to a bandwidth of 1 kHz which fulfills the design. In the 500 A case, the current rises slower. This is due to that the voltage limiter is activated during the current rise. The current derivative is therefore limited as well. During this interval, the current derivative is constant since the voltage drop across the inductance is the voltage limit if the resistive voltage drop is neglected. After the voltage limiter is deactivated, the current rise given by the linear controller is faster than the non-linear controller. This attributes to the larger proportional gain used in the linear controller since it uses the unsaturated inductance to calculate the proportional gain.

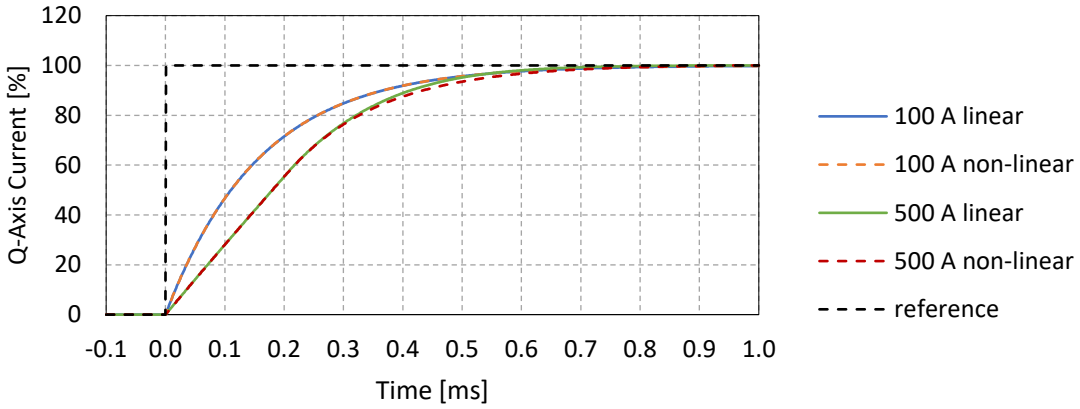

Figure 6-22 Step response of q-axis current ($I_{\mathrm{d.ref}} = 0$ [A], $I_{\mathrm{q.ref}} = 100$ & 500 [A]).

6.1.5 Prototype and Experimental Setup

6.1.5.1 Machine

The machine, the excitation system as well as the three-phase inverter are prototyped. The stator and rotor of the machine are shown in Figure 6-23. Tests for parameter identification have been performed and the measured parameters are concluded in Table 6-5.

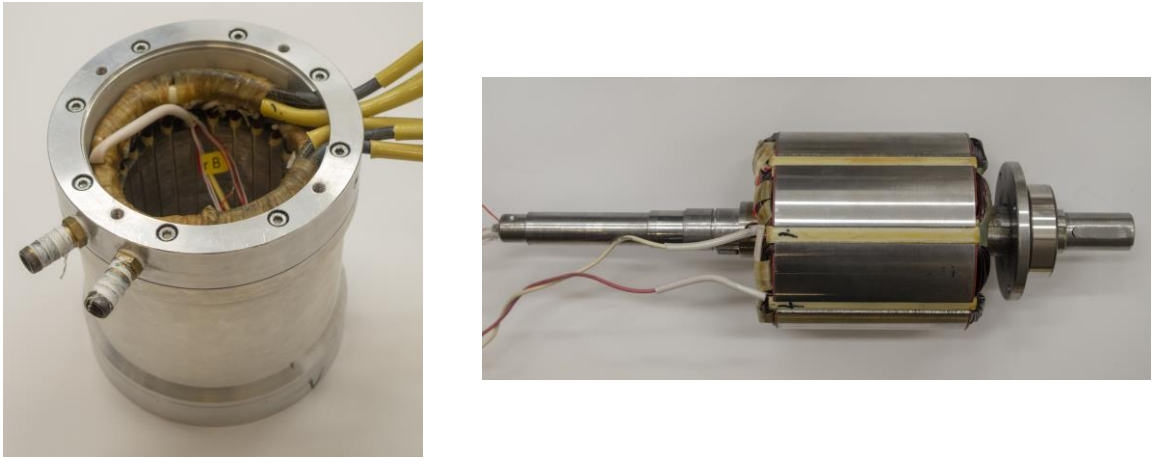

(a) Stator (b) Rotor

Figure 6-23 Protype of the mild hybrid EESM.

Table 6-5. EESM parameters identified in test.

Parameter	Symbol	Value	Unit
Stator Winding Resistance	R_s	4	mΩ
Field Winding Resistance	R_f	5	Ω
Stator D-Axis Inductance (unsaturated)	L_d	24.4	μH
Stator Q-Axis Inductance (unsaturated)	L_q	20.6	μH
Stator Leakage Inductance	L_σ	6	μH
Field Winding Inductance	L_f	130	mH
Mutual Inductance (unsaturated)	L_m	1.0	mH

6.1.5.2 Power Electronic Inverters

The three-phase inverter to drive the stator and the H-bridge inverter to excite the field are shown in Figure 6-24. Due to the high current that needs to flow in the stator winding, switching spikes across the switches in the three-phase inverter are treated carefully. Capacitors are added close to the terminals to damp the high frequency resonances. In addition, Zenner diodes are added on both upper and lower switches to absorb the ringing energy. In the H-bridge inverter prototype, switches in the same leg are placed close to each other to minimize the loop inductance. dc-link capacitors are placed close to the switches as well to damp the switching ringing. As for the driver circuit, a universal MOSFET driver PCB is designed. This circuit is suitable for both MOSFET power modules and discrete switches. And it is used for both three-phase inverter and H-bridge inverter in this study.

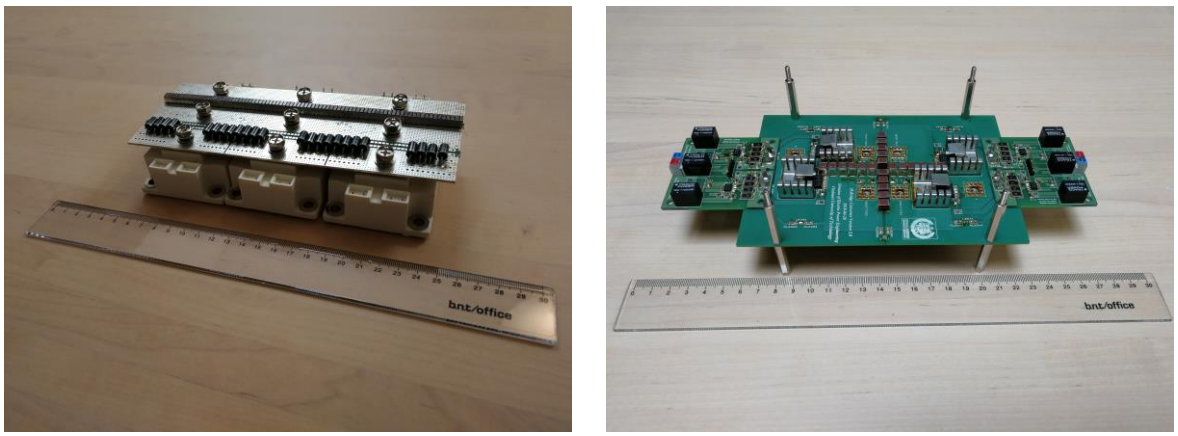

(a) Three-phase inverter (b) H-bridge inverter

Figure 6-24 Protype of the power electronic inverters.

6.1.5.3 Rotating Transformer and Rectifier

Protype of the rotating transformer is shown in Figure 6-25. Protype of the rectifier is shown in Figure 6-26. The primary and secondary pot cores are identical. The inner side of the pot cores are covered with Kapton tape which provides galvanic isolation and dissipates heat from the copper winding. The windings are then molded with epoxy so that the windings, pot cores are together with aluminum case. The diodes of the rectifier are fixed to the back of the

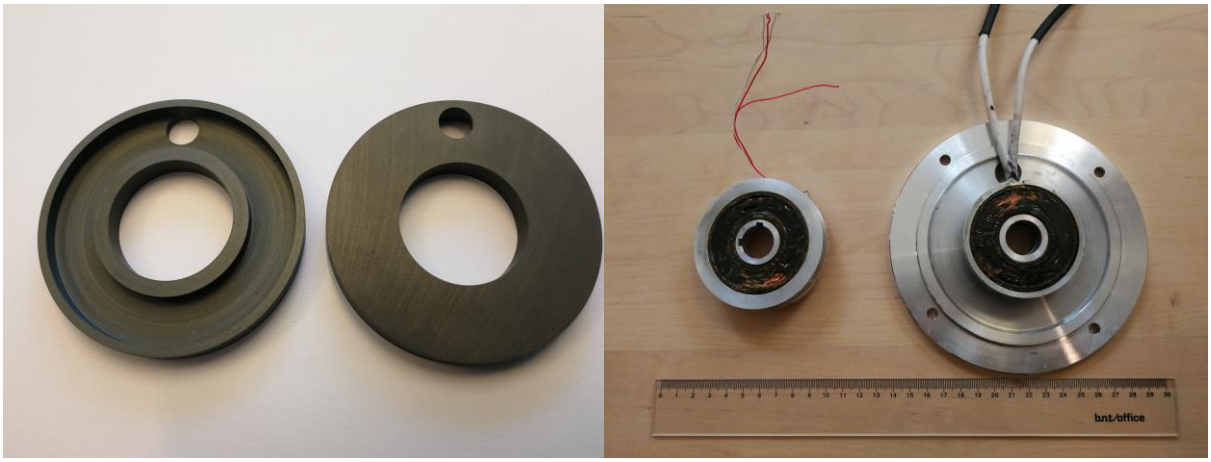

(a) Ferrite pot cores (b) Rotating transformer

Figure 6-25 Protype of the rotating transformer.

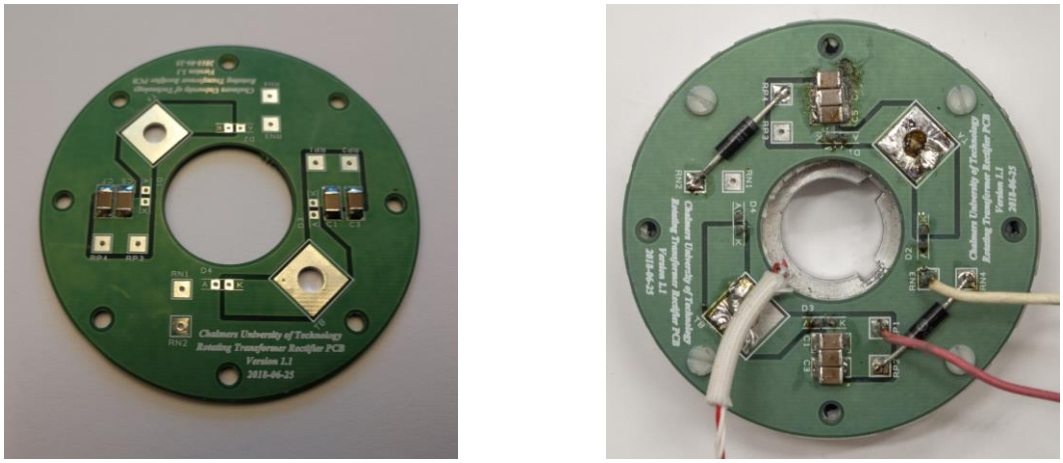

(a) Rectifier PCB (b) Rectifier soldered on the aluminum case

Figure 6-26 Protype of the rectifier.

aluminum case. The legs of the diodes are bended 90° and connected to the rectifier PCB. The rectifier PCB is attached to the back of the aluminum case.

The inductances of the transformer are dependent on the airgap and the relationship is shown in Figure 6-27. The coupling factor is defined as

$$k = \frac{M}{\sqrt{L_{11} \cdot L_{22}}} \tag{6-4}$$

The mutual inductances measured from both sides show some differences, and with a higher airgap, the difference becomes smaller. This is due to the fact that the relative position of both transformer sides is difficult to be kept exactly the same in different measurements. The total flux consists of mutual flux and leakage flux. For small airgaps, the mutual flux is the major part of the total flux. A minor change of relative position influences the mutual flux significantly. In contrast, for large airgaps, the mutual flux occupies a smaller portion of the total flux, which becomes not so sensitive to relative position change. Therefore, the

difference in the mutual inductance measured from both sides becomes small. In the verification, the mean values of the measurements from both sides are used as the inputs of the simulations.

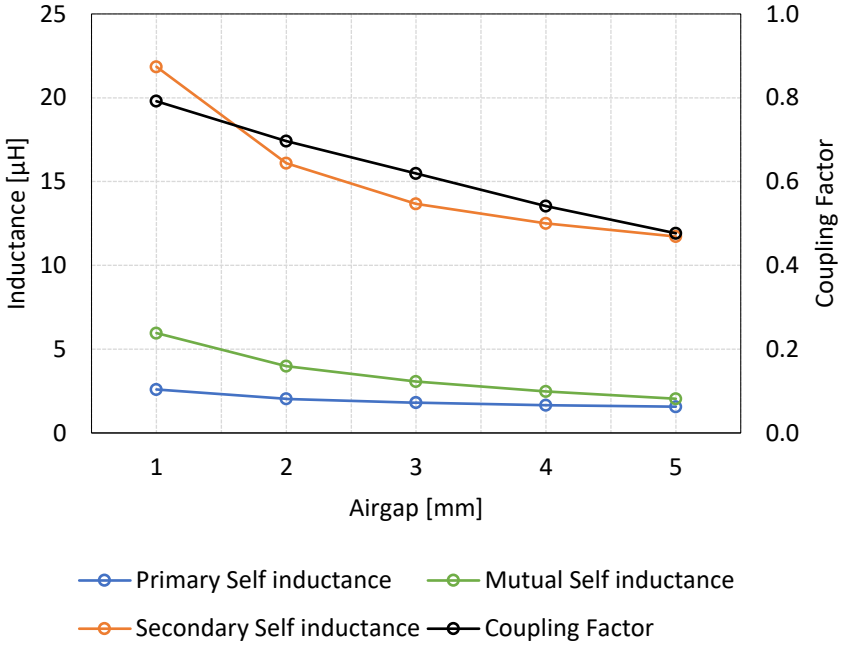

Figure 6-27 Inductances and coupling factor of the transformer with 1, 2, 3, 4 and 5 mm airgap.

6.1.5.4 Measurement, Signal Processing, Control and Experimental Setup

The connection and measurement points of the system are illustrated in Figure 6-28. A dc power source supplies power to a three-phase inverter and an H-Bridge inverter. The three-phase inverter delivers power to the three phases A, B and C in the stator, while the H-Bridge inverter delivers power to the rotating transformer for field excitation. The neutral point of the three phases are not connected. The machine is connected to a load machine through a torque sensor. An incremental encoder is installed on the shaft. In order to do field-oriented control of the machine, the three-phase currents are measured and the pulses from the incremental encoder are fed into a DSP. The DSP used in this study is TMS320F28379D from Texas Instrument. The three-phase voltages are measured with an oscilloscope, not for control but for power calculation. The dc-link voltage is measured for calculation of PWM duty cycles. The dc-link current going to the H-bridge inverter is measured for field current estimation. In addition, PT100 temperature sensors are inserted into the winding to monitor the winding temperature.

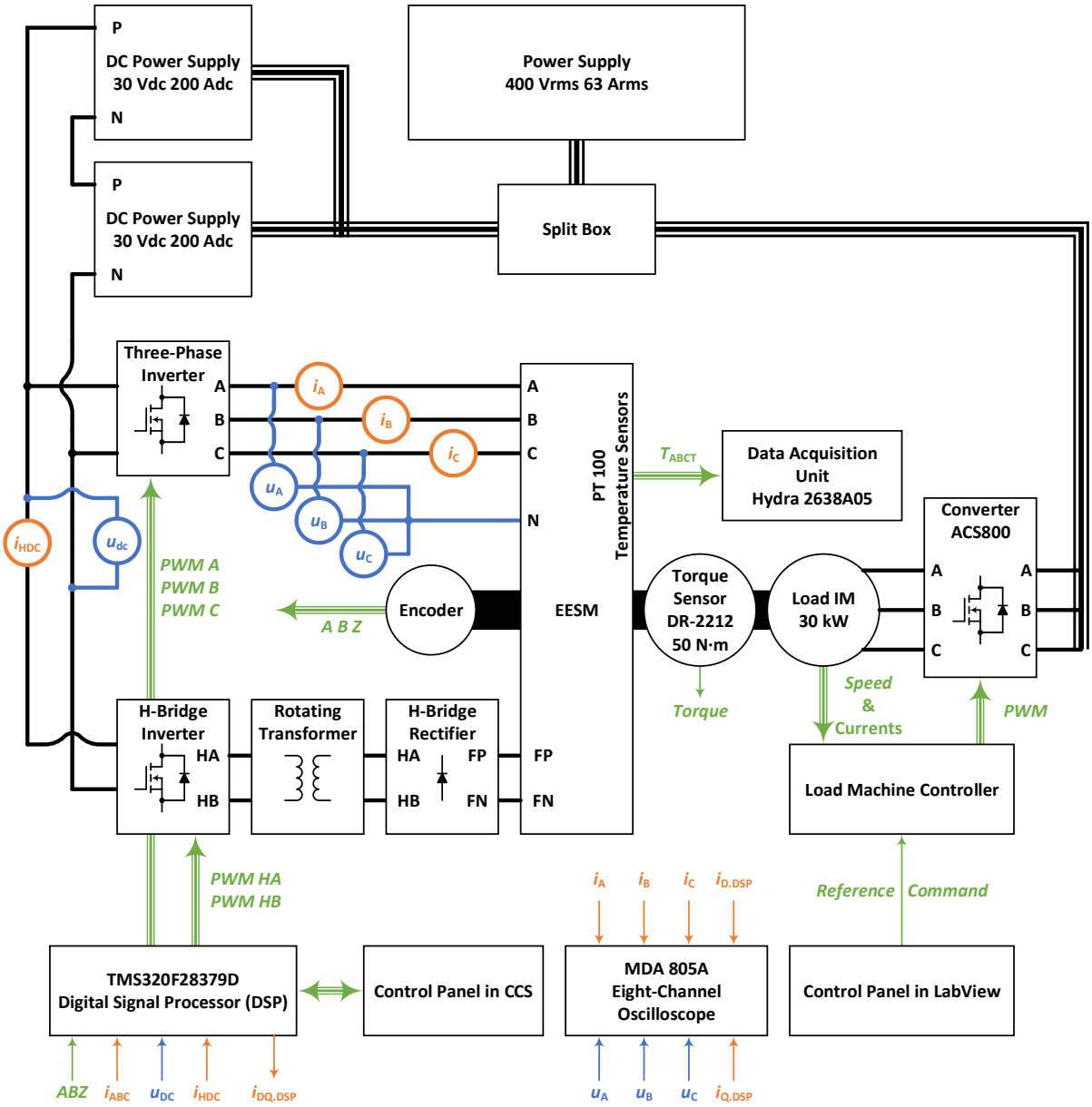

Figure 6-28 System connection.

The photos of the experimental setup is shown in Figure 6-29. Subplot (a) shows the power electronics and the measurements as well as the machine which have been described in the previous sections. Subplot (b) shows the control and monitor station. The details of the signal processing circuits and the control programme are illustrated as follows.

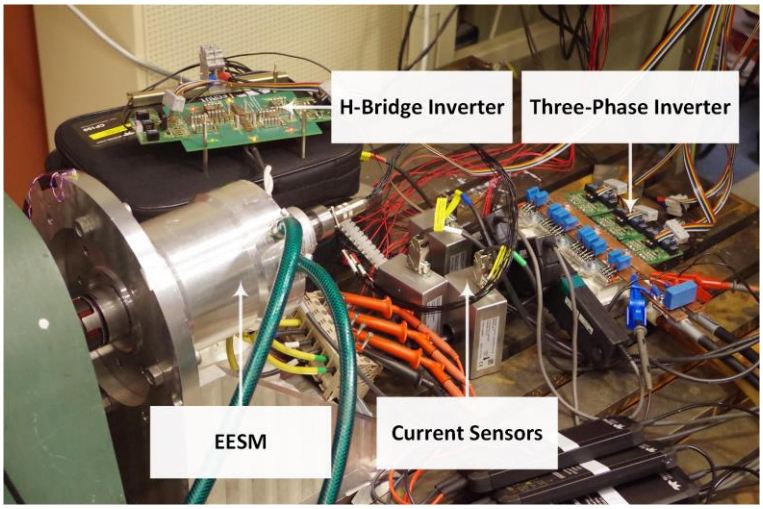

(a) Test bench

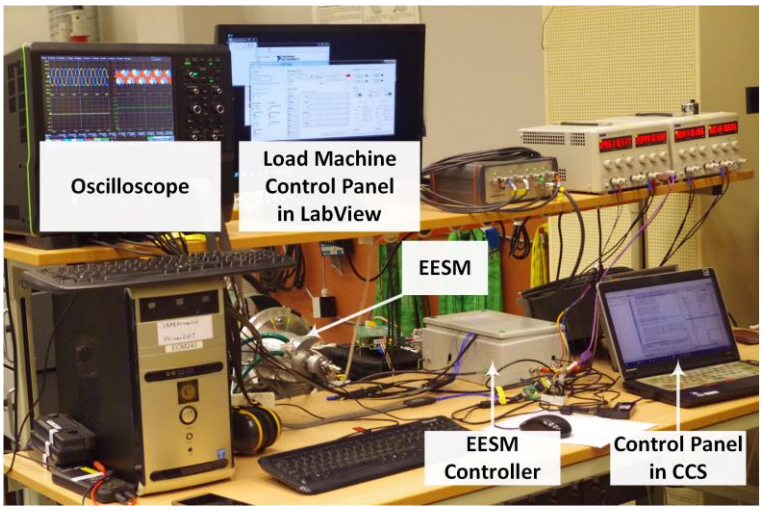

(b) Control station

Figure 6-29 Experimental setup.

Each current sensor provides a voltage signal between ±10 V. Through a processing circuit shown in Figure 6-30, the signal is scaled to between 0 and 3 V and fed into the ADC of DSP. OPAMP 1 is a voltage follower which provides high input impedance and low output impedance. This avoids the current sensor from being overloaded. Then, a resistive voltage divider scales the signal from ±10 V to ±1.5 V. A capacitor of 100 nF is added here to filter out noise. Thereafter, OPAMP 2 is used to shift the voltage signal from ±1.5 V to between 0 and -3 V, by adding 1.5 V from a voltage reference chip. In the end, the signal is inverted by OPAMP 3 to between 0 and 3 V.

The voltage measurement utilizes a Hall sensor, as shown in Figure 6-31. A resistor is added in parallel with the voltage to measure and a current goes through the resistor into the Hall sensor which is proportional to the voltage level. Since Hall effect is utilized, the output is galvanically isolated from the power circuit. The Hall sensor outputs a secondary side current which is proportional to the primary side current. And by adding a proper value of resistance at the output of the Hall sensor, the voltage across the resistor becomes within the range of between 0 and 3 V and is proportional to the voltage on the primary side. This voltage then can be fed into the ADC of the DSP.

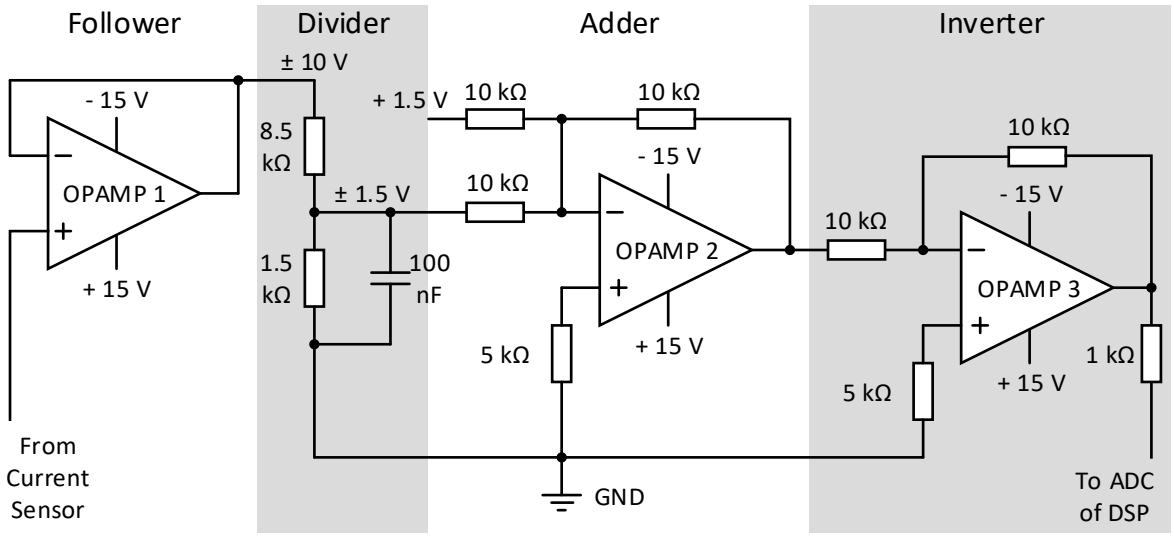

Figure 6-30 Current measurement signal processing circuit of each channel (totally four channels).

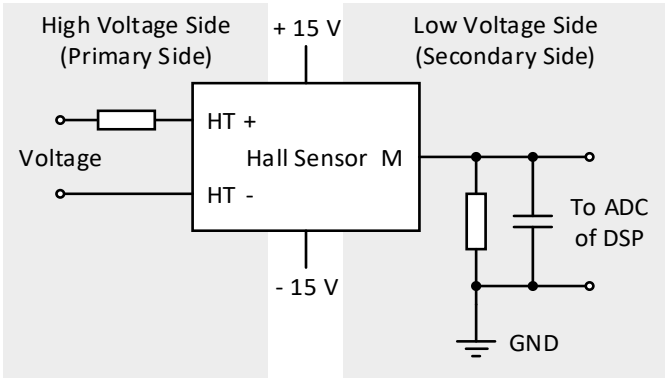

Figure 6-31 Voltage measurement circuit.

The encoder provides TTL signal, which needs to be scaled into the range between 0 and 3.3 V before going to the EQEP of the DSP. The signal processing circuit is as shown in Figure 6-32. Firstly, the pulses in pairs are fed into a differential line receiver which compares the positive and negative signals and outputs differential mode. This is used to reject common mode noise. Then a transceiver scales the voltage level from 5 V to 3.3 V. Thereafter, the signal is safe to go to the EQEP module of the DSP.

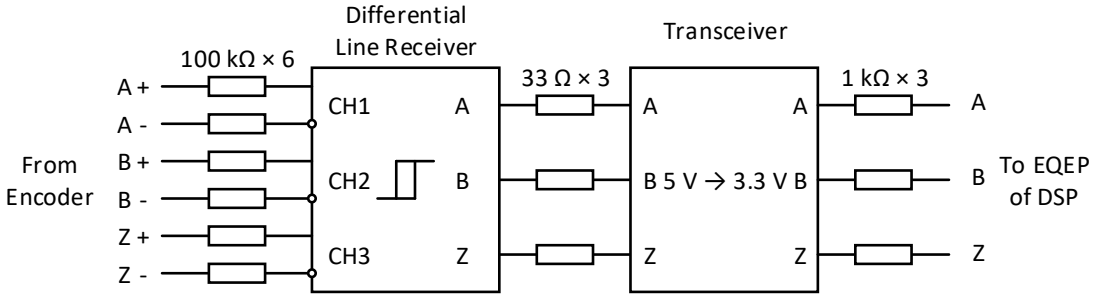

Figure 6-32 Encoder signal processing circuit.

The current, voltage and encoder signal processing circuits are implemented on a signal processing PCB. The PCB design of the circuit can be found in Appendix E. A photo was taken as shown in Figure 6-33. The current measurement signals come to the PCB through the BNC connectors on the northwest corner. The power supply, encoder signals and voltage signals are placed from north to south along the right side. A TMS320F28379D launchpad was stacked on the top on the southwest. The PWM output pins are placed along the southwest edges close to the launchpad. The controller including the signal PCB and the launchpad is sealed in an iron box to avoid electromagnetic interference (EMI).

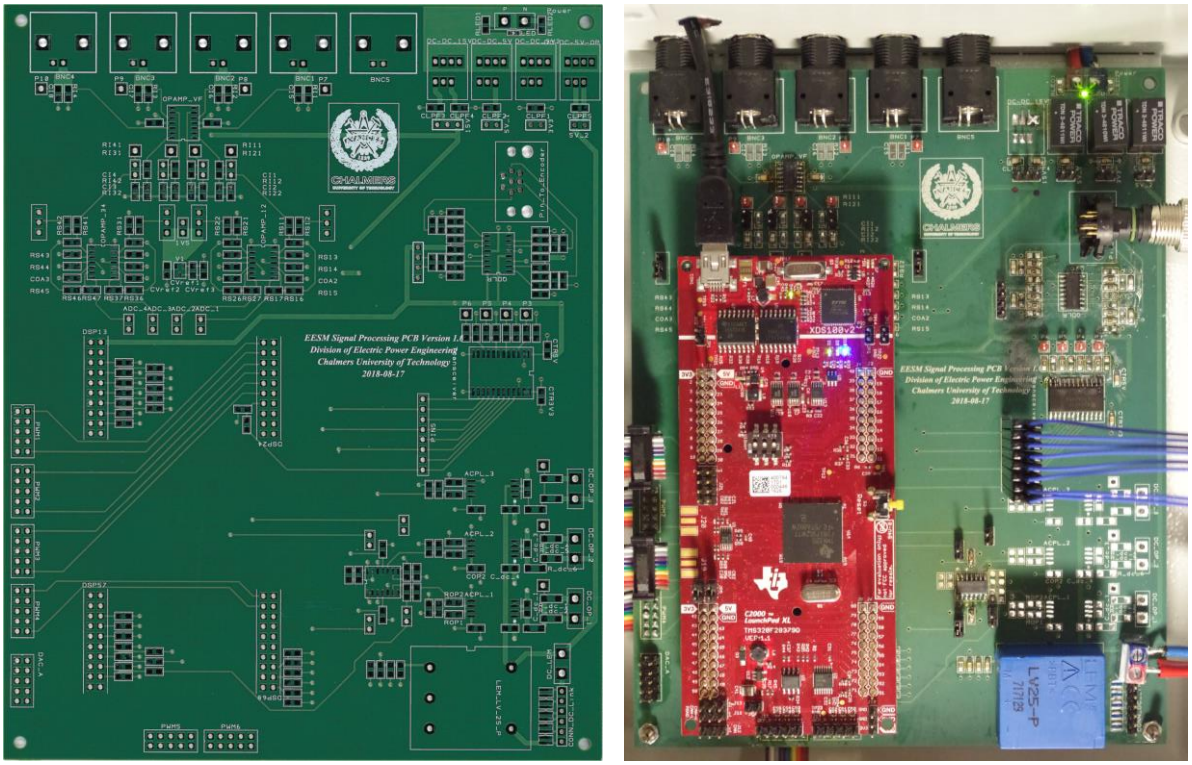

(a) Signal processing PCB (b) Controller hardware sealed in a steel box

Figure 6-33 Controller.

Figure 6-34 shows the sequence of the DSP programme. Initialization is performed in the beginning, which includes the initializations of the clock and the GPIO ports, as well as the configuration of periodical interruptions. The interruption period is set as the same as the period of switching cycle. Then the periodical interruptions start. In each interruption, sampling, processing of the sampling, control calculation, PWM calculation and PWM as well as DAC update are performed in a sequence.

The time allocation of each periodical interruption is illustrated in a schematic shown in Figure 6-35. Over-sampling is a technique that takes four samples of each signal successively, and then takes the average of the medium two values as the measured value for processing. This technique is applied to reject EMI and get stable measurement values. Over sampling is performed before each interruption. Thereafter, the values in EQEP registers are processed to calculate the rotor speed and position. This is to make sure that the rotor position is taken at the beginning of the interruption so that the rotor angle at the end of the interruption can be compensated as accurate as possible by

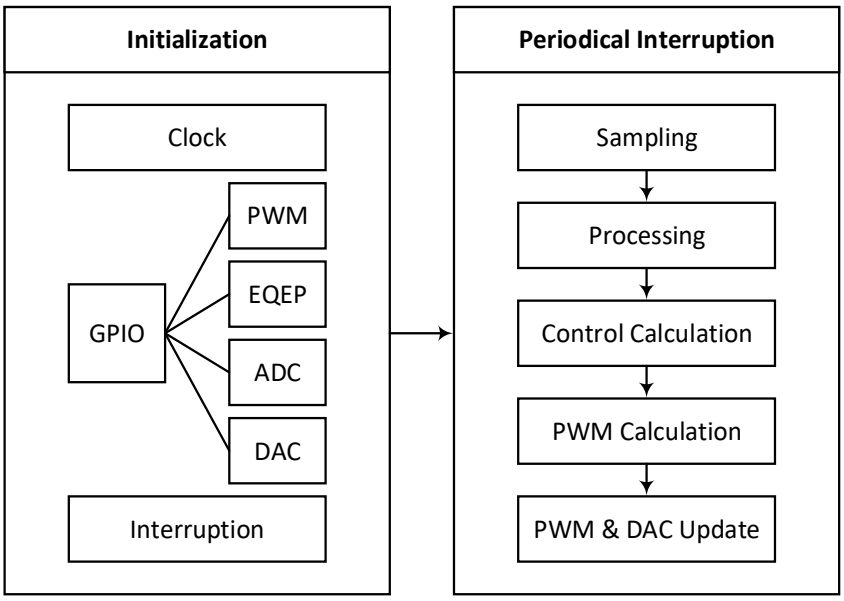

Figure 6-34 Sequence in controller.

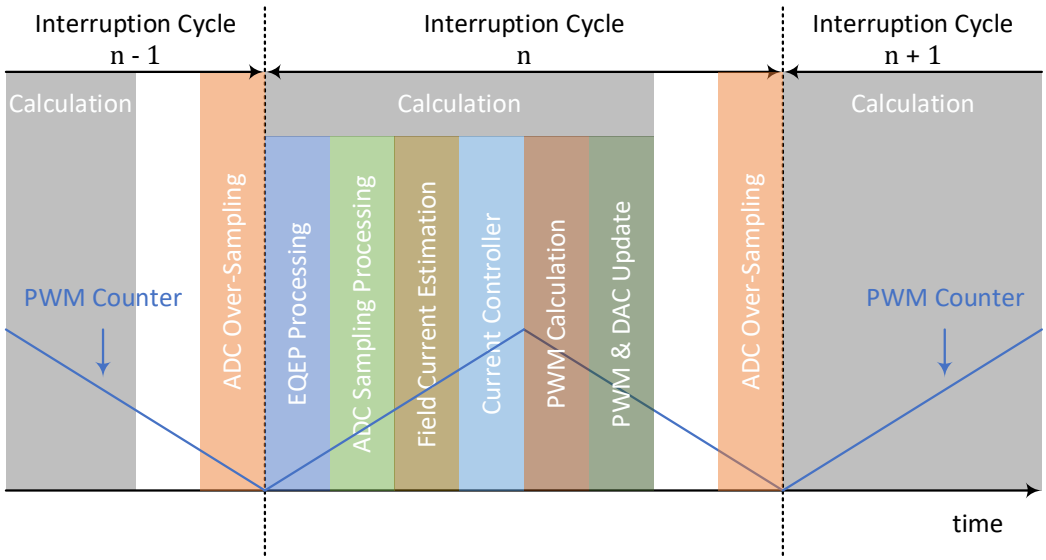

Figure 6-35 Process during interruption.

$$\theta_{\mathrm{r.2}} = \theta_{\mathrm{r.1}} + \omega_{\mathrm{r.1}} \cdot T_{\mathrm{sw}} \tag{6-5}$$

where $\theta_{\mathrm{r.1}}$ and $\omega_{\mathrm{r.1}}$ are the angle and speed measured by the EQEP module at the beginning of the interruption respectively, T_{sw} is the period of switching cycle and $\theta_{\mathrm{r.2}}$ is the estimated angle at the end of the interruption. Thereafter, ADC sampling is processed and field current is estimated. In current control, $\theta_{\mathrm{r.1}}$ is the one used for abc-dq transformation, whereas $\theta_{\mathrm{r.2}}$ is the one used for dq-abc transformation. In the end, PWM duty cycles are calculated and the outputs are updated.

6.1.6 Experimental Verification of Machine Design

The flux linkages ψ_{d} and ψ_{q} excited by i_{d}, i_{q} and i_{f} are compared in Figure 6-36. The measurement shows slightly higher values than FEM. And, the curve is not saturated until 500

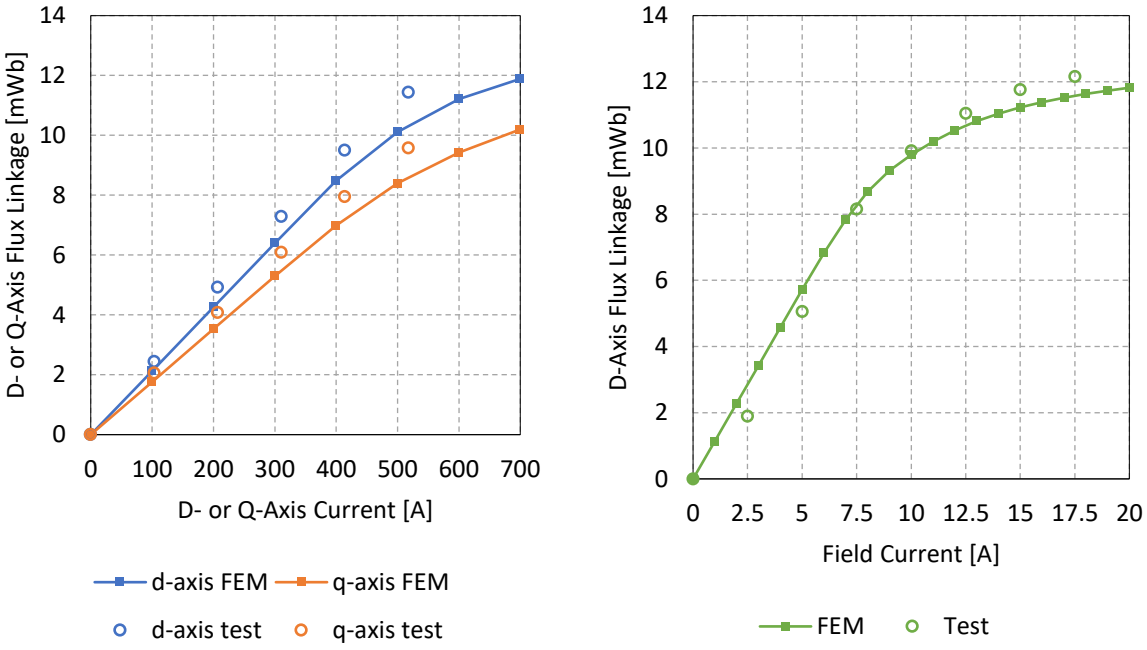

(a) Stator current excitation in d- and q-axis

(b) Field current excitation

Figure 6-36 Excitation.

A in measurement whereas saturation appears at around 400 A in FEM. However, the ratio between d- and q-axis excitations are approximately the same. These are probably due to the under-estimation of the stacking factor in FEM calculation, as well as the margin of the BH curve introduced in the datasheet of the lamination steel. Another interesting observation is that to reach a d-axis flux linkage level of 10 mT, the MMF per pole pair needed by the field current

$$MMF_{\mathrm{f}} = I_{\mathrm{f}} \cdot N_{\mathrm{f}} = 10 \times 150\ [\mathrm{A}] = 1500\ [\mathrm{A}] \tag{6-6}$$

is much lower than the MMF per pole pair needed by the stator current

$$MMF_{\mathrm{s}} = 1.5 \cdot I_{\mathrm{s}} \cdot N_{\mathrm{s}} = 1.5 \times 500 \times 6\ [\mathrm{A}] = 4500\ [\mathrm{A}] \tag{6-7}$$

This indicates that field current excites the d-axis path more efficiently with the same amount of MMF.

The torque production capability by the interaction of q-axis current and field current is verified experimentally. The field current ranges from 5 A to 15 A in a step of 5 A, while the q-axis current ranges from 100 A to 500 A in a step of 100 A. The measurements are performed at a speed of 750 rpm, due to the fact that a higher speed consumes more power than the power source equipped in the laboratory. In addition, the application of this motor is for the start-up of a mild hybrid vehicle in which a sufficient output torque is more important than output power.

The time sequences of field current at 15 A and q-axis current at 500 A are presented in Figure 6-37 (a) and (b). The machine is firstly excited by the field current and then the q-axis current

is injected to produce torque. This sequence is introduced because the controller is designed by assuming the machine is linear whereas the machine is actually non-linear in both d- and q-axis flux path as shown in Figure 6-36. This sequence makes sure that the controller only

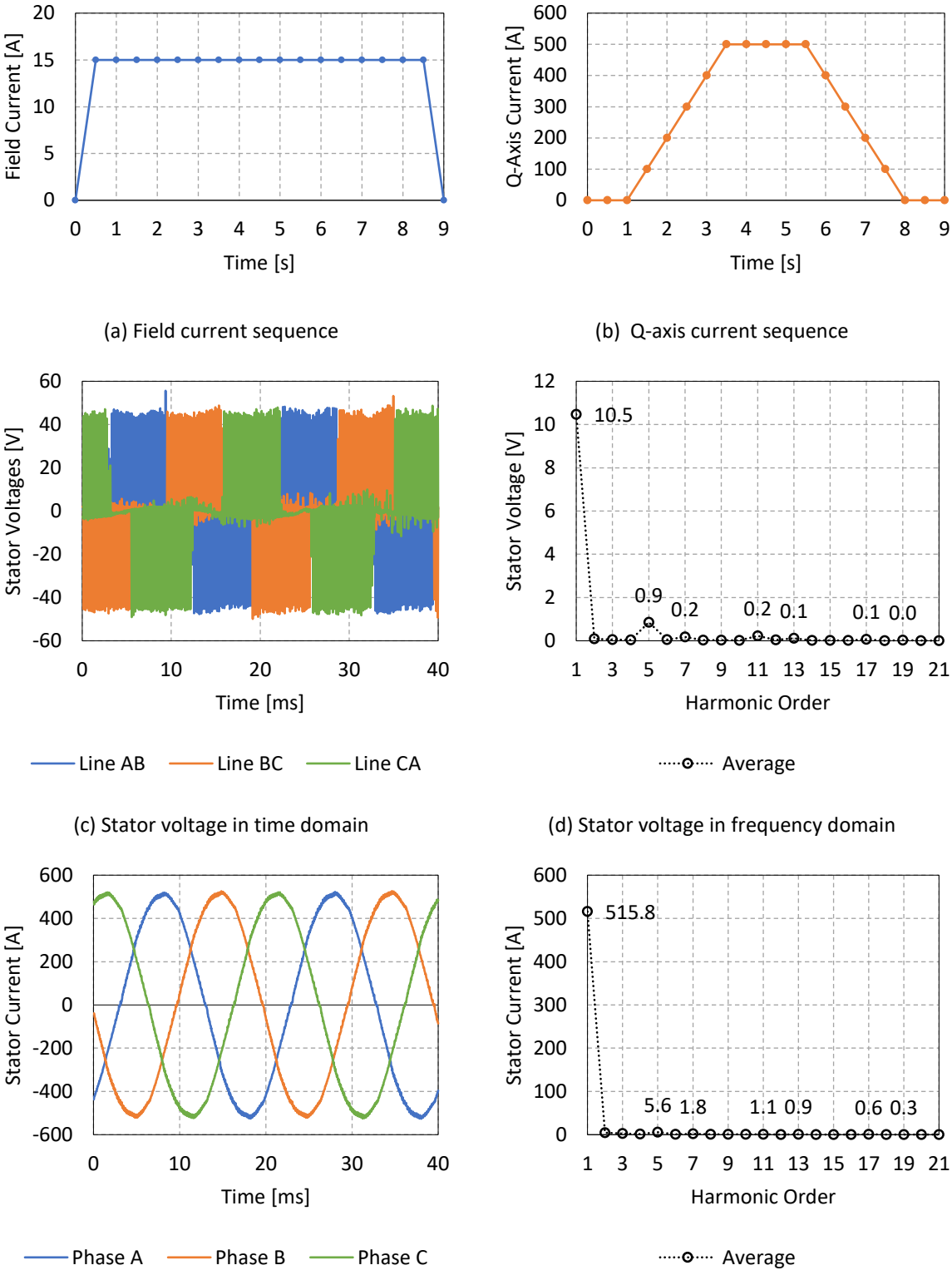

Figure 6-37 Verification of torque production (example of $I_{\mathrm{d}} = 0$ [A] , $I_{\mathrm{q}} = 500$ [A] , $I_{\mathrm{f}} = 15$ [A]).

needs to take care of one non-linear quantity per time to avoid any possible failure caused by non-linearity.

The time-domain waveforms and the frequency-domain harmonic distributions of voltages and currents are presented in (c) – (f). The 5th voltage harmonic is the major component in the distribution. This is due to the 5th EMF harmonic as shown in Figure 6-2. The current harmonics are much lower and the waveform in time-domain is quire sinusoidal.

The torque measurements from torque transducer are presented in Figure 6-38 (a). The measurements fit the FEM results quite well. The measurements are slightly higher due to the slightly higher flux linkages shown in Figure 6-36. The efficiency and displacement power factor are presented in Figure 6-38 (b) and (c). The displacement power factor (DPF) is defined as the power factor considering only the fundamental components of voltage and current. As can be noticed, the efficiency and DPF fit the FEM calculations quite well.

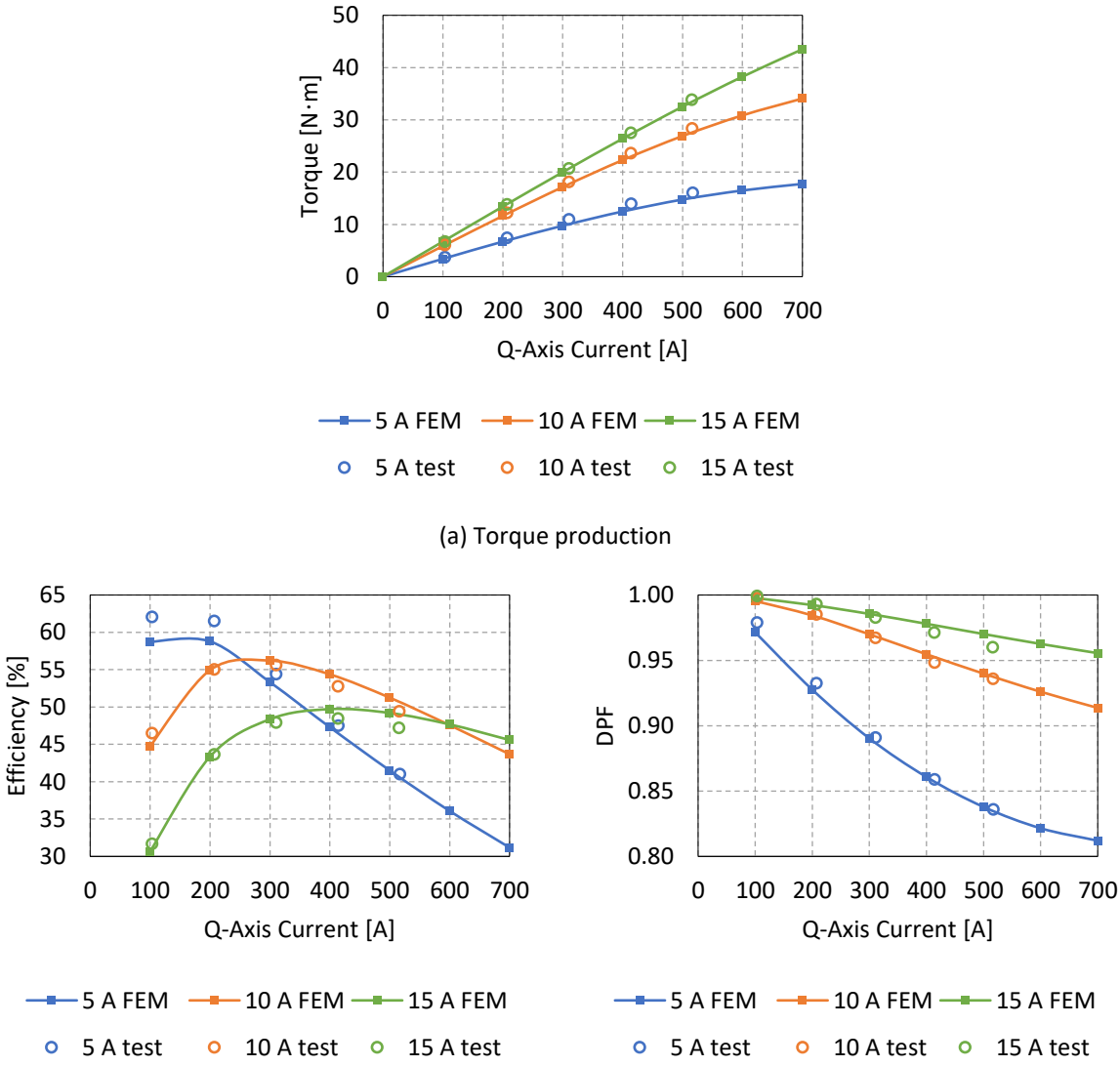

(a) Torque production

(b) Efficiency

(c) Displacement power factor

Figure 6-38 Verification of torque production at 750 rpm.

6.1.7 Experimental Verification of Excitation System

With the protype manufactured, the modeling of the brushless excitation system is verified experimentally. The verifications include variations of four parameters, the dc-link voltage, the airgap, the rectifier output capacitance and the field winding resistance. The variations are introduced to make sure that model is commonly valid for this topology instead of being only valid for a special set of parameters. The verification towards field winding resistance is done by conducting experiments at different temperatures.

6.1.7.1 Transformer Airgap

The field current with respect to duty cycles in experiments and simulations with different airgaps are compared in Figure 6-39. The abbreviation “Sim” indicates “Simulation” while the abbreviation “Exp” indicates “Experiment”. The tests are carried out with 188 nF rectifier output capacitance, 60 V dc-link voltage and approximately 30°C winding temperature. The airgap varies from 1 to 5 mm with a step size of 1 mm. As can be noticed, the simulated results in general fit the experimental results, especially in the 3, 4 and 5 mm airgap cases. However, in the 1 and 2 mm cases, the measured field currents are slightly higher than the simulated ones, probably due to the measurement of mutual inductances. There are probably small differences in the coil alignment between the inductance measurement test and the power transferring test as explained in Section 6.1.5.3. As will be shown later in the parameter sensitivity study section, this difference may be due to a measurement error of mutual inductance of around 1.25%.

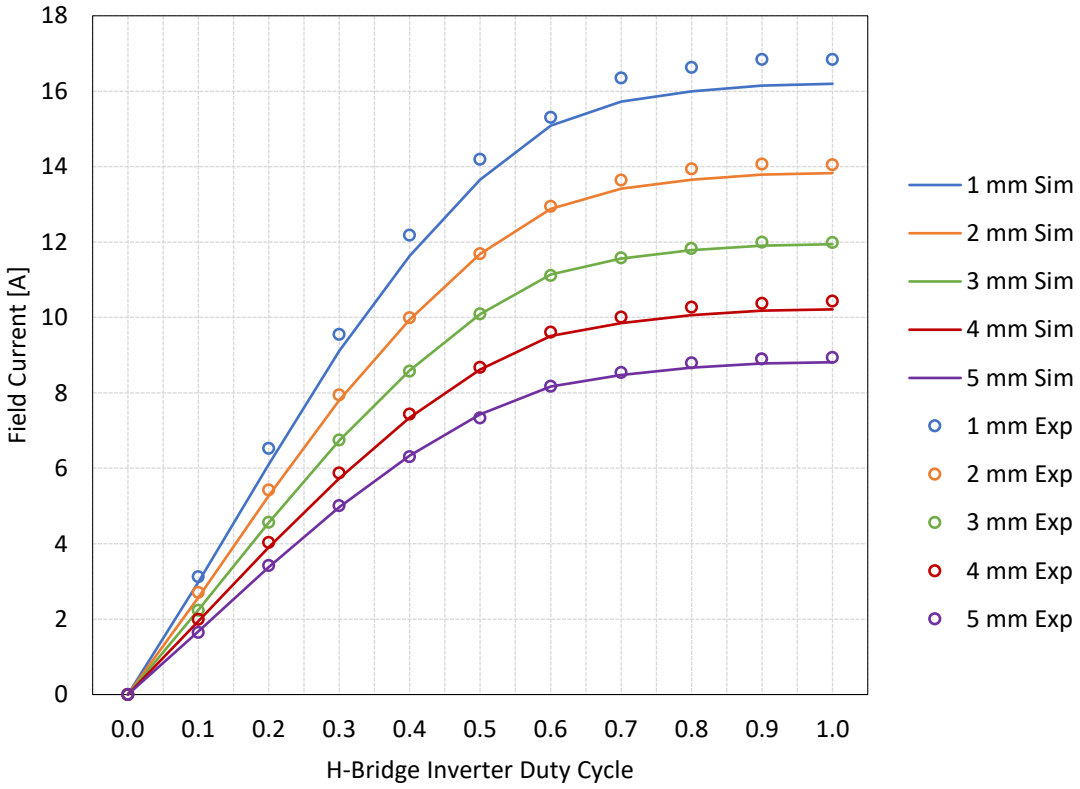

Figure 6-39 Field current against duty cycle with 1, 2, 3, 4 and 5 mm airgap, $C_{\mathrm{f}} = 188$ nF, $U_{\mathrm{dc}} = 60$ V, $T_{\mathrm{f}} = 30$°C.

6.1.7.2 DC-Link Voltage

The field current and dc-link current with respect to duty cycle in experiments and simulations with different dc-link voltages are compared in Figure 6-40 and Figure 6-41 respectively. The tests are carried out with 188 nF rectifier output capacitance, 1 mm airgap and around 30℃ winding temperature. The dc-link voltage varies from 36 V to 60 V with a step size of 12 V. The simulated results in general fit the experimental results. The field current and the dc-link current are proportional to the dc-link voltage for all duty cycles. Apart from that, the dc-link current also shows a different profile than the field current, and the relationship between the two can be described by the power balance of the system. In steady state, the output power equals the input power times the efficiency. Assuming an almost constant efficiency, the dc-link current is proportional to the square of the field current as shown in (2-96). This explains why the field current curves between duty cycle 0.0 and 0.5 in Figure 6-39 are almost linear whereas the dc-link current curves seem to be parabolas in Figure 6-41.

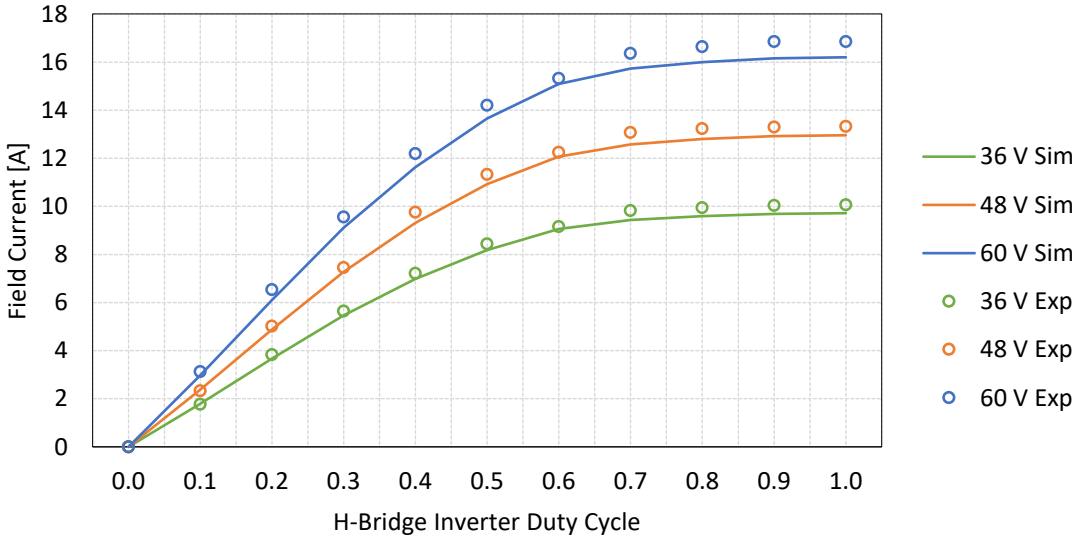

Figure 6-40 Field current against duty cycle with $U_{\mathrm{dc}} = 36, 48, 60$ V, 1 mm airgap, $C_{\mathrm{f}} = 188$ nF, $T_{\mathrm{f}} = 30$℃.

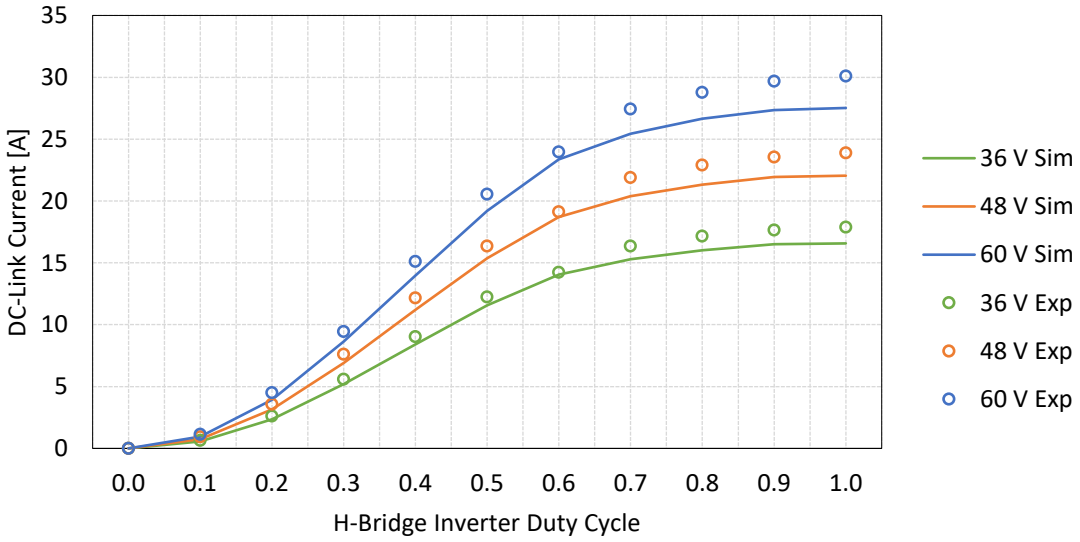

Figure 6-41 DC-link current against duty cycle with $U_{\mathrm{dc}} = 36, 48, 60$ V, 1 mm airgap, $C_{\mathrm{f}} = 188$ nF, $T_{\mathrm{f}} = 30$℃.

6.1.7.3 Field Winding Capacitance

The waveforms given by the circuit with different rectifier output capacitance from experiments and simulations are compared in Figure 6-42. Plots (a) – (e) are with $C_{\mathrm{f}} = 47$ nF

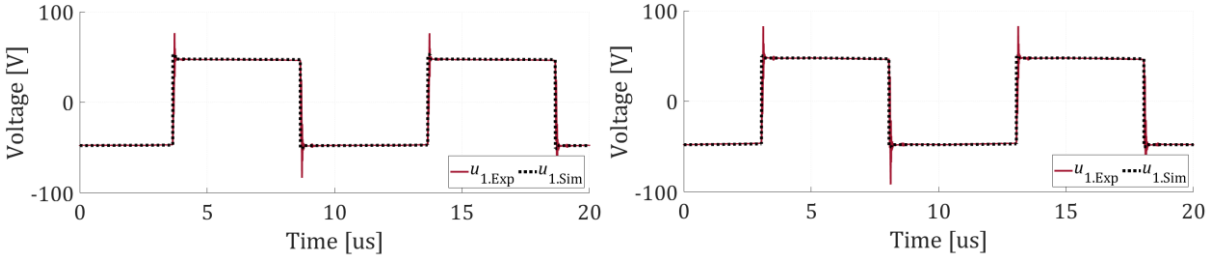

(a) Primary side voltage ($C_{\mathrm{f}} = 47$ nF)

(f) Primary side voltage ($C_{\mathrm{f}} = 188$ nF)

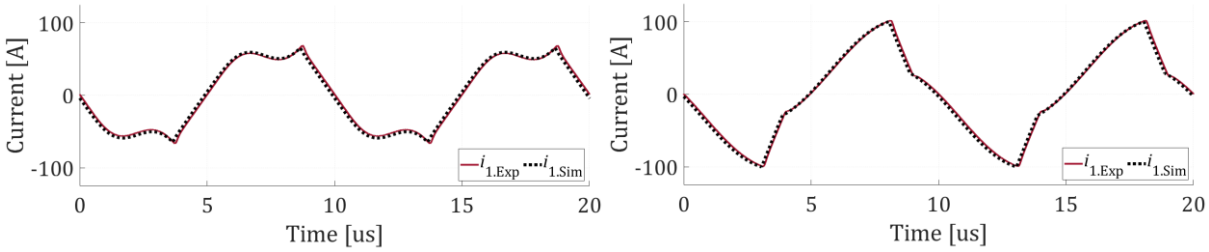

(b) Primary side current ($C_{\mathrm{f}} = 47$ nF)

(g) Primary side current ($C_{\mathrm{f}} = 188$ nF)

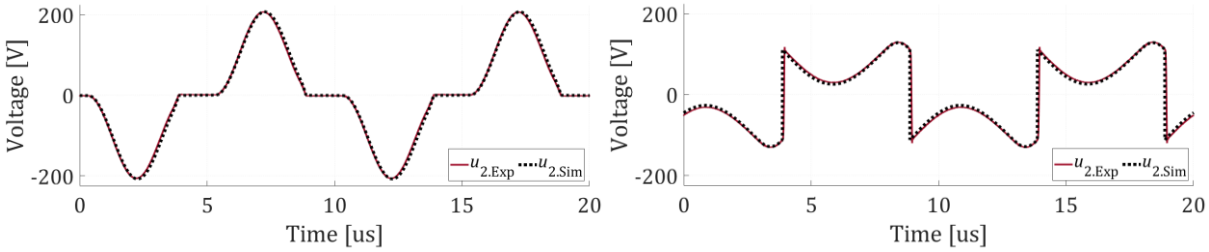

(c) Secondary side voltage ($C_{\mathrm{f}} = 47$ nF)

(h) Secondary side voltage ($C_{\mathrm{f}} = 188$ nF)

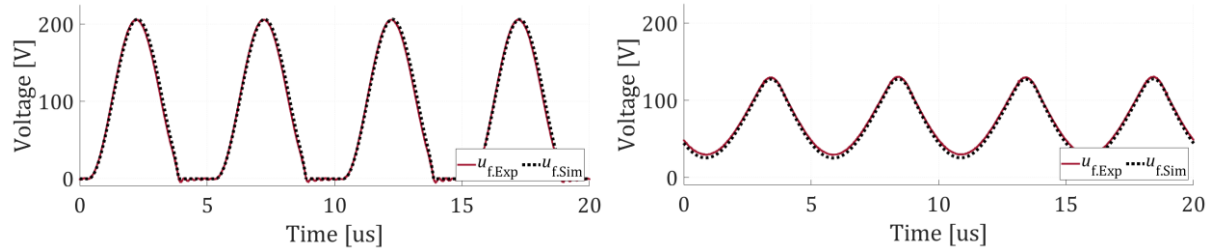

(d) Field voltage ($C_{\mathrm{f}} = 47$ nF)

(i) Field voltage ($C_{\mathrm{f}} = 188$ nF)

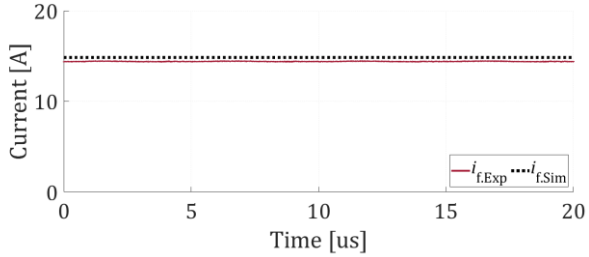

(e) Field current ($C_{\mathrm{f}} = 47$ nF)

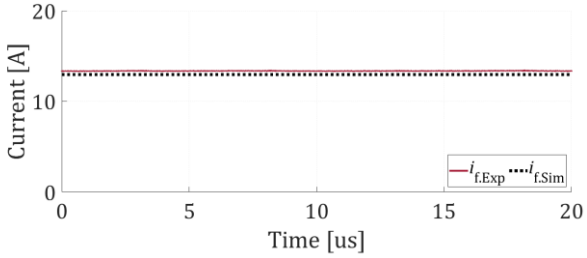

(j) Field current ($C_{\mathrm{f}} = 188$ nF)

Figure 6-42 Voltage and current waveforms with 1 mm airgap, $U_{\mathrm{dc}} = 48$ V, $T_{\mathrm{f}} = 30$°C, 0.99 duty cycle.

whereas Plots (f) – (j) are with $C_{\mathrm{f}} = 188\ \mathrm{nF}$. The tests are carried out with 48 V dc-link voltage, 1 mm airgap and around 30℃ winding temperature. The start time instants of the waveforms are adjusted so that the primary side voltage waveforms are aligned in phase. As can be noticed, in all the subplots from (a) to (j), the simulated waveforms fit the experimental ones quite well.

In (d), with 47 nF capacitor, the field voltage drops to and stays at zero for some time interval. This indicates the commutation mode operation, when the four diodes conduct simultaneously, as described in Section 2.3.2.4. In comparison, in (i), a higher field winding capacitance of 188 nF keeps the field voltage always above zero. This is due to the larger capacitance which keeps the voltage relatively stable. In this case, there is no commutation time interval. Consequently, the secondary side voltage shown in (c) stays at zero for a time interval before changing the polarity, whereas in (h), the secondary side voltage changes polarity immediately.

Apart from that, in both (a) and (f), switching voltage spikes at the primary side can be observed in experiments, whereas the model does not show any spike in simulations. This is due to the fact that the model simplifies the MOSFET characteristics and does not describe the parasitic inductance on the PCB. Hence this model is suitable to analyze the system level performance instead of details during switching transients.

At the output of the excitation system, two quantities are of interest, the maximum field current and the maximum field voltage peak. The field voltage peak is the peak value in the field winding voltage waveform. For instance, the field voltage peak is 209 V in the 47 nF case shown in Figure 6-42 (d), and 132 V in the 181 nF case shown in Figure 6-42 (i). In general, a high field current with a low voltage peak is preferable, which means a high capability of power delivery and a low stress applied across the rectifier diodes. The field voltage peak and the field current are compared in Figure 6-43. The measurements and simulations are performed with 48 V dc-link voltage, 1 mm airgap, around 30℃ winding temperature and at 0.99 duty cycle. The maximum field current as well as the maximum field voltage peak appear at the maximum duty cycle, and this is why the case at 0.99 duty cycle is presented. The

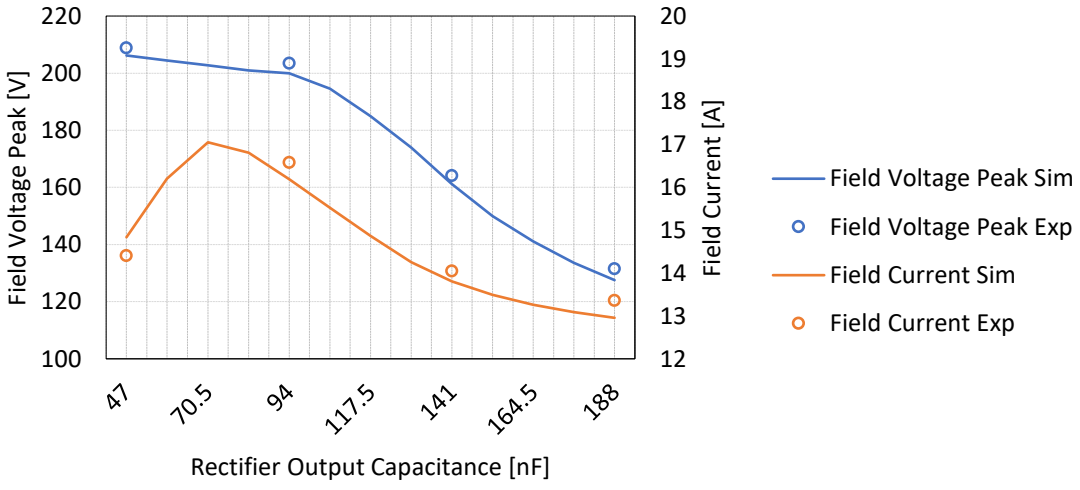

Figure 6-43 Field voltage peak and field current with $C_{\mathrm{f}} = 47, 96, 141, 188\ \mathrm{nF}$, 1 mm airgap, $U_{\mathrm{dc}} = 48\ \mathrm{V}$, $T_{\mathrm{f}} = 30℃$, 0.99 duty cycle.

capacitance varies from 47 nF to 188 nF with 47 nF as the step size. As can be noticed, the simulated results generally fit the experimental results. By adding capacitance, the field voltage peak decreases, whereas the field current increases in the beginning but decreases as more capacitance is added. Investigations show that this non-monotonous profile is due to the resonance between the rectifier output capacitance and the transformer inductances when the rectifier diodes conduct. Considering the transformer parameters shown in Figure 6-27, to get a resonance frequency at around 100 kHz, 66.5 nF is needed which is close to where the maximum field current appears in the curve.

6.1.7.4 Field Winding Resistance

During EESM operation, the field winding will be heated up by the copper loss. The temperature increase will increase the resistance of the winding leading to further decrease in the field current, as shown in Figure 6-44. The measurements and simulations are done with 60 V dc-link voltage, 1 mm airgap and 188 nF rectifier output capacitance. The presented curves are with the field winding temperature from 40℃ to 100℃ with 20℃ as the step size. As can be noticed, the field current decreases linearly with respect to the temperature increase both in simulation and experiment. The mismatch between the simulated and experimental results is due to the limited accuracy of the measurement of mutual inductance. However, the shape of the curves and the gaps in between are consistent between the simulated and experimental results. These curves also indicate that an open-loop control of field current is very sensitive to temperature variations. As a solution, an observer needs to be developed to estimate the field current, so that the effects of the temperature variations can be compensated for.

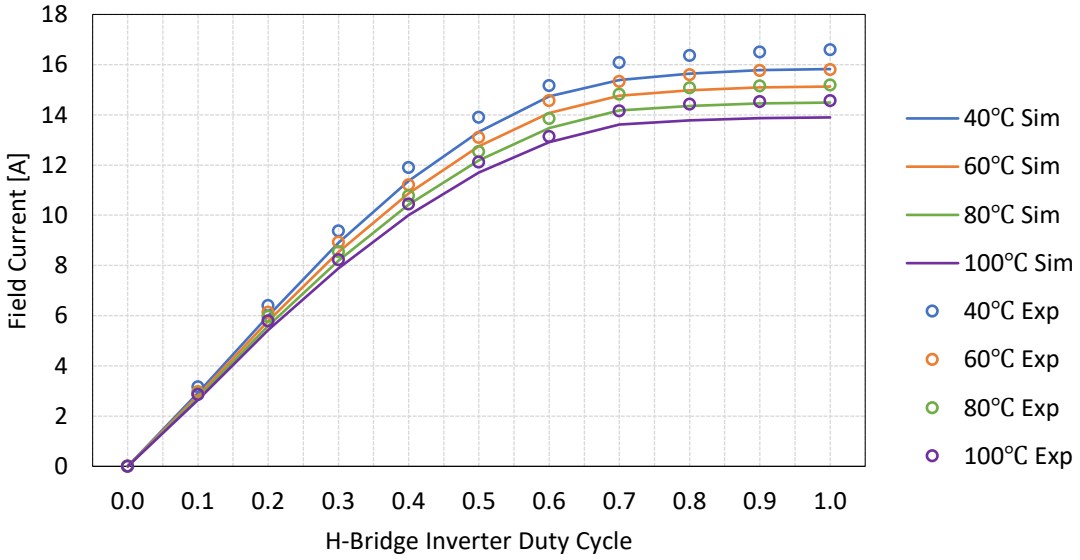

Figure 6-44 Field current against duty cycle with $T_{\mathrm{f}} = 40, 60, 80, 100℃$, 1 mm airgap, $C_{\mathrm{f}} = 188\ \mathrm{nF}$, $U_{\mathrm{dc}} = 60\ \mathrm{V}$.

6.1.7.5 System Analysis and Optimization with the Model

Further analysis of the excitation system can be done with the help of the model to derive design guidelines for the purpose of optimization. First, a parameter sensitivity study is performed to identify the most sensitive parameters, followed by a selection of rectifier

output capacitance and finally, loss analysis is performed to identify the component requiring specific attention.

6.1.7.6 Sensitivity Study of Parameters in the Excitation System

Parameter sensitivity study is essential in understanding the characteristics of the system. The sensitive parameters need to be detected, so that sufficient attention will be paid to these parameters during the design. In addition, if necessary, trade-offs can be made to guarantee the key parameters whereas to sacrifice the parameters with less importance.

Figure 6-45 shows the sensitivity study of the mutual inductance. Mutual inductance variations of ±2.5%, ±5.0% are introduced and the profile of field current against duty cycle is presented. As can be noticed, a variation of mutual inductance by +5.0% increases the field current by 15%, which means the mutual inductance is a key parameter which influences the field current effectively. In addition, the experimental results lay within the +0.0% case and the +2.5% case, and this indicates that probably a +1.25% measurement error of mutual inductance causes the error between the simulations and the experiments as observed earlier. Therefore, specific attention should be paid in estimation and measurement of mutual inductance.

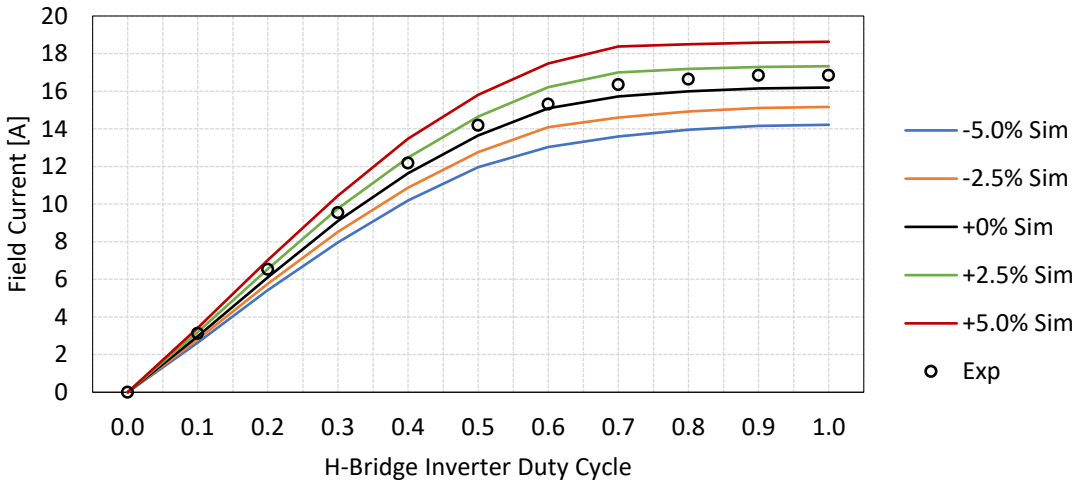

Figure 6-45 Field current against duty cycle with ±2.5%, ±5.0% mutual inductance variations, $T_{\mathrm{f}} = 30℃$, 1 mm airgap, $C_{\mathrm{f}} = 188\ \mathrm{nF}$, $U_{\mathrm{dc}} = 60\ \mathrm{V}$.

6.1.7.7 Selection of Rectifier Output Capacitance

The rectifier rotates together with the rotor and therefore components in the rectifier circuit should be as few as possible. However, capacitors are needed to guarantee the performance of the circuit, e.g. a high field current is needed to guarantee a certain power transfer capability, and a low field voltage peak is preferable to limit the stress of the diodes. The field current and the field voltage peak are therefore checked with a parametric sweep of rectifier output capacitance, as shown in Figure 6-46.

An optimal selection depends on the target. In case the peak voltage is not of concern, then the capacitance gives the highest field current is the optimal solution, which is 94 nF. However, in case the maximum field current is already higher than required, then attention mostly

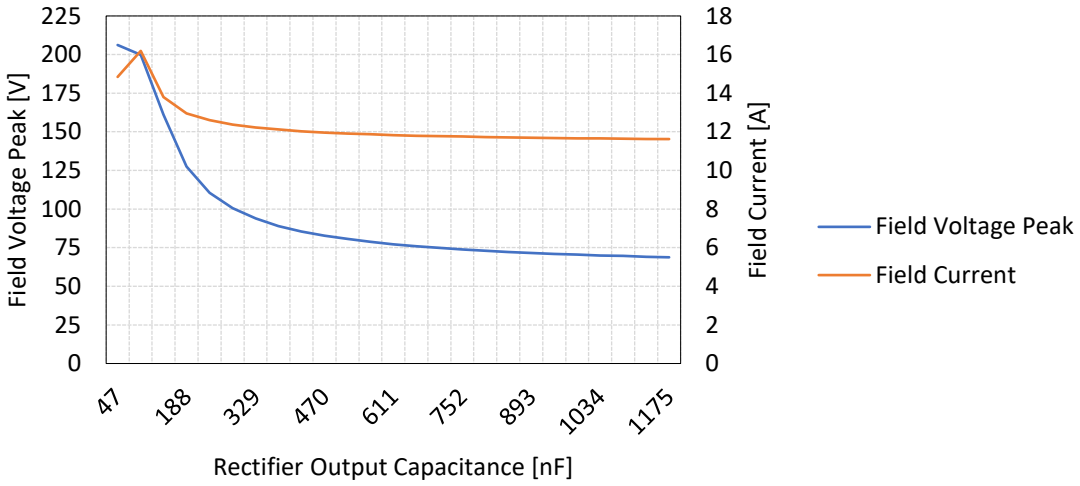

Figure 6-46 Simulated field peak voltage and field current with variations of rectifier output capacitance, $T_{\mathrm{f}} = 30°\mathrm{C}$, 1 mm airgap, $U_{\mathrm{dc}} = 48\ \mathrm{V}$.

needs to be paid to the voltage peak. As can be noticed, the voltage peak decreases fast in the beginning. The most significant drop of both quantities occurs at around 141 nF. If more capacitance than 329 nF is added, the voltage peak does not vary so much. A roughly good choice can be made with capacitance between 141 nF and 329 nF.

6.1.7.8 Loss Analysis

The fundamental frequency of the excitation system is 100 kHz, and due to the bandwidth limitation of the measurement devices, the loss of each component in the excitation system cannot be measured accurately. Fortunately, with the help of the model, it becomes possible to figure out roughly how the losses are distributed among different parts of the system. Thereafter, the component contributing to the major loss of the system can be detected, and the efficiency can be improved accordingly in the next design iteration.

Figure 6-47 shows the total efficiency from dc-link to field winding with $T_{\mathrm{f}} = 30°\mathrm{C}$, 1 mm airgap, $C_{\mathrm{f}} = 188\ \mathrm{nF}$. Admittedly, the simulated values are different from the experimental values, probably due to the limited accuracy of the measurements as well as the simplification

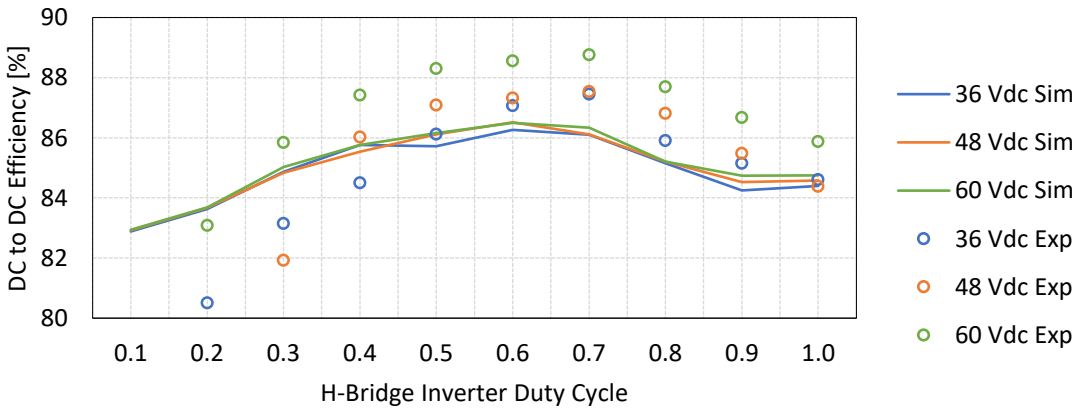

Figure 6-47 Efficiency from dc-link to field winding with $U_{\mathrm{dc}} = 36, 48, 60\ \mathrm{V}$, $T_{\mathrm{f}} = 30°\mathrm{C}$, 1 mm airgap, $C_{\mathrm{f}} = 188\ \mathrm{nF}$.

of the modeling, but the tendencies of the curves are consistent. The efficiency increases when the duty cycle increases from 0.1 to 0.6 or 0.7, and thereafter, the efficiency starts to decrease. This may be because the lowest harmonic contents appear at around 0.7 duty cycle, where a low percentage of reactive current is consumed.

The efficiency of each component is compared, and the transformer gives the lowest efficiency. Figure 6-48 shows the efficiency curve of the transformer, and the shape of the curve is similar to the overall efficiency curve as shown in Figure 6-47. It can therefore be concluded that it is mostly the efficiency of the transformer that decides the shape of the overall system efficiency curve.

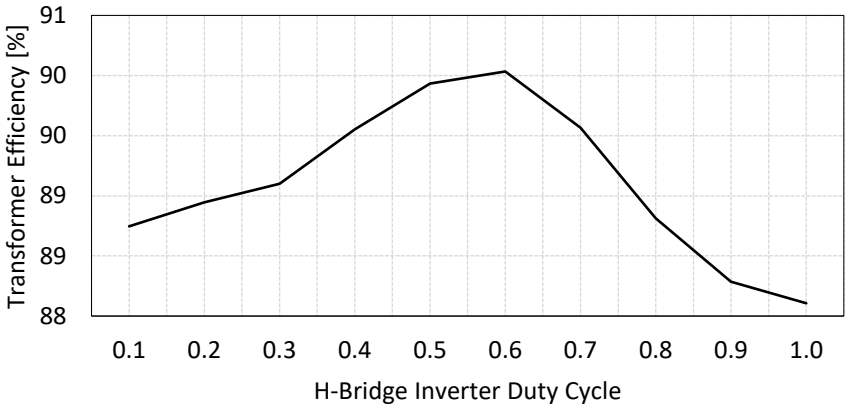

Figure 6-48 Efficiency of the transformer with $U_{\mathrm{dc}} = 60$ V, $T_{\mathrm{f}} = 30$°C, 1 mm airgap, $C_{\mathrm{f}} = 188$ nF. The $U_{\mathrm{dc}} = 36, 48$ V cases look very similar.

Figure 6-49 shows how each component contributes to the overall loss, from the model. The transformer loss is the major loss among all components. This indicates that in this excitation system, a better design of the transformer would probably improve the efficiency of the entire system significantly.

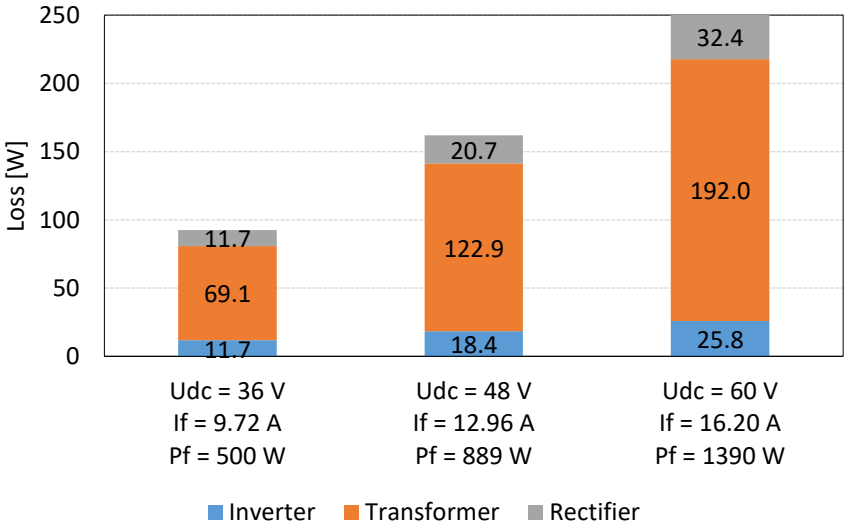

Figure 6-49 Distribution of the loss among components in the circuit with $U_{\mathrm{dc}} = 36, 48, 60$ V, $T_{\mathrm{f}} = 30$°C, 1 mm airgap, $C_{\mathrm{f}} = 188$ nF, 0.99 duty cycle.

6.1.8 Experimental Verification of Dynamic Control

6.1.8.1 Field Current Estimation

The same sequence of duty cycle as shown in Figure 6-17 is performed to verify the algorithm experimentally. The winding temperature starts at 30℃ in Figure 6-50 and at 100℃ in Figure 6-51 respectively. Due to a limited number of DAC channels of the DSP, only field current and field winding temperature estimation curves are extracted. Similarly, as in the simulation, the initial temperature estimation is set at 40℃ and the algorithm starts after the algorithm is activated at 0.5 s. The temperature is measured by two PT100 sensors and is also calculated roughly by using the ratio between the field voltage and field current.

The estimated field current and the real field current are compared in (a) and the zoomed-in curves are shown in (c)-(f). The estimation generally follows the real current quite well. In the 100℃ case, an overshoot of field current estimation occurs at 0.5 s in (a), due to the huge gap between the initial temperature assumption and real temperature. The current estimation error is then eliminated as the temperature estimation tracks the real one as shown in (b).

As can also be noticed that, the estimation error is higher at 0.5 duty cycle than at 1.0 duty cycle. This can be explained by Figure 6-41. At a lower duty cycle, the differences between the curves are smaller. Since the algorithm utilizes the difference between dc-link currents at

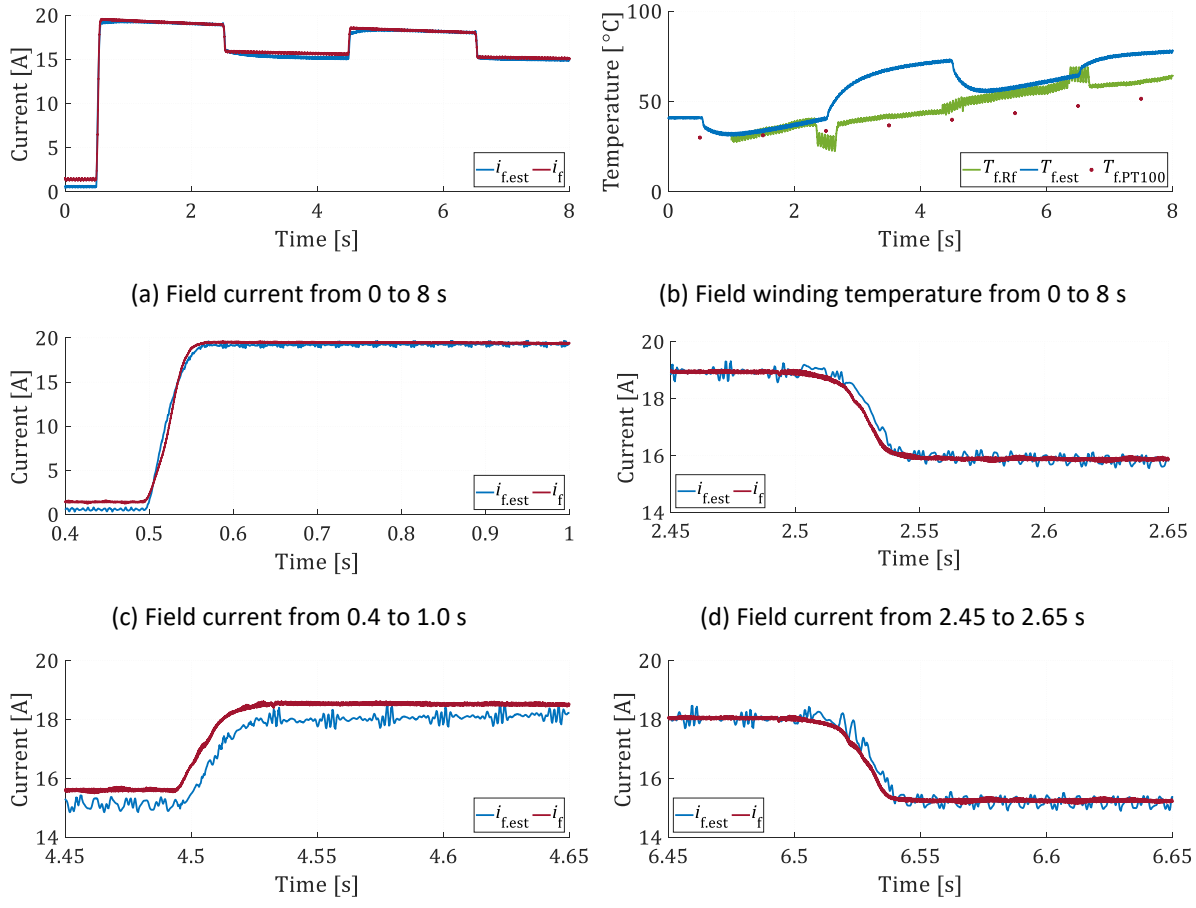

(a) Field current from 0 to 8 s

(b) Field winding temperature from 0 to 8 s

(c) Field current from 0.4 to 1.0 s

(d) Field current from 2.45 to 2.65 s

(e) Field current from 4.45 to 4.65 s

(f) Field current from 6.45 to 6.65 s

Figure 6-50 Duty cycle sequence test at 30℃.

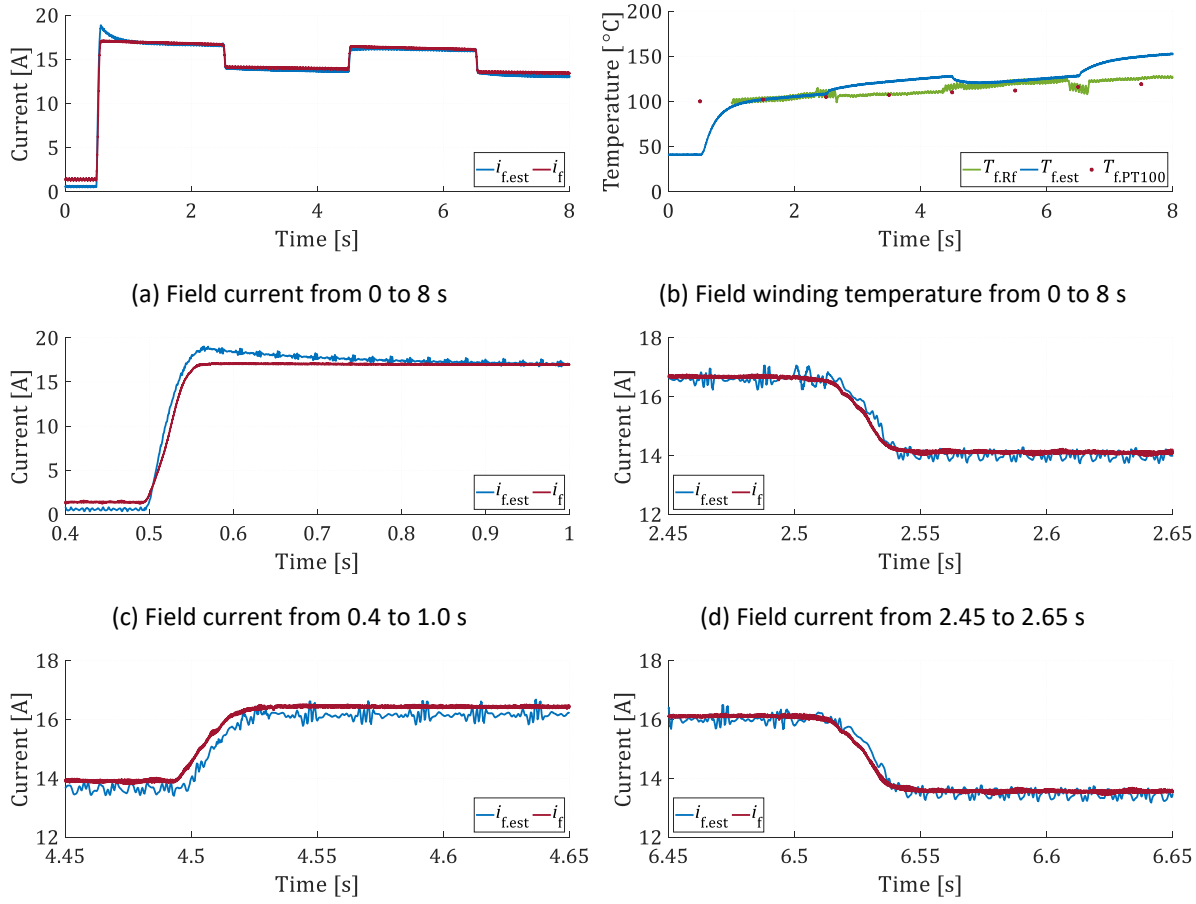

(a) Field current from 0 to 8 s

(b) Field winding temperature from 0 to 8 s

(c) Field current from 0.4 to 1.0 s

(d) Field current from 2.45 to 2.65 s

(e) Field current from 4.45 to 4.65 s

(f) Field current from 6.45 to 6.65 s

Figure 6-51 Duty cycle sequence test at 100°C.

different temperatures as the feedback to correct the temperature estimation, a smaller difference of dc-link currents makes the temperature estimation more difficult. Analytically, an increase of temperature gives an increase of R_{f}, and from the analytical solution shown in (2-99), the difference in dc-link current can be expressed as

$$\Delta I_{\mathrm{dc}} \propto \frac{1-\cos(\pi d)}{R_{\mathrm{f.1}} R_{\mathrm{f.2}}} (R_{\mathrm{f.2}} - R_{\mathrm{f.1}}) \tag{6-8}$$

where $R_{\mathrm{f.1}}$ and $R_{\mathrm{f.2}}$ are the resistances at different temperatures. The part $\frac{1-\cos(\pi d)}{R_{\mathrm{f.1}} R_{\mathrm{f.2}}}$ can be regarded as an amplification factor of the resistance difference $(R_{\mathrm{f.2}} - R_{\mathrm{f.1}})$. A higher duty cycle therefore gives a higher amplification factor $\frac{1-\cos(\pi d)}{R_{\mathrm{f.1}} R_{\mathrm{f.2}}}$ and therefore a higher ΔI_{dc}. This is the reason why a higher duty cycle shows a better resolution of temperature estimation.

6.1.8.2 Field Current Control

Figure 6-52 presents the experimental result which starts at 30℃. The current reference $i_{\mathrm{f.ref}}$ and current estimation $i_{\mathrm{f.est}}$, are output from the DAC of the DSP, whereas the real current i_{f} is measured by a current probe. As can be noticed, the real current follows the reference well. The real current lags the reference by less than 10 ms and it rises from 0 A to 18 A within 50 ms.

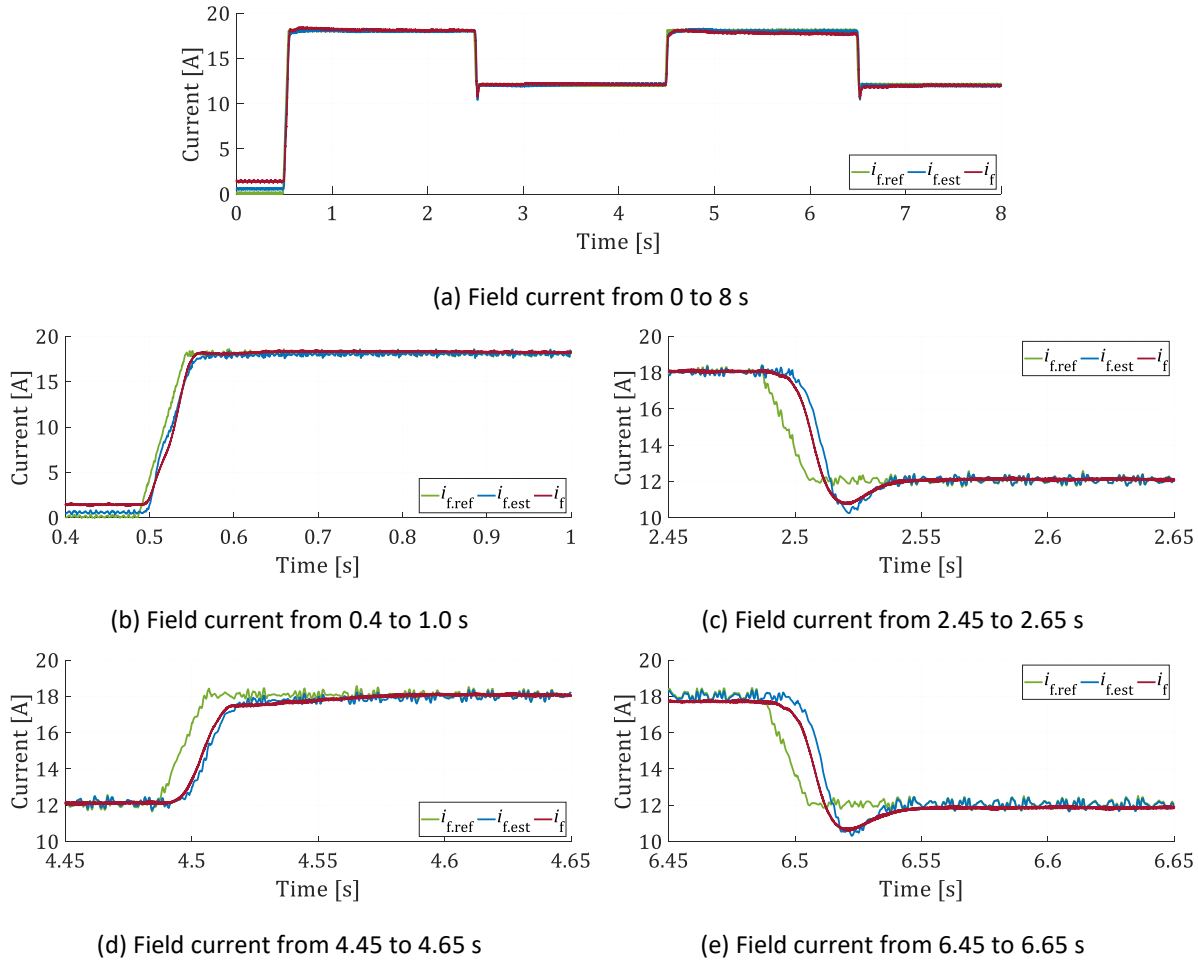

(a) Field current from 0 to 8 s

(b) Field current from 0.4 to 1.0 s

(c) Field current from 2.45 to 2.65 s

(d) Field current from 4.45 to 4.65 s

(e) Field current from 6.45 to 6.65 s

Figure 6-52 Closed-loop field current control at 30℃.

Figure 6-53 presents the experimental result which starts at 100℃. The same sequence is applied. As can be noticed, starting at 100℃, due to the increase of resistance, the field current cannot reach 18 A even with duty cycle 1.0. Hence a gap always exists between the real field current and the 18 A reference. The gap enlarges gradually since the temperature increases during the test. During the transients around 0.5 s, the field current is temporarily over-estimated because estimator needs time to catch up with the real temperature. The temperature estimation adjusts until around 1.0 s, the current estimation comes back to the real value.

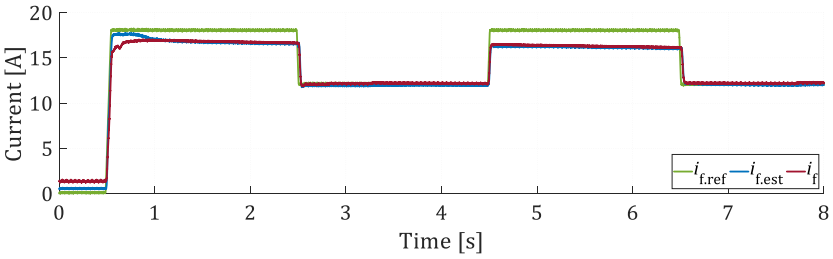

(a) Field current from 0 to 8 s

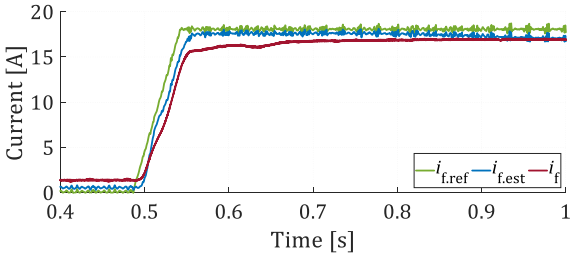

(b) Field current from 0.4 to 1.0 s

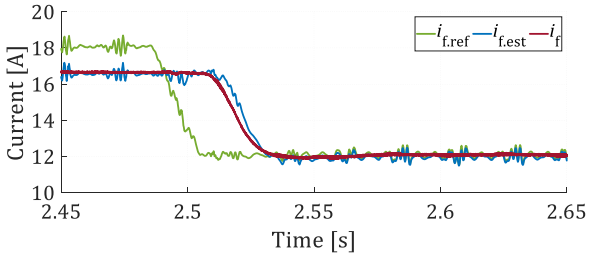

(c) Field current from 2.45 to 2.65 s

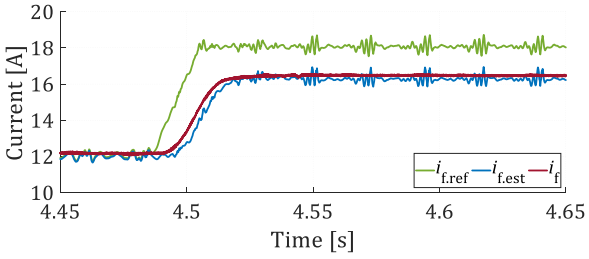

(d) Field current from 4.45 to 4.65 s

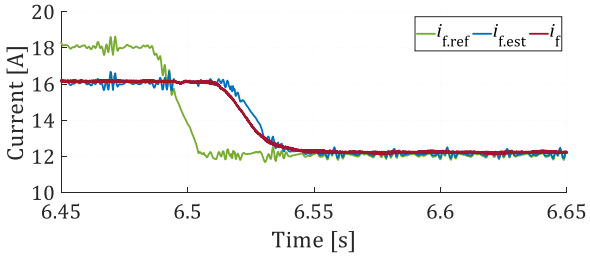

(e) Field current from 6.45 to 6.65 s

Figure 6-53 Closed-loop field current control at 100°C.

6.1.8.3 Stator Current Control

The step responses of q-axis current of 100 A and 200 A are tested as shown in Figure 6-54 (a) and (b) respectively. Instead of shaping the system into a first-order system, overshoots are allowed to get a faster response. In current control, the current reference is sent to the current control loop as a ramp which prohibits overshoot in reality.

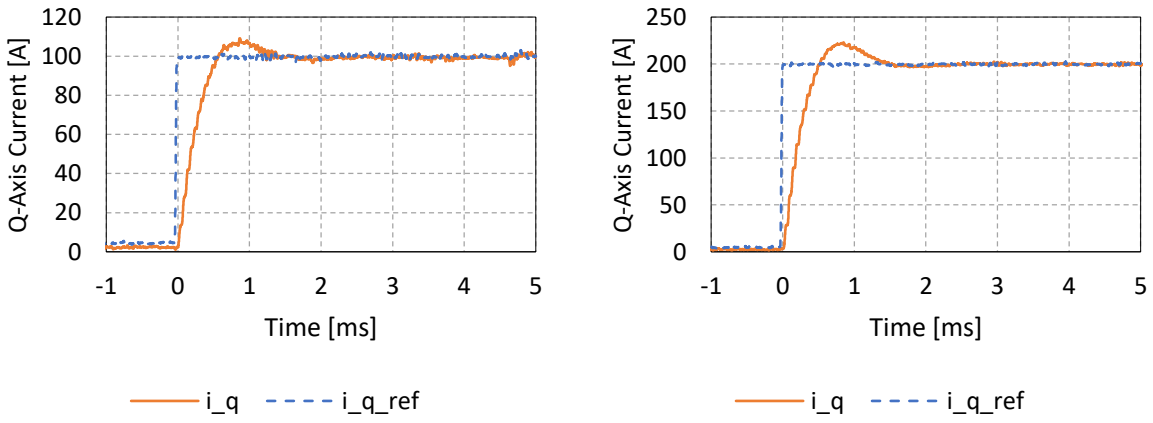

(a) $I_{\mathrm{d.ref}} = 0$ [A], $I_{\mathrm{q.ref}} = 100$ [A]

(b) $I_{\mathrm{d.ref}} = 0$ [A], $I_{\mathrm{q.ref}} = 200$ [A]

Figure 6-54 Step response of q-axis current.

6.2 EESM Development for Electric Passenger Cars

6.2.1 Machine Design

6.2.1.1 Open-Slot and Closed-Slot

A comparison is done between open- and closed-slot designs. 360 steps are calculated in each electrical cycle to catch the peaks of the back-EMF and torque ripple. The flux distributions in FEM are given in Figure 6-55. In the closed-slot design, a bridge of 1 mm short circuits one

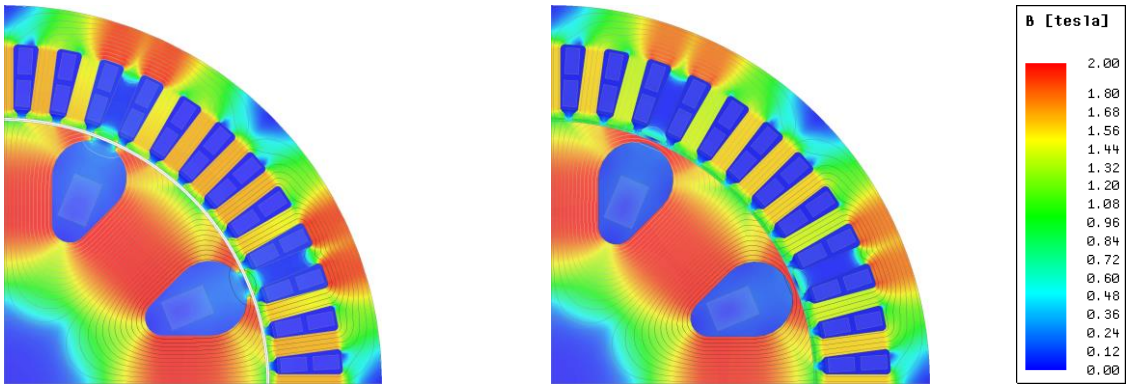

(a) Open-slot design (b) Closed-slot design

Figure 6-55 Flux distribution in no-load operation in FEM.

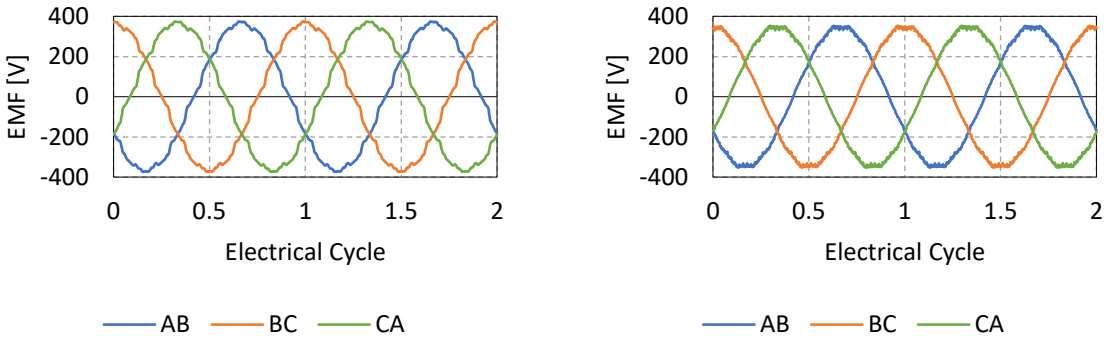

(a) Open-slot design (b) Closed-slot design

Figure 6-56 Back-EMF in time-domain.

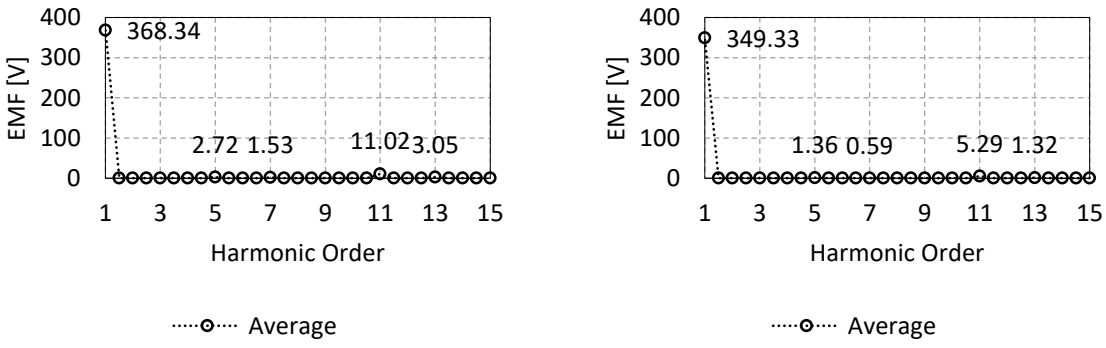

(a) Open-slot design (b) Closed-slot design

Figure 6-57 Back-EMF in frequency-domain.

pole and an adjacent pole on each side. As a result, the flux densities along the airgap and the stator iron-core become lower. The back-EMF waveforms in time-domain and frequency-domain are compared in Figure 6-56 and Figure 6-57 respectively. The closed-slot design suppresses the 5^{th}, 7^{th}, 11^{th} and 13^{th} harmonics by 50% in general, with a cost of 5% in fundamental EMF.

The torque production capability of the two designs are compared. Figure 6-58 shows the flux distribution of each case. The stator flux path is less saturated in the closed-slot design. This brings two consequences. Firstly, the rotor flux linked by the stator winding is lower. Hence

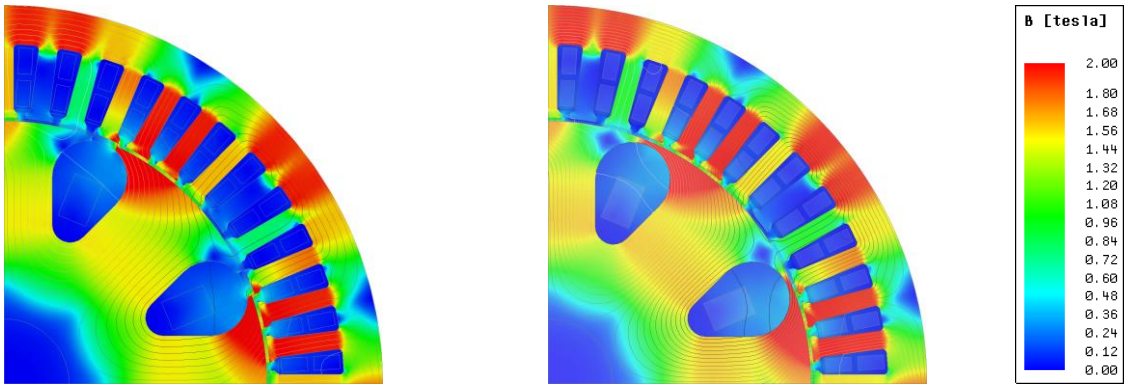

(a) Open-slot design (b) Closed-slot design

Figure 6-58 Flux distribution in peak torque operation in FEM.

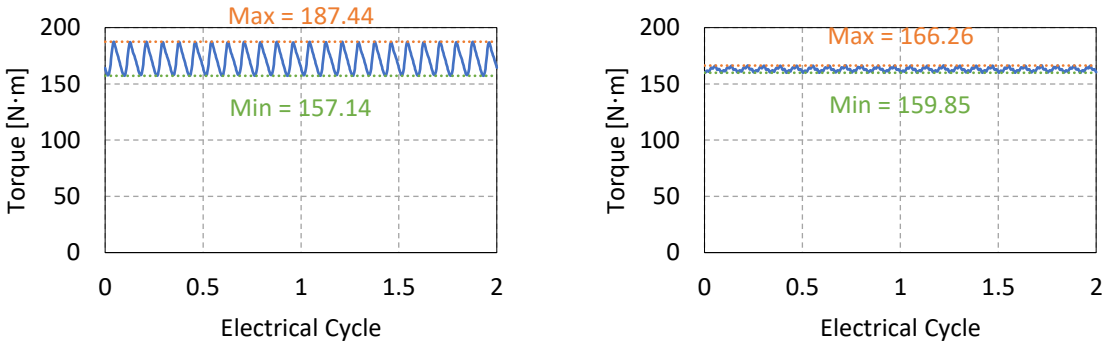

(a) Open-slot design (b) Closed-slot design

Figure 6-59 Torque in time-domain.

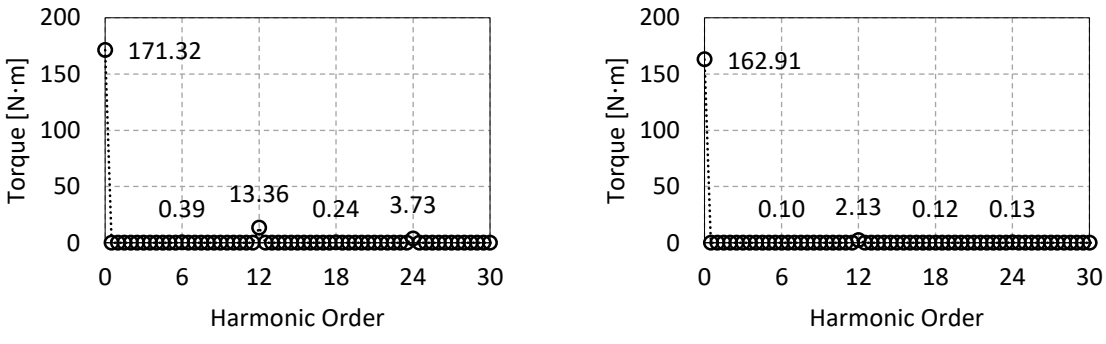

(a) Open-slot design (b) Closed-slot design

Figure 6-60 Torque in frequency-domain.

with the same stator current, the synchronous torque is lower. Secondly, the saliency caused by saturation of d-axis becomes not significant, which means the reluctance torque is limited. These two points contribute to a lower torque in total. Figure 6-59 shows the torque waveform in time domain while Figure 6-60 shows the torque in frequency domain. As can be noticed, by closing the slot, the average torque is reduced by 5%, but the torque ripple in N·m is reduced by 21%. The means that the torque ripple mainly attributes to the 12^{th} slot harmonic. The closed-slot design smooths the flux distribution in the airgap which reduces the 12^{th} slot harmonic. It is therefore decided to move forward with the closed-slot design.

6.2.1.2 Assistance of Ferrite

The study of assistance of ferrite is of interest to see what ferrite can contribute to the performance of EESM. A piece of BM9 ferrite with thickness of 1 - 5 mm is added on the top of the rotor slot. As an example, the ferrite with thickness of 5 mm is shown in Figure 6-61 (b) and Figure 6-62 (b). The remaining area of the slot is filled with copper. A maximum current density of 25 A/mm^2 is utilized to decide the maximum field current in each design.

By comparing Figure 6-61 (a) with (b), it can be noticed that the flux density of rotor pole is reduced. This is due to the fact that the flux from the ferrite pieces cancels a part of flux in rotor pole. This is consistent with the comparison performed in Figure 6-63 (a). With an increase amount of ferrite, the rotor pole flux reduces.

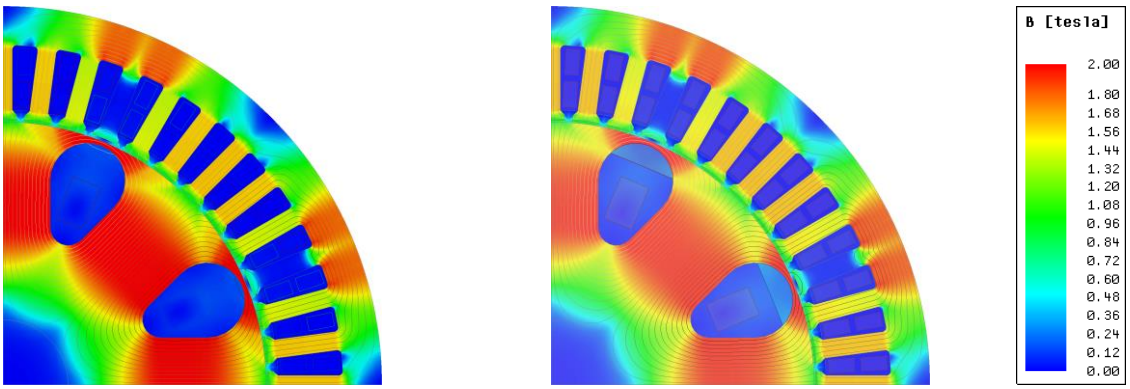

(a) BM9 thickness @ 0 mm (b) BM9 thickness @ 5 mm

Figure 6-61 Flux distribution of no-load operation in FEM.

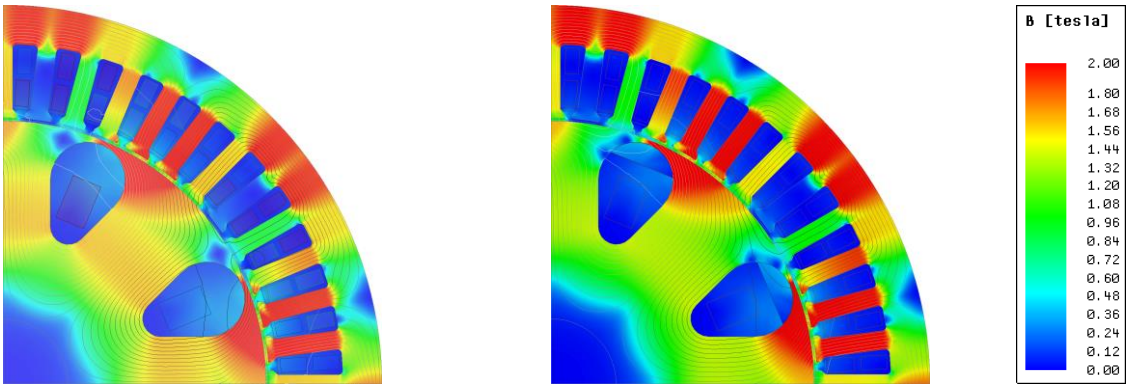

(a) BM9 thickness @ 0 mm (b) BM9 thickness @ 5 mm

Figure 6-62 Flux distribution of peak torque operation in FEM.

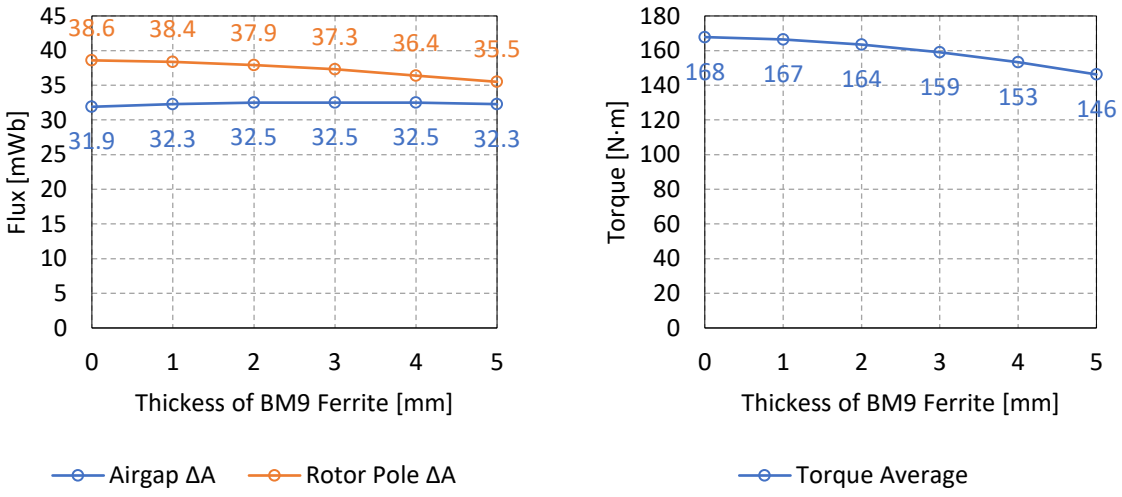

(a) Flux at no-load operation (b) Peak torque

Figure 6-63 Flux at no-load and peak torque.

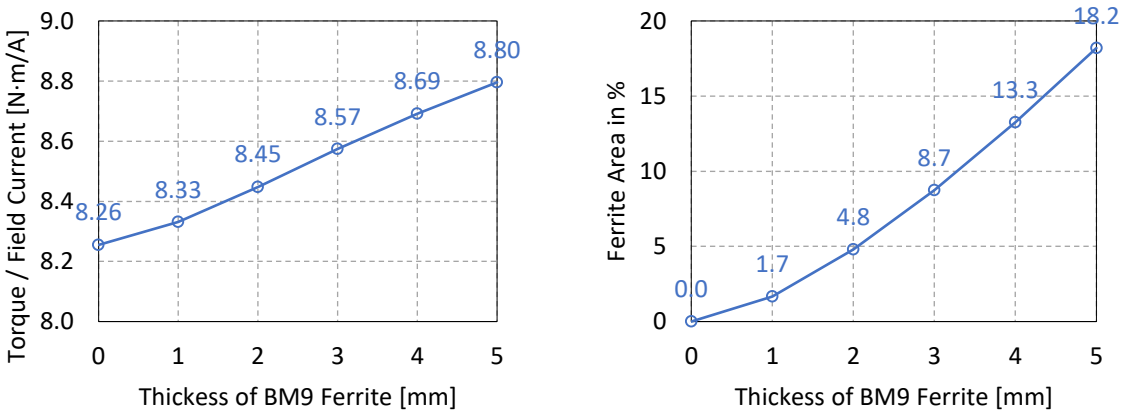

(a) Torque / field current (b) Ferrite area in percentage

Figure 6-64 Flux at no-load and peak torque.

However, the airgap flux increases firstly and then decreases as an increasing amount of ferrite is added. The increase in the beginning is due to the saturation of the bridge caused by the ferrite which saves the flux generated by the copper to go to the airgap. The decrease is due to that, when the bridge is already saturated adding more ferrite does not help more, whereas the occupation of copper area by the ferrite to reduce the flux generated by copper becomes more significant.

Figure 6-63 (b) shows the peak torque of each case. As the amount of ferrite added increases, the torque level decreases. Adding 5 mm of ferrite decreases the torque by 13%. Since the airgap flux is almost the same, this is due to the reduction of salience and therefore a reduction of reluctance torque. With no ferrite, the MTPA angle is 108° whereas with 5 mm of ferrite, the MTPA angle reduces to 99°. The reduction of MTPA angle indicates a reduction of reluctance torque. This attributes to the ease of the d-axis saturation by the ferrite.

Figure 6-64 (a) presents the ratio between torque and field current. As can been noticed, though the torque is reduced, the ratio between torque and field current increases. And this means the field current is used more effectively in the sense of torque production. Figure 6-64 (b) presents the percentage that ferrite occupies the slot. An occupation of 20% ferrite, which means a decrease of 20% copper loss, increases the torque-to-field-current ratio by 6.54% and decreases the torque by 13.1%.

It can therefore be concluded that an introduction of ferrite in rotor slot

- Excites the machine less effectively than copper winding and reduces torque production.
- Reduces copper losses.
- Eases rotor pole saturation which means a thinner rotor pole body becomes possible.

Due to the relative complex manufacturing process, the prototype is decided to be with no assistance of ferrite.

6.3 EESM Development for Heavy Duty Vehicle

6.3.1 Machine Design

Table 6-6 shows the parameters of a 4-polepair 48-slot EESM for heavy duty vehicles. The flux distribution of no-load and peak torque in FEM are presented in Figure 6-65. The rotor flux density is lower at peak torque due to an injection of negtive d-axis current. The stator teeth become more saturated at peak torque due to armature reaction.

Table 6-6 Parameters of a 4-polepair 48-slot EESM for heavy duty vehicle.

Parameter	Symbol	Value	Unit
Active Length		300	mm
Stator Outer Diameter	$ODstator$	270	mm
Stator Inner Diameter	$IDstator$	200	mm
Air Gap	g	1.25	mm
Stator Slot Width	$Bs1$	7.25	mm
Stator Slot Depth	$Hs2$	20	mm
Rotor Slot Width	$Bs1$	39	mm
Rotor Slot Depth	$Hs2$	19	mm
Number of Turns in Stator per Slot per Layer		4	
Number of Turns in Rotor per Pole Pair		400	
Steel Material		B30AHV1500	

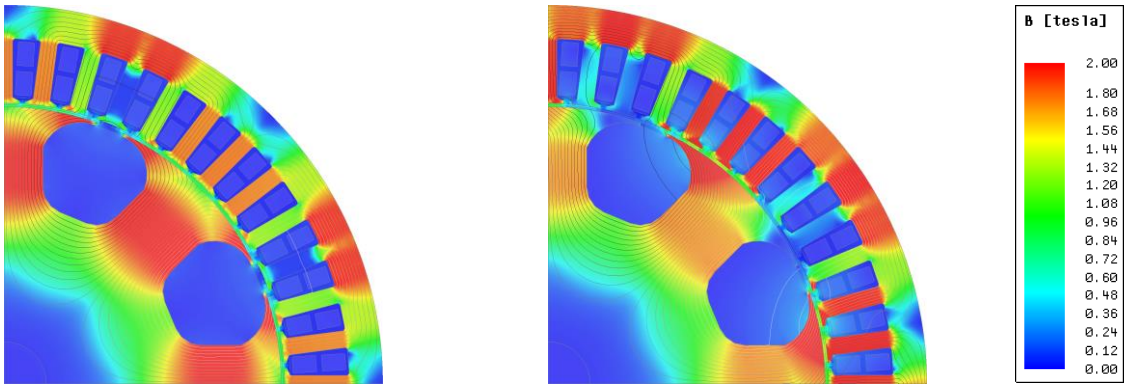

(a) No-load (b) Peak torque

Figure 6-65 Flux distribution in FEM.

The EMF at no-load operation and the peak torque are presented in Figure 6-66 and Figure 6-67 respectively. The major harmonic components are the 11th and 13th harmonic component, which contributes to the major torque ripple at the order of 12.

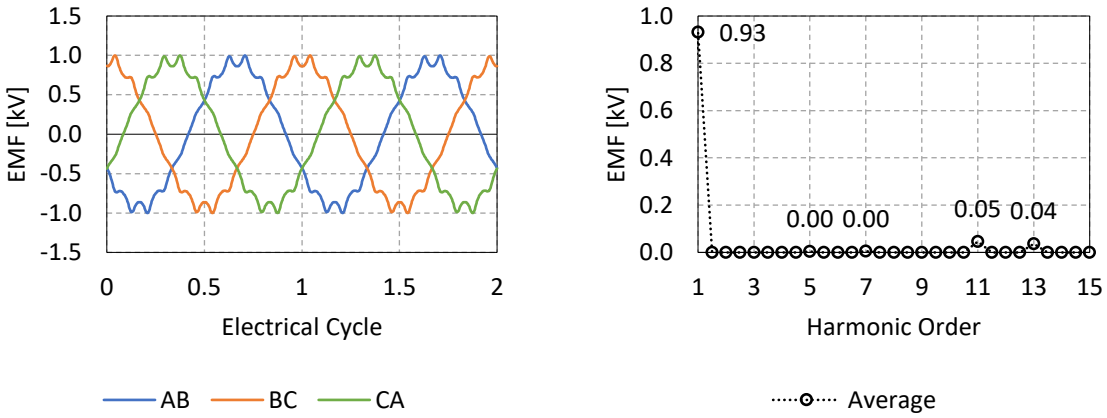

(a) Time domain (b) Frequency domain

Figure 6-66 No-load line back-EMF waveform in FEM.

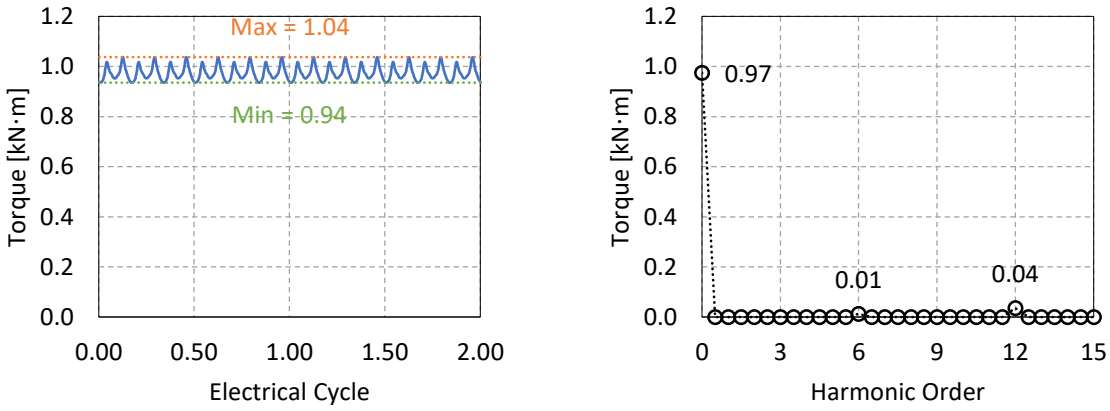

(a) Time domain (b) Frequency domain

Figure 6-67 Peak torque in FEM.

The operation points are calculated through iteration algorithm. The efficiency map is shown in Figure 6-68. Only copper losses and iron-core losses are considered in the efficiency calculation here. As can be noticed, efficiency higher than 95% can still be achieved at a speed over 8000 rpm. This is due to the low field winding copper loss in field weakening region of EESM. Table 6-7 shows the performance of the continuous operation point and best efficiency point. The power factors are nearly unity and the efficiencies are around 95% in both points. Field winding copper loss is reduced dramatically in the best efficiency point due to field weakening. As can be noticed, the advantage of adjustable field in EESM brings a significant

Table 6-7 Parameters of a 4-polepair 48-slot EESM for mild hybrid vehicle.

Performance Index	Continuous Operation	Best Efficiency Operation	Unit
Speed	5000	8000	rev/min
	524	838	rad/s
Torque	350	50	N·m
EM Power	183.26	41.89	kW
Stator Copper Loss	5.59	0.29	kW
Rotor Copper Loss	3.28	0.17	kW
Total Copper Loss	8.87	0.46	kW
Iron-Core Loss	2.33	1.64	kW
Total Loss	11.20	2.09	kW
Input Power	194.46	43.98	kW
Efficiency	94.26	95.22	%
Power Factor	0.99	0.99	
Efficiency · PF	93.75	94.72	%

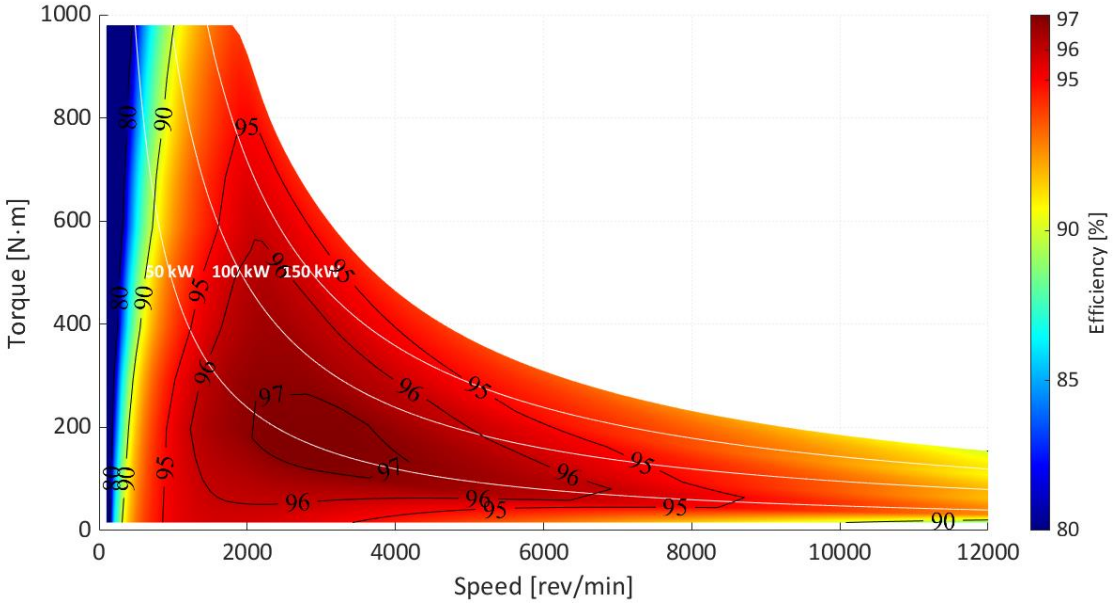

Figure 6-68 Efficiency map of a 1200 V 200 kW EESM in heavy duty application. Only copper loss and iron-core loss are taken into consideration.

benefit in field weakening operation. To make fully use of this characteristic, in heavy-duty applications, it is a reasonable choice to place both the continuous operation point and the best efficiency point in the field weakening region.

Chapter 7

Conclusions and Future Work

7.1 Conclusions

This study Aims at investigating the potential of EESM with high frequency brushless excitation in EV applications. Modeling, design and control are the aspects of interest in this study. To cover a wide range of applications, this study includes the developments of three EESM drive systems, one for mild hybrid vehicles, one for electric passenger cars and one for heavy duty vehicles.

To achieve a comprehensive understanding of the system and to perform design and analysis, the modeling of EESM for traction applications are firstly investigated. The modeling part includes the modeling of the machine as well as the high frequency brushless excitation system. Models are established both in steady state and in dynamics. The nonlinear characteristics of magnetic material are taken into consideration. Based on the machine model, the vector loci of current, voltage, torque and power factor in dq-frame are analytically derived. The envelop of operation area in torque-speed map is solved analytically as well. Further, with the steady-state machine model, the optimization of EESM steady state operation is studied. The algorithms to achieve unity power factor, copper loss minimization and field current minimization are analyzed. The study shows that to achieve unity power factor at high speed, the field excitation needs to be stronger than the armature reaction.

As the start of the design, the specifications for each of the three applications are profiled. The varieties in specifications indicate the differences in design strategies. As a general design procedure, this study adopts the design steps with interactions of FEM analysis and steady state operation point iterations. Then the design strategies are established according to each set of design specifications for the parameter tuning of the machine geometry. As the design for mild hybrid vehicles, the strategy of machine design is to widen the flux path to avoid saturation. In terms of the design for electric passenger cars, a good balance is required between the cross-section of the copper area and the cross-section of the flux path in the iron core. The comparison between open-slot and closed-slot designs is an interesting point. The closed-slot design reduces the torque ripple by 50% by sacrificing the average torque by 5%. The idea to introduce the assistance of ferrite is attractive as well. One piece of ferrite is added to the top of the rotor slot. The study shows that ferrite excites the machine less effectively than copper winding, but it helps reduce the copper losses and makes the torque production per unit of field current more effectively. As for the machine design for heavy-duty vehicles, after the guarantee of peak torque production, the design focuses on improving the efficiencies at the continuous operation point (94.26%) and the best efficiency point (95.22%). The investigation shows that, the adjustable field in EESM brings a significant benefit in field

weakening operation. The excellent capability of field weakening is an essential advantage of EESM in heavy duty applications.

A 48 V EESM with high frequency brushless excitation for mild hybrid vehicles is prototyped. The experimental results of both machine and exciter are consistent with the FEM calculation results. This verifies the modeling and the methods that are applied in the design and analysis process.

One challenge for the prevalence of EESM is the inaccessibility of field winding after the EESM has been assembled. To tackle this, an algorithm to estimate the field winding current and temperature is developed. In the algorithm, the dc-link current is utilized as a feedback to correct the estimations. The current and temperature variations are tracked quite well. One step further, a closed-loop field current control is established. The tracking of field current reference is within an error of 2% in experimental verifications. This closed-loop field current control enables a complete dynamic closed-loop control of the EESM.

7.2 On-Going and Future Work

The prototyping of the designed 360 V 70 kW EESM is on-going. The design is going to be verified experimentally. The experimental results will be compared with a PMSM which is equipped with the same hair-pin stator. If time and facilities permit, driving cycle tests are to be performed and the test results are to be compared as well.

The prototyping of the 200 kW EESM is on the plan as well. The dc-link voltage level may be adjusted to match the design of the power electronic converter. Due to the high power level, to test the machine, probably a back-to-back topology will be established, in which two machines are connected through shafts, one in torque control and one in speed control. Each machine is driven by an inverter. A dc power supply is connected to the dc-link which compensates for the losses of the system.

In terms of the control study, state feedback control and sensorless control are of interest. State feedback control is claimed to provide a better dynamic performance compared with traditional PI control. And since EESM provides one more control freedom by the field current, sensorless with a utilization of field current is of interest.

References

[1] Y. L. Petit, "Electric Vehicle Life Cycle Analysis and Raw Material Availability," Transport & Environment, 2017.

[2] A. Nordelöf, M. Messagie, A.-M. Tillman, M. L. Söderman and J. V. Mierlo, "Environmental impacts of hybrid, plug-in hybrid, and battery electric vehicles—what can we learn from life cycle assessment?," *The International Journal of Life Cycle Assessment,* vol. 19, no. 11, p. 1866–1890, 2014.

[3] International Energy Agency, "Global EV Outlook 2019," International Energy Agency, 2019.

[4] International Energy Agency, "Global EV Outlook 2017," International Energy Agency, 2017.

[5] J. D. Widmer, R. Martin and M. Kimiabeigi, "Electric Vehicle Traction Motors without Rare Earth Magnets," *Sustainable Materials and Technologies,* vol. 3, pp. 7-13, 2015.

[6] Macmill Magnets Co., Ltd., "Permanent Magnets," Macmill Magnets Co., Ltd., [Online]. Available: http://www.macmillmagnet.com/Permanentmagnets.html.

[7] Webcraft GmbH, "Physical Magnet Data," Webcraft GmbH, [Online]. Available: https://www.supermagnete.de/eng/data_table.php.

[8] H. R. Kirchmayr, "Permanent Magnets and Hard Magnetic Materials," *Journal of Physics D: Applied Physics,* vol. 29, no. 11, pp. 2763 - 2778, 1996.

[9] N. L. Guo, N. Bo, X. H. Wang, M. Li and P. Sun, "Simplified Calculation of the Maximum Energy Product for the Hard/Soft/Hard Trilayers," *Journal of Superconductivity and Novel Magnetism,* vol. 30, no. 10, pp. 2835 - 2840, 2017.

[10] D. G. Dorrell, A. M. Knight, M. Popescu, L. Evans and D. A. Staton, "Comparison of Different Motor Design Drives for Hybrid Electric Vehicles," in *2010 IEEE Energy Conversion Congress and Exposition*, Atlanta, 2010.

[11] C. C. Pavel, C. Thiel, S. Degreif, D. Blagoeva, M. Buchert, D. Schüler and E. Tzimas, "Role of substitution in mitigating the supply pressure of rare earths in electric road transport applications," *Sustainable Materials and Technologies,* vol. 12, pp. 62 - 72, 2017.

[12] Y. Yang, A. Walton, R. Sheridan, K. Güth, R. Gauß, O. Gutfleisch, M. Buchert, B.-M. Steenari, T. V. Gerven, P. T. Jones and K. Binnemans, "REE Recovery from End-of-Life NdFeB Permanent MagnetScrap: A Critical Review," *Journal of Sustainable Metallurgy,* vol. 3, no. 1, pp. 3 - 30, 2017.

[13] K. Binnemans, P. T. Jones, B. Blanpain, T. V. Gerven, Y. Yang, A. Walton and M. Buchert, "Recycling of Rare Earths: A Critical Review," *Journal of Cleaner Production,* vol. 51, pp. 1-22, 2013.

[14] E. M. Illiano, "Design of a Highly Efficient Brushless Current Excited Synchronouos Motor for Automotive Purposes," Swiss Federal Institute of Technology in Zurich (ETH Zurich), Zurich, 2014.

[15] E. M. Illiano, "Design of a Brushless Separately Excited Synchronous Motor," BRUSA Elektronik AG, Sennwald, 2014.

[16] L. Huang, Z. Zhu and W. Chu, "Optimization of Electrically Excited Synchronous Machine for Electrical Vehicle Applications," in *Machines and Drives (PEMD 2016), 8th IET International Conference on Power Electronics*, Glasgow, UK, 2016.

[17] A. D. Gioia, I. P. Brown, Y. Nie, R. Knippel, D. C. Ludois, J. Dai, S. Hagen and C. Alteheld, "Design and Demonstration of a Wound Field Synchronous Machine for Electric Vehicle Traction With Brushless Capacitive Field Excitation," *IEEE Transactions on Industry Applications,* vol. 54, no. 2, pp. 1390 - 1403, 2018.

[18] M. Tosi, "Rotary Transformer Design for Brushless Electrically Excited Synchronous Machines," University of Padua, Padua, 2014.

[19] T. Raminosoa and R. Wiles, "Contactless Rotor Excitation for Traction Motors," in *2018 IEEE Energy Conversion Congress and Exposition (ECCE)*, Portland, 2018.

[20] C. Stancu, T. Ward, K. M. Rahman, R. Dawsey and P. Savagian, "Separately Excited Synchronous Motor With Rotary Transformer for Hybrid Vehicle Application," *IEEE Transactions on Industry Applications,* vol. 54, no. 1, pp. 223-232, 2018.

[21] H. Krupp and A. Mertens, "Rotary Transformer Design for Brushless Electrically Excited Synchronous Machines," in *2015 IEEE Vehicle Power and Propulsion Conference (VPPC)*, Montreal, 2015.

[22] Y. Luan, B. Lin, X. Ma and X. Zhu, "Innovative Contactless Energy Transfer Accessory for Rotary Ultrasonic Machining and Its Circuit Compensation Based on Coil Turns," *IEEE Transactions on Industrial Electronics,* vol. 64, no. 10, pp. 7810 - 7818, 2017.

[23] Y. Liu, D. Pehrman, O. Lykartsis, J. Tang and T. Liu, "High frequency exciter of electrically excited synchronous motors for vehicle applications," in *2016 XXII International Conference on Electrical Machines (ICEM)*, Lausanne, Switzerland, 2016.

[24] R. Wang, S. Pekarek and M. Bash, "Alternative excitation strategies for a wound rotor synchronous machine drive," in *2012 IEEE Energy Conversion Congress and Exposition (ECCE)*, Raleigh, NC, USA, 2012.

[25] K. Liang, W. Xuhui and F. Tao, "A new method to plan the optimal field excitation current trajectory in a hybrid excitation machine," in *2011 International Conference on Electrical Machines and Systems (ICEMS)*, Beijing, China, 2011.

[26] O. Haala, B. Wagner, M. Hofmann and M. März, "Optimal current control of externally excited synchronous machines in automotive traction drive applications," *International Journal of Electrical, Computer, Energetic, Electronic and Communication Engineering,* vol. 7, no. 9, pp. 1133-1139, 2013.

[27] Y. Kim and K. Nam, "Copper-Loss-Minimizing Field Current Control Scheme for Wound Synchronous Machines," *IEEE Transactions on Power Electronics,* vol. 32, no. 2, pp. 1335 - 1345, 2017.

[28] J. Choi, I. Jeong, K. Nam and S. Jung, "Sensorless control for electrically energized synchronous motor based on signal injection to field winding," in *IECON 2013 - 39th Annual Conference of the IEEE Industrial Electronics Society*, Vienna, Austria, 2013.

[29] Y. Zhou and S. Long, "Sensorless Direct Torque Control for Electrically Excited Synchronous Motor Based on Injecting High-Frequency Ripple Current Into Rotor Winding," *IEEE Transactions on Energy Conversion,* vol. 30, no. 1, pp. 246 - 253, 2014.

[30] S. Choe, E. Jung and S.-K. Sul, "Sensorless Control of Synchronous Machine With an Inverter Integrated Rotor," *IEEE Transactions on Industry Applications,* vol. 50, no. 4, pp. 2584 - 2591, 2013.

[31] S. Feuersänger and M. Pacas, "Rotor position identification in synchronous machines by using the excitation machine as a sensor," in *2016 IEEE Symposium on Sensorless Control for Electrical Drives (SLED)*, Nadi, Fiji, 2016.

[32] M. Hinkkanen, H. A. A. Awan, Z. Qu, T. Tuovinen and F. Briz, "Current Control for Synchronous Motor Drives: Direct Discrete-Time Pole-Placement Design," *IEEE Transactions on Industry Applications,* vol. 52, no. 2, pp. 1530 - 1541, 2015.

[33] D. A. Staton and A. Cavagnino, "Convection Heat Transfer and Flow Calculations Suitable for Electric Machines Thermal Models," *IEEE Transactions on Industrial Electronics,* vol. 55, no. 10, pp. 3509 - 3516, 2008.

[34] A. Boglietti, A. Cavagnino, M. Lazzari and M. Pastorelli, "A Simplified Thermal Model for Variable-Speed Self-Cooled Industrial Induction Motor," *IEEE TRANSACTIONS ON INDUSTRY APPLICATIONS,* vol. 39, no. 4, pp. 945 - 952, 2003.

[35] A. Boglietti, A. Cavagnino, M. Popescu and D. Staton, "Thermal Model and Analysis of Wound-Rotor Induction Machine," *IEEE Transactions on Industry Applications,* vol. 49, no. 5, pp. 2078 - 2085, 2013.

[36] J. Tang and Y. Liu, "Design and Experimental Verification of a 48 V 20 kW Electrically Excited Synchronous Machine for Mild Hybrid Vehicles," in *2018 XIII International Conference on Electrical Machines (ICEM)*, Alexandroupoli, 2018.

[37] J. Tang, Y. Liu and S. Nimananda, "Modeling and Experimental Verification of High-Frequency Inductive Brushless Exciter for Electrically Excited Synchronous Machines," *IEEE Transactions on Industry Applications,* vol. 55, no. 5, pp. 4613 - 4623, 2019.

[38] J. Tang and Y. Liu, "Comparison of Copper Loss Minimization and Field Current Minimization for Electrically Excited Synchronous Motor in Mild Hybrid Drives," in *19th European Conference on Power Electronics and Applications (EPE'17 ECCE Europe)*, Warsaw, Poland, 2017.

[39] R. Grune, "Verlustoptimaler Betrieb einer elektrisch erregten Synchronmaschine für den Einsatz in Elektrofahrzeugen," Technische Universität Berlin, Berlin, 2012.

[40] W. C. Duesterhoeft, M. W. Schulz and E. Clarke, "Determination of Instantaneous Currents and Voltages by Means of Alpha, Beta, and Zero Components," *Transactions of the American Institute of Electrical Engineers,* pp. 1248 - 1255, 1951.

[41] R. H. Park, "Two-Reaction Theory of Synchronous Machines Generalized Method of Analysis - Part I," *Transactions of the American Institute of Electrical Engineers,* pp. 716 - 727, 1929.

[42] C. L. Fortescue, "Method of Symmetrical Co-Ordinates Applied to the Solution of Polyphase Networks," *AIEE Transactions,* vol. 37, p. 1027–1140, 1918.

[43] D. A. Staton, T. J. Miller and S. E. Wood, "Maximising the Saliency Ratio of the Synchronous Reluctance Motor," *IEE Proceedings B - Electric Power Applications,* vol. 140, no. 4, pp. 249 - 259, 1993.

[44] G. Bertotti, "Physical interpretation of eddy current losses in ferromagnetic materials. I. Theoretical considerations," *Journal of Applied Physics,* vol. 57, no. 6, pp. 2110 - 2117, 1985.

[45] Y. Liu, S. K. Kashif and A. M. Sohail, "Engineering Considerations on Additional Iron Losses due to Rotational Fields and Sheet Cutting," in *2008 18th International Conference on Electrical Machines*, Vilamoura, Portugal, 2008.

[46] H. Akagi, E. H. Watanabe and M. Aredes, "The Instantaneous Power Theory," in *Instantaneous Power Theory and Applications to Power Conditioning*, Tokyo / Rio de Janeiro, Wiley-IEEE Press, 2007, pp. 41 - 107.

[47] D. Annaratone, "Steady Conduction," in *Engineering Heat Transfer*, Milano, Springer, 2010, pp. 13 - 28.

[48] J. Pyrhönen, T. Jokinen and V. Hrabovcová, "Insulation of Electrical Machines," in *Design of Rotating Electrical Machines*, Wiley, 2014, pp. 495 - 522.

[49] D. Staton, A. Boglietti and A. Cavagnino, "Solving the More Difficult Aspects of Electric Motor Thermal Analysis in Small and Medium Size Industrial Induction Motors," *IEEE Transactions on Energy Conversion,* vol. 20, no. 3, pp. 620 - 628, 2005.

[50] A. Boglietti, A. Cavagnino and D. Staton, "Determination of Critical Parameters in Electrical Machine Thermal Models," *IEEE Transactions on Industry Applications,* vol. 44, no. 4, pp. 1150 - 1159, 2008.

[51] D. Annaratone, "Convection," in *Engineering Heat Transfer*, Milano, Springer, 2010, pp. 63 - 138.

[52] D. A. Howey, P. R. N. Childs and A. S. Holmes, "Air-Gap Convection in Rotating Electrical Machines," *IEEE Transactions on Industrial Electronics,* vol. 59, no. 3, pp. 1367 - 1375, 2010.

[53] J. Fan, C. Zhang, Z. Wang and E. G. Strangas, "Thermal Analysis of Water Cooled Surface Mount Permanent Magnet Electric Motor for Electric Vehicle," in *2010 International Conference on Electrical Machines and Systems (ICEMS)*, Incheon, 2010.

[54] I. S. Bjorklund and W. M. Kays, "Heat Transfer Between Concentric Rotating Cylinders," *Journal of Heat Transfer,* vol. 81, no. 3, pp. 175 - 183, 1959.

[55] K. M. Becker and J. Kaye, "Measurements of Diabatic Flow in an Annulus With an Inner Rotating Cylinder," *Journal of Heat Transfer,* vol. 84, no. 2, pp. 97 - 104, 1962.

[56] K. M. Becker and J. Kaye, "The Influence of a Radial Temperature Gradient on the Instability of Fluid Flow in an Annulus With an Inner Rotating Cylinder," *Journal of Heat Transfer,* vol. 84, no. 2, pp. 106 - 110, 1962.

[57] D. Annaratone, "Radiation," in *Engineering Heat Transfer*, Milano, Springer, 2010, pp. 139 - 190.

[58] *Drive motor system for electric vehicles—Part 2: Test methods,* The Standardization Administration of the People's Republic of China, 2015.

[59] J. Tang and Y. Liu, "Study of Voltage Spikes and Temperature Rise in Power Module Based Integrated Converter for 48 V 20 kW Electrically Excited Synchronous Machines," in *APEC 2018*, San Antonio, Taxes, USA, 2018.

[60] R. L. Steigerwald, "A Comparison of Half-Bridge Resonant Converter Topologies," *IEEE Transactions on Power Electronics,* vol. 3, no. 2, pp. 174 - 182, 1988.

[61] V. Ruuskanen, M. Niemela, J. Pyrhonen, S. Kanerva and J. Kaukonen, "Modelling the brushless excitation system for a synchronous machine," *IET Electric Power Applications,* vol. 3, no. 3, pp. 231 - 239, 2009.

[62] H. Ge, J. W. Jiang, J. Ye and A. Emadi, "Behavior Study of Permanent Magnet Synchronous Machines Based on a New Normalized Model," *IEEE Transactions on Industrial Electronics,* vol. 66, no. 10, pp. 7539 - 7550, 2019.

[63] G. Choi and T. M. Jahns, "Investigation of Key Factors Influencing the Response of Permanent Magnet Synchronous Machines to Three-Phase Symmetrical Short-Circuit Faults," *IEEE Transactions on Energy Conversion,* vol. 31, no. 4, pp. 1488 - 1497, 2016.

[64] E. A. Grunditz, "Design, material and mass of machine parts," in *Design and Assessment of Battery Electric Vehicle Powertrain, with Respect to Performance, Energy Consumption and Electric Motor Thermal Capability*, Gothenburg, Chalmers Univrsity of Technology, 2016, pp. 100-102.

[65] D. Staton and J. Goss, "Open Source Electric Motor Models," Motor Design Ltd, Berlin, 2017.

[66] V. G. Press, "Volvo Trucks presents second electric truck model in three weeks," Volvo Group Press, 05 August 2018. [Online]. Available: https://www.volvogroup.com/en-en/news/2018/may/news-2912374.html. [Accessed 28 September 2019].

[67] Mercedes Benz, "eActros: Heavy-duty electric truck," Mercedes Benz, [Online]. Available: https://www.mercedes-benz.com/en/vehicles/trucks/eactros-heavy-duty-electric-truck/. [Accessed 25 September 2019].

[68] N. Mohan, T. M. Undeland and W. P. Robbins, "Three-Phase Inverter," in *Power Electronics: Converters, Applications, and Design*, John Wiley & Sons, Inc, 2003, pp. 225 - 236.

[69] Texas Instruments, "Phase-Shifted Full-Bridge, Zero-Voltage Transition Design Considerations Application Report," Texas Instruments, Dallas, 2011.

[70] L. Harnefors, "Current Control," in *Control of Variable-Speed Drives*, Applied Signal Processing and Control, Department of Electronics, Mälardalen University, 2002, pp. 19 - 29.

[71] S. Skoog, "Experimental and model based evaluation of mild hybrid fuel consumption gains and electric machine utilization for personal vehicle application," in *2017 IEEE Transportation Electrification Conference and Expo, Asia-Pacific (ITEC Asia-Pacific)*, Harbin, 2017.

[72] C. Nordling and J. Österman, "T - 1 Mechanics and Thermal Physics," in *Physics Handbook for Science and Engineering*, Uppsala, Studentlitteratur AB, 2006, pp. 27 - 42.

[73] Cogent Power, "Typical Data for SURA M235-35A," Cogent Power, Surahammar, 2008.

[74] Cogent Power, "Typical Data for SURA M250-35A," Cogent Power, Surahammar, 2006.

[75] Y. Tang, "AC Machinery Fundamentals," in *Electrical Machinery (Chinese)*, Beijing, China Machine Press, 2014, pp. 135 - 176.

Appendix A Instantaneous Power Basics

From the instantaneous voltage and current values, the instantaneous power can be calculated [46]. Under αβ-frame, the complex power can be formulated as

$$\begin{aligned}\underline{s} = p + \mathrm{j}q &= \frac{3}{2K^2} \cdot \underline{u}^{(\alpha\beta)} \cdot \underline{i}^{(\alpha\beta)^*} \\ &= \frac{3}{2K^2} \cdot \left(u_\alpha + \mathrm{j}u_\beta\right) \cdot \left(i_\alpha - \mathrm{j}i_\beta\right) \\ &= \frac{3}{2K^2}\left(u_\alpha i_\alpha + u_\beta i_\beta\right) + \mathrm{j}\frac{3}{2K^2}\left(u_\beta i_\alpha - u_\alpha i_\beta\right)\end{aligned} \tag{A-1}$$

Transformed into dq-frame, the complex power can be expressed as

$$\begin{aligned}\underline{s} = p + \mathrm{j}q &= \frac{3}{2K^2} \cdot \underline{u}^{(\alpha\beta)} \cdot \underline{i}^{(\alpha\beta)^*} = \frac{3}{2K^2} \cdot \left[\underline{u}^{(\mathrm{dq})} \cdot \mathrm{e}^{\mathrm{j}\theta}\right] \cdot \left[\underline{i}^{(\mathrm{dq})} \cdot \mathrm{e}^{\mathrm{j}\theta}\right]^* \\ &= \frac{3}{2K^2} \cdot \left[\underline{u}^{(\mathrm{dq})} \cdot \underline{i}^{(\mathrm{dq})^*}\right] \cdot \left[\mathrm{e}^{\mathrm{j}\theta} \cdot \mathrm{e}^{-\mathrm{j}\theta}\right] \\ &= \frac{3}{2K^2}\left(u_\mathrm{d} i_\mathrm{d} + u_\mathrm{q} i_\mathrm{q}\right) + \mathrm{j}\frac{3}{2K^2}\left(u_\mathrm{q} i_\mathrm{d} - u_\mathrm{d} i_\mathrm{q}\right)\end{aligned} \tag{A-2}$$

With amplitude-invariant transformation ($K = 1$), the active power, reactive power, apparent power as well as power factor can be formulated as

$$p = \frac{3}{2}\left(u_\mathrm{d} i_\mathrm{d} + u_\mathrm{q} i_\mathrm{q}\right) \qquad q = \frac{3}{2}\left(u_\mathrm{q} i_\mathrm{d} - u_\mathrm{d} i_\mathrm{q}\right) \tag{A-3}$$

$$\begin{aligned}s &= \sqrt{p^2 + q^2} \\ &= \frac{3}{2}\sqrt{\left(u_\mathrm{d} i_\mathrm{d} + u_\mathrm{q} i_\mathrm{q}\right)^2 + \left(u_\mathrm{q} i_\mathrm{d} - u_\mathrm{d} i_\mathrm{q}\right)^2} \\ &= \frac{3}{2}\sqrt{(u_\mathrm{d} i_\mathrm{d})^2 + \left(u_\mathrm{q} i_\mathrm{q}\right)^2 + \left(u_\mathrm{q} i_\mathrm{d}\right)^2 + \left(u_\mathrm{d} i_\mathrm{q}\right)^2}\end{aligned} \tag{A-4}$$

$$\cos\varphi = \frac{p}{s} = \frac{p}{\sqrt{p^2 + q^2}} = \frac{1}{\sqrt{1 + \left(\frac{q}{p}\right)^2}} = \frac{1}{\sqrt{1 + \left(\frac{u_\mathrm{q} i_\mathrm{d} - u_\mathrm{d} i_\mathrm{q}}{u_\mathrm{d} i_\mathrm{d} + u_\mathrm{q} i_\mathrm{q}}\right)^2}} \tag{A-5}$$

Appendix B Material Properties

B.1 Thermal Properties

B.1.1 Air

The density of air under 1 atm and 0 °C is 1.293 kg/m^3. This value can be scaled by pressure and temperature according to the law of perfect gas as [51]

$$\rho_{\mathrm{air}} = 1.293 \cdot \frac{p}{1.013} \cdot \frac{273.15}{T} = \frac{348.65 \cdot p}{273.15 + t} \tag{B-1}$$

where ρ_{air} is in kg/m^3, p is in bar, T is in K and t is in °C. The isobaric specific heat capacity, thermal conductivity and dynamic viscosity of air can be approximated as [51]

$$c_{\mathrm{p.air}} = 1003.79 + 75.53 \cdot \frac{t}{1000} + 216 \cdot \left(\frac{t}{1000}\right)^2 \tag{B-2}$$

$$\lambda_{\mathrm{air}} = 0.02326 + 0.06588 \cdot \frac{t}{1000} \tag{B-3}$$

$$\mu_{\mathrm{air}} = \left[17.069 + 47.469 \cdot \frac{t}{1000} - 18.708 \cdot \left(\frac{t}{1000}\right)^2\right] \cdot 10^{-6} \tag{B-4}$$

where $c_{\mathrm{p.air}}$ is in J/(kg·K) and t is in °C, λ_{air} is in W/(m·K), μ_{air} is in kg/(m·s) and t is in °C. The formula is valid between 0 °C and 300 °C.

The kinematic viscosity (also called "momentum diffusivity") is the ratio of the dynamic viscosity μ to the density of the fluid ρ. It is usually denoted by the Greek letter ν (nu):

$$\nu = \frac{\mu}{\rho} \tag{B-5}$$

The Prandtl's Number [51] therefore can be approximated as

$$Pr_{\mathrm{air}} = 0.7382 - 0.0554 \cdot \frac{t}{1000} \tag{B-6}$$

where t is in °C. The formula is valid when the temperature is between 0 °C and 300 °C.

B.1.2 Water

The density of water can be approximated as [51]

$$\rho_{\mathrm{water}} = 1006.68 - 20.07 \cdot \frac{t}{100} - 25.15 \cdot \left(\frac{t}{100}\right)^2 \tag{B-7}$$

where $\rho_{\mathrm{H_2O}}$ is in $[\mathrm{kg/m^3}]$ and t is the temperature in $[℃]$. The formula is valid when the temperature is between $10\,℃$ and $300\,℃$ and the pressure is between $5\,[\mathrm{bar}]$ and $100\,[\mathrm{bar}]$. From [72],

The specific heat capacity of water under constant pressure can be approximated as [51]

$$c_{\mathrm{p.water}} = 4219.58 - 187.25 \cdot \frac{t}{100} + 172.17 \cdot \left(\frac{t}{100}\right)^2 \qquad \text{(B-8)}$$

where $c_{\mathrm{p.H_2O}}$ is in $[\mathrm{J/(kg \cdot K)}]$ and t is the temperature in $[℃]$. The formula is valid when the temperature is between $20\,℃$ and $250\,℃$ and the pressure is between $5\,[\mathrm{bar}]$ and $100\,[\mathrm{bar}]$. The thermal conductivity of water can be approximated as [51]

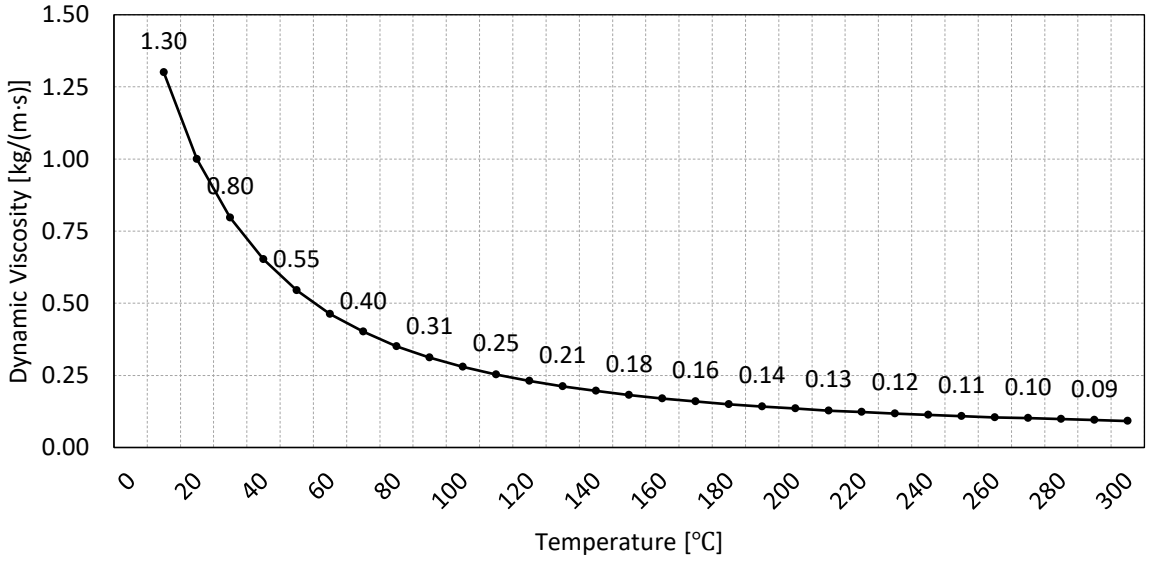

Figure B-1 Dynamic viscosity in 10^{-6} kg/ms of water.

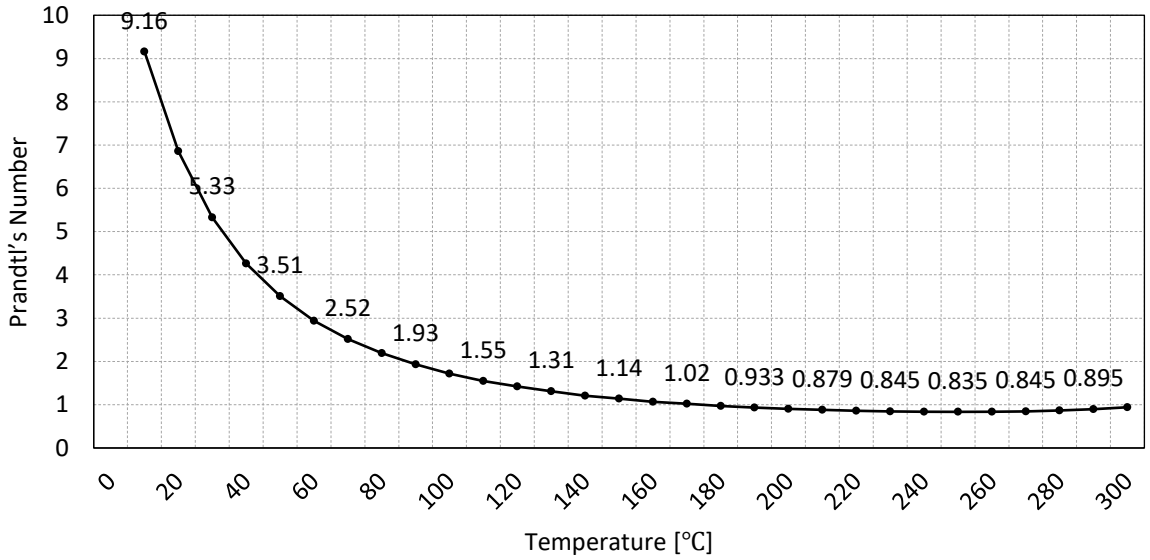

Figure B-2 Prandtl's Number of water.

$$\lambda_{\text{water}} = 0.5755 + 0.1638 \cdot \frac{t}{100} - 0.05767 \cdot \left(\frac{t}{100}\right)^2 \qquad \text{(B-9)}$$

where λ_{H_2O} is in $[\mathrm{W/(m \cdot K)}]$ and t is the temperature in $[℃]$. The formula is valid when the temperature is between $10\,℃$ and $300\,℃$ and the pressure is between $5\,[\mathrm{bar}]$ and $100\,[\mathrm{bar}]$. The dynamic viscosity and Prandtl's Number of water are dependent on a lot of aspects, and therefore it seems not possible to develop a simple formula for approximation of dynamic viscosity and Prandtl's Number [51].

B.1.3 Metal

The thermal conductivity of metals are presented in Figure B-3 [47].

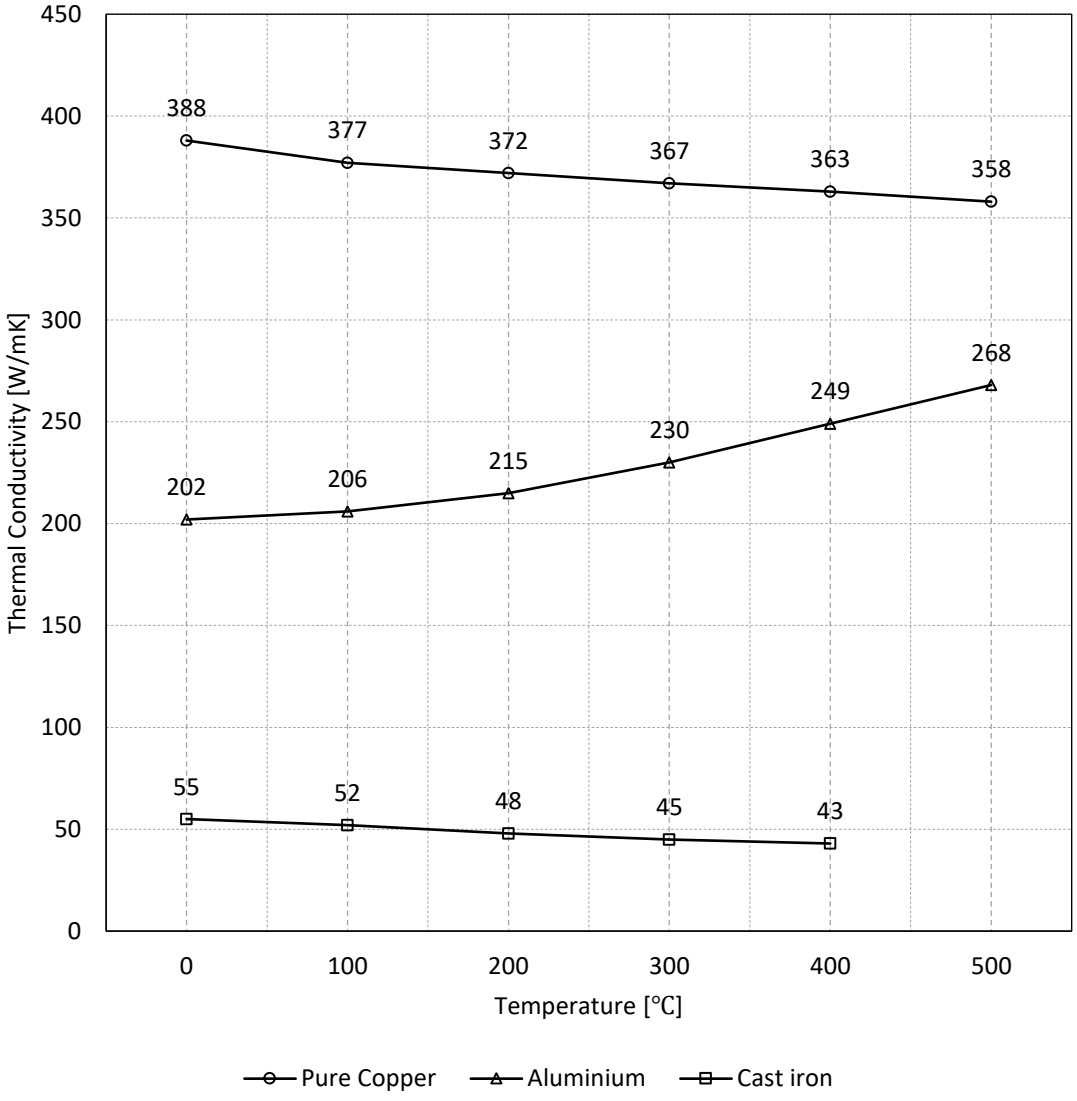

Figure B-3 Thermal conductivity of metals [47].

B.2 Electromagnetic Properties

The Iron-Core loss parameters of SURA M235-35A, B35AV1500 and B35AV1900 are presented in Figure B-4 [73] [74]. The B-H curves of the laminations are presented in Figure B-4.

Table B-1. Iron-Core loss parameters.

Lamination Grade	ρ_m	k_h	k_c
	kg/m^3	W/m^3	W/m^3
SURA M235-35A	7600	204.5	0.3239
SURA M250-35A	7600	219.3	0.3446
B35AV1500	7650	130.7	0.3279
B35AV1900	7650	156.2	0.5543

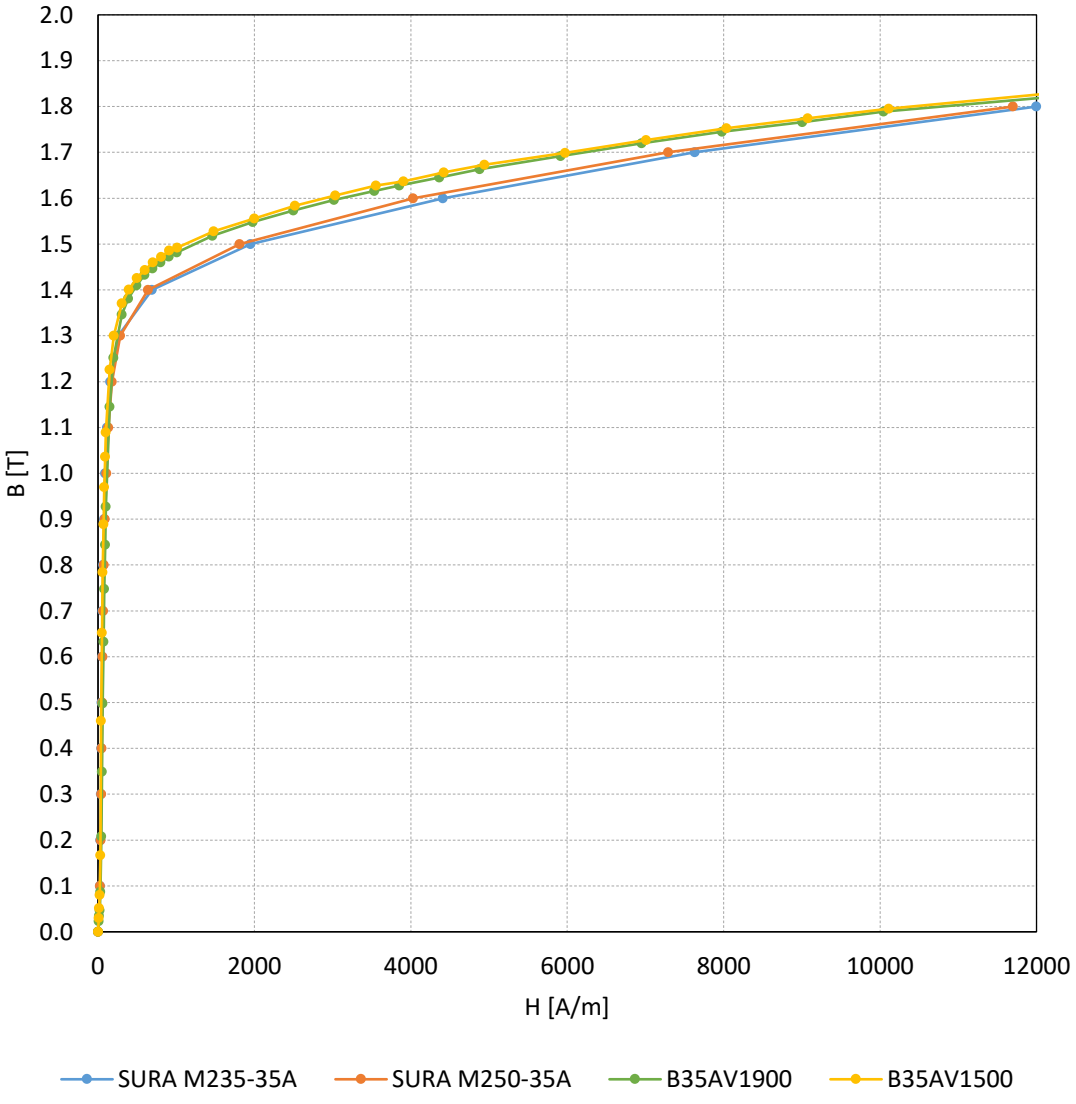

Figure B-4 BH curve of lamination steels.

Appendix C Winding Factor Basics

C.1 Distribution Factor

The distribution factor is the ratio between the EMF from a distributed winding and the one from concentrated winding. Considering the EMF vectors with amplitude as E_{m} distributed in space with a slot angle of α, as shown in Figure C-1 (a), the composed EMF vector is [75]

$$E_{\mathrm{q1}} = 2R\sin\frac{q\alpha}{2} = E_{\mathrm{m}}\frac{\sin\frac{q\alpha}{2}}{\sin\frac{\alpha}{2}} \tag{C-1}$$

The start and end points of the EMF vectors are distributed along a circle with the radius of

$$R = \frac{E_{\mathrm{m}}}{2\sin\frac{\alpha}{2}} \tag{C-2}$$

The winding factor is the ratio between E_{q1} and qE_{m}, i.e. vector summation and scalar summation:

$$k_{\mathrm{d1}} = \frac{E_{\mathrm{q1}}}{qE_{\mathrm{m}}} = \frac{\sin\frac{q\alpha}{2}}{q\sin\frac{\alpha}{2}} \tag{C-3}$$

C.2 Pitch Factor

The pitch factor is the ratio between the EMF from short-pitch winding and the one from full-pitch winding. Considering the EMF vectors with amplitude as E_{m} distributed in space with a pole pitch of τ and a coil pitch of y, as shown in Figure C-1 (b), the composed EMF vector is [75]

$$E_{\mathrm{q1}} = 2E_{\mathrm{m}}\cos\frac{\pi}{2}\left(1-\frac{y}{\tau}\right) = 2E_{\mathrm{m}}\sin\frac{\pi}{2}\frac{y}{\tau} \tag{C-4}$$

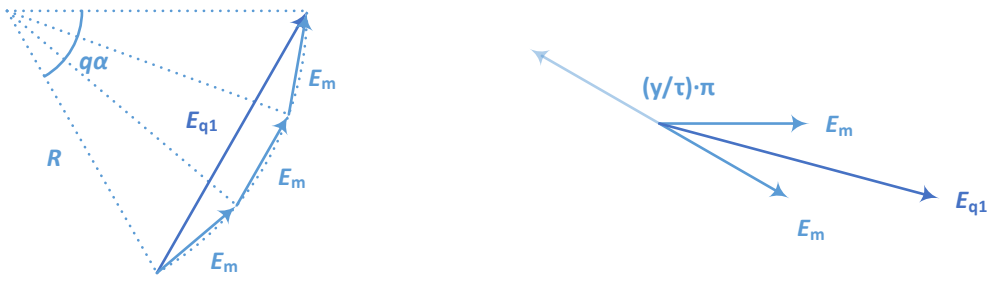

(a) (b)

Figure C-1 General winding factor formulas.

The short-pitch winding factor is the ratio between E_{q1} and $2E_{\mathrm{m}}$, i.e. vector summation and scalar summation:

$$k_{\mathrm{p1}} = \frac{E_{\mathrm{q1}}}{2E_{\mathrm{m}}} = \sin\frac{\pi}{2}\frac{y}{\tau} \tag{C-5}$$

C.2 Winding Factor

The winding factor k_{w1} is the multiplication of k_{d1} and k_{p1} [75]

$$k_{\mathrm{w1}} = k_{\mathrm{d1}} \cdot k_{\mathrm{p1}} \tag{C-6}$$

In general, considering a harmonic order of ν, then

$$k_{\mathrm{d}\nu} = \frac{\sin\nu\frac{q\alpha}{2}}{q\sin\nu\frac{\alpha}{2}} \qquad k_{\mathrm{p}\nu} = \sin\left(\nu\frac{y}{\tau}90°\right) \qquad k_{\mathrm{w}\nu} = k_{\mathrm{d}\nu} \cdot k_{\mathrm{p}\nu} \tag{C-7}$$

As an example, the winding factor at harmonic order from 1 to 51 of 8-Pole 48-Slot with short pitch of 1 slot, i.e. $m = 3$, $p = 4$, $q = 2$, $y = 5$, is as shown in Figure C-2.

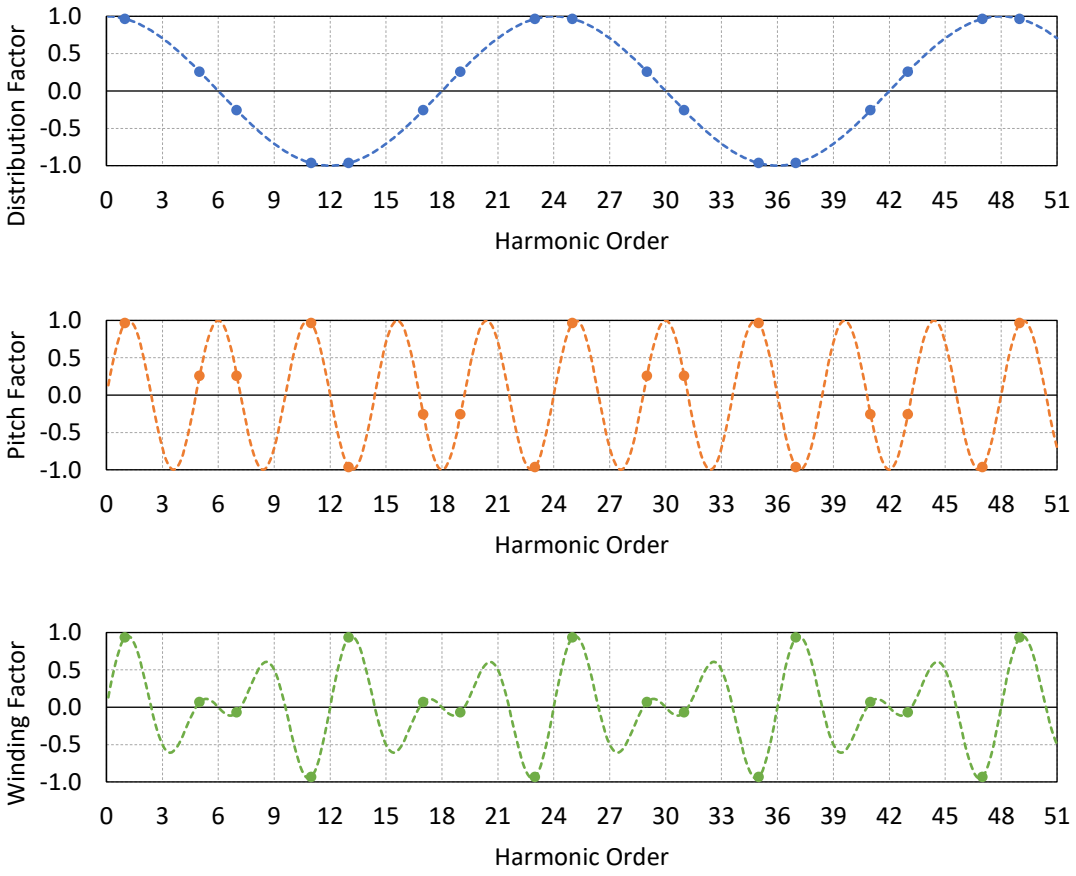

Figure C-2 Winding factor ($m = 3$, $p = 4$, $q = 2$, $y = 5$).

Appendix D Torque Ripple and Harmonics

Due to the fact that electromagnetic torque can be formulated as electromagnetic power divided by mechanical speed

$$T_{\mathrm{em}} = \frac{p_{\mathrm{em}}}{\Omega_{\mathrm{r}}} \tag{D-1}$$

to analyze the harmonics in electromagnetic power is sufficient to conclude the harmonics in electromagnetic torque. There are two approaches to achieve the conclusion, through three-phase quantity analysis or through dq-quantity analysis.

D.1 Approach Through Three-Phase Quantity Analysis

The instantaneous electromagnetic torque can be formulated as electromagnetic power divided by mechanical speed

$$T_{\mathrm{em}} = \frac{p_{\mathrm{em}}}{\Omega_{\mathrm{r}}} = \frac{e_{\mathrm{a}}(t) \cdot i_{\mathrm{a}}(t) + e_{\mathrm{b}}(t) \cdot i_{\mathrm{b}}(t) + e_{\mathrm{c}}(t) \cdot i_{\mathrm{c}}(t)}{\Omega_{\mathrm{r}}} \tag{D-2}$$

where the instantaneous EMF of each phase $e(t)$ and the instantaneous current of each phase $i(t)$ contain harmonic contents

$$e(t) = \sum_{\mu=1}^{\infty} e_{\mu}(t) \quad and \quad i(t) = \sum_{\nu=1}^{\infty} i_{\nu}(t) \tag{D-3}$$

Therefore, the product of each EMF harmonic and each current harmonic gives the corresponding power component

$$\begin{aligned} p_{\mu\nu}(t) &= e_{\mu\mathrm{a}}(t) \cdot i_{\nu\mathrm{a}}(t) + e_{\mu\mathrm{b}}(t) \cdot i_{\nu\mathrm{b}}(t) + e_{\mu\mathrm{c}}(t) \cdot i_{\nu\mathrm{c}}(t) \\ &= \left|E_{\mu}\right| \cdot |I_{\nu}| \cdot \begin{Bmatrix} \cos\left(\mu \cdot \omega t + \varphi_{\mu}\right) \cdot \cos(\nu \cdot \omega t + \varphi_{\nu}) \\ + \cos\left(\mu \cdot (\omega t - 120°) + \varphi_{\mu}\right) \cdot \cos(\nu \cdot (\omega t - 120°) + \varphi_{\nu}) \\ + \cos\left(\mu \cdot (\omega t + 120°) + \varphi_{\mu}\right) \cdot \cos(\nu \cdot (\omega t + 120°) + \varphi_{\nu}) \end{Bmatrix} \\ &= \frac{\left|E_{\mu}\right| \cdot |I_{\nu}|}{2} \cdot \begin{Bmatrix} \cos\left[(\mu + \nu) \cdot \omega t + \left(\varphi_{\mu} + \varphi_{\nu}\right)\right] \\ + \cos\left[(\mu - \nu) \cdot \omega t + \left(\varphi_{\mu} - \varphi_{\nu}\right)\right] \\ + \cos\left[(\mu + \nu) \cdot (\omega t - 120°) + \left(\varphi_{\mu} + \varphi_{\nu}\right)\right] \\ + \cos\left[(\mu - \nu) \cdot (\omega t - 120°) + \left(\varphi_{\mu} - \varphi_{\nu}\right)\right] \\ + \cos\left[(\mu + \nu) \cdot (\omega t + 120°) + \left(\varphi_{\mu} + \varphi_{\nu}\right)\right] \\ + \cos\left[(\mu - \nu) \cdot (\omega t + 120°) + \left(\varphi_{\mu} - \varphi_{\nu}\right)\right] \end{Bmatrix} \end{aligned} \tag{D-4}$$

The three $(\mu + \nu)$ terms can be one group and the three $(\mu - \nu)$ terms can be another group. The $(\mu + \nu)$ group or the $(\mu - \nu)$ group will be cancelled out if it is not a multiple of three, and

only the group that is a multiple of three can exist. In other words, if $\mu - \nu \neq 3 \cdot n$, where n is a natural number, then the $(\mu - \nu)$ terms will be cancelled, which means

$$p_{\mu\nu}(t) = \frac{3}{2} \cdot |E_\mu| \cdot |I_\nu| \cdot \cos\left[(\mu + \nu) \cdot \omega t + \left(\varphi_\mu + \varphi_\nu\right)\right] \quad \text{(D-5)}$$

And if $\mu + \nu \neq 3 \cdot n$, then the $(\mu + \nu)$ terms will be cancelled, which means

$$p_{\mu\nu}(t) = \frac{3}{2} \cdot |E_\mu| \cdot |I_\nu| \cdot \cos\left[(\mu - \nu) \cdot \omega t + \left(\varphi_\mu - \varphi_\nu\right)\right] \quad \text{(D-6)}$$

For instance, in terms of $\mu = 5$ and $\nu = 1$, since $\mu - \nu = 4 \neq 3 \cdot n$, then

$$p_{\mu\nu}(t) = \frac{3}{2} \cdot |E_5| \cdot |I_1| \cdot \cos\left[6 \cdot \omega t + \left(\varphi_{E_5} + \varphi_{I_1}\right)\right] \quad \text{(D-7)}$$

and as for $\mu = 7$ and $\nu = 1$, since $\mu + \nu = 8 \neq 3 \cdot n$

$$p_{\mu\nu}(t) = \frac{3}{2} \cdot |E_7| \cdot |I_1| \cdot \cos\left[6 \cdot \omega t + \left(\varphi_{E_7} - \varphi_{I_1}\right)\right] \quad \text{(D-8)}$$

which means the 5th and 7th back-EMF harmonic will contribute to the 6th harmonic in torque.

The current is half-wave symmetric so ν must be an odd number. In case of Y-connection, zero-sequence cannot flow which means ν cannot be a multiple of three as well. Hence

$$\nu = 6 \cdot n \pm 1 \quad \text{(D-9)}$$

This is because all the numbers above 6 can be expressed as $6 \cdot n - 2$, $6 \cdot n - 1$, $6 \cdot n$, $6 \cdot n + 1$, $6 \cdot n + 2$ and $6 \cdot n + 3$, among which, $6 \cdot n$ and $6 \cdot n \pm 2$ are even numbers, while $6 \cdot n$ and $6 \cdot n + 3$ are multiples of three, and this indicates that the only remaining ones are $\nu = 6 \cdot n \pm 1$.

The back-EMF is half-wave symmetric so μ must be an odd number. In addition, since $\mu \pm \nu = 3 \cdot n$, while ν cannot be a multiple of three, μ cannot be a multiple of three either. Hence although all the odd μ exists, only the term

$$\mu = 6 \cdot n \pm 1 \quad \text{(D-10)}$$

contributes to the torque. This further indicates that the EMF harmonic components $6 \cdot n \pm 1$, i.e. 5, 7, 11, 13 etc. are the ones that should be paid attention to.

D.2 Approach Through DQ Quantity Analysis

This can also be explained in dq-frame. The currents in abc-frame

$$\begin{bmatrix} i_{\nu \mathrm{a}} \\ i_{\nu \mathrm{b}} \\ i_{\nu \mathrm{c}} \end{bmatrix} = I_\nu \begin{bmatrix} \cos(\nu \cdot \omega t + \varphi_\nu) \\ \cos[\nu \cdot (\omega t - 120°) + \varphi_\nu] \\ \cos[\nu \cdot (\omega t + 120°) + \varphi_\nu] \end{bmatrix} \tag{D-11}$$

can be transformed to αβ-frame as

$$\begin{aligned} \begin{bmatrix} i_{\nu\alpha} \\ i_{\nu\beta} \end{bmatrix} &= \frac{2}{3} \begin{bmatrix} 1 & -\frac{1}{2} & -\frac{1}{2} \\ 0 & \frac{\sqrt{3}}{2} & -\frac{\sqrt{3}}{2} \end{bmatrix} \begin{bmatrix} i_{\nu \mathrm{a}} \\ i_{\nu \mathrm{b}} \\ i_{\nu \mathrm{c}} \end{bmatrix} = \frac{2}{3} I_\nu \begin{bmatrix} 1 & -\frac{1}{2} & -\frac{1}{2} \\ 0 & \frac{\sqrt{3}}{2} & -\frac{\sqrt{3}}{2} \end{bmatrix} \begin{bmatrix} \cos(\nu \cdot \omega t + \varphi_\nu) \\ \cos[\nu \cdot (\omega t - 120°) + \varphi_\nu] \\ \cos[\nu \cdot (\omega t + 120°) + \varphi_\nu] \end{bmatrix} \\ &= \frac{2}{3} I_\nu \begin{bmatrix} \cos(\nu \cdot \omega t + \varphi_\nu) - \frac{1}{2}\cos[\nu \cdot (\omega t - 120°) + \varphi_\nu] - \frac{1}{2}\cos[\nu \cdot (\omega t + 120°) + \varphi_\nu] \\ \frac{\sqrt{3}}{2}\cos[\nu \cdot (\omega t - 120°) + \varphi_\nu] - \frac{\sqrt{3}}{2}\cos[\nu \cdot (\omega t + 120°) + \varphi_\nu] \end{bmatrix} \end{aligned} \tag{D-12}$$

The α component is

$$i_{\nu\alpha} = \frac{2}{3} \cdot I_\nu \cdot \frac{3}{2} \cos(\nu \cdot \omega t + \varphi_\nu) = I_\nu \cdot \cos(\nu \cdot \omega t + \varphi_\nu) \tag{D-13}$$

and the β component is

$$\begin{aligned} i_{\nu\beta} &= \frac{2}{3} \cdot I_\nu \cdot \left\{ \frac{\sqrt{3}}{2} \cos[\nu \cdot (\omega t - 120°) + \varphi_\nu] - \frac{\sqrt{3}}{2} \cos[\nu \cdot (\omega t + 120°) + \varphi_\nu] \right\} \\ &= \frac{\sqrt{3}}{3} \cdot I_\nu \cdot \{\cos(\nu \cdot \omega t - \nu \cdot 120° + \varphi_\nu) - \cos(\nu \cdot \omega t + \nu \cdot 120° + \varphi_\nu)\} \\ &= \frac{2\sqrt{3}}{3} \cdot I_\nu \cdot \sin(\nu \cdot \omega t + \varphi_\nu) \sin(\nu \cdot 120°) \end{aligned} \tag{D-14}$$

In case of $\nu = 6n - 1$,

$$\begin{aligned} \begin{bmatrix} i_{\nu \mathrm{d}} \\ i_{\nu \mathrm{q}} \end{bmatrix} &= \begin{bmatrix} \cos \omega t & \sin \omega t \\ -\sin \omega t & \cos \omega t \end{bmatrix} \begin{bmatrix} i_{\nu\alpha} \\ i_{\nu\beta} \end{bmatrix} = I_\nu \begin{bmatrix} \cos \omega t & \sin \omega t \\ -\sin \omega t & \cos \omega t \end{bmatrix} \begin{bmatrix} \cos(\nu \cdot \omega t + \varphi_\nu) \\ -\sin(\nu \cdot \omega t + \varphi_\nu) \end{bmatrix} \\ &= I_\nu \begin{bmatrix} \cos \omega t \cdot \cos(\nu \cdot \omega t + \varphi_\nu) - \sin \omega t \cdot \sin(\nu \cdot \omega t + \varphi_\nu) \\ -\sin \omega t \cdot \cos(\nu \cdot \omega t + \varphi_\nu) - \cos \omega t \cdot \sin(\nu \cdot \omega t + \varphi_\nu) \end{bmatrix} \\ &= I_\nu \begin{bmatrix} \cos[(\nu + 1) \cdot \omega t + \varphi_\nu] \\ -\sin[(\nu + 1) \cdot \omega t + \varphi_\nu] \end{bmatrix} \end{aligned} \tag{D-15}$$

In case of $\nu = 6n + 1$

$$\begin{aligned}\begin{bmatrix} i_{\nu\mathrm{d}} \\ i_{\nu\mathrm{q}} \end{bmatrix} &= \begin{bmatrix} \cos\omega t & \sin\omega t \\ -\sin\omega t & \cos\omega t \end{bmatrix} \begin{bmatrix} i_{\nu\alpha} \\ i_{\nu\beta} \end{bmatrix} = I_\nu \begin{bmatrix} \cos\omega t & \sin\omega t \\ -\sin\omega t & \cos\omega t \end{bmatrix} \begin{bmatrix} \cos(\nu\cdot\omega t+\varphi_\nu) \\ \sin(\nu\cdot\omega t+\varphi_\nu) \end{bmatrix} \\ &= I_\nu \begin{bmatrix} \cos\omega t\cdot\cos(\nu\cdot\omega t+\varphi_\nu)+\sin\omega t\cdot\sin(\nu\cdot\omega t+\varphi_\nu) \\ -\sin\omega t\cdot\cos(\nu\cdot\omega t+\varphi_\nu)+\cos\omega t\cdot\sin(\nu\cdot\omega t+\varphi_\nu) \end{bmatrix} \\ &= I_\nu \begin{bmatrix} \cos[(\nu-1)\cdot\omega t+\varphi_\nu] \\ \sin[(\nu-1)\cdot\omega t+\varphi_\nu] \end{bmatrix}\end{aligned} \tag{D-16}$$

The derivations for the EMF harmonics are similar. As a summary, Table D-1 shows the transformation from abc-frame to dq-frame

Table D-1. Harmonics in dq-frame.

$\begin{bmatrix} i_{\nu\mathrm{a}} \\ i_{\nu\mathrm{b}} \\ i_{\nu\mathrm{c}} \end{bmatrix} = I_\nu \begin{bmatrix} \cos(\nu\cdot\omega t+\varphi_\nu) \\ \cos[\nu\cdot(\omega t-120°)+\varphi_\nu] \\ \cos[\nu\cdot(\omega t+120°)+\varphi_\nu] \end{bmatrix}$	$\overset{\nu=6n-1}{\Longrightarrow} \begin{bmatrix} i_{\nu\mathrm{d}} \\ i_{\nu\mathrm{q}} \end{bmatrix} = I_\nu \begin{bmatrix} \cos[(\nu+1)\cdot\omega t+\varphi_\nu] \\ -\sin[(\nu+1)\cdot\omega t+\varphi_\nu] \end{bmatrix}$
	$\overset{\nu=6n+1}{\Longrightarrow} \begin{bmatrix} i_{\nu\mathrm{d}} \\ i_{\nu\mathrm{q}} \end{bmatrix} = I_\nu \begin{bmatrix} \cos[(\nu-1)\cdot\omega t+\varphi_\nu] \\ \sin[(\nu-1)\cdot\omega t+\varphi_\nu] \end{bmatrix}$
$\begin{bmatrix} e_{\nu\mathrm{a}} \\ e_{\nu\mathrm{b}} \\ e_{\nu\mathrm{c}} \end{bmatrix} = U_\mu \begin{bmatrix} \cos(\mu\cdot\omega t+\varphi_\mu) \\ \cos[\mu\cdot(\omega t-120°)+\varphi_\mu] \\ \cos[\mu\cdot(\omega t+120°)+\varphi_\mu] \end{bmatrix}$	$\overset{\mu=6n-1}{\Longrightarrow} \begin{bmatrix} e_{\mu\mathrm{d}} \\ e_{\mu\mathrm{q}} \end{bmatrix} = U_\mu \begin{bmatrix} \cos[(\mu+1)\cdot\omega t+\varphi_\mu] \\ -\sin[(\mu+1)\cdot\omega t+\varphi_\mu] \end{bmatrix}$
	$\overset{\mu=6n+1}{\Longrightarrow} \begin{bmatrix} e_{\mu\mathrm{d}} \\ e_{\mu\mathrm{q}} \end{bmatrix} = U_\mu \begin{bmatrix} \cos[(\mu-1)\cdot\omega t+\varphi_\mu] \\ \sin[(\mu-1)\cdot\omega t+\varphi_\mu] \end{bmatrix}$

Hence the electromagnetic power can be expressed in dq-frame as

$$p_{\mu\nu}(t) = \frac{3}{2}\cdot\mathrm{real}\{e\cdot i^*\} = \frac{3}{2}\cdot\mathrm{real}\{(e_{\mu\mathrm{d}}+\mathrm{j}e_{\mu\mathrm{q}})\cdot(i_{\nu\mathrm{d}}-\mathrm{j}i_{\nu\mathrm{q}})\} = \frac{3}{2}\cdot[e_{\mu\mathrm{d}}i_{\nu\mathrm{d}}+e_{\mu\mathrm{q}}i_{\nu\mathrm{q}}] \tag{D-17}$$

D.3 Summary

Summary can be concluded in Table D-2.

Table D-2. Summary of torque ripples and harmonics

$\boldsymbol{p_{\mu\nu}(t)}$	$\boldsymbol{\nu=6n-1}$	$\boldsymbol{\nu=6n+1}$
$\boldsymbol{\mu=6n-1}$	$\frac{3}{2}\cdot E_\mu\cdot I_\nu\cdot\cos\left[(\mu-\nu)\cdot\omega t+\varphi_\mu-\varphi_\nu\right]$	$\frac{3}{2}\cdot E_\mu\cdot I_\nu\cdot\cos\left[(\mu+\nu)\cdot\omega t+\varphi_\mu-\varphi_\nu\right]$
$\boldsymbol{\mu=6n+1}$	$\frac{3}{2}\cdot E_\mu\cdot I_\nu\cdot\cos\left[(\mu+\nu)\cdot\omega t+\varphi_\mu-\varphi_\nu\right]$	$\frac{3}{2}\cdot E_\mu\cdot I_\nu\cdot\cos\left[(\mu-\nu)\cdot\omega t+\varphi_\mu-\varphi_\nu\right]$

Appendix E PCB Layout

The PCB layout in this study are attached here.

- Figure E-1 shows a signal processing PCB with four layers. It can convert four voltage-source signals and four current- or voltage-source signals to 0 – 3.3 V for the DSP. It can also power an encoder and receive the encoder signals with common-mode rejection.

- Figure E-2 shows a gate driver PCB for one converter leg. The design is intended to be as universal as possible. It can drive discrete semiconductors as well as power modules. The switching signals to the PCB can be through electrical wires or through fiber-optical cables.

- Figure E-3 shows a dc-link PCB with capacitors possibly populated on both sides. Zenner diodes can be placed on the top side, across positive and negative of the dc-link, and across drain and source of the lower switch of each leg as well.

- Figure E-4 shows an H-bridge inverter PCB with surface-mounted semiconductors. This is used to deliver power to the rotating transformer in the brushless excitation system. Efforts have been spent to minimize the inductance along the dc-link capacitor – upper switch – lower switch loop in order to reduce the switching ripples as much as possible.

- Figure E-5 shows an H-bridge rectifier PCB with surface-mounted capacitors across the output terminals. This is used to deliver power from the rotating transformer to the field winding in the brushless excitation system. The surface-mounted capacitors are to mitigate the switching resonances between transformer inductances and the diode parasitic capacitance.

E.1 Control & Signal Processing PCB

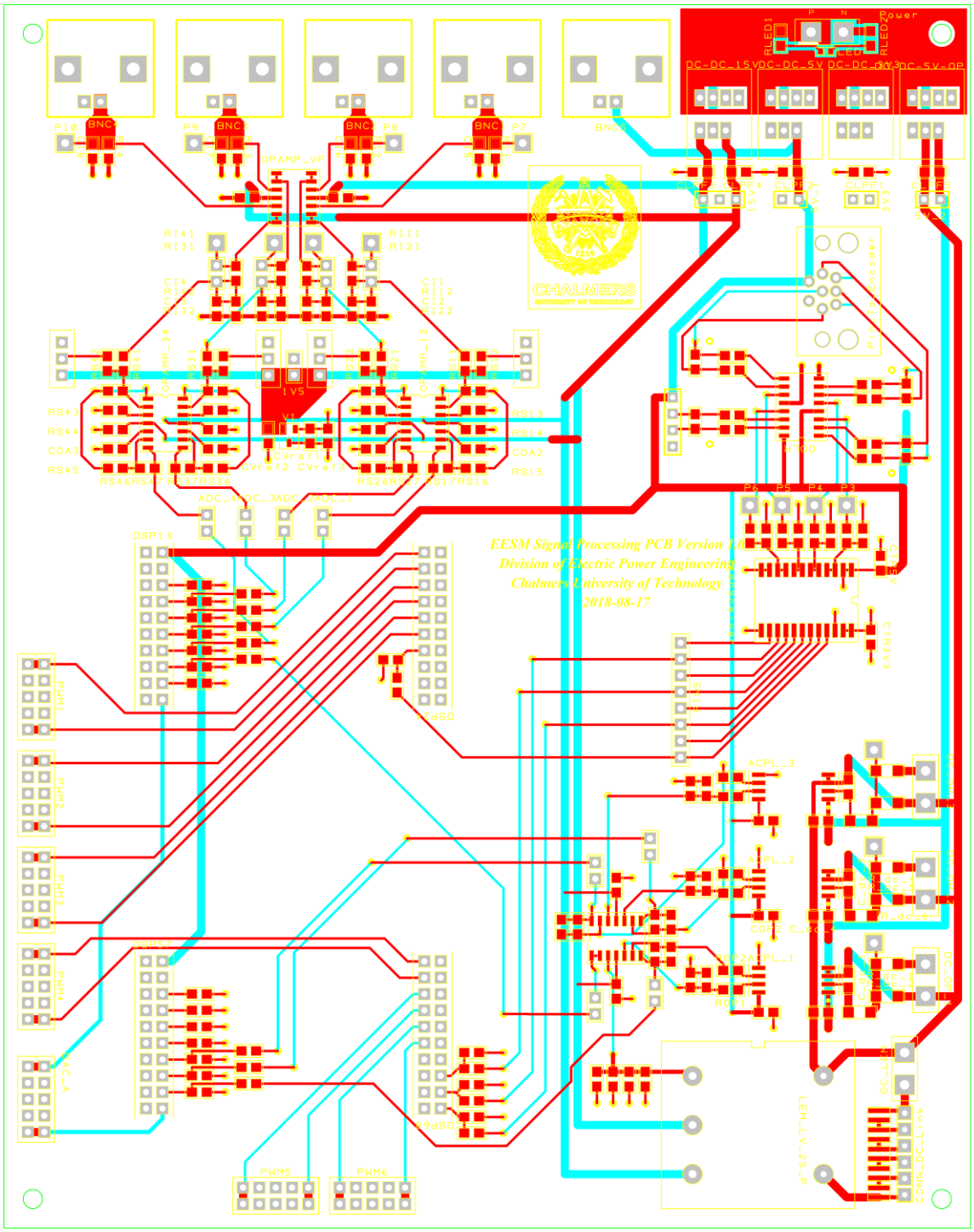

Figure E-1 Control & Signal Processing PCB Design.

E.2 Gate Driver PCB for Three-Phase Inverter

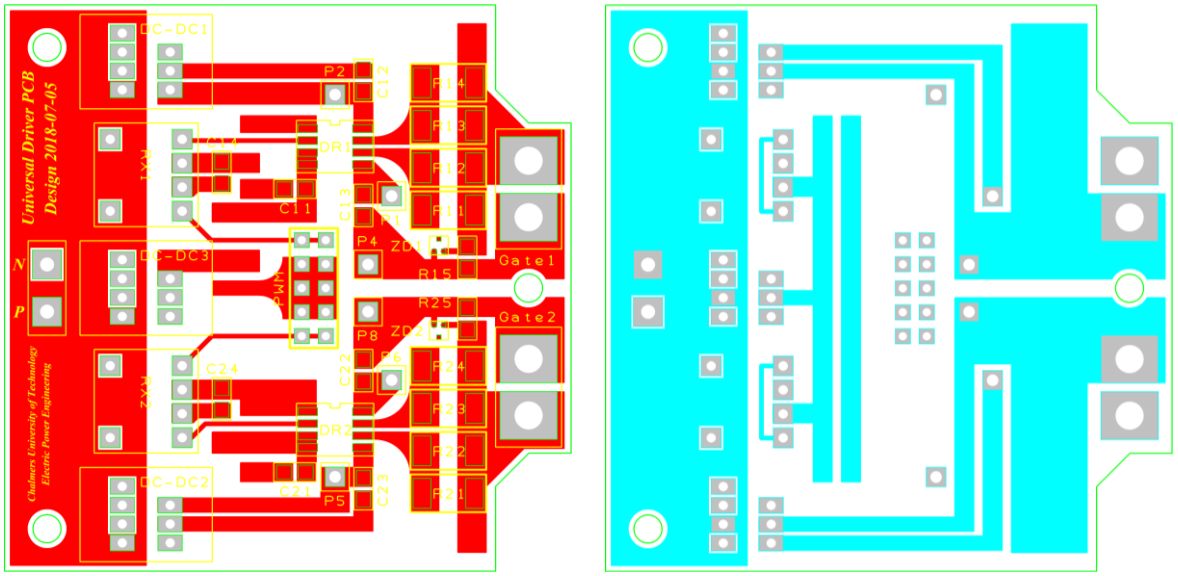

(a) Top side (b) Bottom side

Figure E-2 Gate Driver PCB for Three-Phase Inverter.

E.3 DC-Link PCB

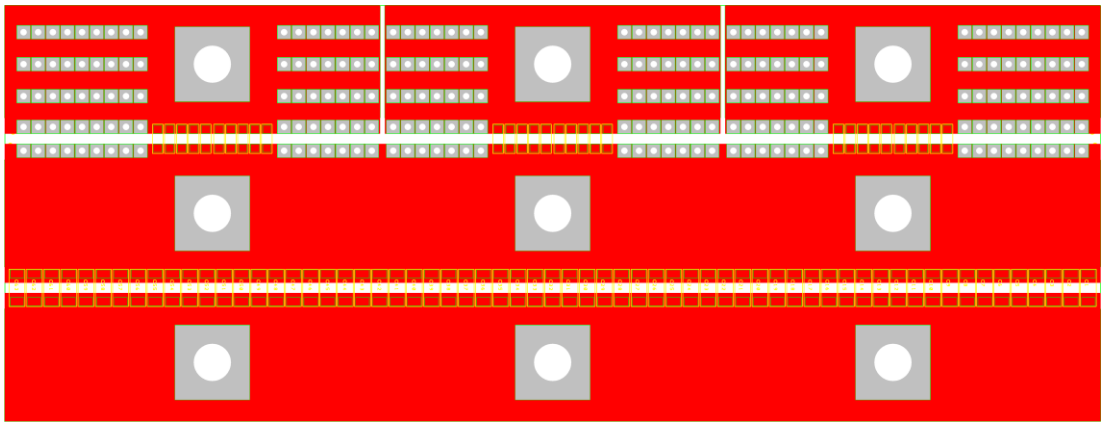

(a) Top side

(b) Bottom side

Figure E-3 DC-Link PCB.

E.4 H-Bridge Inverter PCB

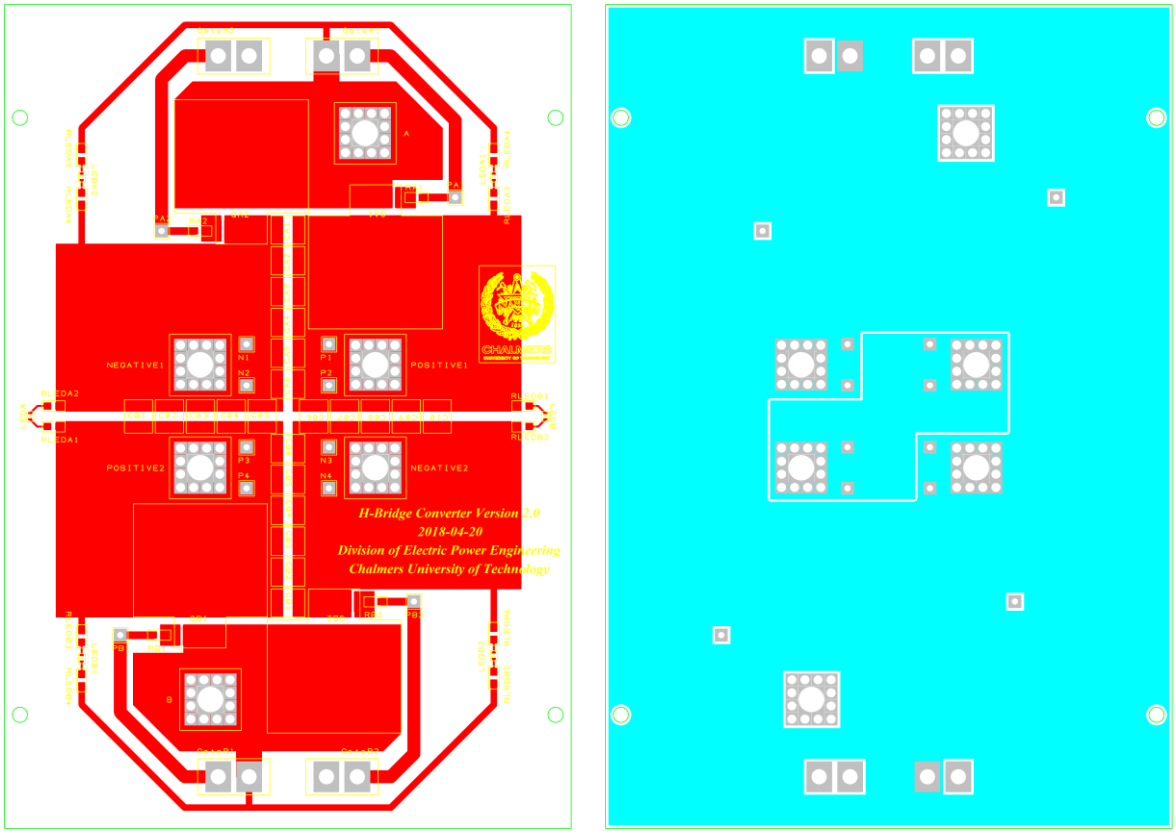

(a) Top side (b) Bottom side

Figure E-4 H-bridge inverter for high frequency brushless excitation.

F.5 H-Bridge Rectifier PCB

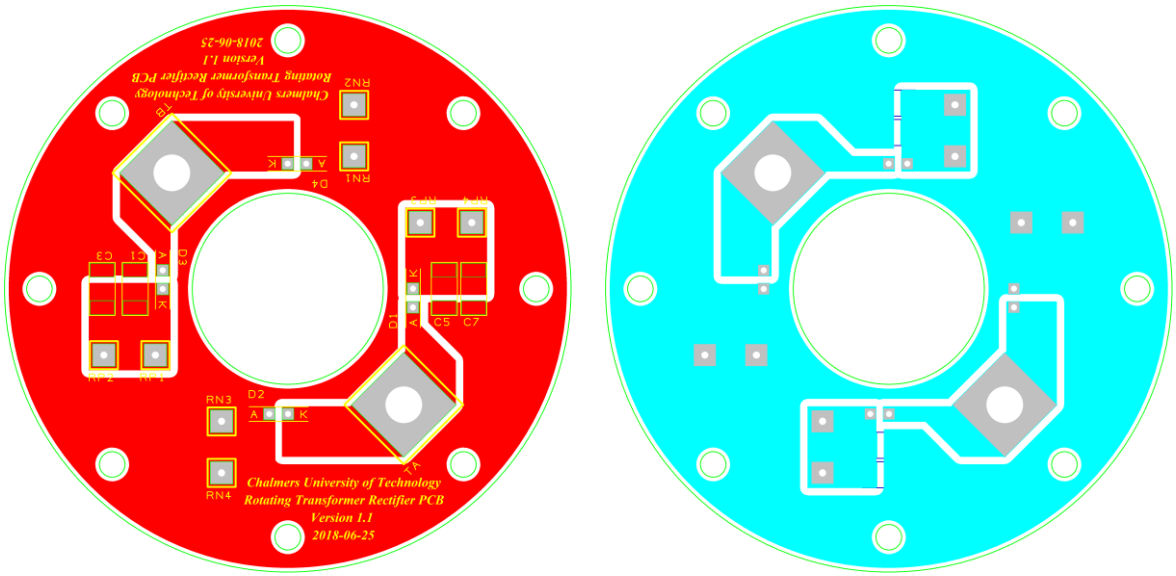

(a) Top side (b) Bottom side

Figure E-5 H-bridge rectifier for high frequency brushless excitation.